PETROGENESIS OF HYBRID PORPHYRY PIPES AND EVOLUTION OF ALKALINE MAGMAS IN THE KANABEAM IGNEOUS COMPLEX, SOUTHERN NAMIBIA

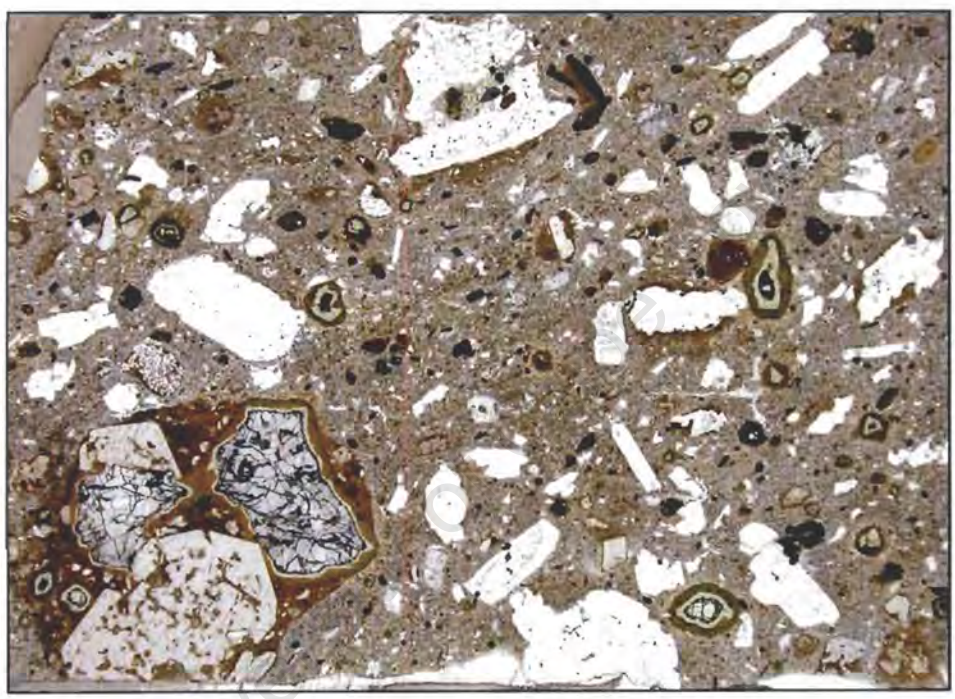

Natalie Kirsty Dunn

Thesis Presented for the Degree of

MASTER OF SCIENCE

Department of Geological Sciences

UNIVERSITY OF CAPE TOWN

December 2001

DECLARATION

I hereby declare that all of the work presented in this thesis is my own, except where otherwise stated in the text.

NK Dunn

Signed by candidate

ABSTRACT

The linear Kuboos Bremen Igneous Province (KBIP) stretches 270km from the South African Atlantic coast north-eastwards into southern Namibia, and was emplaced at approximately 500Ma. One central complex within the KBIP is the Kanabeam Igneous Complex (KIC) where practically all the rock types found in the province are represented and include nepheline syenites, quartz syenites as well as granites. In addition to these plutonic phases a number of late stage, xenolith rich porphyry pipes were emplaced, exploiting contact zones between earlier plutons. Xenolith types include gabbro possibly derived from unexposed deeper parts of the KIC, syenites (more proximal components of the KIC), trachytes from an inferred overlying volcanic edifice, basement granites, gneisses and metasediments as well as Nama Group sediments.

Petrographic examination in the porphyries has revealed that there are numerous minerals out of textural equilibrium, including olivine, pyroxene and plagioclase. Other minerals such as biotite, amphibole and alkali feldspar appear more stable. Observed textural and mineralogical heterogeneity of the porphyry groundmass is thought to result from mingling and mixing of a number of observed distinct magmas to form hybrids, a process consistent with the mineralogical disequilibria. Bulk geochemical patterns of the hybrid porphyries are predictably variable but two compositional groups can be recognised. A tephriphonolitic group appears to be the product of phonolite-tephrite mingling and a trachyandesitic group formed by tephrite-trachyte interaction. Both hybrid magmas appear to have mixed with a partially crystalline gabbro producing higher than expected Fe_2O_3, MgO and ferro-magnesian trace elements. This gabbro is likely to be the source of the olivine, pyroxene and plagioclase xenocrysts. Radiogenic isotope patterns indicate that the tephriphonolite and trachyandesite magma end members were crustally contaminated by AFC type processes.

Dedication

To my parents

To get this far would never have been possible without you.

And to Josh

All your patience paid off.

ACKNOWLEDGEMENTS

Thanks goes to Prof David Reid my supervisor who was a mentor, support and a driving force. Without his guidance and research funding this thesis would never have been possible.

My parents who have provided the support and education to get me this far in my career and have paid the price for the best education that money could buy. Thank you for getting me this far. The rest of the road was shear guts and determination.

To Maarten de Wit who provided much needed work that enabled me to fund myself during the course of the thesis, I am forever grateful. It would never have been possible without funding.

My extended family, Glenn von Zeil the warden, Mrs Jordaan and Mrs Fortune the supervisors and my fellow colleagues, the subwardens of Groote Schuur complex during 1999 and 2000 are thanked for their support and assistance when the times called for it.

Shireen Govender who taught me how to prepare and run samples on the mass spectrometer, and Fran Pocock and Ernest who assisted during the preparation and running of samples by XRF were all important in the completion of this work and are acknowledged. Thanks are extended to Andreas Spath and Ilsa who aided in ICP-MS preparation and analysis. David and Roger who work diligently in the basement preparing both thin and polished sections are also thanked.

The University of Durban Westville is acknowledged for the use of their Super Probe and Trevor and Alan are thanked for the guidance and assistance that he provided during the running of the probe.

To my friends thanks for all the good times and the support and to Josh who always knew this was possible.

Lastly I am grateful to the Department of Geological Sciences, University of Cape Town who allowed me to register for my MSc.

TABLE OF CONTENTS

1 INTRODUCTION

The Kuboos-Bremen Igneous Province (KBIP), first described by Söhnge and De Villiers (1948) consists of predominantly alkaline felsic rocks ranging from granite to nepheline syenite and including carbonatite. Within the 10 discrete complexes identified by Kröner and Blignault (1976) as making up the KBIP, practically all the rock types associated with intra-continental alkaline magmatism are represented. Mafic rocks however, comprise <5% of the KBIP and are confined to xenoliths of gabbroic composition within the felsic units but this could be a factor of erosion. Kanabeam, a centrally located complex within the KBIP (Figure 1.1) occurs in southern Namibia and plays host to a group of rocks investigated in this thesis.

The main focus of the study is a suite of late stage intrusive pipes, dykes and plugs within the nepheline syenites of the Kanabeam Igneous Complex (KIC). The late stage porphyry pipes in the KIC are found in two clusters within the complex. Geochemical and petrographic characterisation has been utilised in modelling their petrogenesis and mode of emplacement.

Preliminary investigation as well as descriptions by Reid (1991) revealed that assimilation and/or magma mixing possibly played a role in the formation of the pipes. These processes are investigated in this thesis. The plutonic diversity of Kanabeam is also explored as these units may provide a key to the parental magmas of the pipes. The diversity of rock types encountered at Kanabeam also offers the opportunity to study a wide range of closely related (in space and time) quartz and nepheline bearing rocks. The possibility that these two lineages may be genetically related in the KIC is explored as well as the possibility that either or both lineages may have contributed to the pipes.

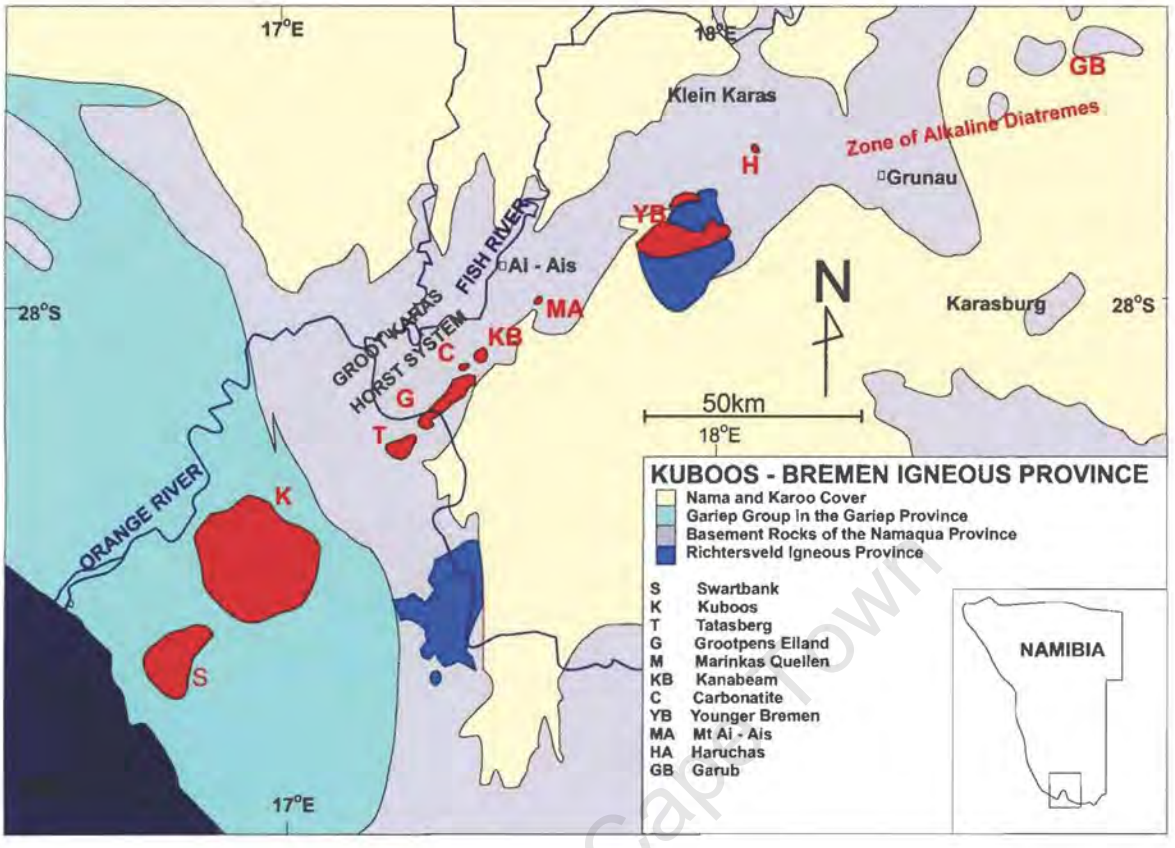

Figure 1.1 The Kuboos-Bremen Igneous Province. Distribution of igneous centres in relation to its continental setting (after Kröner and Blignault, 1976).

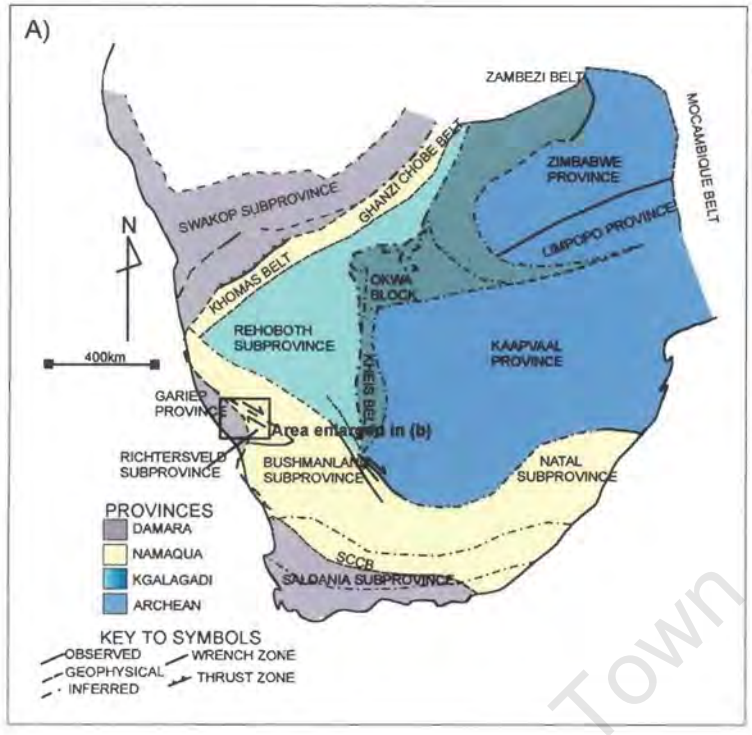

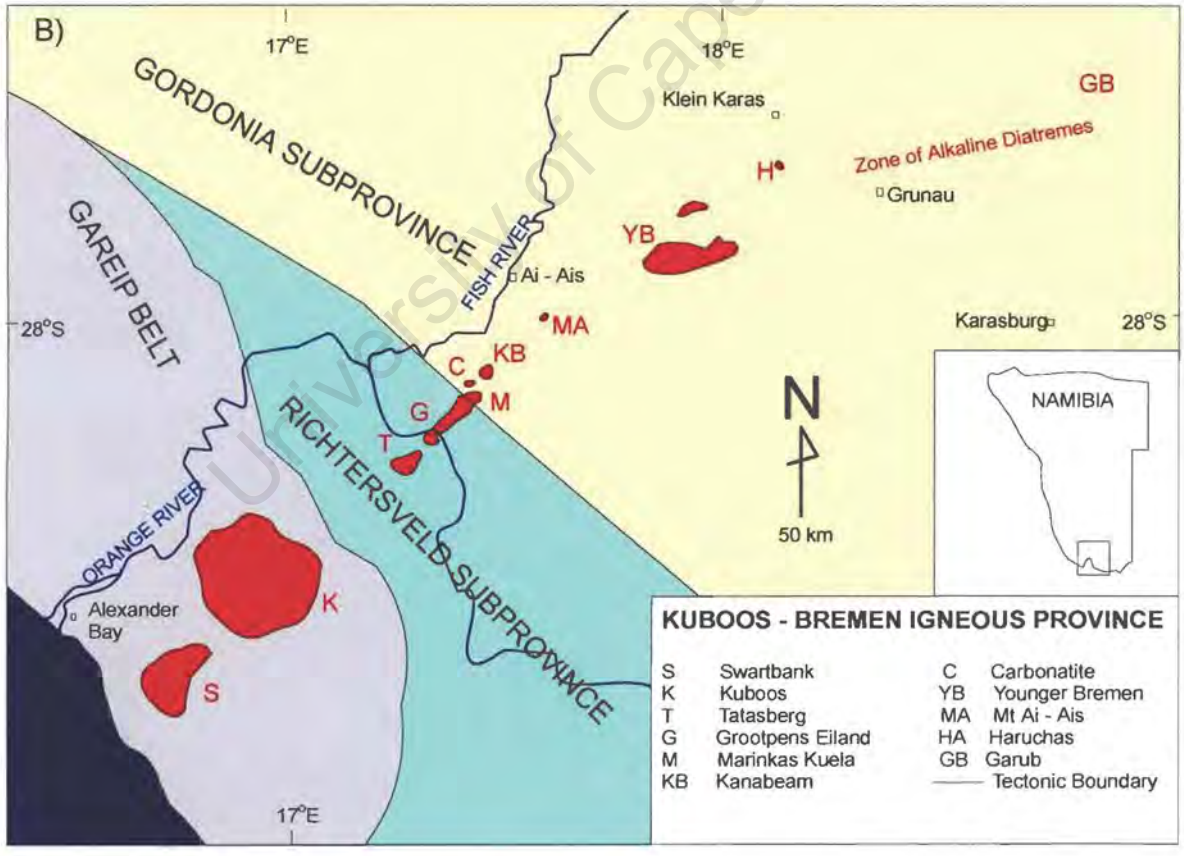

Figure 2.1 A) Geological provinces of southern Africa (after Hartnady *et al.*, 1985). B) Map showing the distribution of igneous centres that make up the Kuboos Bremen Igneous Province in relation to tectonic features with cover sequences removed. The Namaqua Province has been subdivided into subprovinces whereas provinces are only shown in Figure 1.1.

2 GEOLOGICAL SETTING

2.1 Introduction

The Kuboos-Bremen Igneous Province (KBIP) consists of 10 alkaline igneous centres that straddle the border between north-western South Africa and southern Namibia. The KBIP forms a remarkable 270km lineament that cuts across three major tectono-stratigraphic provinces (Figure 2.1) (Martin, 1965), including

1) Namaqua Province (Paleo- to Mesoproterozoic metamorphic complexes)
2) Gariep Province (Neoproterozoic orogenic belt)
3) Nama Group (Late Neoproterozoic to Early Cambrian foreland basin)

Previously published zircon ages for the KBIP range from 525±60Ma to 507±6Ma and Rb-Sr errorchron ages range from 553+13Ma to 514+9Ma (Allsopp *et al.*, 1979; Frimmel, 2001) but new data reported in this thesis (Chapter 7) indicate that the province was intruded between 488 and 512Ma (average Ar-Ar ages).The age relationship of the KBIP to the other stratigraphic units is summarised in Table 2.1.

Table 2.1 A summary of the geologic history of the area containing the KBIP.

<table>
<tr><th>Age</th><th>Igneous Event</th><th>Deformation/ Metamorphism</th><th>Sedimentation</th></tr>
<tr><td>30Ma</td><td>Phonolites</td><td rowspan="5">Gondwana Breakup</td><td rowspan="3"></td></tr>
<tr><td>49Ma</td><td>Carbonatites</td></tr>
<tr><td>72Ma</td><td>Kimberlites</td></tr>
<tr><td>130Ma
180Ma</td><td>Karoo/Etendeka</td><td>Karoo Supergroup</td></tr>
<tr><td>500?Ma
520Ma</td><td>Kuboos-Bremen Igneous Province</td><td></td></tr>
<tr><td rowspan="3">600Ma</td><td rowspan="4">Gannakouriep Mafic Dyke Swarm</td><td rowspan="2">Gariep Orogeny - Internal Zone</td><td>Nama Group</td></tr>
<tr><td>Gariep Group – Mamora Terrane</td></tr>
<tr><td rowspan="2">700Ma</td><td rowspan="2">Gariep Rift Phase– External Zone</td><td rowspan="2">Gariep Group – Port Nolloth Zone</td></tr>
<tr><td>800Ma</td></tr>
<tr><td>1000Ma</td><td>Richtersveld Igneous Province</td><td></td><td></td></tr>
<tr><td colspan="4">Namaqua Province</td></tr>
</table>

2.2 Namaqua Province

The Namaqua Metamorphic Province forms the basement to the region and is subdivided into 3 subprovinces

- The Richtersveld Subprovince ~2000-1700Ma with limited metamorphism
- The Gordonia Subprovince } Protolith up to ~2000Ma with 1000Ma
- The Bushmanland Subprovince } metamorphism

The north-west trending Namaqua Belt is thought to represent part of the Mesoproterozoic Kibaran belts that occur throughout Africa. The mobile belt is bound by the Southern Cape Conductive Belt in the south and the Namaqua Front in the north, while the Kheis and Kaapvaal Provinces are found in the east (Figure 2.1) (Blignault *et al.*, 1983; Kröner and Blignault, 1976). Deep seismic reflection profiles indicate that at 15 to 40km there is rock of dioritic or gabbroic composition underlying the province (Hartnady *et al.*, 1985).

The mobile belt has undergone extensive structural and metamorphic tectonism at around 1200-1000Ma, which has led to a penetrative gneissosity and foliation (Blignault *et al.*, 1983). The tectono-stratigraphic units are east-west trending while close to the orogenic front of the Gariep Belt, north-south overprinting (eg shear zones) is well developed (Frimmel and Frank, 1998).

Regional thrust faults that bound the ~2000Ma terranes of the Namaqua Mobile Belt (Table 2.2) show approximately 100km of movement from the north-east due to compression and accretion at about 1400Ma (Colliston *et al.*, 1991; Van der Merwe and Botha, 1989; Van Aswegen, 1983; Van der Merwe, 1986; Praekelt *et al.*, 1996). The tectono-stratigraphic units are east-west trending (Figure 2.2). The KBIP intrudes the Grunau and the Pofadder terranes and cross cuts the fabric defined by compression (Figure 2.2 A and B)

Table 2.2 Published ages of some of the terranes found within the Namaqua Mobile Belt.

Terrane	*Age*	*Source*
Grunau terrane	2000Ma	Blignault et al 1983 Colliston, 1990
Poffadder terrane	2000Ma	Barton, 1983 Blignault etal 1983 Reid 1977
Steinkopf terrane	1800Ma	Barton 1983 Van der Merwe, 1986 Van Aswegen, 1983
Aggeneys terrane	2000-1650 Ma	Armstrong et al., 1988 Reid et al., 1987

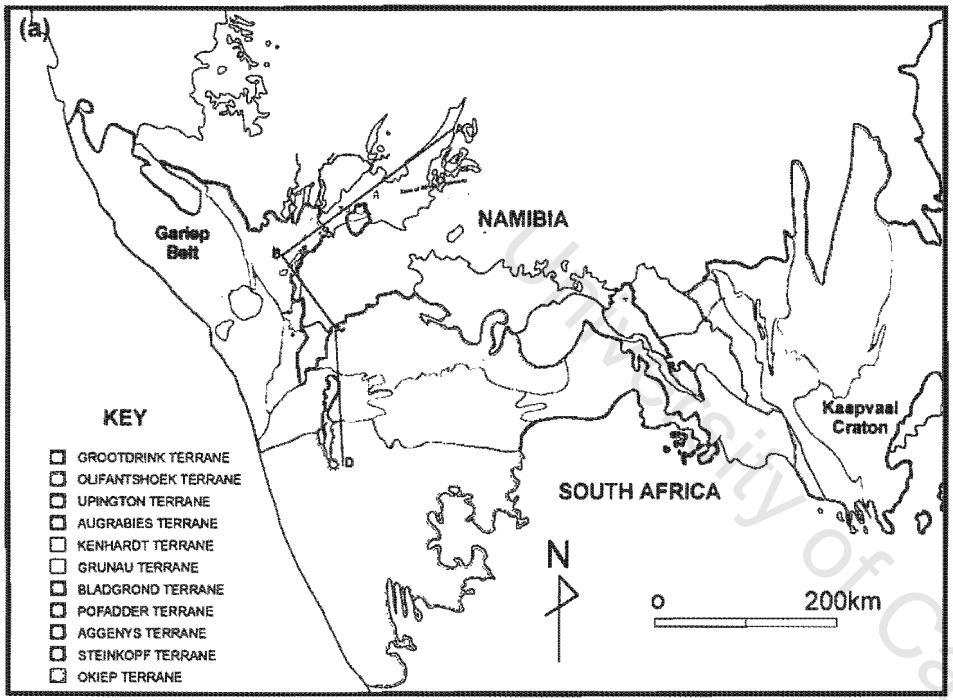

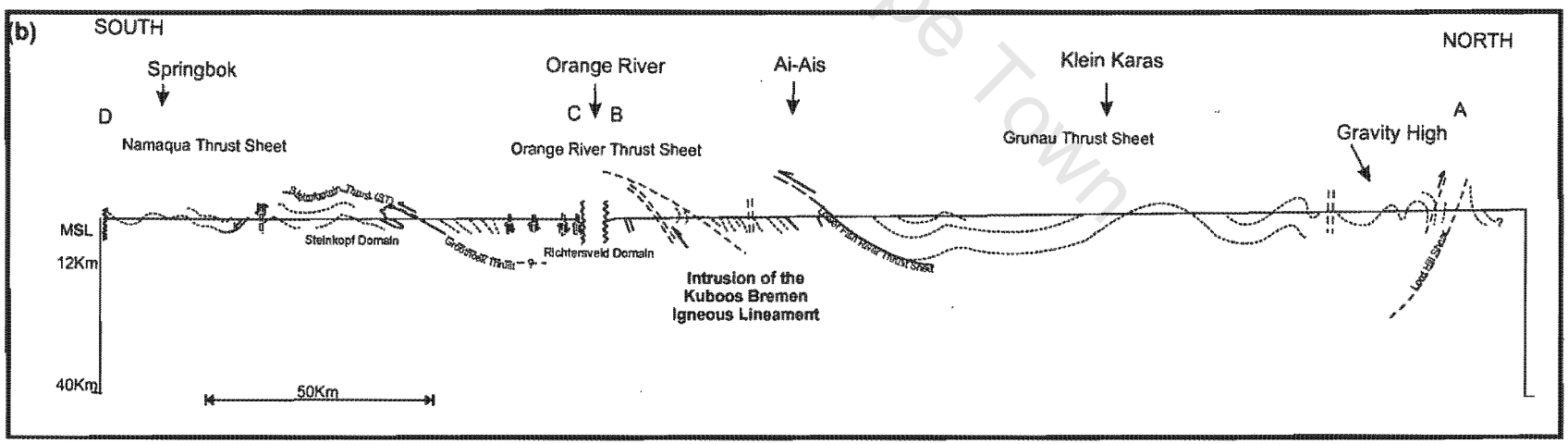

Figure 2.2 (a) The tectono-stratigraphic subdivision of the western part of the Namaqua-Natal mobile belt. Sources: Blignault *et al.* (1974, 1980); Botha (1986); Colliston *et al.* (1986, 1989); Geological Map of South West Africa/Namibia (1980); Geological Map of South Africa (1984); Praekelt *et al.* (1984); Strydom (1982); Strydom *et al.* (1987) (After Blignault *et al.*, 1983).

(b) A cross section along the line ABCD as seen in (a) (adapted from Blignault *et al.*, 1983).

2.2.1 Richtersveld Subprovince

The Richtersveld Subprovince, an ancient Paleo-Mesoproterozoic arc complex formed at approximately 2000Ma (Reid, 1997), occurs as a wedge shaped area along the Orange River, east of the Gariep Province and west of the Gordonia Subprovince forming a tectonic zone within the Namaqua Province (Bertrand, 1976; Jackson, 1976; Joubert, 1976; Toogood, 1976; Ritter, 1978). It comprises calc-alkaline igneous rocks of the intrusive Vioolsdrift Suite and extrusive Orange River Group that are thought to originate from a common basaltic parental magma (Reid, 1977).

2.2.2 Gordonia and Bushmanland Subprovinces

This region has been described by Hartnady *et al.* (1985) as consisting of medium to high grade gneisses in tectonic contact with the northern edge of the Richtersveld Subprovince. The Gordonia and Bushmanland Subprovinces consist of 2000Ma rocks which have been involved in a 1200 to 1000Ma tectono-thermal event. Although they share similar geologic histories and lithologies only the former is cut by the KBIP.

The two tectonic events recognised from the Bushmanland and Gordonia Subprovinces are

- isoclinal folding and associated axial planar foliations contemporaneous with granulite facies metamorphism (Joubert, 1971; Blignault *et al.*, 1974)
- large-scale open folds and regional shear zones (Kröner and Blignault, 1976).

2.3 Gariep Province

The Kuboos and Swartbank plutons intrude the Gariep orogen the, youngest tectonic unit cut by the KBIP. The Gariep Province forms a belt of metasedimentary and igneous rock forming part of the late Pan African mobile belts in southern Africa. Rifting of the Kalahari-Brazil craton at 750 to 720Ma led to a series of sedimentary basins that are now preserved in the para-autochthonous Port Nolloth Zone. This zone was subsequently tectonised during the collisional phase with thrusting and isoclinal folding to the east being preserved (Frimmel and Frank, 1998). As the Kuboos-Bremen line is unaffected by any of the tectonism and metamorphism associated with the Gariep Province, the intrusions are clearly post orogenic.

2.4 Gannakouriep Mafic Dyke Swarm

The Gannakouriep Mafic Dyke Swarm intruded during the Late Precambrian and was the result of east-west crustal extension during the Gariepian Orogeny. The dykes have a pervasive north-south trend that cross cuts rocks of both the Gariep and Namaqua Provinces (Reid, 1979; Reid 1982). The mafic dyke swarm is intruded by the KBIP (Allsopp *et al.*, 1979).

2.5 The Nama Group

The Nama Group, interpreted as a stable platform in a foreland basin formed during the Pan African Orogeny, is the youngest stratigraphic unit cut by the complexes of the KBIP (Germs, 1972; Smithies, 1992). The Nama Group rests unconformably on the Numees Formation of the Gariep Group (Kröner and Germs, 1971) and rocks of the Namaqua Metamorphic Province (Smithies, 1992). Horstmann (1987) postulated that the Nama has a maximum age of 540Ma while a minimum age is given by intrusion of the Bremen Complex at 530±10Ma (Rb-Sr) and 521±11Ma (U-Pb) (Allsopp *et al.*, 1979). Palaeontological and paleomagnetic data give ages of 550-650Ma (Tankard *et al.*, 1982). The lower portion of the group consists of shallow marine and fluvial deltaic sediments including organic rich carbonates fed westwards from the Kaapvaal Craton while the upper sediments were derived from the Gariep Belt in the east. Age data show that deposition of the 2500m thick pile of Nama sediments was rapid (Tankard *et al.*, 1982). Nama roof pendants found in a number of the KBIP complexes indicate that the Nama predates the KBIP. Nama conglomerates have been observed within Grootpenseiland North and South (Smithies, 1992). The Bremen Complex is observed to cut the Nama Group (Middlemost, 1967).

2.6 Kuboos-Bremen Igneous Province

The KBIP complexes that lie to the south-west (Swartbank, Kuboos and Tatasberg) are predominantly silica-oversaturated (granites) while in the north-east the silica-undersaturated rock types (nepheline syenites) dominate while the Marinkas Quellen Carbonatite lies centrally in the igneous province (Table 2.3; Figure 2.1B and C).

The Kuboos Pluton, 507±6Ma (Frimmel, 2000), intrudes the Gariep Province, as does the Swartbank Pluton, while the Tatasberg Pluton intrudes the Richtersveld Subprovince. Kanabeam intrudes the Gordonia Subprovince's highly deformed granitoids and meta-sediments while the other complexes found in Namibia intrude both the Namaqua Mobile

Belt's metasediments and the younger Nama Group (Reid, 1991; Reid 1998).

Table 2.3 Igneous Centres that make up the KBIP. Rock types found in each of these intrusions are also listed (after Reid, 1991).

Centre	*Description*
Swartbank	Granite
Kuboos	Granite, Syenite
Tatasberg	Granite
Grootpenseiland	Granite, Nepheline Syenite, Syenite
Marinkas Quellen	Granite, Nepheline Syenite, Syenite
Marinkas Quellen North	Carbonatite, Fenite
Kanabeam	Granite, Nepheline Syenite, Syenite, Quartz Syenite, Alkali Monzonite, Alkali Gabbro
Mt Ai Ais	Alkaline Breccia Pipes
Bremen	Granite, Nepheline Syenite
Haruchas	Nepheline Syenite
Grunau	Parakimberlite-Carbonatite-Melilite-Lamprophyre Swarm

There is no regional basement trend parallel to the KBIP (Table 2.4) however, trends that are similar to the KBIP include the Gannakouriep dykes and the Groot Karas horst system. The horst system provides a basement window within the Karoo and Nama sediments within which the KBIP has been exposed (Figure 2.2). The Gannakouriep dyke swarm also becomes increasingly north-east to south-west trending in this basement window.

Table 2.4 Summary of deformation of the tectonic provinces that the Kuboos Bremen Igneous Province intrudes (after Hartnady *et al.*, 1985)

Province (Subprovince)	*Terrane*	*Regional Trend*	*Deformation Ages (Ma)*
Namaqua (Richtersveld)		East-West	2000-1730
Namaqua (Gordonia)	Kakamas	North West	1200-1000
	Upington	North West	1300-950
Gariep Belt	Mamora	North-South	700-530
	Port Nolloth	North North-west	686-525

2.7 *Grootpenseiland and Marinkas Quellen Complexes*

Smithies (1992) carried out a detailed study on the Grootpenseiland and the Marinkas Quellen Complexes (GPC and MQC), two complexes that show, like the KIC, silicate rocks that range from nepheline syenite to alkali-granite. These complexes were dated at approximately 520Ma (Rb-Sr), an age consistent with the Pan-African ages of the

Province (Smithies, 1992). Like the KIC these complexes show similar patterns of silica saturation where, silica-undersaturated rocks occur in the south-west and silica-oversaturated rocks in the north-east. As the rock types found in these complexes are highly felsic they cannot represent primary magma compositions.

A magma that fractionated alkali-feldspar, clinopyroxene and amphibole is thought to have given rise to the silica undersaturated side-wall cumulates of GPC and MQC, while foyaite present in the MQC has a composition that reflects fractionation of alkali feldspar, as well as interaction with the dolomite country rocks (Smithies, 1992). Major and trace element data from Smithies (1992) revealed that the critically saturated alkali syenites most likely evolved via protracted feldspar fractionation while the critically saturated alkali–feldspar syenite found in the GPC is a cumulate and that these two rock types cannot be genetically related. The silica-saturated rocks of GPC and MQC include a compositional range from monzonite to granite reflecting fractionation of feldspar and mafic phases while the alkali granite that intruded later could not be related to any of the preceding rock types through fractionation processes (Smithies, 1992).

Smithies (1992) proposed an upper mantle source for the silicate magmas as they are characterised by low time-integrated Rb-Sr and high time-integrated Sm-Nd ratios. Smithies (1992) showed, using Pb, Sr and O isotope data, that the melts must have interacted with a crustal component. The silica-oversaturated rocks have undergone a greater degree of interaction than the silica-undersaturated rocks resulting in a rock series that has evolved on either side of the feldspar join in Petrogeny's Residua System (Smithies, 1992).

3 GEOLOGY OF THE KANABEAM COMPLEX

3.1 Introduction

The Kanabeam Complex is located north-east of the Orange River in Namibia and intrudes the highly deformed granitoids and metasediments of the Namaqua Province. Despite its relatively small dimensions, 2km by 3km, Kanabeam contains practically all the lithologies found within the KBIP (Figure 3.1, also see Table 2.2). Table 3.1 shows the intrusive components, order of emplacement and abbreviations associated with each of the Kanabeam units.

Table 3.1: Intrusive components of the Kanabeam Complex (oldest at the bottom, after Reid, 1991).

Main Lithology	*Units*	*Description*
Late Dykes		Mafic to Felsic rock types
Porphyry Pipes	PP	Tephriphonolitic and Trachyandesitic Pipes
Microgranite	MG	
Granite Porphyry	GP	
Granite	G	
Microsyenite	MS	
Quartz Syenite	QS	
Nepheline Syenite	NS6	Porphyritic Melasyenite
	NS5	Foyaite
	NS4	Granular Alkali Syenite
	NS3	Dark Alkali Monzonite
	NS2	Grey Syenite
	NS1	White Alkali Syenite

Emplacement of the Kanabeam complex involved intrusion of ring dykes and circular plugs in a multiple fashion. Field relationships indicate that there is an intrusive age progression from the south-west (oldest) to north-east (youngest) which follows the regional lineament of the province. As the intrusive axis shifted the degree of silica saturation increased (Figure 3.2).

3.2 Plutonic Units

The plutonic units that are found within this complex can be divided into

- Feldspathoid bearing units -- The Nepheline Syenite Sub-Complex (NSS)
- Quartz bearing units

The lithologies that make up these two groups are described in Table 3.2 and Table 3.3 respectively.

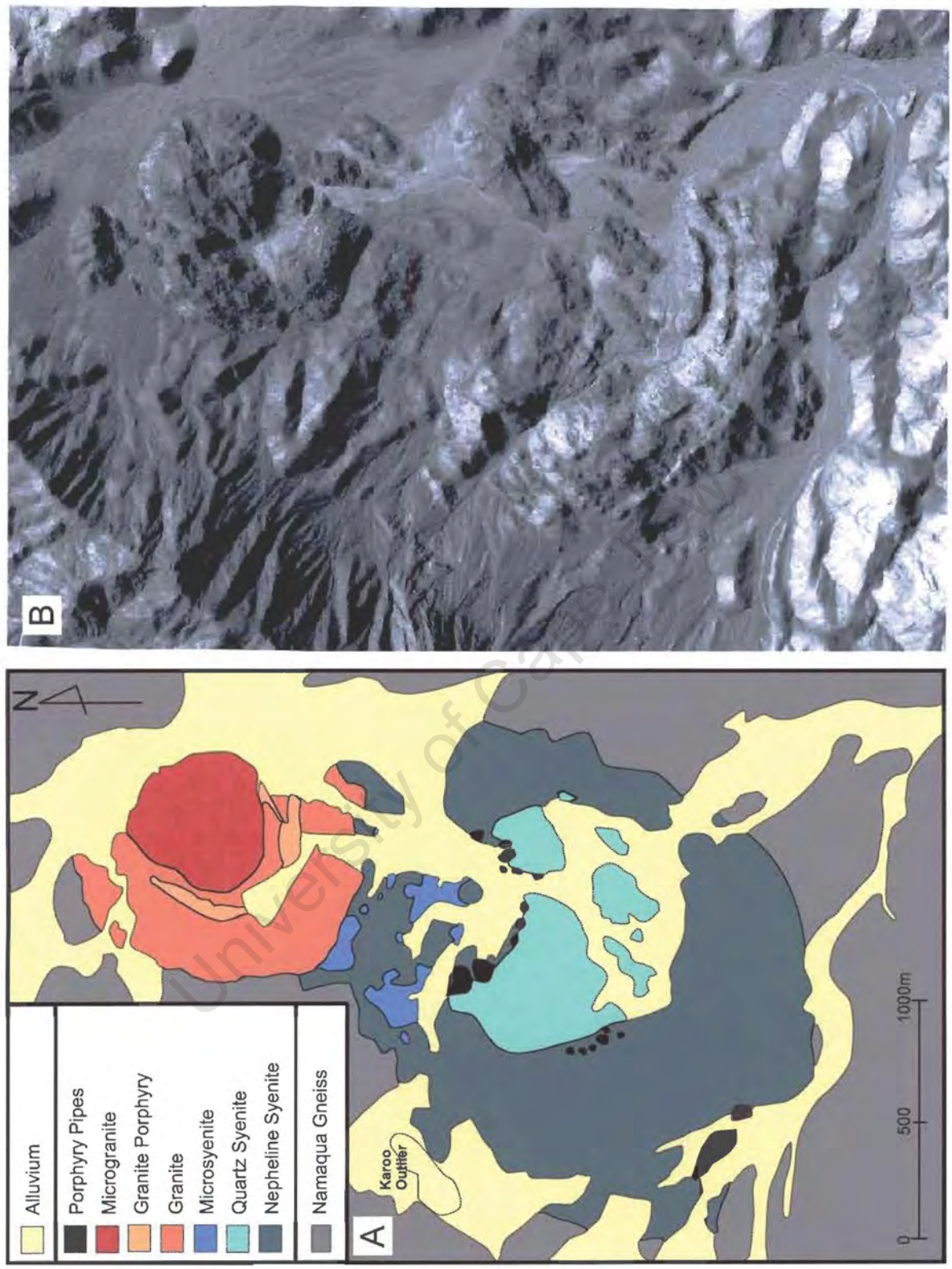

Figure 3.1 A) Geology of the Kanabeam Complex. Dykes have been omitted to aid clarity (after Reid, 1991). Detailed mapping of the nepheline syenites can be found in Figure 3.3. B) Air photograph showing the Kanabeam Complex.

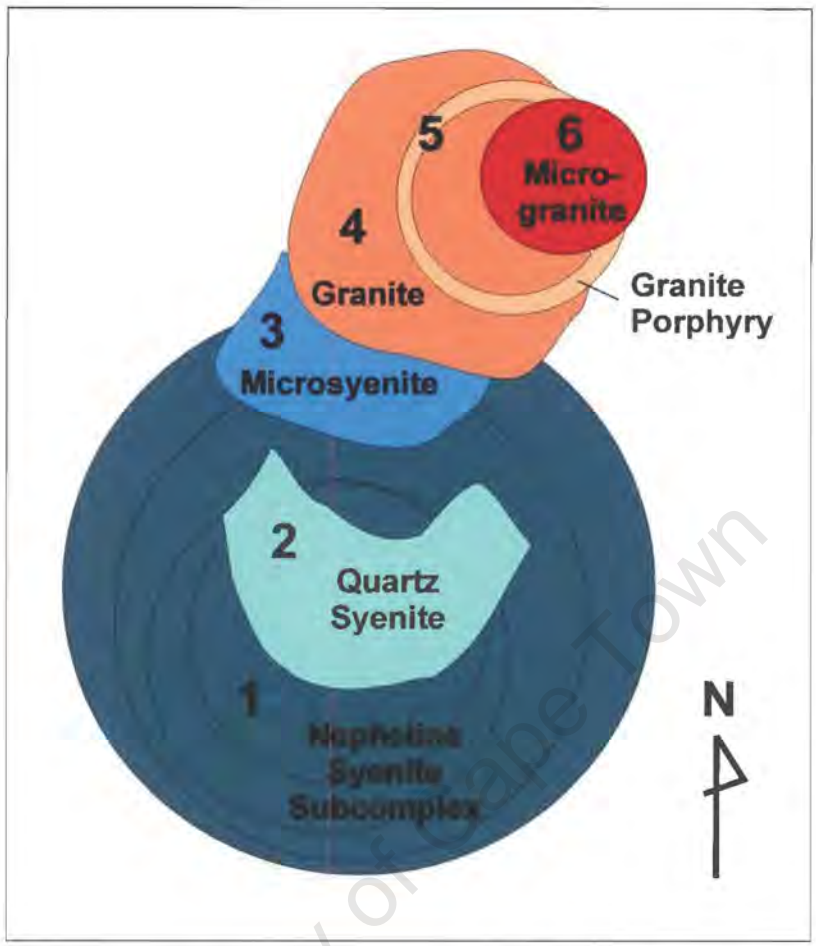

Figure 3.2 Intrusive history of the Kanabeam Complex. The first units to intrude are (1) nepheline syenites followed by (2) quartz syenite, and (3) microsyenite. Silica-oversaturated magmatism then took over and the granite (4), granite porphyry (5) and lastly the microgranite (6) were emplaced (after Reid, 1991).

A primary geochemical classification of samples from the plutonic units of the complex is based here on the total alkalis versus silica plot of Cox *et al.* (1979) adapted by Wilson (1989) for plutonic rocks (Figure 3.3). The predominant felsic nature of the plutonic components is reflected in the high total alkalis and silica being largely confined to the nepheline syenite, syenite and granite fields. Less common intermediate to mafic lithologies found as xenoliths within the plutonic units, plot in the mildly alkaline syeno-diorite to gabbro fields.

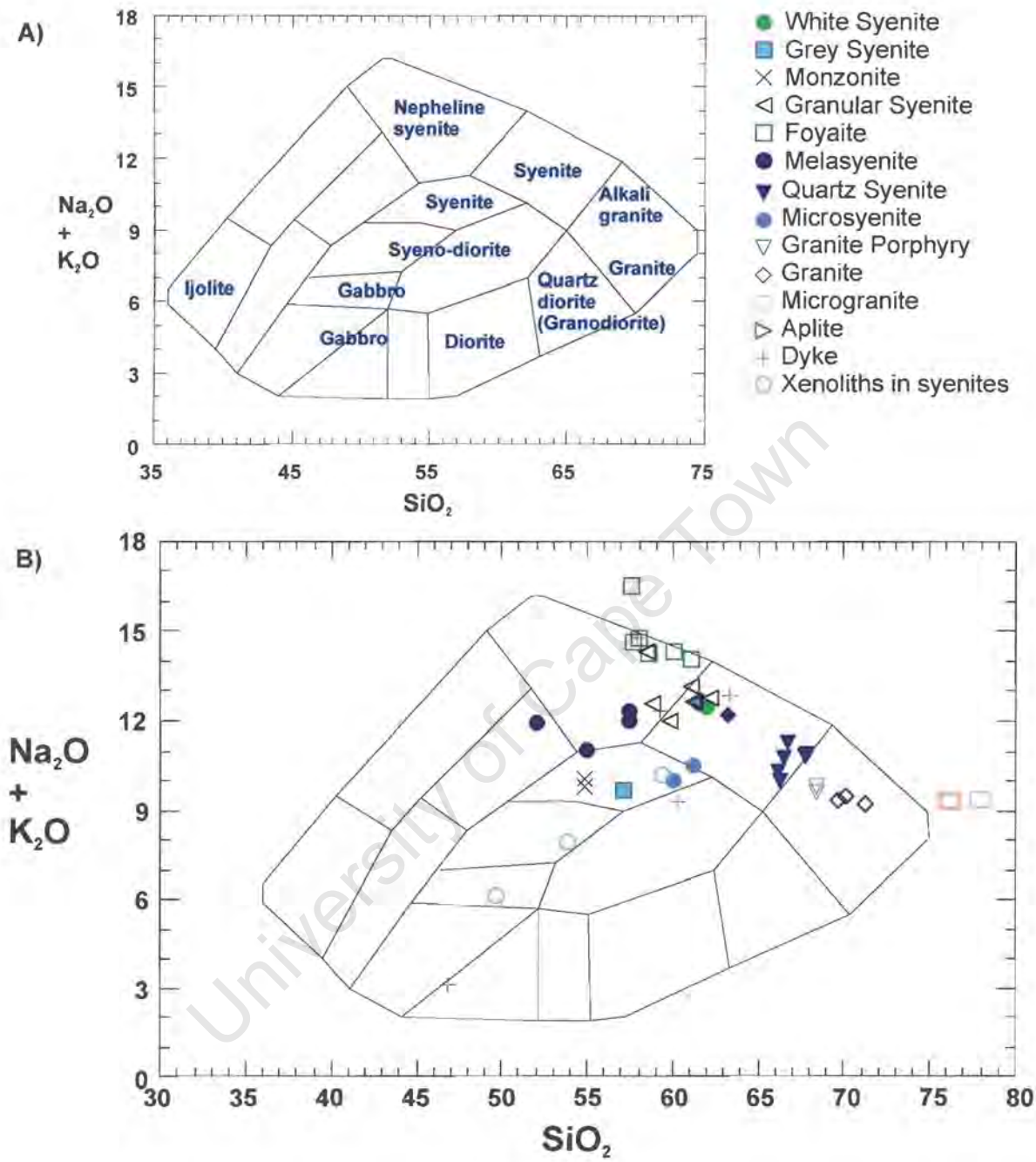

Figure 3.3 A) The chemical classification and nomenclature of plutonic rocks using the total alkalis versus silica diagram of Cox *et al.* (1979) adapted by Wilson (1989) for plutonic rocks. B) Total alkalis versus silica plot for classification of the plutonic units of the KIC.

The nepheline syenites within Kanabeam are all spatially closely related and as such can be regarded as a sub-complex. They form the southern most intrusive phases within Kanabeam and consist of six major rock types. These six rock types have been distinguished on the basis of modal composition, texture and field relations. All of the NSS units appear to be circular plugs or rings that share a common intrusive axis and as such each older unit is truncated by a younger one. The relationship between each of the units within the sub-complex is shown in Figure 3.4.

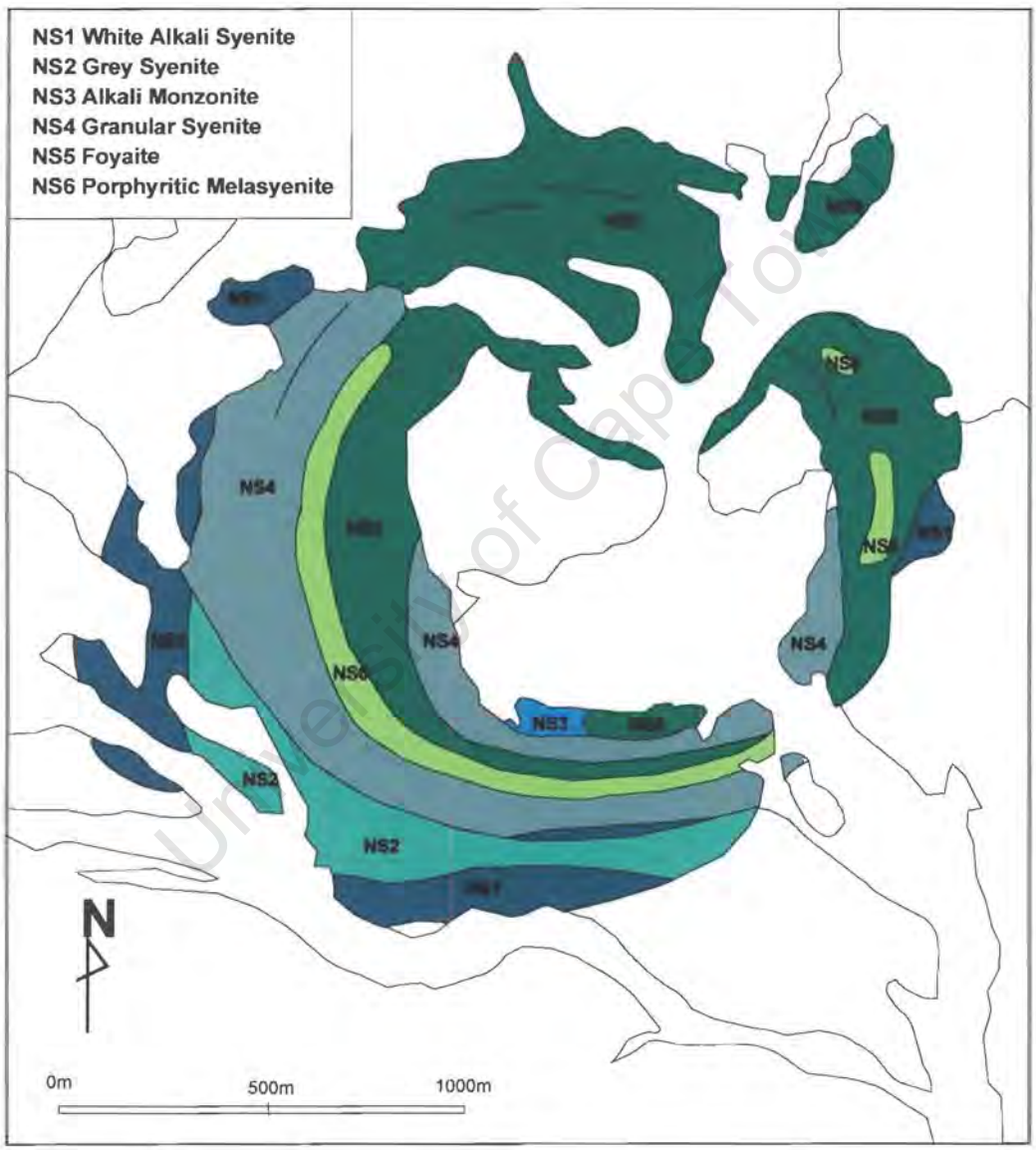

Figure 3.4. Detailed geology of the Nepheline Syenite Sub-complex. Other lithologies of the complex and surrounding areas have not been shaded to aid clarity. NS1 = oldest, NS6 = youngest (after Reid, 1991).

Table 3.2 Summary of the units that make up the NSS.

NAME	LOCATION WITHIN NSS	GRAIN SIZE	MINERALOGY	COMMENTS
Porphyritic melasyenite NS6	Intrudes the granular syenite in a narrow ring that can be traced around three quadrants of the sub-complex.	Coarse	**Alkali feldspar (56%)**: large, up to 15mm long. **Clinopyroxene (10%)**: fine grained, pale green subhedra **Hornblende (12%)**: green brown **Biotite (8%)**: inter-grown with and mantles hornblende **Nepheline (10%)** **Magnetite (2%)** **Sodalite (2%)**	Well exposed near vertical contacts of this unit are observed against the older syenites. The pronounced vertical banding parallel to the contacts is defined by the preferred orientation and variation in mode of the feldspar laths.
Foyaite NS5		Fine grained to pegmatoidal (20cm feldspar tablets)	**Alkali feldspar (63%)**: prismatic **Nepheline (18%)**: found abundantly between coarse alkali feldspar prisms **Clinopyroxene (8%)**: dominant deep green, sodic clinopyroxene **Sodalite (4%)**: present between coarse grained alkali feldspar along with nepheline **Alkali Amphibole (3%)**: strongly pleochroic, bluish green **Biotite (2%)**: confined to small mantles or intergrowths **Magnetite (2%)**: granular	Proportion of nepheline to alkali feldspar rarely exceeds 50% (except in pegmatoidal patches)
Granular Syenite NS4	Outer contact along eastern side of the sub-complex.	Coarse (granular) There is common development of very coarse to pegmatoidal patches of syenite.	**Alkali Feldspar (79%)** **Hornblende (8%)**: dominant mafic mineral **Nepheline (6%)**: interstitial. Red brown colour ation when found within pegmatoidal patches, possibly the result of secondary alteration, **Biotite (6%)** **Clinopyroxene (1%)**: pale green cores within hornblende **Magnetite**: minor	On average there is less feldspathoid in the granular syenite than in the foyaite
Alkali monzonite NS3	South central sector, within an internal ridge. It is truncated by foyaite. There is also a possible extension of this ring or remnants of another found as small indistinct zones within the younger syenites in the north-west and north-east.	Coarse grained	**Plagioclase (52%)**: large grey white laths **Hornblende (15%)**: deep red brown **Alkali feldspar (15%)**: mantles plagioclase **Diopside (6%)**: relict cores within hornblende **Nepheline (6%)**: interstitial between large plagioclase laths **Biotite (3%)** **Magnetite (2%):** secondary associated with relict cores of diopside within hornblende **Sodalite (1%)**	In hand specimen it has a mottled appearance. Described as a nepheline bearing hornblende monzonite.
Grey Syenite NS2	Cuts white syenite and forms outermost intrusion on south-eastern contact. It appears to pinch out in south-western area. Does not outcrop in the northern or eastern areas	Variable: sometimes porphyritic	**Alkali feldspar (60%)**: large **Plagioclase (20%)** **Hornblende (12%)**: dominant **Biotite (6%)**: mantles magnetite and hornblende **Clinopyroxene (1%)**: relict cores, pale to colourless **Magnetite (1%)** **Nepheline**: minor interstitial, altered **Quartz**: accessory were nepheline is absent	Dark grey hornblende syenite Texture and mineral variability suggests contamination or hybridization
White syenite NS1	Southern outer contact of the complex. Traceable around the south-western side where it is observed in narrow gullies that have cut into the extensive scree fans of the Gamkab escarpment. Along the eastern margin of the NSS it is truncated by granular syenite (ns4) and foyaite (ns5)	Average 4-6mm	**Alkali feldspar (81%)**: Granular rather than prismatic habit. The feldspar appears to have undergone turbid alteration and shows coarse vein and patch perthite (or anti-perthite) texture. **Amphibole (8%)**: green brown, predominates and rings clinopyroxene **Plagioclase (5%)** **Biotite (5%)** **Magnetite (1%)** **Nepheline:** minor **Quartz**: minor where nepheline is absent	Net veined with quartz syenite Feldspathised country rock xenoliths are found throughout the quartz syenite

Table 3.3 Summary of the quartz bearing lithologies of the KIC.

NAME	LOCATION	GRAIN SIZE	MINERALOGY	COMMENTS
Microgranite MG	Northern most intrusion of KIC	Fine to medium grained	**Alkali feldspar (60%)** **Quartz (37%)** **Amphibole (2%)** **Biotite (1%)** **Sulphides:** trace, indicated by sulphur release when rock is broken	Small circular plug Knife sharp contact with the surrounding granite whose alkali feldspar crystals have been truncated. Widespread alteration in the form of sentisation and kaolinisation of the feldspars and limonisation of the mafic minerals. Anomalous Cu, Mo, Pb and Zn concentrations appear to be associated with this weathering.
Granite Porphyry GP	Discontinuous ring within the later granite, to the west and south of the microgranite plug.	Medium to fine	**Alkali feldspar (57%):** abundant, coarse grained phenocryst mineral **Plagioclase (22%)** **Quartz (15%):** less prominent phenocrysts than the other KBIP quartz bearing lithologies and therefore the granite porphyry appears to be transitional to a quartz syenite **Clinopyroxene (3%)** **Biotite (3%)** **Hornblende (1%)**	Contacts between the later granite and granite porphyry are covered in scree but outcrop geometry suggests that the porphyry is younger than the granite. The evidence is however conflicting as there are both xenoliths and cross cutting veins of granite porphyry within the granite. The plagioclase, quartz, clinopyroxene, biotite and hornblende occur as both microphenocrysts as well as a hypidomorphic intergrowth within matrix
Granite G	Cuts both the microsyenite and NSS along their northern boarders and therefore forms the northern progression of the KIC	Coarse	**Alkali feldspar (57%)** **Quartz (20%)**: variable amounts Plagioclase (15%) **Hornblende (4%)** **Biotite (3%)** **Magnetite (1%)**	Some regions are transitional into quartz syenite as a result of variable quartz content. A porphyritic texture is developed locally but the granite is more commonly equigranular. Some dark fine grained mafic xenoliths occur (minor amounts).
Microsyenite MS	In the northern portion of the nepheline syenite the microsyenite occurs as a swarm of small plugs and dykelets. It is truncated by the granite.	Fine grained	**Alkali feldspar (63%)** **Plagioclase (20%)** **Hornblende (10%)** **Biotite (6%)** **Magnetite (1%)**	The swarm of small plugs and dykelets are possibly an offshoot of a larger body at depth. Contact migmatisation of microsyenite and nepheline syenite has developed. In thin section the microsyenite has a sub-ophytic texture with a network of divergent feldspar (both alkali feldspar and plagioclase) laths.
Quartz syenite QS	Within the centre of the NSS	Medium to coarse grained, equigranular to sub-porphyritic	**Alkali feldspar (62%)** **Quartz (15%)** **Plagioclase (12%)** **Amphibole (6%)** **Biotite (4%)** **Magnetite (1%)**	Most of the outer contact appears to follow pre-existing ring structures in the NSS, however, the northern contact is convex inwards resulting in the quartz syenite having a kidney shape. The quartz syenite cross cuts rings of the NSS in the north-east corner, and some pegmatoidal patches large alkali feldspar phenocrysts, within the NSS, are observed to be truncated by the knife sharp contact. In some cases there is a decrease in grain size towards the NSS. The pluton is characterised by small, fine-grained, mafic, partly digested xenoliths. A zone containing "blebs" of porphyritic rock type, possibly the result of liquid immiscibility, is situated close to the contact with the NSS and close to the porphyry pipes. This is possibly the result of liquid immiscibility when a more mafic magma chilled during its injection into the cooler quartz syenite.

3.3 Late Dykes

Mafic and felsic dykes of widely varying appearances cross cut the whole complex. One feldspar porphyry dyke is significant in that it follows a fracture that extends beyond the complex boundaries and coincides with the long axis of the complex. It may represent the fracture that controlled the intrusion of the ring dykes.

3.4 Porphyry Pipes

A series of small pipes intrude the outer contact between the quartz syenite (QS), and the NSS (Figure 3.5). Several pipes straddle the QS-NSS contact, and others are found either entirely within the QS or NSS. The pipes consist of two groups; a southern group (P1-6) and a northern group (P7-18) (Figure 3.5). The curvilinear distribution of the pipes seems to suggest deep-seated control by a ring dyke (or dykes). Further poorly exposed bodies of dark porphyry truncate the NSS near the south-west corner. Individual descriptions of the porphyries sampled for this study are found in Table 3.4.

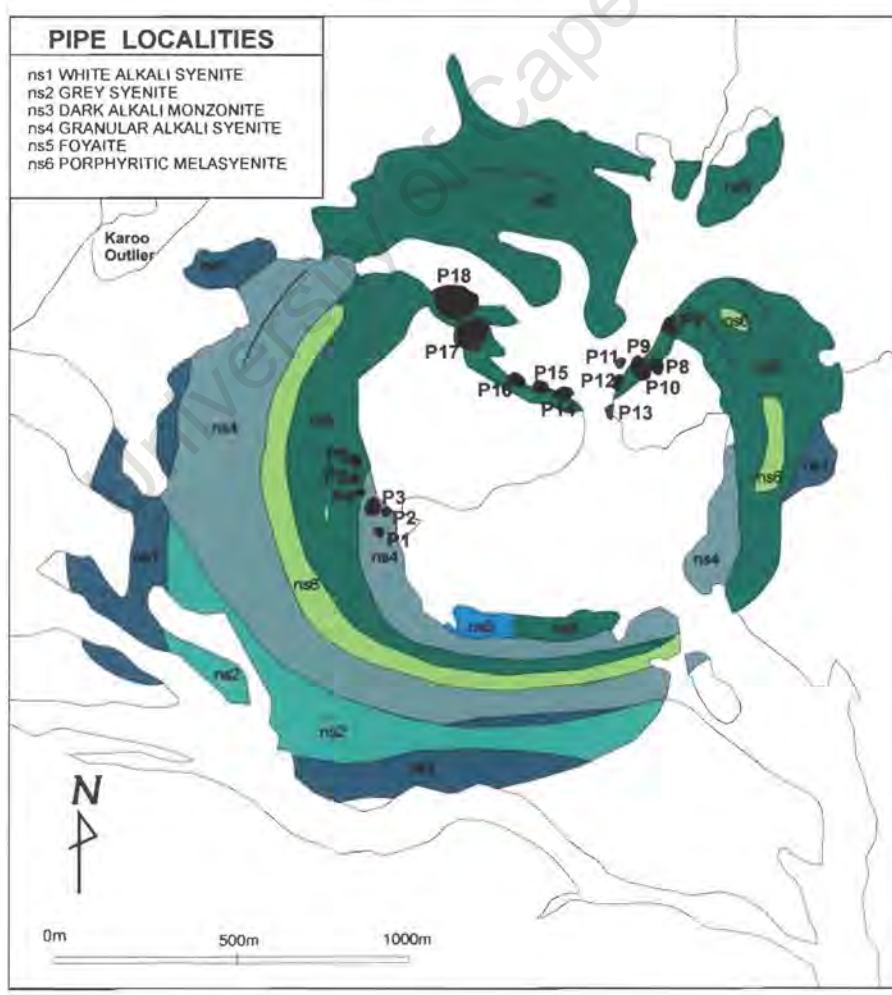

Figure 3.5 Localities of porphyry pipes (P1-18) sampled for this study, in relation to the NSS . Other units have not been shaded to aid clarity.

Most of the pipes are topped by boulder piles, the result of surface weathering processes (Figure 3.6). Consequently there is little outcrop and any zonation or other features within the pipes may be obscured. In most cases this zoning may be inferred by variation seen in the boulders. Pale grey aphanitic material found both on one of the margins and as "ring like" zones within P1 was sampled separately as it may represent a pulse of parental magma that escaped mixing with others during the formation of the pipes.

Figure 3.6 Field photographs showing the type and form of outcrop of the porphyry pipes and the NSS rocks that they intrude. For location of the pipes see *Pipe Locality Map*, Figure 3.4. Both photographs were taken facing westward. Photographs courtesy DL Reid.

Photographs of boulders from P3 illustrate the wide diversity of xenoliths found within the pipes (Figure 3.7 and 3.8). Some gabbro and ultramafic xenoliths (Figure 3.9) that are found extensively in most of the pipes were sampled for geochemical and petrographic work as these may indicate a basic magma sampled at depth.

A)

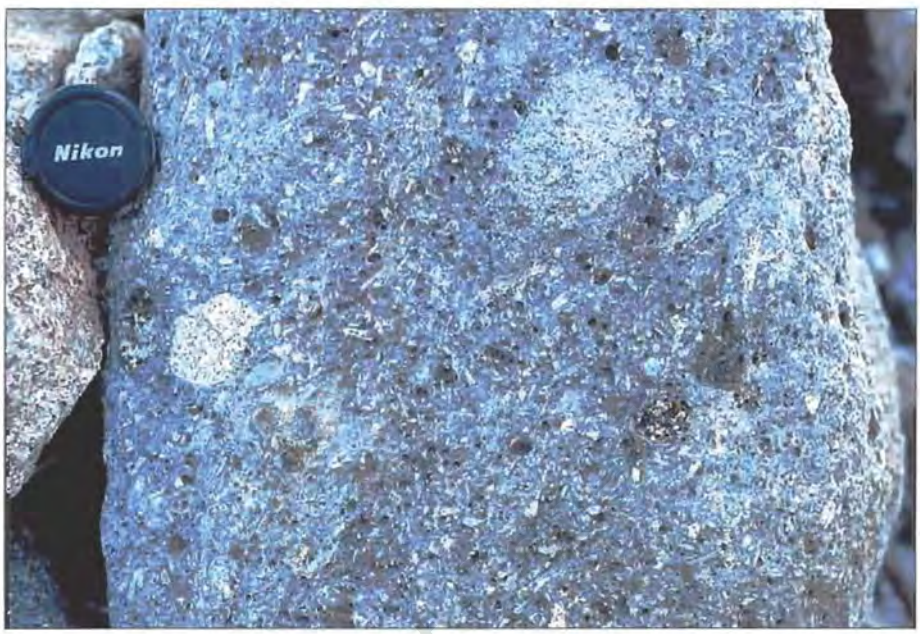

B)

Figure 3.7. Outcrops of the xenolith-rich porphyry pipe, P3. (A) Lens cap measures approximately 6cm in diameter. (B) Penknife approximately 10cm long. For location of the pipes see *Pipe Locality Map*, Figure 3.4 . Photographs courtesy DL Reid.

Figure 3.8. Loose boulder of xenolith-rich pipe P3. Penknife for scale. For location of the pipes see *Pipe Locality Map* , Figure 3.4. Photograph courtesy DL Reid.

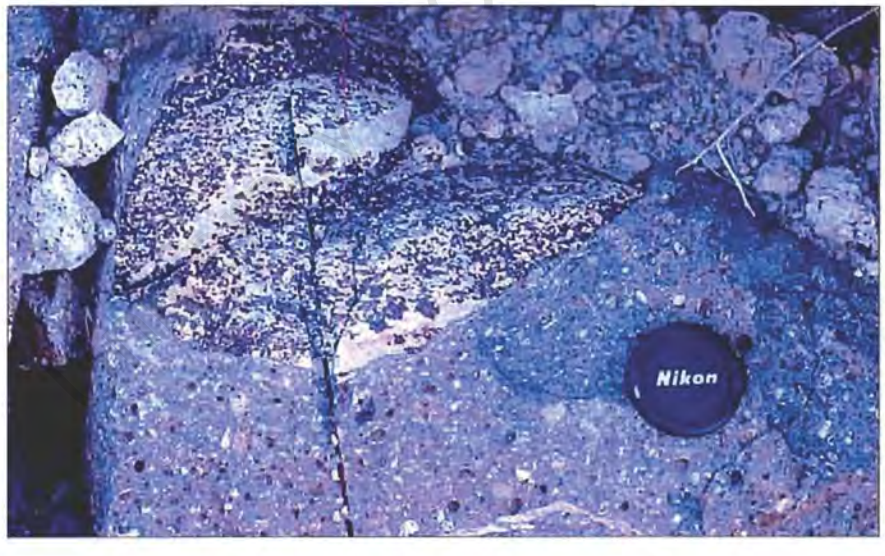

Figure 3.9 Gabbro xenolith in pipe P16. Lens cap for scale. For location of the pipes see *Pipe Locality Map*, Figure 3.4. Photograph courtesy DL Reid.

3.4.1 Primary Geochemical Classification

A primary geochemical classification of the pipes is based on the total alkali versus silica plot (TAS plot), a simple classification that is commonly employed (Le Maitre *et al.*, 1989). The terminology for this scheme is presented in Figure 3.10A. Although the pipes looked superficially similar in the field, the TAS plot (Figure 3.10B) reveals the presence

of 3 different chemical groups differing mainly in total alkalis. Pipes P1-6 are composed of tephriphonolite (TP), while P7-18 are primarily trachyandesite (TA) although one sample is trachytic. The pale grey felsic material found within P1 is phonolitic (P) in composition. The chemical distinction between the two pipe groups is consistent with the geographical locality of the pipes where the TP samples come from the southern pipes and the TA samples come from those in the north.

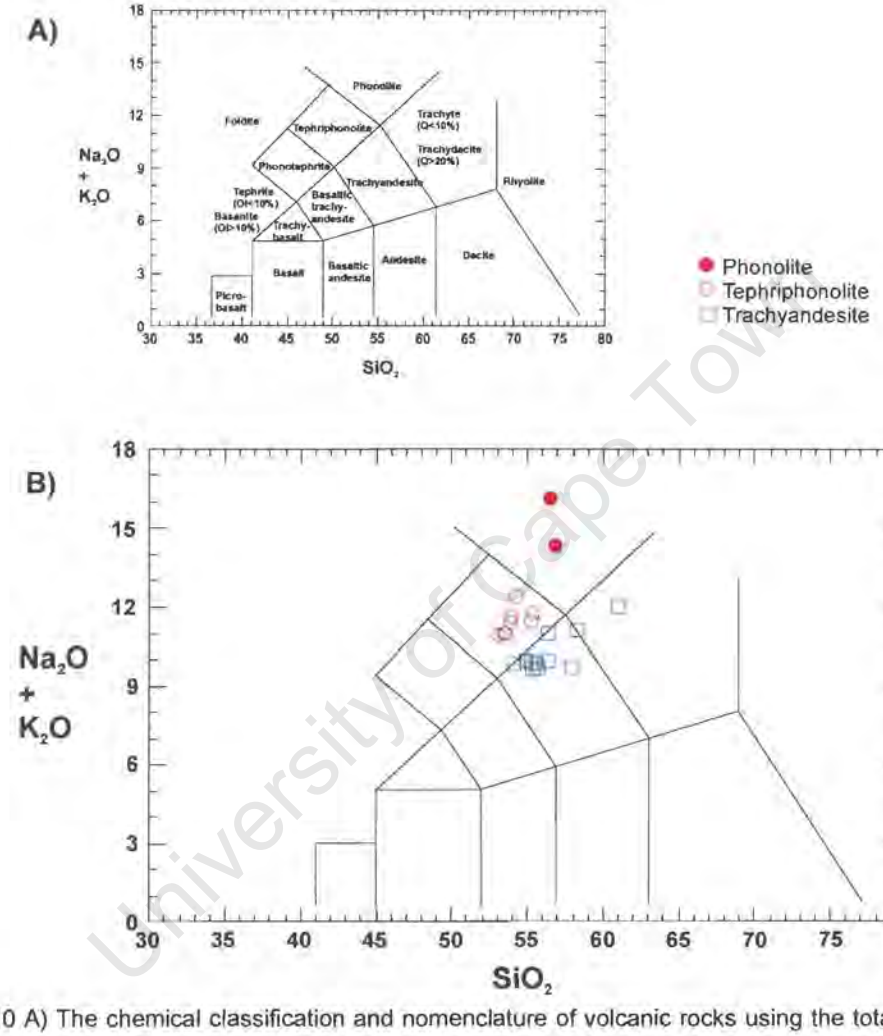

Figure 3.10 A) The chemical classification and nomenclature of volcanic rocks using the total alkalis versus silica (TAS) diagram of Le Maitre *et al.* (1989). Q = normative quartz; Ol = normative olivine. B) TAS diagram for preliminary classification of the pipes.

3.4.2 Age Relationships

The age relations of the pipes in Kanabeam are difficult to determine due to the lack of radiometric dating and the absence of a contact relationship between these rocks and the younger granitic rocks in the north-east. From contact relationships within Kanabeam it is known that the porphyry pipes were emplaced after the NSS, the QS and the MS, but it is unknown whether they intruded before or after the quartz bearing units.

Table 3.4 Compilation of field characteristics of the Kanabeam porphyry pipes (continues on following page).

PIPE	LOCATION	SIZE (m)	GRAIN SIZE	XENOLITHS	PHENOCRYSTS XENOCRYSTS	ALTERATION/ WEATHERING	DYKES/ VEINS	REMARKS
1	south	20m by 25m	fine to aphanitic	Large variety of small (<4cm in diameter) felsic sub-rounded xenoliths. Where these occur the pipe appears to be xenolith choked. Some larger well rounded gabbro xenoliths that vary from 5cm up to 15cm also occur.	Abundant altered crystals that are most likely relict olivine.	Dark grey and red surface weathering.	Extensive coarse grained nepheline syenite dykes especially on the highest side of the pipe on the hill.	Composite pipe that has zones of light grey material with no feldspar phenocrysts. Brecciated areas occur whare there is abundant feldspar.
2	south	30x15m	fine to aphanitic	Less xenoliths than the other pipes (~2% rather than ~5%). The gabbro xenoliths are well rounded and show extreme weathering. They are up to 10cm in diameter. Xenoliths that appear to be derived from other units in the KC also occur within this pipe. Meta-sedimentary xenoliths also occur here.	Abundant alkali feldspar laths	red brown	Syenite veins noted.	The fine-grained nature of tha rock has resulted in a smooth weathering surface. Some minor porphyritic zones occur where there are large phenocrysts. Zonation in the form of grain size was also noted.
3	south	Pipe exposed in hill slope, 25m vertical extent, width 25m at top narrowing to 15m at bottom.	fine	Bimodal distribution with the maximum being 5cm (smaller than the other pipes). The small gabbro xenoliths are well rounded. Country rock (Namaqua gneiss) xenoliths make up the larger sized portion.	There is a diverse size distribution with the larger phenocrysts found in the central portion of the pipe. Some zones lack phenocrysts. Alkali feldspar phenocrysts 1-2mm wide and <10mm in length.	Mostly dark red brown but white surface weathering occurs where the matrix is aphanitic and lacking in phenocrysts and xenoliths	Two sets of veining that cross cut each other 4cm wide vein cross cuts 2mm vein.	The pipe has a much larger cross section at the top of the ridge than at the bottom of the slope.
4	south	15m by 20m	fine	Large population of small sized xenoliths (2mm and 7mm). They include both well-rounded gabbro and blocky (almost rectangular) syenitic xenoliths. In some cases there is no distinct boundary between the xenoliths and pipe matrix. Some xenoliths up to 20cm in size.	Large alkali feldspar phenocrysts up to 2cm long and 0.5cm wide. Amphibole is also observed.		Minimal veining.	Forms a ridge within the syanites. This pipe is more porphyritic than the rest. There are 2 zones within tha pipe that are sapa-rated by a transitional area that contains finer grained material with gabbro xenoliths.
5	south	6m in diameter	fine	Xenolith population makas up about 20% of the rock. The well-rounded xenoliths range from 2mm to between 10 and 15cm.	Alkali feldspar phenocrysts constitute about 10% of the material.	iron rich brown staining	Fine grained syenitic veins that are about 10cm wide	
6	south	3m in diameter	fine	There are a number of syenitic and gabbroic xenoliths present.	No preferred orientation of alkali feldspar laths	Gabbro xenoliths show preferential weathering compared to the pipe material. Dark brown		Smallast of tha pipes in the area.

Table 3.4 Compilation of field characteristics of the Kanabeam porphyry pipes (continued from previous page).

PIPE	LOCATION	SIZE (m)	GRAIN	XENOLITHS	PHENOCRYSTS/	ALTERATION/	DYKES/VEINS	REMARKS
7	east central	10m by 10m	coarse	Some syenitic xenoliths that appear to be partly incorporated into the matrix. Small <5cm pale mete-sedimentary	Large abundant alkali feldspar laths and large altered crystals olivine.		<2cm veins of syenitic composition	There is no marked contact between the pipe and the host rock.
8	east central	10m by 15m	fine	Gabbro and syenite xenoliths.	Alkali feldspar phenocrysts		Small dyke-like features <1cm wide protrude the pipe	Pale grey in comparison to the other pipes
9	east central		fine	Gabbro xenoliths	Alkali feldspar phenocrysts			Dark grey matrix.
10	east central		fine	Xenolith population greater than P7 and P8.	Large abundant alkali feldspar laths.			
11	east central		fine	Xenoliths include coarse-grained gabbros and finer grained hypabyssal or volcanic material. A quartz rich basement xenolith (gneiss) observed.	Alkali feldspar is a common feature. Other megacrysts (?) olivine show extensive reaction are up to 2cm.	dark grey-black	Large syenitic veins	Graded contact with nepheline syenite. In one area of the contact a feldspar (1-2cm crystals) pegmatite occurs.
12	east central		fine	Gabbro xenoliths	Extensive alkali feldspar phenocrysts as well as a large diversity of mafics including amphibole and altered		3cm wide felsic veins. Larger veins contain xenoliths of pipe material.	Coarsening of crystals near the contact but no development of pegmatoidal material.
13	west central	15m by 20m	fine	Well-rounded gabbroic and sub-rounded fine-grained meta-sedimentary xenoliths were noted.	Alkali feldspar phenocryst have preferentially crystallised around the margin of the pipe. It also occurs as phenocrysts within the pipe matrix.	Small pits on rock surface where xenoliths have been removed though weathering.		
14	west central	15m in diamater	finer than the other pipes	More fine grained xenoliths than the other pipes. They are sub-rounded to angular. A wide variety of grain sizes and textures within the xenolith population.	Alkali feldspar and amphibole phenocrysts	Red brown.		Pipe appears to be a breccia.
15	west central		fine	Lack of medium xenoliths however, some small xenoliths <1cm were noted.	Lacks phenocrysts		Extensive veining between P14 and P15 has the same appearance as the pipes	No brecciation observed.
16	west central		fine	High grade metasedimentery xenoliths (not Nama Group). Mafic and fine-grained xenoliths (metasedimenary? or volcanic?) occur.	Alkali feldspar phenocrysts		Strongly veined with syenite. Veins blow out from a few centimeters to 10s of centimeters. A pink syenitic dyke cross	In some zones the pipe becomes brecciated.
17	west central		fine	Angular xenolith choked matrix of gabbro, felsic igneous material as well as metasediments. The igneous xenoliths show more rounding than the metasediments.	Long and narrow 2-3cm alkali feldpars.		Pipe is broken up into blocks of about 2m surrounded on all sides by veins and dykes	
18	west central		fine	Xenolith choked breccia with a wide variety of grain and xenolith sizes. Gabbro and fine-grained metasediments.	Alkali feldspar phenocrysts.			Appears to be a volcanic breccia.

4 PETROGRAPHY AND MINERAL CHEMISTRY

4.1 Introduction

All the pipes investigated are composed of an intrusive porphyry breccia consisting of a wide variety of xenoliths, xenocrysts and phenocrysts set in a microcrystalline magmatic (as opposed to tuffaceous) matrix. This chapter contains the detailed petrographic description of these porphyries, and focuses on matrix characteristics, xenocryst and phenocryst assemblages and classification of xenolith types. Under low magnification the main feature of samples collected from the tephriphonolites (P1-6) is that they contain a larger proportion of xenoliths and phenocrysts than the trachyandesites (P6-18). The pipes were previously described as being "xenolith choked" (Reid, 1991) which occasionally results in difficulty recognising the xenolith boundaries within the matrix (Plate 4.1).

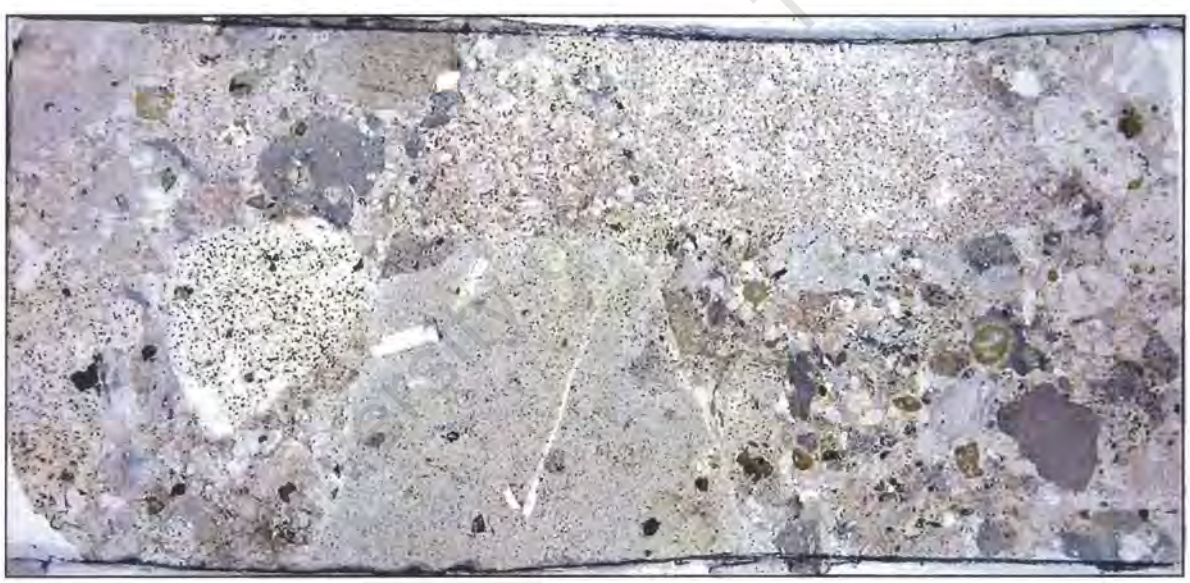

Plate 4.1: Photograph of a thin section of trachyandesite sample ND33. A wide diversity of xenoliths dominate the groundmass. Included are several syenitic, metasedimentary and mafic xenoliths along with individual isolated xenocrysts (for example, green olivine). Plane light, field of view (FOV)=4cm.

Samples range from essentially aphyric varieties with a few sparsely distributed microphenocrysts to highly porphyritic rocks, where phenocrysts, occasionally up to centimetre size, constitute a high proportion of the rock. Mineral assemblages of the pipes comprise coexisting populations of xenocryst/phenocryst minerals including olivine, clinopyroxene, amphibole, biotite and feldspar. Table 4.1 provides a summary of the minerals found within the pipes. Following this is a description of the mineral species and their textures as observed in thin sections.

Table 4.1. Summary of mineralogy of the pipes in the KIC. Abbreviations: Ne=nepheline, Plag=plagioclase, Alk F=alkali feldspar, Ap=apatite, Ol=olivine, Di=diopside, Au=augite, Hbl=hornblende, Bi=biotite, Op=opaque, P=phenocryst X=xenocryst, R=reaction product/alteration product, M=matrix.

	Pipe	Ne	Plag	Alk F	Ap	Ol	Di	Au	Hbl	Bi	Op
Southern Pipes	P1	M	X	P/M	P/M		X	P/M	P/M/R	R/P/M	P
	P2	M	X	P/M	P	X	X	P	P/M/R	M/R	P
	P3	M	X	P/M	M	X	X	P/M	P/M/R	P/M/R	P/M
	P4	M	X	P/M	P/M	X	X	P/M	P/M/R	P/R	P
	P5	M	X	P/M			X	P	P/M/R	R/M	P
	P6	M	X	P/M	M		X	P	P/M/R	P/M/R	P
Northern Pipes	P7	M		P/M	P		X	P	P/M/R	P	
	P8	M	X	P				P	P	P	
	P9	M	X/M	M						M	
	P10	M	X	P	P		X	P	P	P/R	P
	P11	M	X	P	P		X	P	R		
	P12	M	X	P/M	P		X	P/M		R/M	M/P
	P13	M	X/M	P/M	P/M			P/M	P	R/M	P/M
	P14	M		P/M				M	M	M/R	M
	P15			P/M				M		P	M/P
	P17	M	X	P/M	M			P/M	R	M/R	P/M
	P18	M		P/M	M	X		P/M		P/M	P/M

Mineral compositions, also included in this chapter, were determined with emphasis placed on the dominant phenocryst and xenocryst phases including olivine, clinopyroxene, amphibole and feldspar. Variations in their mineral chemistry may be of use in identifying the possible magmas involved in the petrogenesis of these rocks. Compositions of several of the major mineral phases were determined by electron microprobe analysis at the University of Durban Westville, using the Jeol. Electron Probe Microanalyser (Model JXA-8800RL). Other data from previous work carried out at the University of Cape Town supplemented the microprobe analysis. A complete set of the data can be found in the appendices.

Generally the pipe matrix is very fine grained but does vary greatly within and between pipes. There are three sorts of variation including; grain size, texture and composition, with grain size and composition tending to be related. For example, where compositions are more mafic, the grain size is much finer while more felsic compositions are coarser. Within the matrix the mafic phase is predominantly fine-grained hornblende and biotite while the felsic phase consists of alkali feldspar and feldspathoids. The fine-grained nature of the matrix in most cases results in difficulty identifying individual mineral grains. Although these rocks are described as being felsic, there are areas within the matrix where the matrix is mesocratic and a few examples where it is melanocratic. The more mafic samples examined contain much higher proportions of amphibole and biotite and have fewer phenocrysts.

Domains of pale green-brown groundmass appear to exhibit an irregular relationship with medium brown groundmass domains (Plate 4.2). Most of the samples exhibit a seriate granular texture, and in some cases from the southern trachyandesite pipes moderately developed trachytic textures are observed in the partial alignment of feldspar phenocryst laths.

A)

B)

Plate 4.2: Whole thin section photographs of tephriphonolite (A) ND47 and (B) MWKC1. Evidence for mingling seen in contrasting light and dark irregular zonation of the fine groundmass. Note the higher abundance of mafic xenocrysts and opaque oxides within the darker zones. Plane light, FOV =4cm.

4.2 Phenocrysts and Xenocrysts

In this study, the term phenocryst will be reserved for crystals that appear to be in textural equilibrium with a finer-grained hosting groundmass. With respect to the pipes, the term xenocryst will be used when referring to any crystal that is not in textural equilibrium with hosting groundmass. However, altered olivine and plagioclase within gabbro xenoliths that occur within the pipes, will not be termed xenocrysts, as it may be assumed that any secondary alteration is not due to primary disequilibrium between olivine crystals and original, residual melt. Pseudomorphs after amphibole, however, are

not termed xenocrysts as they are most likely the product of amphibole that has crystallised at depth. During decompression the amphibole becomes unstable and a corona or reaction rim can develop. This is a feature common in many volcanic high level intrusions having compositions similar to those seen in the pipes.

Petrographic textural disequilibrium features are observed as coronas mantling xenocrysts of olivine and clinopyroxene. Inferred reaction between xenocrysts and host groundmass is manifested in multiple concentric mineral replacement bands that grade toward a relict xenocryst core. Pseudomorphs are in some cases complete but in most instances a proportion of the original mineral remains within the centres of the coronas (Plate 4.3 and 4.4). The margins of some mafic xenoliths have also undergone the same mineral replacement process.

4.2.1 Olivine

Xenocrystic olivine, Fo_{68} to Fo_{84}, is commonly found within the southern tephriphonolite pipes (Figure 4.1) while olivine that has a composition of Fo_{78} occurs within the gabbro xenoliths found within both the northern and the southern pipes. Olivine, and pseudomorphs after olivine, are absent in the northern, trachyandesite pipes. As only one gabbro xenolith was analysed the small variation in composition observed may not truly reflect the complete spectrum in the numerous xenoliths encountered. As the xenocryst olivine and xenolith olivine have overlapping Fo compositions it is likely that they are related as variation in xenocrystic olivine compositions may have resulted from incorporation of olivine from the disaggregation of several different gabbro xenoliths. Fo compositions may have also, been modified by mineral-melt reactions.

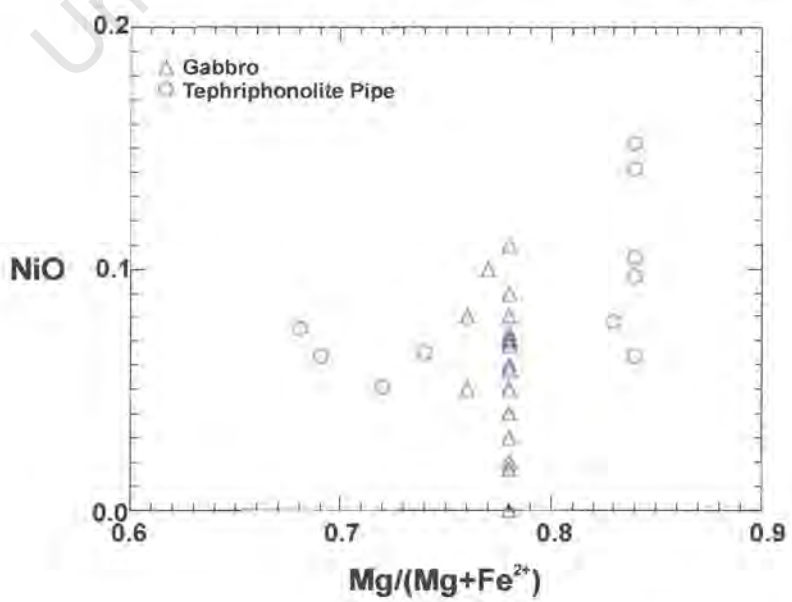

Figure 4.1 NiO versus Mg# for olivines from a gabbro xenolith (DRK72) and a tephriphonolite pipe (ND8 P3).

The xenocrystic olivine described above, is surrounded by multiple coronas that indicate instability of the mineral when immersed in the melt. Compositional variation from rim to core within the olivine xenocrysts is precluded by the development of the reaction coronas. Varying degree of replacement have resulted in differences in the number of coronas that have formed (Plates 4.3 and 4.4). The layer closest to the olivine is clinopyroxene with some minor nepheline. Where the clinopyroxene becomes well developed another corona results. The next corona can be divided into two zones, a fine granular zone and an acicular zone. Within the former, amphibole is the dominant mineral while the latter is a mixture of amphibole, biotite and minor euhedral apatite. Hornblende within the matrix is much more abundant around the pseudomorphs.

A common alteration feature of most of the olivine xenocrysts is an opaque layer, possibly magnetite, which surrounds and penetrates the mineral grains along cracks (Plate 4.3 and 4.4). Another alteration feature is the presence of chlorite and green biotite in association within the coronas described above. In this case chlorite and green biotite are likely products of secondary alteration of brown biotite.

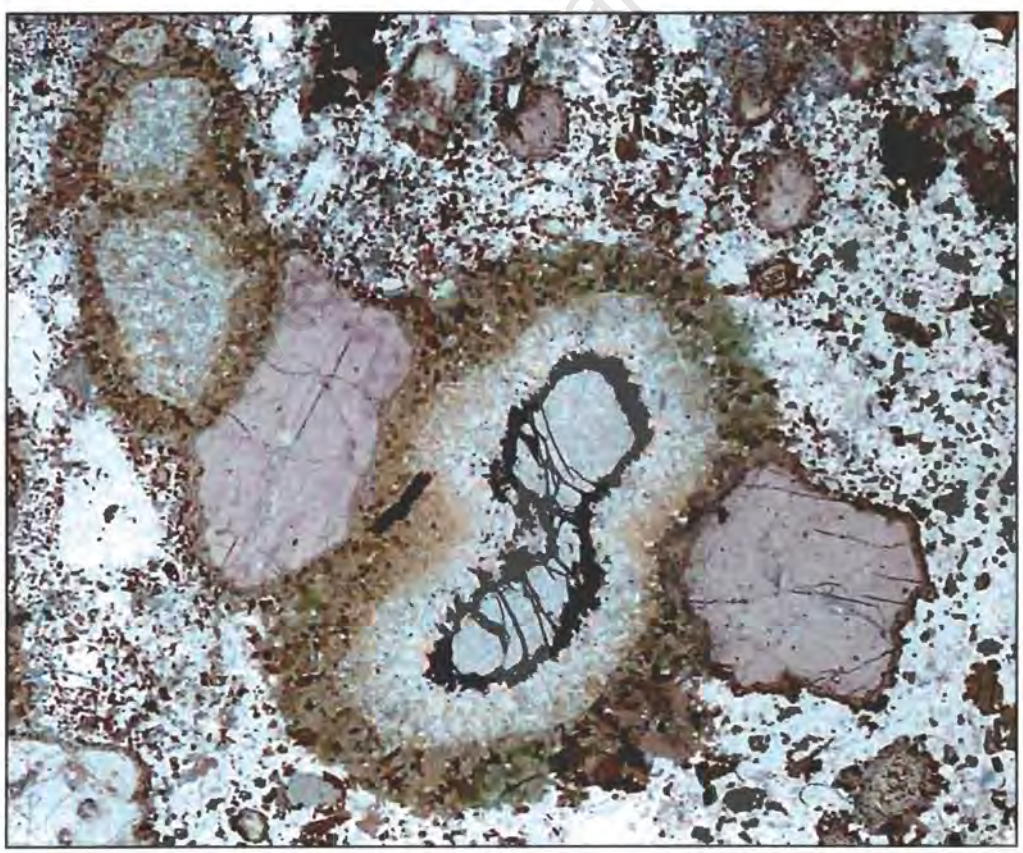

Plate 4.3: Photomicrograph of trachyandesite sample ND12. Disaggregated gabbroic xenolith within the trachyandesitic groundmass, including relict amphibole, clinopyroxene and olivine along with secondary hornblende and amphibole. Plane polarised light (PPL), FOV=5mm.

A)

B)

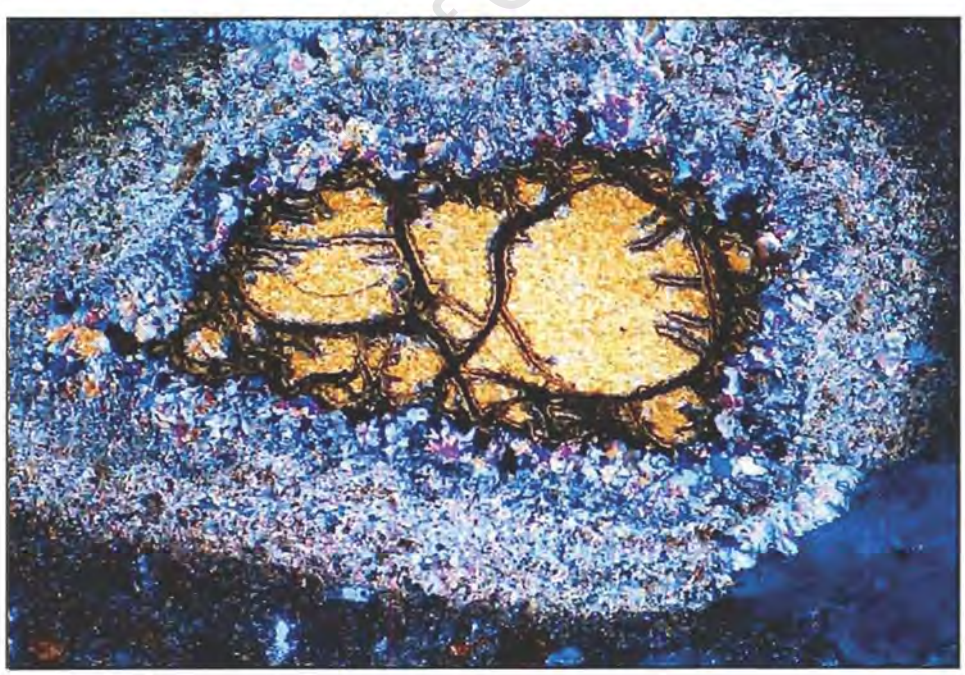

Plate 4.4: Photomicrograph of tephriphonolite sample ND1. The compositional variation of multiple coronas mantling an olivine xenocryst. (A) in PPL, (B) in crossed polarised light (XPL). Note that the relict euhedral crystal faces of the olivine are evident within the coronas. FOV=2.5mm.

4.2.2 Clinopyroxene

Clinopyroxene, an abundant mineral in the tephriphonolite samples, has a varied composition. Clinopyroxene mineral analyses were therefore carried out on a gabbro xenolith, the porphyries and the pyroxene-bearing syenites from the NSS. All the clinopyroxene formulae were calculated using MINPET Version 2.02, a mineralogical and petrological data processing system. The compositional variability of the clinopyroxenes is illustrated in Figure 4.2 and 4.3, which are triangular diagrams involving three solid solution end members enstatite(En)-ferrosilite(Fs)-wollastonite(Wo) and diopside(Di)-hedenbergite(He)-aegirine(Ae). In some instances single clinopyroxene crystals have compositional zoning, which is marked by a change in colouration from mauve to green.

A large majority of the clinopyroxenes are similar to those found in the gabbro xenoliths, namely diopside (Figure 4.2B and C). Mineral instability has resulted in the formation of a zone of hornblende around some grains where they are in contact with the groundmass (Plate 4.5). Altered mauve clinopyroxene, diopside, commonly occurs in both groups of pipes but is more dominant in the tephriphonolites (Figure 4.2C). The diopsides in the pipes may be derived by xenolith disaggregation.

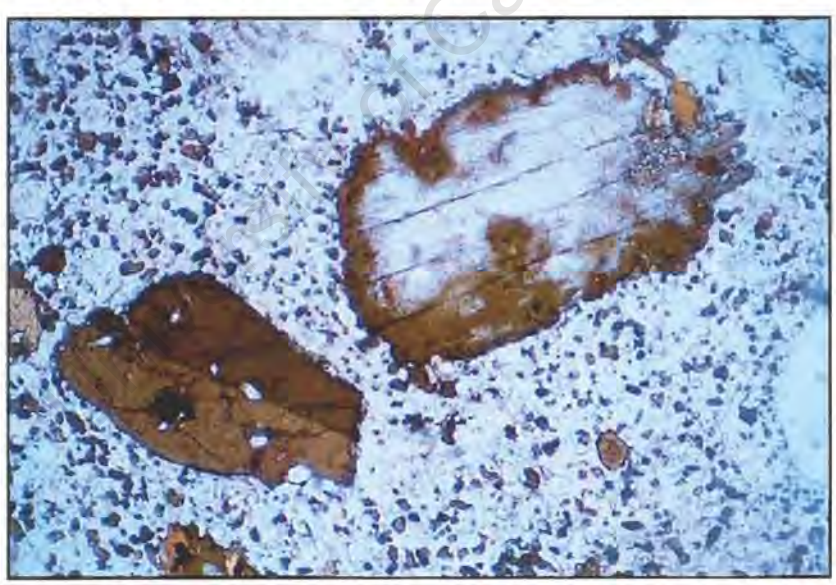

Plate 4.5: Photomicrograph of tephriphonolite sample ND2. The outsized rectangular grain to the right is diopside, displaying fine secondary green hornblende on the grain boundary. PPL, FOV=2.5mm.

Where several crystals occur in association, a zone of mafic fine-grained material is observed surrounding the cluster. Although these clinopyroxenes are also diopsidic, they do not have a hornblende rim (Plate 4.6). The mafic fine-grained zone may represent the xenocrysts reacting with the melt. These features, crystal aggregates or disaggregated xenoliths are less prominent in the trachyandesites than in the tephriphonolites.

A)

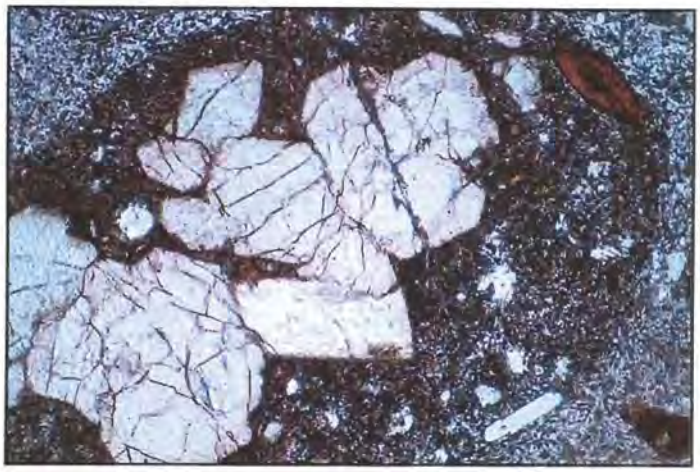

B)

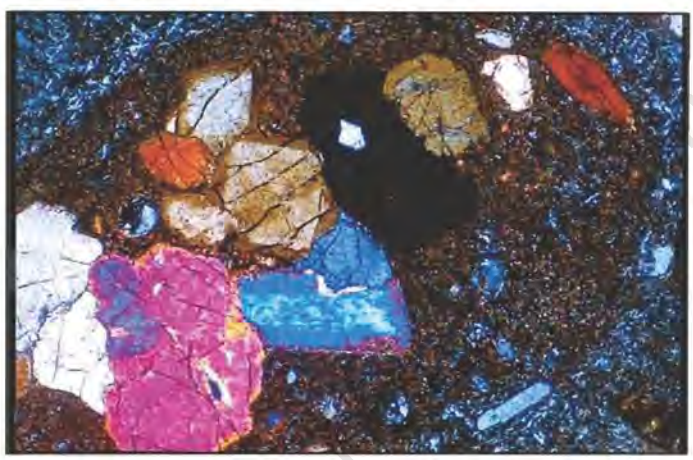

Plate 4.6: (A): Photomicrograph of trachyandesite sample ND8. Disaggregated xenolith comprised almost entirely of diopside. Note the dark matrix immediately surrounding the diopside, along with a sharp gradational transition into the felsic pipe groundmass. PPL. (B): ND8 in XPL. Both pictures, FOV=2.5mm.

A pale green, slightly pleochroic pyroxene is identified both within the matrix and as phenocrysts. It shows negligible to light alteration and has low to medium relief. Also observed within the mineral are twin planes. This pyroxene is much more common in the northern trachyandesite pipes where it forms a large percentage of the matrix. In the southern tephriphonolite pipes, it is a minor mineral phase. This clinopyroxene is identified as augite (Figure 4.2C).

The clinopyroxene in the NSS is generally calcic, however more sodic clinopyroxene is found in the more differentiated NSS units (NS4, NS5 and NS6). Clinopyroxene from the NSS varies between diopside/hedenbergite (NS2), hedenbergite (NS4 and NS6) and ferro-augite (NS4, NS5 and NS6) (Figure 4.2B). The Wo-En-Fs diagram (Figure 4.2B) illustrates a general progression of the NSS clinopyroxenes where the magnesium rich clinopyroxene is found in earlier intrusions while more iron rich hedenbergite and augitic clinopyroxene is found in later intrusions.

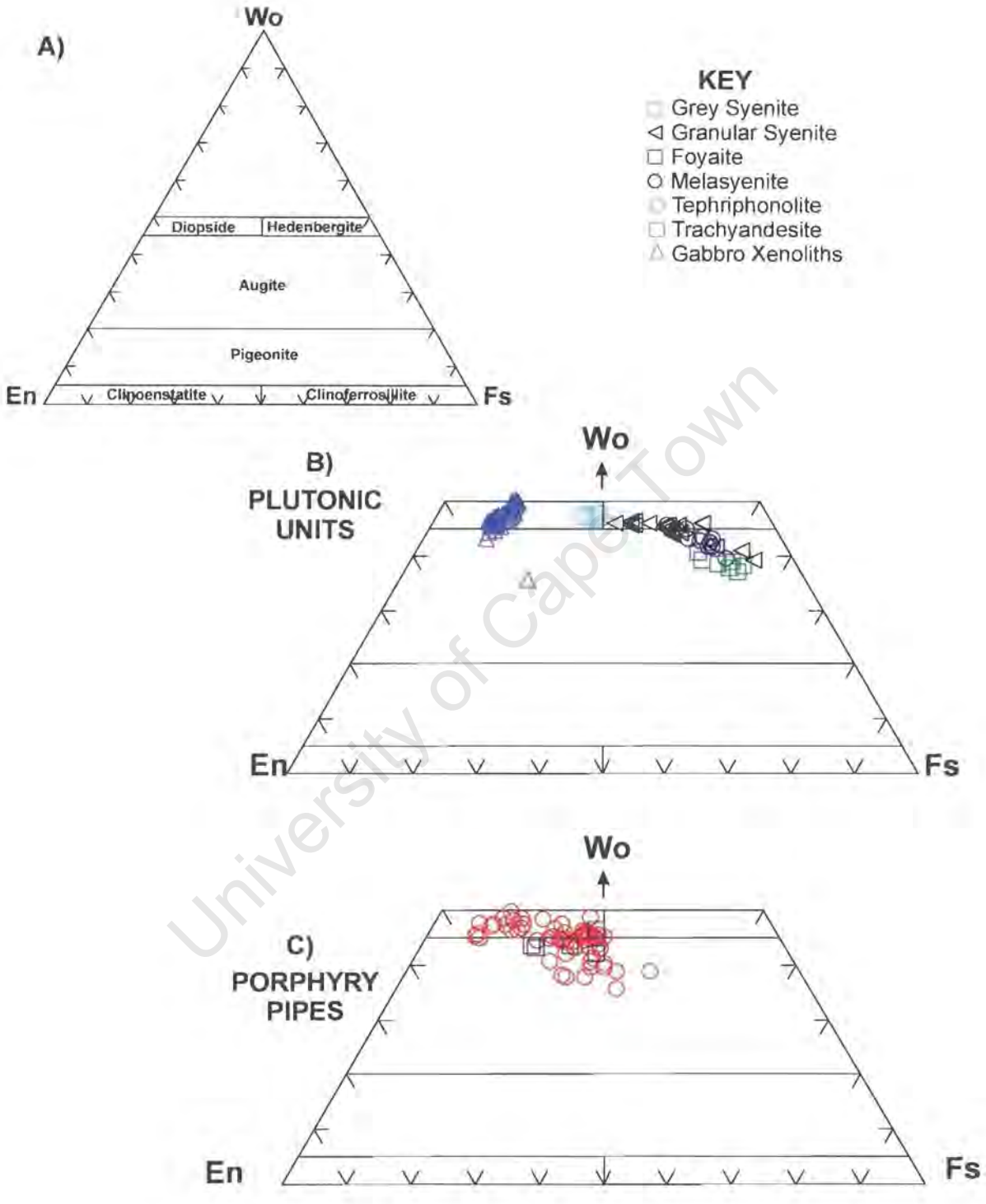

Figure 4.2 En-Fs-Wo diagram showing compositions of clinopyroxenes in the KIC. A) Nomenclature of clinopyroxenes after Morimoto *et al.* (1988) B) NSS and gabbro xenoliths clinopyroxenes. C) Clinopyroxene phenocrysts and xenocrysts from the pipes.

For comparison with the tephriphonolite pipes and nepheline syenites of the KIC, a number of compositional trends from other nepheline syenites have been plotted on the Di-He-Ae diagram (Figure 4.3). The trends from East Greenland, the Canary Islands and Brazil (ie those with a 'straighter' trend to Ae) are a function of Fe^{3+} production which results from a higher oxidation state. The pipe magmas (represented by phenocryst clinopyroxenes), being closer to these, are observed to have experienced higher oxidation states than the NSS environment. This indicates that while the NSS may have formed by fractional crystallisation, the pipes may have an origin where the higher oxidation state is a function of mixing history. The differences in the oxidation states could also be the result of differences in magma volumes.

Figure 4.3 also reveals a trend in clinopyroxene compositions from the NSS where Na and Fe increase and Mg decreases in the general order of intrusion of the NSS. The gabbro xenoliths have low Fe and Na and high Mg clinopyroxenes that are compositionally the same as the xenocrystic clinopyroxenes from the pipes.

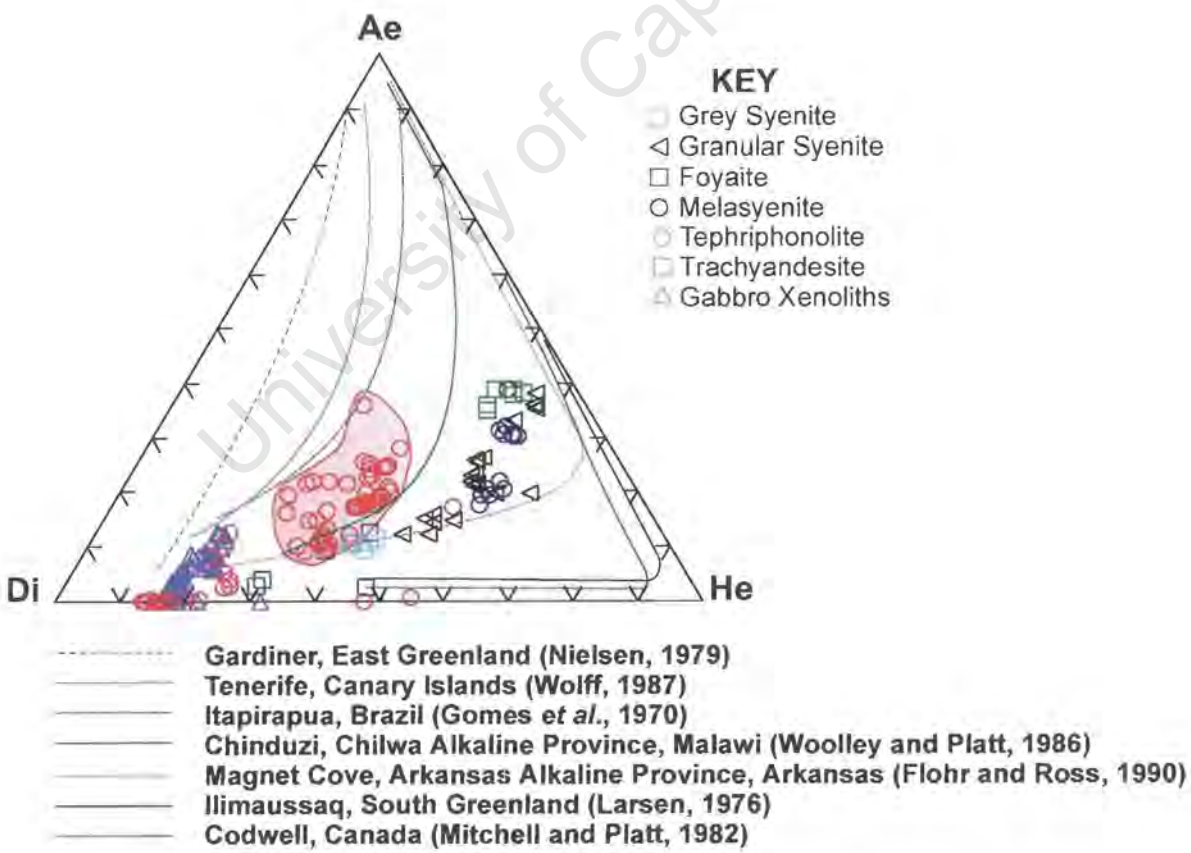

Figure 4.3 Di-He-Ae diagram of the clinopyroxenes from the KIC. The shaded area represents clinopyroxene phenocryst compositions within the tephriphonolite pipes. Comparative clinopyroxene trends from other nepheline syenites are referenced on the diagram.

Variation in non-quadrilateral components Al^{6} and Al^{4} with Mg# in the clinopyroxenes (Figure 4.4) allows for the distinction of three groups. The first group contains diopsidic clinopyroxenes from both the pipe groundmass and the gabbro xenoliths. This group has high Mg# accompanied by high variability in Al^{4} where the diopsidic clinopyroxenes from the pipes have a wider spread of values than those of the gabbro xenoliths. The second group has intermediate Mg# and variable Al^{4} and consists of augitic clinopyroxenes from the pipes, while the third group has low Mg# and much lower Al^{4} than the other groups and belongs to the NSS. Variation in Cr and Ti have similar patterns where the diopsides from the gabbro xenoliths and the pipes (both diopsides and augites) display the greatest variability.

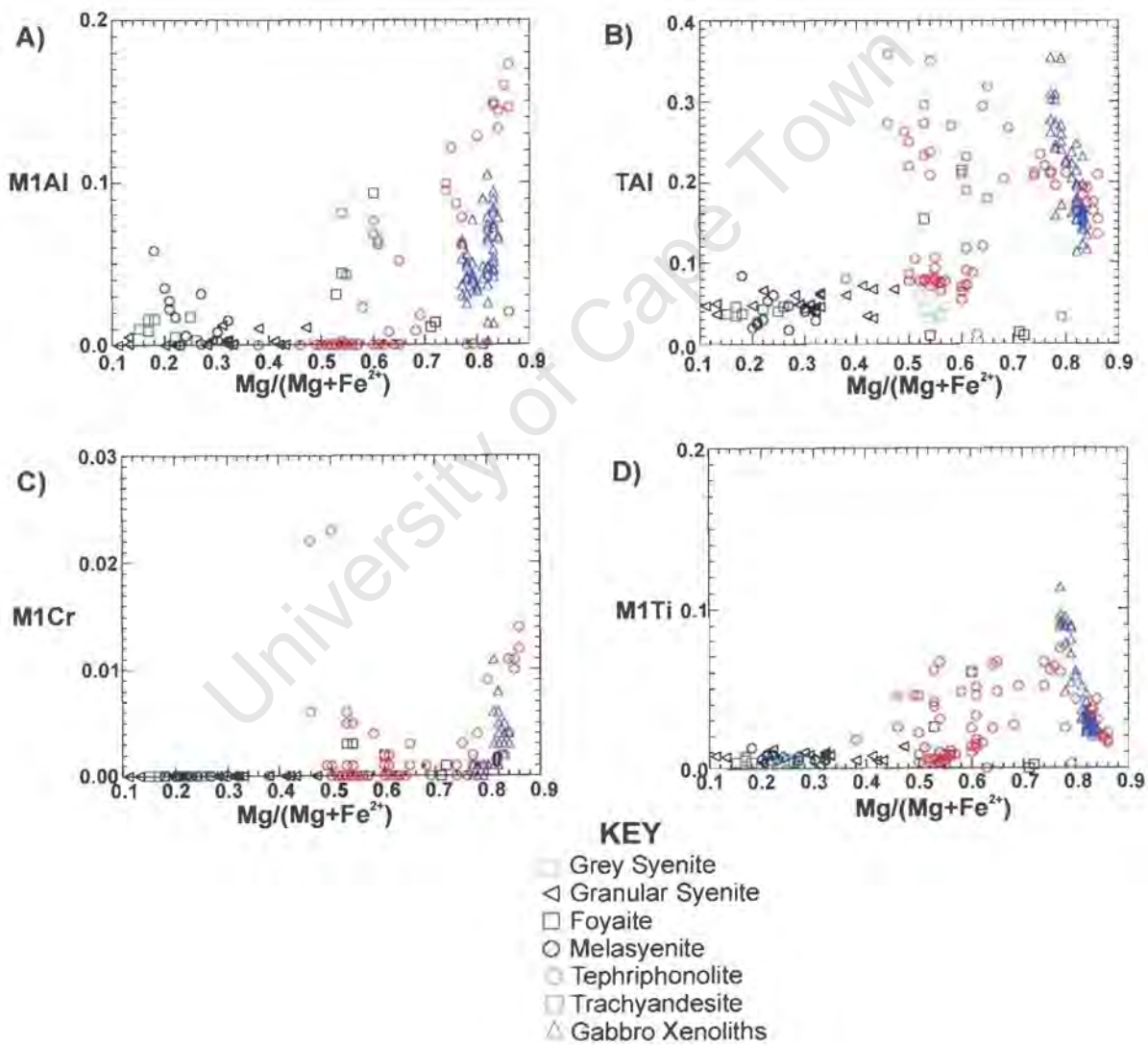

Figure 4.4 Non-quadrilateral components versus Mg for clinopyroxenes in the KIC

A) Al^{6} (M1Al), versus Mg#,

B) Al^{4} (TAL) versus Mg#,

C) Cr (M1Cr) versus Mg# and

D) Ti (M1Ti) versus Mg#.

4.2.3 Amphibole

Amphibole, a common mineral in the pipes is found in four forms:

- phenocrysts (Plate 4.7)
- a late magmatic crystallisation product forming an overgrowth on other minerals, mainly diopsidic clinopyroxene (Plate 4.8)
- amphibole pseudomorphed by finer granular clinopyroxene (Plate 4.9)
- a component of the matrix

Both the matrix and phenocryst amphiboles are dominantly hornblende while blue green amphibole was noted less frequently in thin sections. Hornblende phenocrysts are euhedral and display prominent intersecting cleavage when cut approximately perpendicular to the Z-axis. The blue green amphibole has a poikilitic texture and poor cleavage.

In samples from the northern pipes (P7-18) amphibole has been altered around margins to brown biotite (Plate 4.10). Subhedral to euhedral sections commonly preserve a distinct 6-sided outline. Fine crystals of a low birefringence mineral, possibly alkali feldspar, have replaced the fractured mineral grain in some places.

All iron was assumed to be Fe^{2+} for recalculation of amphibole using MINPET. Compositionally the amphiboles within the NSS, quartz syenite and the pipes are predominantly calcic as they have $(Ca+Na)_B \geq 1.00$ and $Na_B < 0.50$ (Leake *et al.*, 1997) (Figure 4.5A and B). The amphiboles have a variety of compositions resulting from differences in Mg# and Si (Figure 4.5C and D). Although the Mg# of the amphiboles from the NSS and the QS are similar, those of the pipes are higher when plotted against Si they are found to belong to two different types of amphibole. Two amphiboles are recognised in the samples analysed (Figure 4.5C and D):

- Ferro-edenite – in the quartz syenites
- Ferro-pargasite – in the pipes and the NSS including the grey syenite, monzonite, granular syenite, melasyenite and the microsyenite.

Within the positive correlation observed on the Ti versus Mg# diagram (Figure 4.6), the pipe samples have the highest values and the granular syenite the lowest. Quartz syenite and grey syenite have intermediate values while the melasyenite has Ti values that are higher than other samples with the same Mg#. There is no variation in Al^4 for the silica-undersaturated units analysed while the quartz syenite has lower Al^4 than the other samples. This is possibly a reflection of its silica-saturated nature.

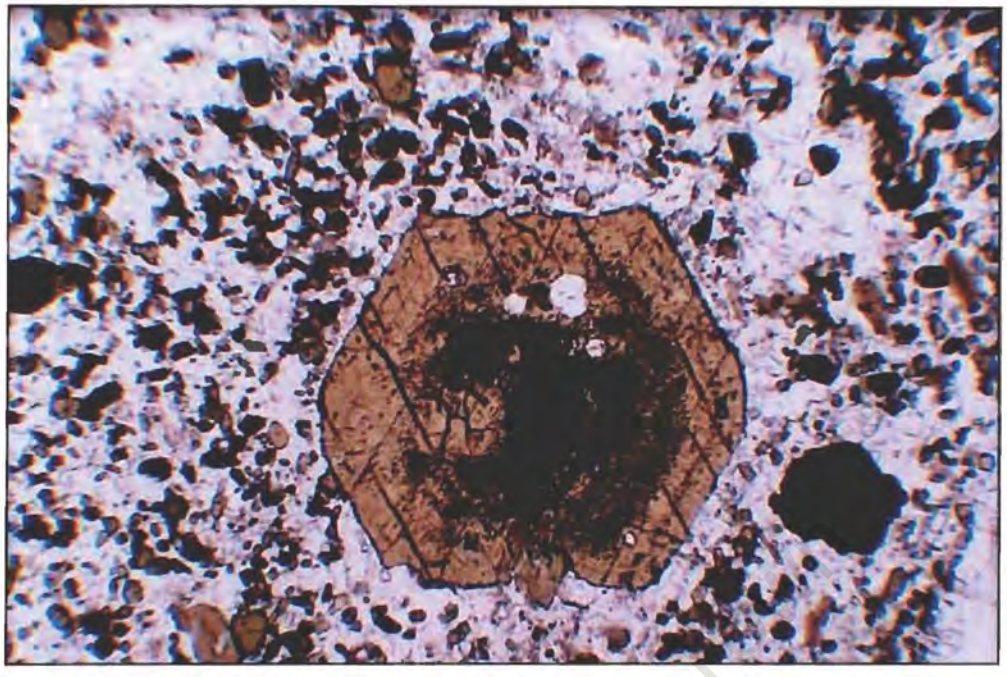

Plate 4.7: Subhedral amphibole (hornblende) phenocryst displaying prominent cleavages intersecting at 120 degrees, with the section cut parallel to {001}. PPL, FOV=2.5mm.

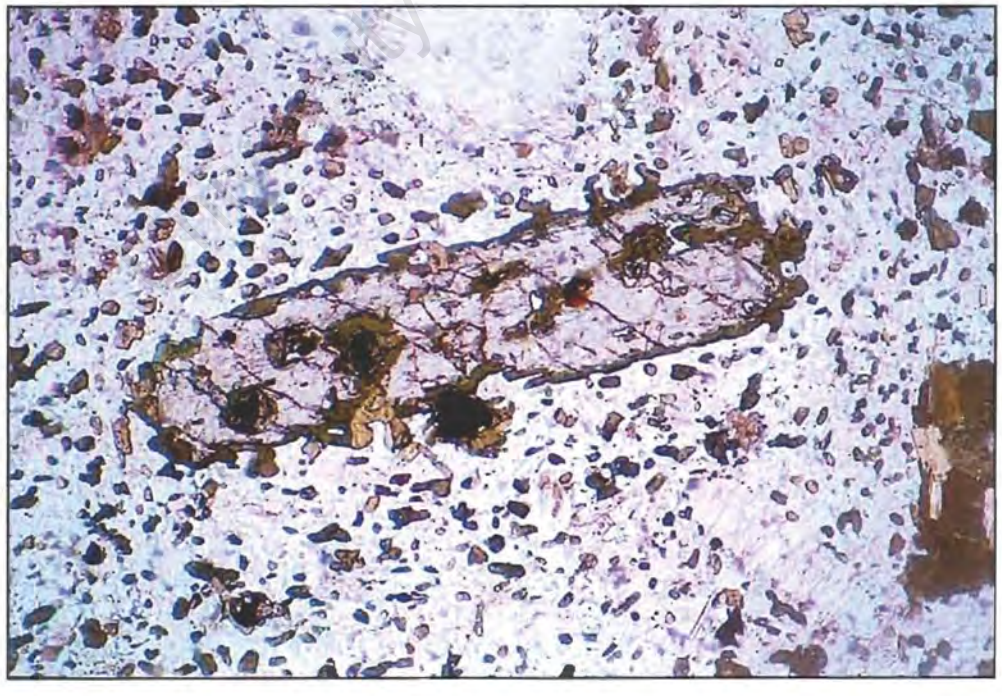

Plate 4.8: Photomicrograph of tephriphonolite sample ND2. Fine amphibole overgrowth mantling colourless poikilitic diopside. PPL, FOV=2.5mm.

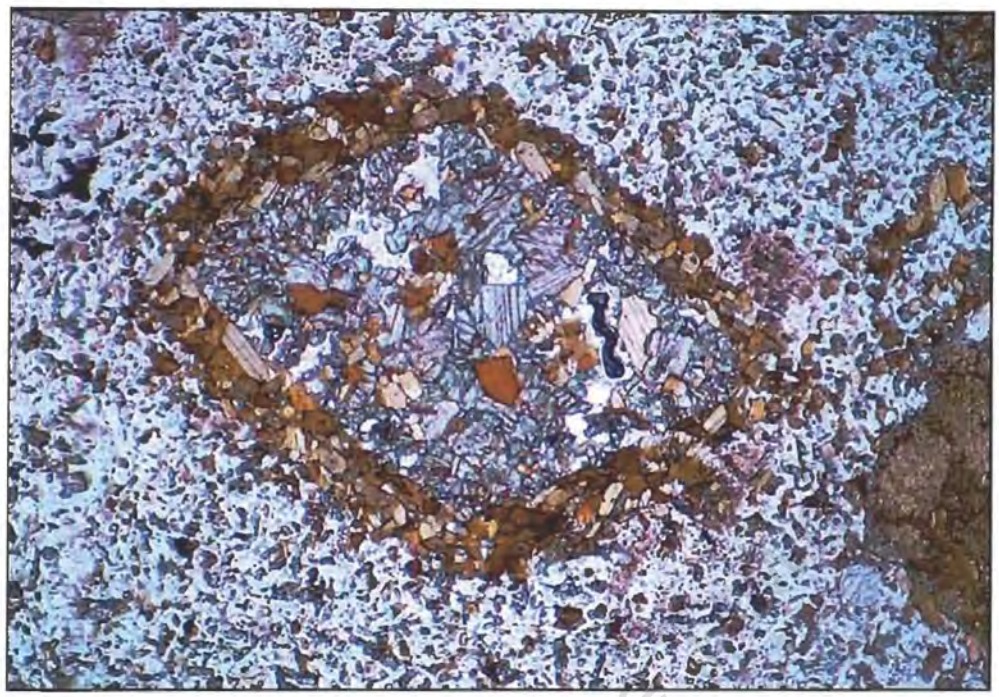

Plate 4.9: Photomicrograph of trachyandesite sample ND28. Fine granular clinopyroxene pseudomorphing euhedral amphibole, in turn mantled by fine secondary biotite. The contact between the clinopyroxene and the biotite marks the original crystal faces of the amphibole phenocryst. PPL, FOV=2.5mm.

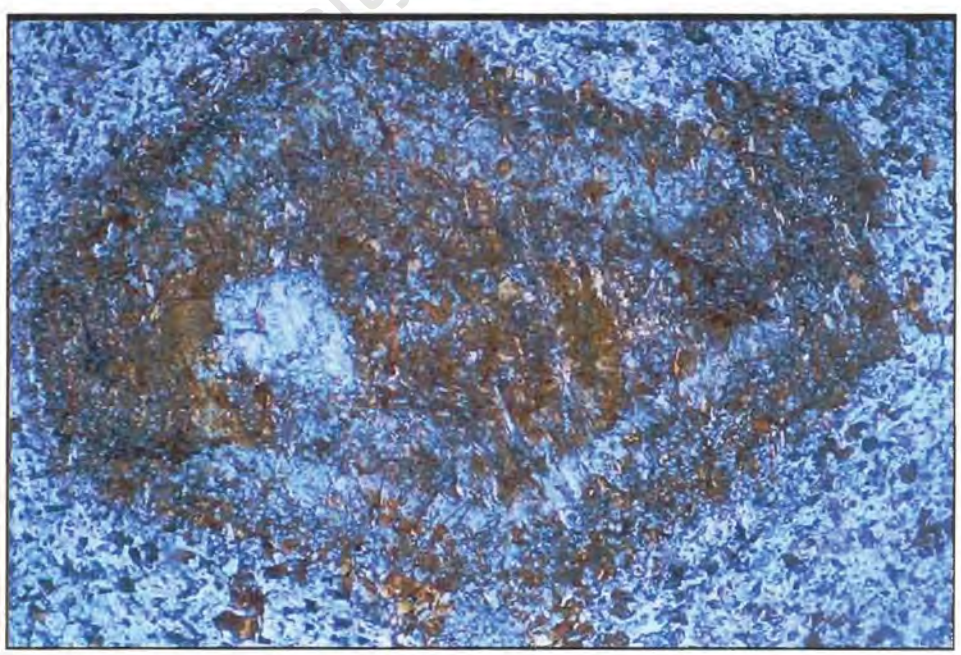

Plate 4.10: Photomicrograph of trachyandesite sample ND25. Fine alkali feldspar and biotite pseudomorphing euhedral amphibole. PPL, FOV=2.5mm.

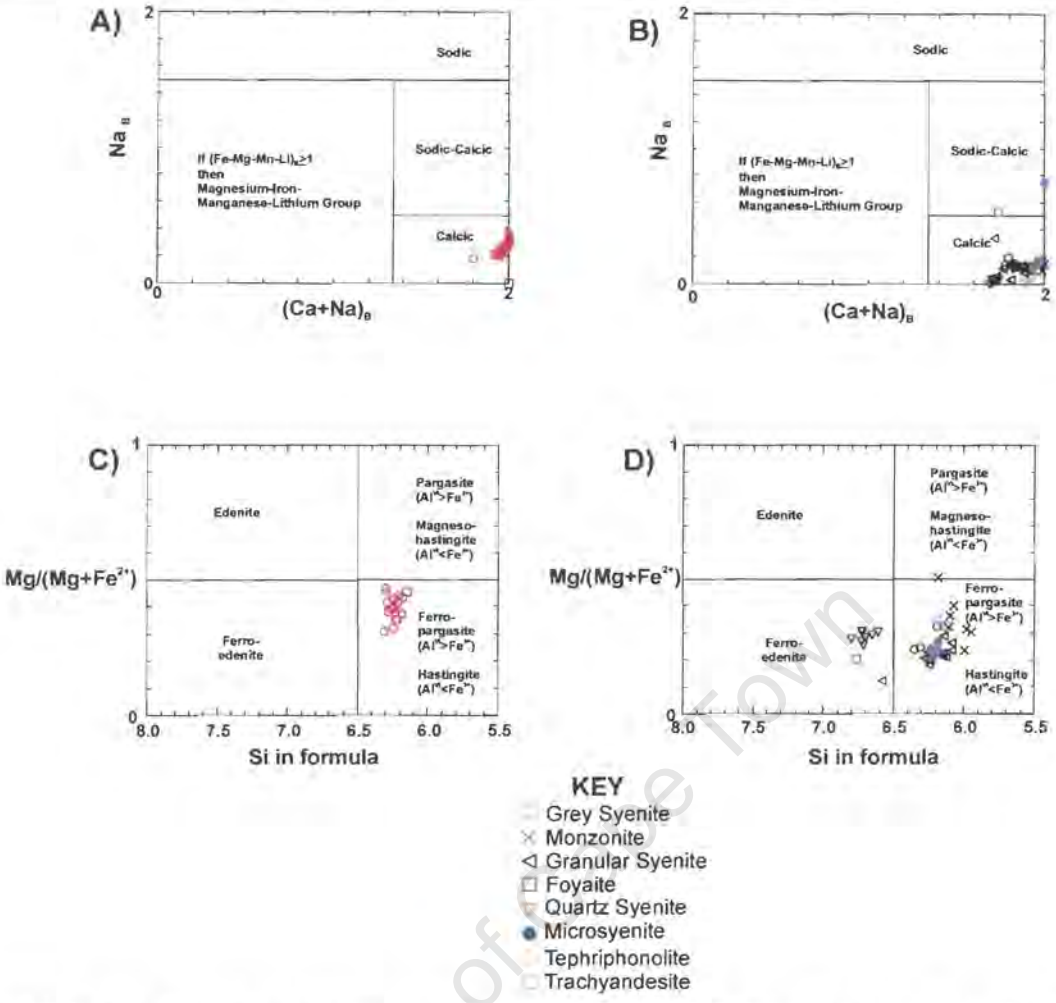

Figure 4.5 Amphibole classification diagrams after Leake *et al.*, (1997) Calcic amphibole classification if $(Na+K)_A \geq 0.50$ and $Ti<0.05$. Graph of $Mg/(Mg+Fe^{2+})$ versus Si. A) for the pipe samples and B) for the NSS and quartz syenite samples.

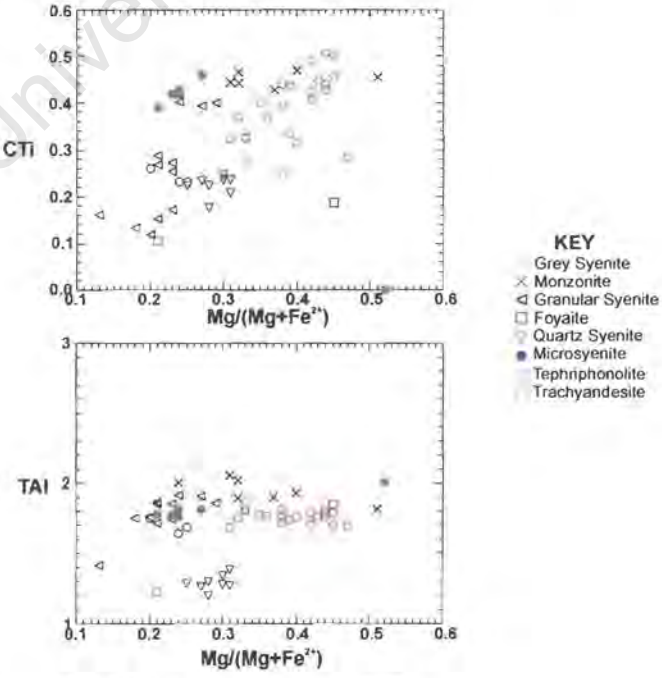

Figure 4.6 Ti and Al versus Mg# for amphiboles from the KIC.

Figure 4.7 is a Ca-Mg-Fe diagram containing data from olivine, clinopyroxene and amphibole analysis from the KIC. It is immediately apparent that the olivine and clinopyroxene of the gabbro xenoliths have similarly high Mg contents and there is a Mg-rich to Fe-rich clinopyroxene trend on the Ca-Mg-Fe diagram. The amphibole trend mirrors that of the clinopyroxene with lower Ca and slightly lower Fe. Both amphiboles and clinopyroxenes from the NSS have higher Mg in the oldest phases of the complex while higher Fe is found in the younger intrusions. The pipes have higher Mg than the NSS units for both clinopyroxene and amphibole, which is indicative of a more primitive parental magma.

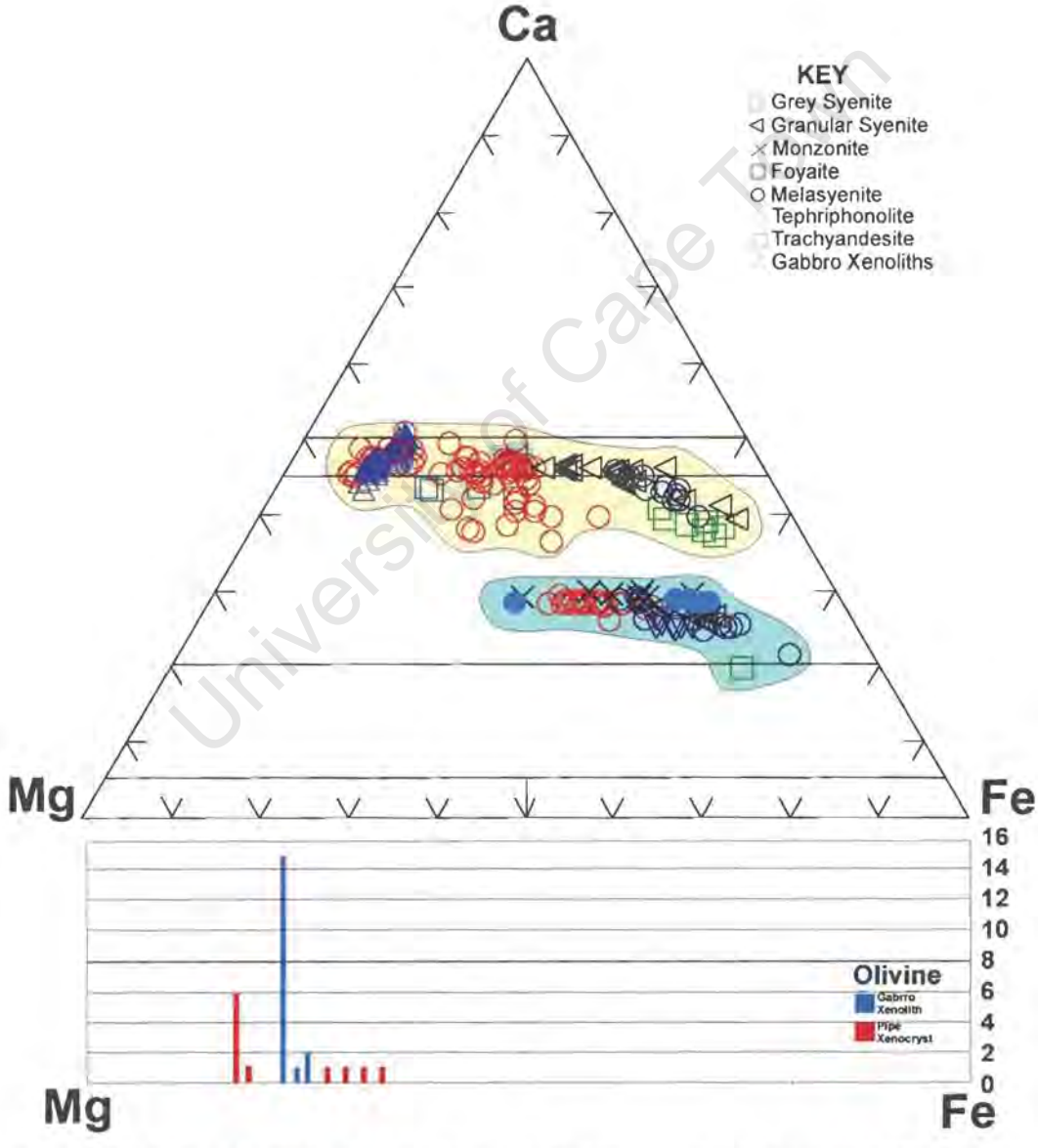

Figure 4.7 Ca-Mg-Fe diagram that includes olivine, clinopyroxene and amphibole data. Olivine compositions are shown in the bar graph below the Ca-Mg-Fe plot while both amphibole and clinopyroxene data are plotted within the Ca-Mg-Fe plot. The yellow field marks the clinopyroxenes while the green is amphiboles.

4.2.4 Biotite

Biotite occurs as:

- brown biotite phenocrysts
- fine replacement and overgrowth mantling (for example amphibole pseudomorphs) (both green and brown biotite)
- minor inclusions in poikilitic hornblende and clinopyroxene phenocrysts

Dark brown to pale brown pleochroic biotite phenocrysts are occasionally mildly deformed, although no mineral alignment is observed. Sparsely poikilitic subhedral phenocrysts are generally medium grained and display no significant secondary alteration. Biotite phenocrysts are found frequently in the matrix of the trachyandesites whereas hornblende is a more common phenocryst phase in the tephriphonolites. Aggregates of fine, subhedral biotite are found mantling olivine, opaque oxides and clinopyroxene (Plate 4.11). The fine aggregates of biotite appear frequently in association with clinopyroxene. The seriate biotite mantles clinopyroxene and progressively becomes finer grained toward the outer perimeter, associated with colour (composition) variation from the rim of the unstable clinopyroxene into the groundmass of the pipe. Mica directly in contact with clinopyroxene occasionally appears as an impure white phlogopite and grades into a pale green to brown colour away from the clinopyroxene, into the groundmass.

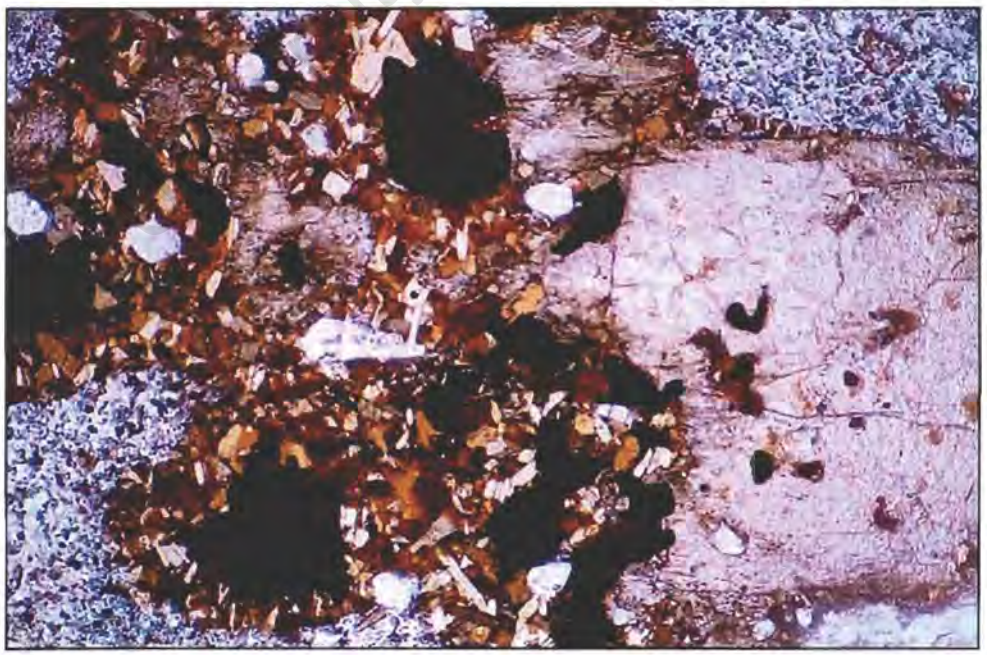

Plate 4.11: Photomicrograph of trachyandesite sample ND25. A fine, seriate secondary aggregation of biotite is seen here associated with opaque oxides, assumed to be magnetite. The large, anhedral grain to the right is clinopyroxene. PPL, FOV=2.5mm.

4.2.5 Feldspar

Alkali feldspar is the more dominant feldspar in pipe samples and occurs as both fine granular matrix and discrete subhedral phenocrysts (Plate 4.12). These phenocrysts frequently exhibit simple twins and are occasionally poikilitic, with fine inclusions of mafic minerals (commonly hornblende and biotite). Irregular, rounded blebs of nepheline are also commonly seen as inclusions. Well-developed perthite textures are common in the form of coarsely developed lamellae. Moderate to heavy secondary alteration to sericite is common, and in many instances is concentrated toward the rim, sometimes obscuring the original grain boundary.

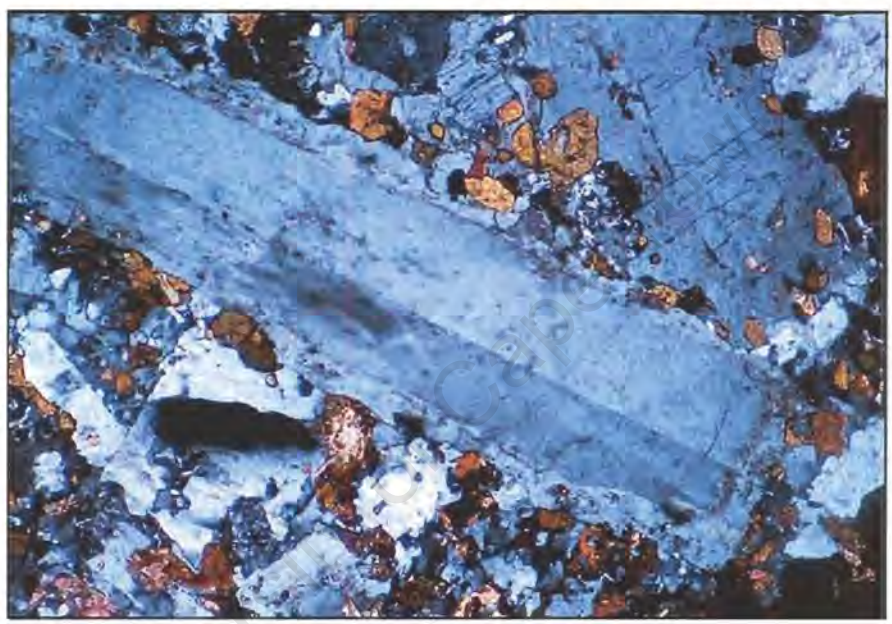

Plate 4.12: Photomicrograph of trachyandesite ND13. Coarse subhedral crystals of alkali feldspar exhibit simple twinning. Additional subsequent growth of alkali feldspar appears to have taken place along the rim. XPL, FOV=2.5mm.

Feldspar analyses from the pipes are plotted on a series of triangular diagrams including albite (Ab), orthoclase (Or) and anorthite (An) the solid solution end members (Figure 4.8). The coarse nature of the exsolution lamellae found within the pipe alkali feldspars allowed for analysis of both phases revealing a wide range in compositions. In some cases the lamellae are inhomogeneously distributed, a fact that may be attributed to recrystallisation in the presence of aqueous alkali solutions (high volatile pressure) (Stephenson, 1976; Parsons and Brown 1988). Figure 4.8 reveals substantial ternary solid solution within the alkali feldspars from the porphyry pipes. The Na-rich alkali feldspars are low temperature feldspars that crystallise under the same thermal conditions as amphibole and biotite, while those that are more K-rich (sanidines) are formed under higher temperatures.

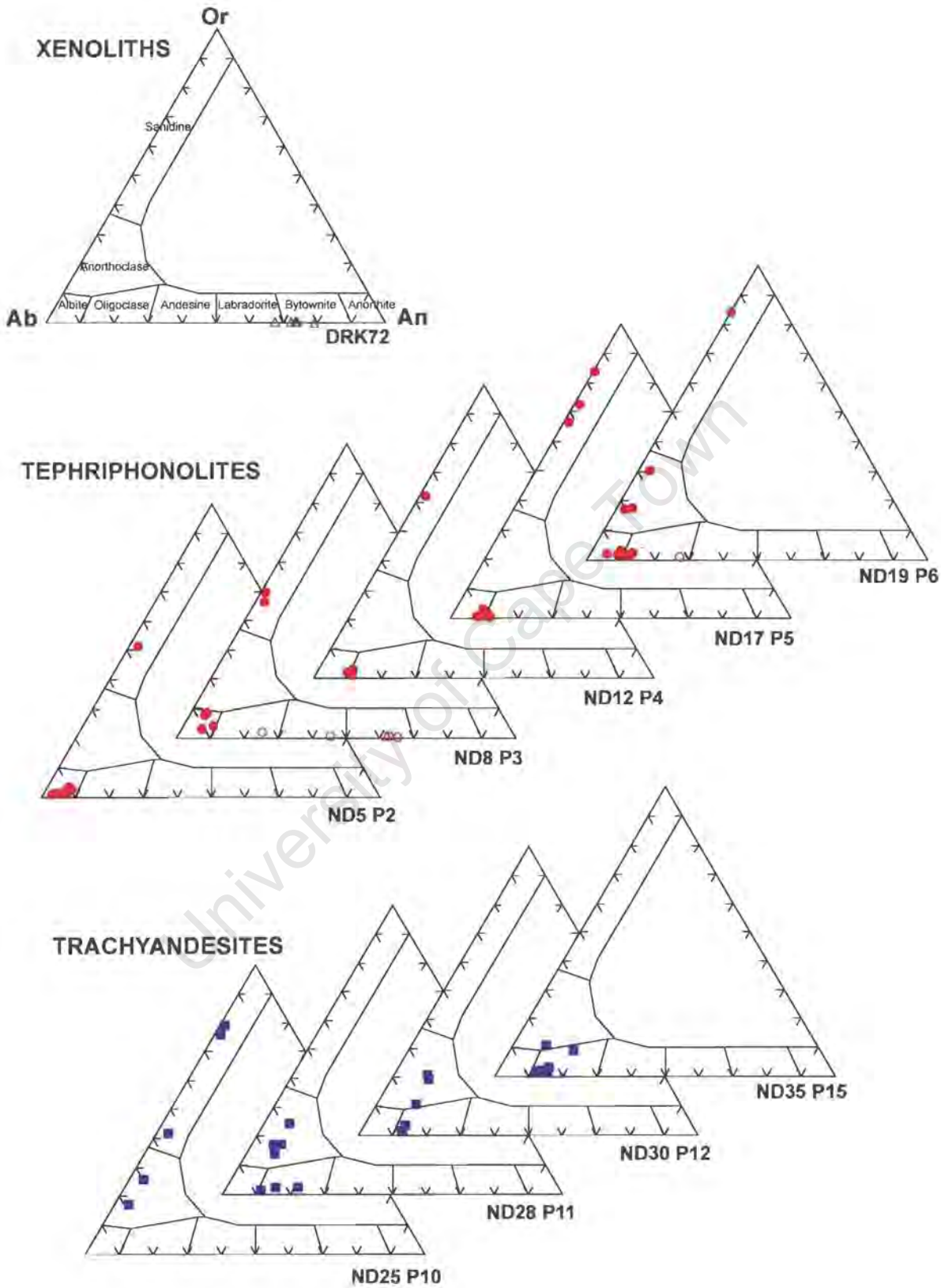

Figure 4.8 Feldspar analyses from the pipe samples. Open symbols represent plagioclase while solid symbols are alkali feldspar analyses.

Plagioclase occurs more commonly as a major constituent within gabbro xenoliths of the pipe samples. Fine plagioclase occurs in trace quantities within the fine-grained tephriphonolitic/trachyandesitic groundmass of pipe samples and in minor quantity as xenocrysts. These xenocrysts are typically anhedral and display moderate to heavy secondary saussuritisation (Plate 4.13). Occasionally, plagioclase takes on a glomeroporphyritic texture within the finer groundmass of the pipes. The plagioclase seen within gabbro xenoliths is heavily altered.

The few plagioclase xenocrysts analysed include relict cores and zones in resorbed crystals. Inspection of the analyses reveals that plagioclase have compositions ranging from An_{70} to An_{80} in the gabbro xenoliths to An_{25} to An_{60} within the porphyry pipes.

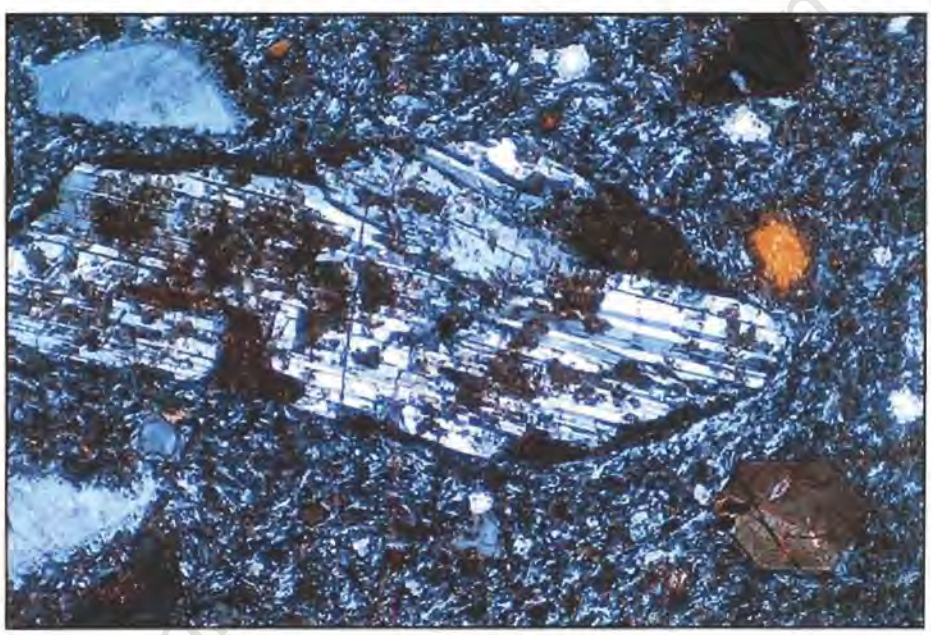

Plate 4.13: Photomicrograph of trachyandesite ND8. A large discrete crystal of plagioclase set within a fine grained groundmass shows moderate to heavy secondary alteration that occurs along the irregular grain boundary as well as within. XPL, FOV=2.5mm.

4.2.6 Nepheline

Medium to fine anhedral nepheline showing light to moderate secondary alteration occurs predominantly within the matrix of the samples, in association with feldspar and hornblende. The samples that have a high nepheline content display a seriate granular texture. Anhedral nepheline phenocrysts found within the matrix are commonly medium sized. There are zones within the matrix where there are higher concentrations of nepheline and less alkali feldspar.

4.2.7 Opaque oxides

Opaque oxides generally occur in trace quantities as anhedral to subhedral equant sub-rounded grains. Grain boundaries tend to have lobate embayments, and are occasionally, but not always, mantled by fine biotite (Plate 4.14). Mantling of the opaque oxides is not always complete, and where absent, opaque oxides display a fine net-textured pattern in association with the groundmass of fine granular clinopyroxene, nepheline and feldspar. Gabbro xenoliths appear to have a considerably higher (although still minor) concentration of opaque oxides, and these too exhibit mantling by secondary biotite. Their grain shape suggests the oxides are possibly magnetite. Frequent mantling around isolated grains found within the pipe groundmass suggests these oxides are in fact xenocrysts. Rare grains (possibly ilmenite) exhibit mantling by a grayish white alteration product that may be leucoxene.

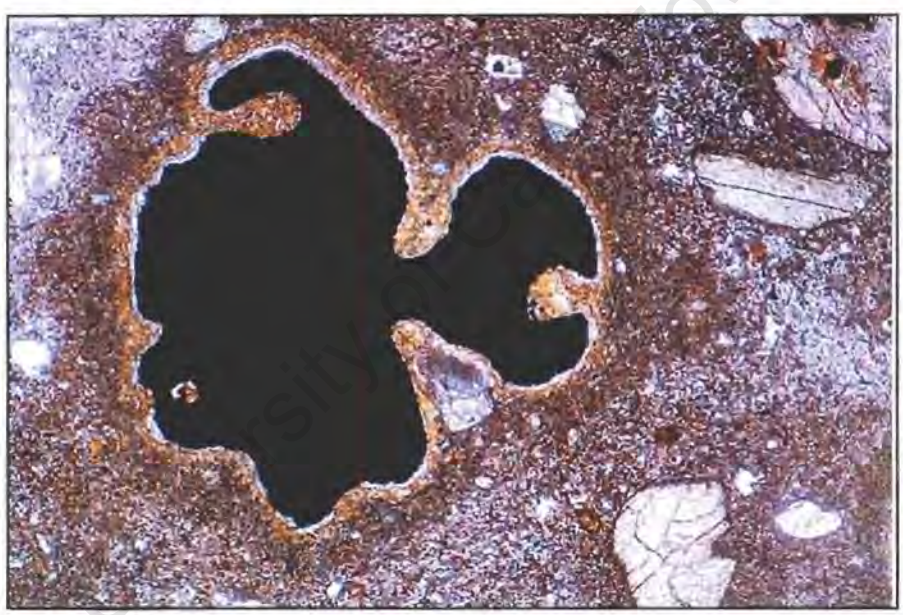

Plate 4.14: Photomicrograph of tephriphonolite sample ND 4. Secondary biotite is seen mantling a complexly resorbed Fe-Ti oxide grain. Note the lobate embayments along rounded grain boundaries. PPL, FOV=2.5mm.

4.2.8 Apatite

Euhedral apatite, a common accessory mineral of igneous rocks, is found in the pipes as:

- discrete phenocrysts (Plate 4.15)
- fine accessory matrix minerals
- small inclusions within amphibole and clinopyroxene reaction rims and phenocrysts (Plate 4.16).

Apatite phenocrysts are euhedral, although frequently slightly rounded at crystal apices. Otherwise, apatite appears to be in textural equilibrium with the groundmass of the pipes, showing no evidence of secondary alteration. Very fine fluid inclusions are observed within the apatite phenocrysts.

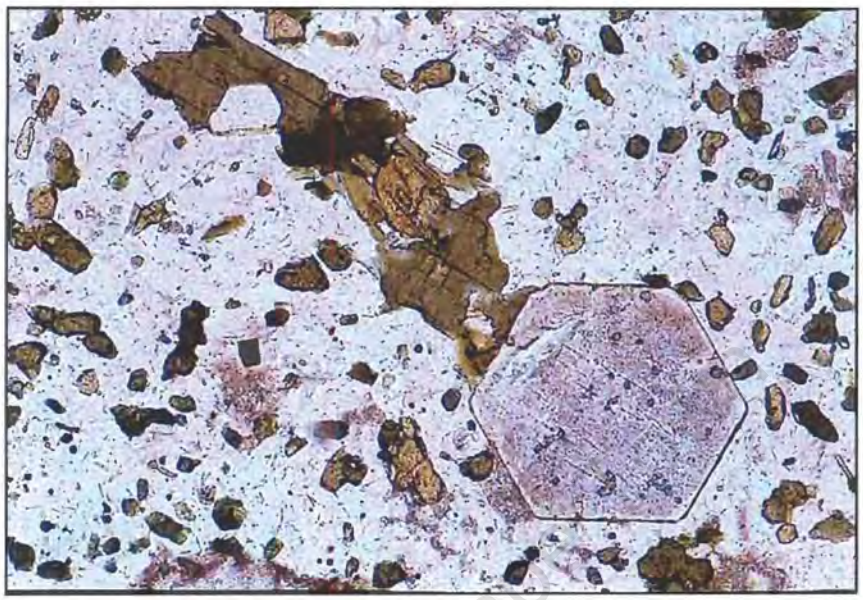

Plate 4.15: Photomicrograph of trachyandesite sample ND21. Euhedral apatite set within a fine matrix. PPL, FOV=1.0mm.

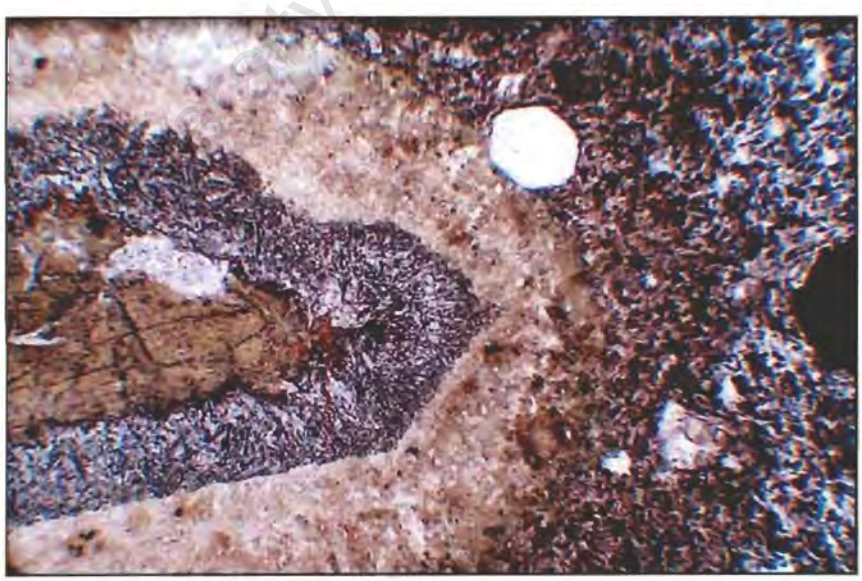

Plate 4.16: Photomicrograph of trachyandesite sample ND 19. Euhedral apatite seen within a reaction corona of fine biotite mantling a relict olivine xenocryst. PPL, FOV=1.5mm.

4.3 Classification of Xenoliths

The porphyry pipes contain the following xenolith types:

- Gabbros
- Syenite (from the KIC)
- Fine grained volcanic rocks (trachyte)
- Basement metamorphic rock (granites, gneisses and metasediments)
- Nama sediments

The gabbros may be derived from either deeper parts of the KIC or a deep-seated intrusion that has no relation to Kanabeam. The syenites are thought to be parts of the KIC, while the trachyte is possibly from a hypothetical volcanic edifice. The gneisses and meta-sediments are derived from country rock. No granite xenoliths that originate from Kanabeam were observed in the samples. This may indicate that the pipes were emplaced before the granites or that they were emplaced too far away from the granites to allow the melt to pick up xenoliths of this type.

4.3.1 Gabbro

Distributed through most pipes are rounded gabbroic xenoliths that vary from microscopic (<1cm) to tens of centimetres (~30cm) in dimension. Minerals within these include clinopyroxene, plagioclase and in some instances olivine and/or magnetite. Grain size within the gabbros varies from 3cm to 0.5mm. Within some gabbro xenoliths there is primary phase layering.

Within the xenoliths where clinopyroxene and olivine are found in contact, primary igneous textures are preserved indicating mineral stability (Plate 4.17). Plagioclase in contact with olivine however, is commonly unstable and appears to have undergone a sub-solidus reaction. The rims that surround the original olivine, where they are in contact with plagioclase, have grown mostly at the expense of the olivine while plagioclase has undergone mineral replacement by nepheline. Clinopyroxene in contact with plagioclase is more stable and rarely a thin symplectitic zone has been developed.

A reaction rim between the host matrix and gabbro xenoliths varies between a millimetre to over a centimetre in width. Euhedral amphibole phenocrysts are found within this transition zone where there is a larger proportion of fine-grained mafic minerals than the usual pipe matrix. These fine-grained mafic minerals are mostly hornblende, although in some examples biotite was identified. Within this zone of increased mafic material there are also relicts of mineral melt reaction in the form of complete olivine pseudomorphs, while the margins of the xenoliths are commonly altered and coronas surrounding relict

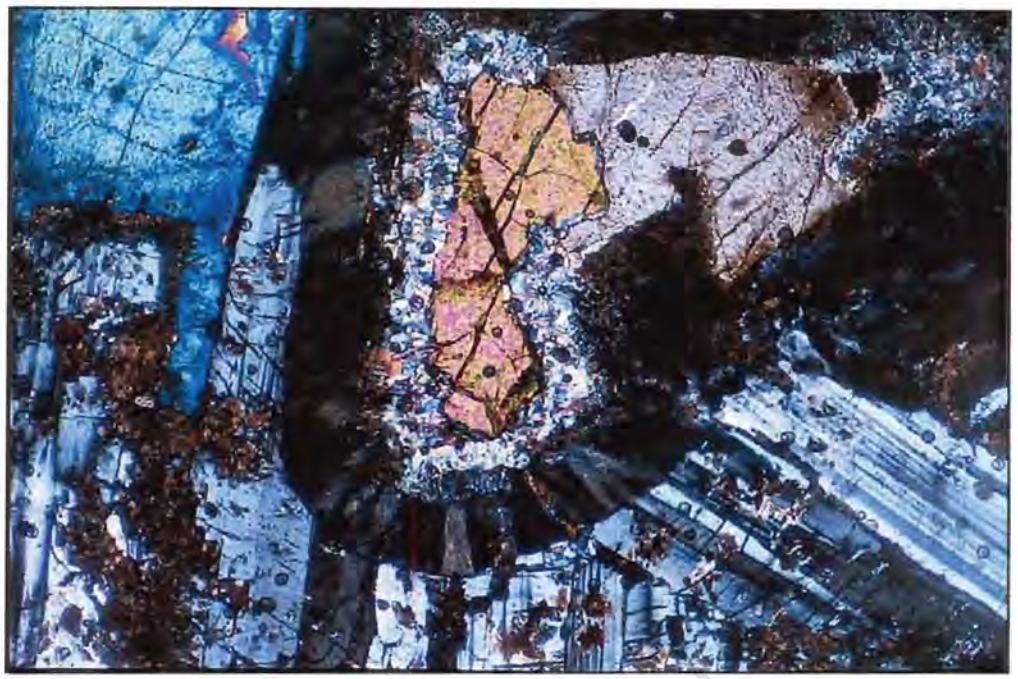

Plate 4.17: Photomicrograph of tephriphonolite sample ND2. Altered subhedral plagioclase within a gabbro xenolith. An olivine relict is seen to the centre, in contact with clinopyroxene to the upper right, whilst clinopyroxene is seen to the upper left of the micrograph. Note that olivine and clinopyroxene are in textural equilibrium, along with clinopyroxene and plagioclase, whereas olivine and plagioclase are not. XPL, FOV=2.5mm.

olivine are sometimes observed.

In close proximity to gabbro xenoliths there are "disaggregated" xenoliths surrounded by fine-grained mafic material. The zonation around the grains is the same as the transitional zone seen around the gabbro xenoliths.

Plagioclase within one fine-grained mafic xenolith of gabbroic composition was not highly altered. This is possibly the result of being more impervious to melt infiltration and therefore magmatic alteration. In this xenolith, however, there is both olivine and magnetite, which is also unusual, as most have either the one or the other.

4.3.2 Syenite

Coarse grained aggregates of feldspar and nepheline with diffuse boundaries are interpreted as being nepheline syenite xenoliths from the sub-complex, on the basis of mineralogy and texture.

4.3.3 Fine-grained volcanic rocks (Trachyte)

Although a large number of fine-grained xenoliths were observed in hand specimen, the distinction between these and the pipe matrix is often difficult. The difficulty lies in the fact that both rock types are very similar in composition. The boundaries often blend with the host matrix making identification even more difficult. Subtle variations in texture and mineralogy however, indicate the presence of these xenoliths.

4.3.4 Basement metamorphic rocks (Gneiss)

Metamorphic mineral assemblages (medium to high grade) and metamorphic textures are features that distinguish basement gneisses and metasediments from KIC syenites, granites and Nama sediments.

4.3.5 Nama Sediments

Nama sediment xenoliths are commonly found within the northern pipes. Quartzites and conglomerates are also commonly observed. The xenoliths are most likely Nama Group (Kuibis Formation) sediments that have been incorporated by the pipes during intrusion. Smithies (1992) reports recrystallised calc-silicate xenoliths interpreted as being derived from Nama Group limestones.

5 WHOLE ROCK GEOCHEMISTRY

5.1 Introduction

A total of 23 representative whole rock samples from the pipes were analysed for major and trace elements by X-ray fluorescence (XRF). Of these a subset of 10 samples was analysed for rare earth elements (REE) by inductively coupled plasma mass spectrometry (ICP-MS). All whole rock analyses were carried out at the University of Cape Town in the Department of Geological Sciences. Data from the pipe samples including their gabbroic xenoliths and related dykes are presented in Table 5.1 and 5.2 while descriptions of techniques employed can be found in the appendices. Major and trace element data for the plutonic rocks at Kanabeam were made available (Reid, 1991 and unpublished data set). For the purposes of this study selected plutonic samples were further analysed for REE by ICP-MS.

Table 5.1 Major, Trace and REE data for the southern pipe samples, gabbro xenoliths within the pipes, and dykes sampled in the near vicinity of the pipes.

Sample	ND44	ND46	ND47	ND48	ND4	ND9	ND10	ND12	ND16A	ND17	ND19	ND20
Pipe No.	P1	P1	P1	D3	P2	D1	P3	P4	P4	P5	P6	P6
SiO_2	54.11	57.03	53.6	63.08	55.5	57.69	54.07	53.28	43.80	53.82	55.39	45.02
TiO_2	0.89	0.12	0.90	0.22	0.79	0.05	0.85	0.93	1.07	0.84	0.80	1.34
Al_2O_3	18.02	20.35	17.87	15.62	18.43	20.23	18.14	17.88	15.40	18.12	18.32	16.71
Fe_2O_3	7.05	5.51	6.98	5.90	6.64	5.58	6.81	7.17	7.17	6.84	6.74	8.85
MnO	0.19	0.28	0.19	0.19	0.19	0.28	0.18	0.18	0.13	0.19	0.19	0.14
MgO	2.60	0.22	2.91	0.02	2.05	0.06	2.39	2.90	10.01	2.59	2.20	9.06
CaO	4.38	1.07	4.74	0.84	3.89	0.71	4.22	4.72	14.17	4.38	4.00	12.81
Na_2O	7.31	8.92	6.89	6.93	7.27	9.39	7.49	7.06	4.08	6.90	7.11	3.33
K_2O	4.10	5.43	4.05	5.91	4.46	5.38	4.15	3.84	1.52	4.06	4.31	0.74
P_2O_5	0.43	0.05	0.47	0.01	0.40	0.02	0.41	0.45	0.33	0.43	0.41	0.35
SO_3	0.06	0.04	0.08	0.00	0.06	0.01	0.04	0.10	0.13	0.10	0.11	0.07
NiO	0.00	0.00	0.00	0.00	0.00	0.00	0.00	0.00	0.02	0.00	0.00	0.02
Cr_2O_3	0.01	0.00	0.01	0.00	0.01	0.00	0.01	0.01	0.04	0.01	0.01	0.02
LOI	0.58	0.44	0.37	0.77	0.50	0.33	0.55	0.68	1.89	0.64	0.76	1.51
H_2O-	0.07	0.05	0.05	0.12	0.10	0.03	0.07	0.09	0.12	0.08	0.05	0.09
TOTAL	99.15	99.02	98.68	98.71	99.68	99.41	98.75	98.54	97.85	98.27	99.6	98.45
Traces by XRF												
Mo	7	9	10	<1	8	8	4	6	21	7	8	2
Nb	152	290	159	588	171	373	159	142	14	157	171	16
Zr	733	1459	762	2051	855	2168	775	662	167	754	830	106
Y	39	66	42	178	42	79	42	37	25	40	43	20
Sr	573	42	620	32	531	24	553	604	1140	579	522	747
U	8	18	8	28	10	19	9	7	3	7	9	<2
Rb	130	224	123	416	141	294	128	112	78	131	147	27
Th	37	87	39	136	43	73	44	32	1112	38	40	3
Pb	29	53	36	142	33	38	36	32	101	31	36	21
Zn	98	109	98	276	102	86	102	98	82	104	106	69
Cu	20	11	36	<1	17	5	19	24	66	22	16	33
Ni	29	2	38	<2	23	1	26	33	122	27	24	97
Co	15	2	17	<3	11	<3	14	16	47	14	12	46
Mn	1350	1680	1369	1437	1403	1726	1340	1365	1056	1435	1455	1068
Cr	63	8	65	5	39	7	45	54	248	53	45	143
V	60	<1	65	<3	48	<1	56	65	161	57	50	180
Ba	1064	59	1134	27	1030	39	1010	1043	1130	1094	998	279
Sc	9	<1	10	1	7	<1	9	10	40	9	8	37
Traces by ICPMS												
Li		37.19				12.94	38.47	47.82	75.52			49.28
Cs		3.97				2.70	2.19	2.69	10.39			2.43
La		223.34				228.60	136.56	131.82	106.07			21.86
Ce		368.16				384.07	244.29	234.88	183.18			48.81
Pr		31.93				31.24	23.76	23.64	18.74			5.93
Nd		85.94				82.45	75.22	75.77	64.65			25.16
Sm		11.66				10.89	10.67	10.63	8.82			4.85
Eu		0.75				0.62	2.29	2.47	2.22			1.67
Gd		8.56				7.85	6.96	7.00	5.83			4.31
Tb		1.51				1.44	1.06	1.04	0.78			0.61
Dy		9.69				9.74	6.58	6.28	4.26			3.55
Ho		2.03				2.15	1.33	1.23	0.77			0.66
Er		6.70				7.59	4.20	3.76	2.08			1.78
Tm		1.04				1.26	0.64	0.56	0.27			0.23
Yb		7.66				9.73	4.59	4.14	1.67			1.47
Lu		1.18				1.49	0.67	0.62	0.21			0.21
Hf		9.54				28.45	12.49	11.20	3.77			2.47
Ta		20.67				24.17	9.26	8.09	0.71			0.84

Table 5.2 Major, Trace and REE data for the northern pipe samples.

Sample	ND21	ND22	ND23	ND25	ND26	ND28	ND30	ND31	ND35	ND38	ND40
Pipe No.	P7	P8	P9	P10	P11	P11	P12	P13	P15	P17	P17
SiO_2	58.43	55.09	54.27	55.84	55.8	55.53	55.39	58.09	61.13	56.56	56.59
TiO_2	0.72	1.12	1.08	1.12	1.05	1.08	1.10	1.02	0.53	1.08	1.03
Al_2O_3	18.3	19.08	19.42	16.62	16.88	16.73	16.53	16.37	17.51	16.68	16.81
Fe_2O_3	5.56	6.71	6.51	7.40	7.15	7.35	8.04	7.13	4.54	7.24	7.58
MnO	0.15	0.12	0.16	0.16	0.16	0.18	0.18	0.16	0.13	0.17	0.15
MgO	1.59	1.46	1.69	2.72	2.45	2.62	2.87	2.41	0.56	2.43	2.39
CaO	3.03	3.67	3.84	4.54	3.95	4.37	3.87	4.09	1.98	4.19	2.33
Na_2O	6.31	5.86	5.83	5.52	5.89	5.71	5.97	5.34	5.70	5.87	6.21
K_2O	4.82	4.08	3.98	4.15	3.91	3.88	3.87	4.31	6.32	4.07	4.77
P_2O_5	0.29	0.52	0.50	0.54	0.52	0.53	0.53	0.48	0.16	0.54	0.52
NiO	0.00	0.00	0.00	0.00	0.00	0.00	0.00	0.00	0.00	0.00	0.00
Cr_2O_3	0.00	0.00	0.00	0.01	0.00	0.00	0.01	0.01	0.00	0.00	0.00
LOI	0.75	0.49	0.54	0.63	0.57	0.59	0.56	0.35	0.18	0.49	0.45
H_2O-	0.11	0.08	0.05	0.08	0.08	0.07	0.12	0.07	0.11	0.08	0.11
TOTAL	99.18	97.69	97.27	98.63	97.77	97.99	98.35	99.39	98.56	98.82	98.37
Traces by XRF											
Mo	6	4	3	6	3	5	4	3	5	4	2
Nb	175	181	186	120	126	120	119	121	209	122	122
Zr	646	554	635	609	606	600	578	599	889	600	605
Y	47	41	39	49	49	49	53	51	64	54	72
Sr	670	1027	1041	565	548	578	528	514	378	554	414
U	7	8	5	5	5	4	5	5	7	5	6
Rb	121	117	117	91	166	171	196	105	180	194	255
Th	34	29	32	26	24	27	23	26	41	25	27
Pb	29	22	21	20	23	28	29	18	28	21	20
Zn	78	83	97	96	123	151	165	88	74	129	172
Cu	10	3	3	11	5	5	7	15	2	7	4
Ni	17	2	3	19	16	18	20	18	4	16	13
Co	8	8	9	15	12	14	12	15	5	15	8
Mn	1111	834	1226	1202	1168	1328	1342	1148	1004	1251	1148
Cr	36	9	6	43	29	34	40	35	8	34	28
V	23	39	34	80	72	75	76	69	4	76	66
Ba	1125	1891	2016	1520	1531	1601	1508	1477	1185	1560	1273
Sc	6	4	5	12	11	11	10	13	4	11	9
Traces by ICPMS											
Li		51.24	44.97		82.48				7.89		
Cs		2.41	4.87		7.17				0.82		
La		149.39	144.63		134.03				172.49		
Ce		271.29	269.09		263.13				320.15		
Pr		27.10	26.79		26.83				32.31		
Nd		88.38	87.00		97.96				104.24		
Sm		12.55	12.09		14.30				15.97		
Eu		3.27	3.35		3.34				2.58		
Gd		8.10	7.83		9.86				10.92		
Tb		1.19	1.13		1.43				1.71		
Dy		6.81	6.57		8.29				10.29		
Ho		1.29	1.26		1.61				2.05		
Er		3.84	3.77		4.77				6.42		
Tm		0.54	0.55		0.68				0.94		
Yb		3.64	3.85		4.71				6.57		
Lu		0.52	0.57		0.72				0.98		
Hf		3.27	7.12		10.78				11.85		
Ta		9.92	9.30		6.04				11.03		

5.2 Major Element Patterns

5.2.1 Harker Variation Diagrams

Figures 5.1 and 5.2 are a series of Harker plots that display major element variation patterns in the porphyry pipes and plutonic units respectively. In terms of major element oxides the tephriphonolite samples form a single coherent group while the trachyandesites are more widely distributed. The single 'trachyandesite' sample that has SiO_2 greater than 60% has been observed to have compositions that are inconsistent with the other samples from these pipes (eg Figure 3.10 where this sample is classified as a trachyte). The two phonolite samples are characterised by very low TiO_2, MgO, CaO and P_2O_5, and predictably higher Na_2O and particularly K_2O.

The SiO_2 content within the NSS varies between approximately 52 and 62%. Variation in other major elements is limited, indicating a fairly coherent group. The microsyenite however, has lower SiO_2 and higher Fe_2O_3, MnO, MgO, CaO and P_2O_5 when compared to other NSS units. Additionally, the microsyenite has higher Fe_2O_3 and MnO than the gabbro xenoliths. Major element variation in the NSS and the porphyry pipes is comparable, although the pipes generally have lower Na_2O, higher Fe_2O_3 and P_2O_5.

The microgranite and aplite have the highest silica values in the KIC. The alkali (Na_2O and K_2O) are similar to those found in the other silica-oversaturated units within the complex. With the exception of Na_2O and K_2O these units have the lowest relative concentrations for all other major elements. Quartz syenite, granite and granite porphyry in the complex all have similar major element compositions including high SiO_2, low Al_2O_3, MnO and Na_2O.

5.2.2 CIPW Normative Composition

The CIPW norms (Appendix 4), used in calculating the differentiation indices and constructing petrogeny's residua diagrams, are also used to determine the silica saturation of the rock types within Kanabeam, as it is known that both nepheline and quartz bearing rock types exist. Distinction of two types of pipes on the basis of total alkalis is also reflected in their respective degrees of silica saturation. Figures 5.3 and 5.4 were calculated after partitioning total Fe so that $Fe_2O_3/FeO=0.5$ the ratio recommended by Middlemost (1989) for rocks with high total alkalis, like those of the KIC.The DI for the samples from the complex were calculated as the normative sum of Q+Or+Ab+Ne+Kp+Lc (Thornton and Tuttle, 1960).

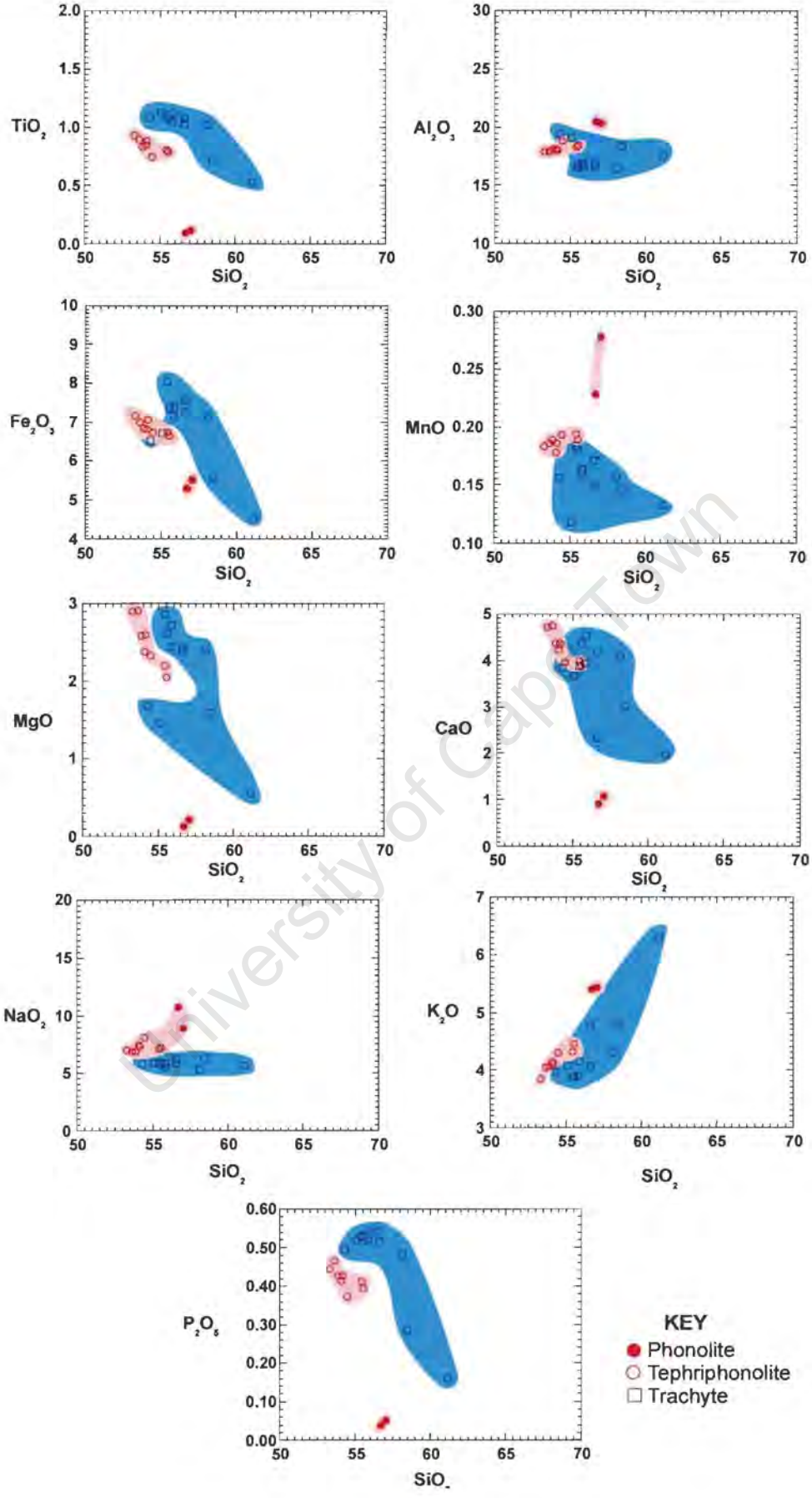

Figure 5.1 Harker variation diagrams for the pipe samples. The data represented here is given in Tables 5.1 and 5.2.

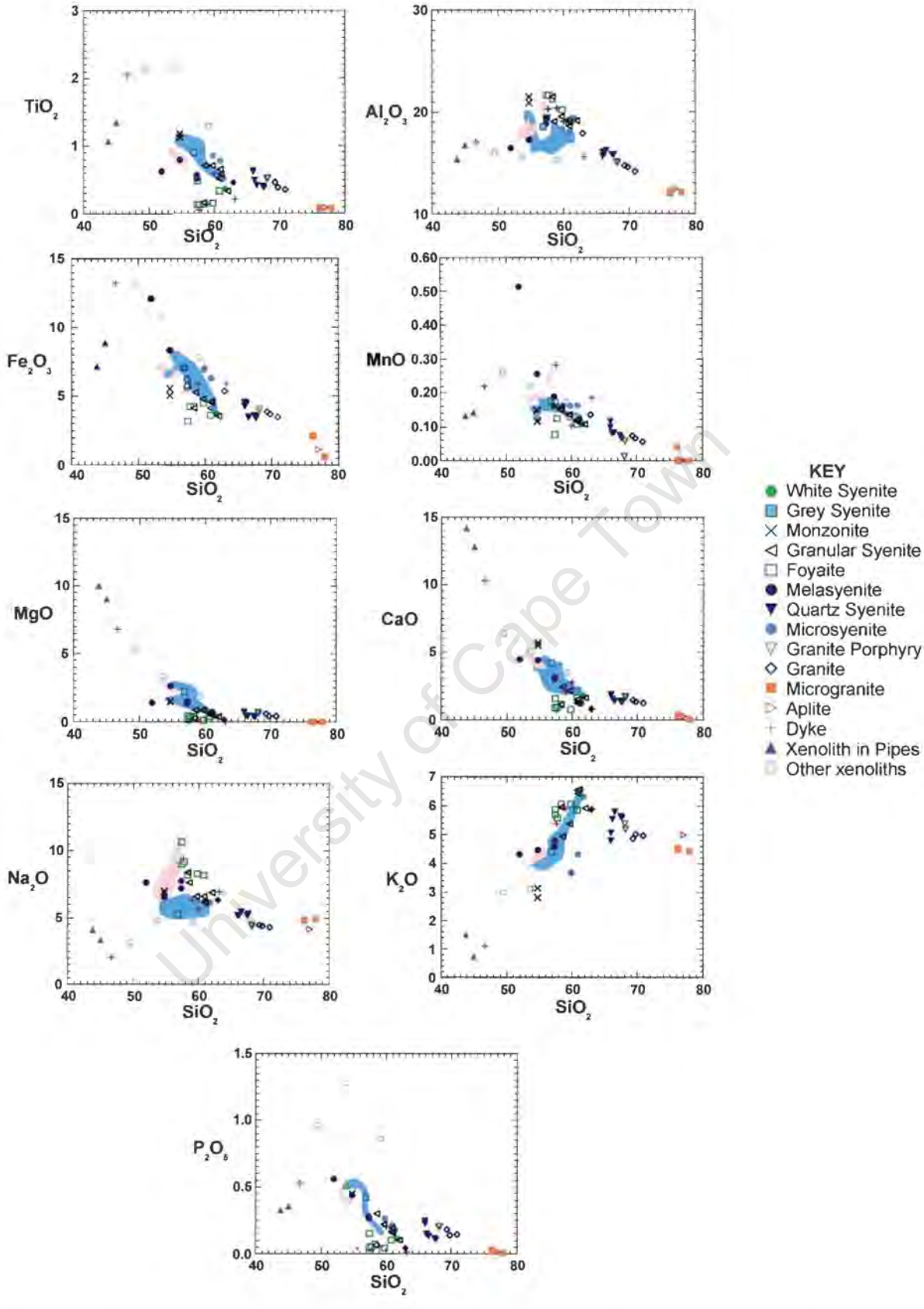

Figure 5.2 Harker variation diagrams for the plutonic samples from the Kanabeam Complex. The data represented here is given in Appendix 3. Pipe compositional variations are shown in pink (tephriphonolites) and blue (trachyandesites).

5.2.2.1 Petrogeny's Residua System

Samples that have more than 70% of the components of Petrogeny's Residua have been plotted in Figure 5.3. There are however pipe samples that are just below this value (68-70%) which are included to complete the data set. Within the ternary system, nepheline ($NaAlSiO_4$) -kalsilite ($KAlSiO_4$)–quartz (SiO_2) the samples from Kanabeam plot within the thermal valley, marking the composition of common residual magmas after fractional crystallisation as described by Bowen (1937) and Schairer (1950).

Predictably the quartz syenite-granite suite trend from the feldspar join to the silica-oversaturated minimum while the units belonging to the NSS trend towards the silica-undersaturated minimum from the feldspar divide. Some of the NSS samples form a trend towards and into the leucite field. If these samples do not contain leucite then the trend may reflect that crystallisation quite plausibly occurred at pressures above 1atm where the leucite field contracts (Figure 5.3).

The two groups within the pipe samples plot as two distinct clusters. The trachyandesites, plot as a cluster along the Ab-Or divide within the silica-undersaturated portion while the second group, the tephriphonolites, form a strong trend towards the silica-undersaturated minimum, and as with other samples from the NSS some points are found within the leucite field at 1atm.

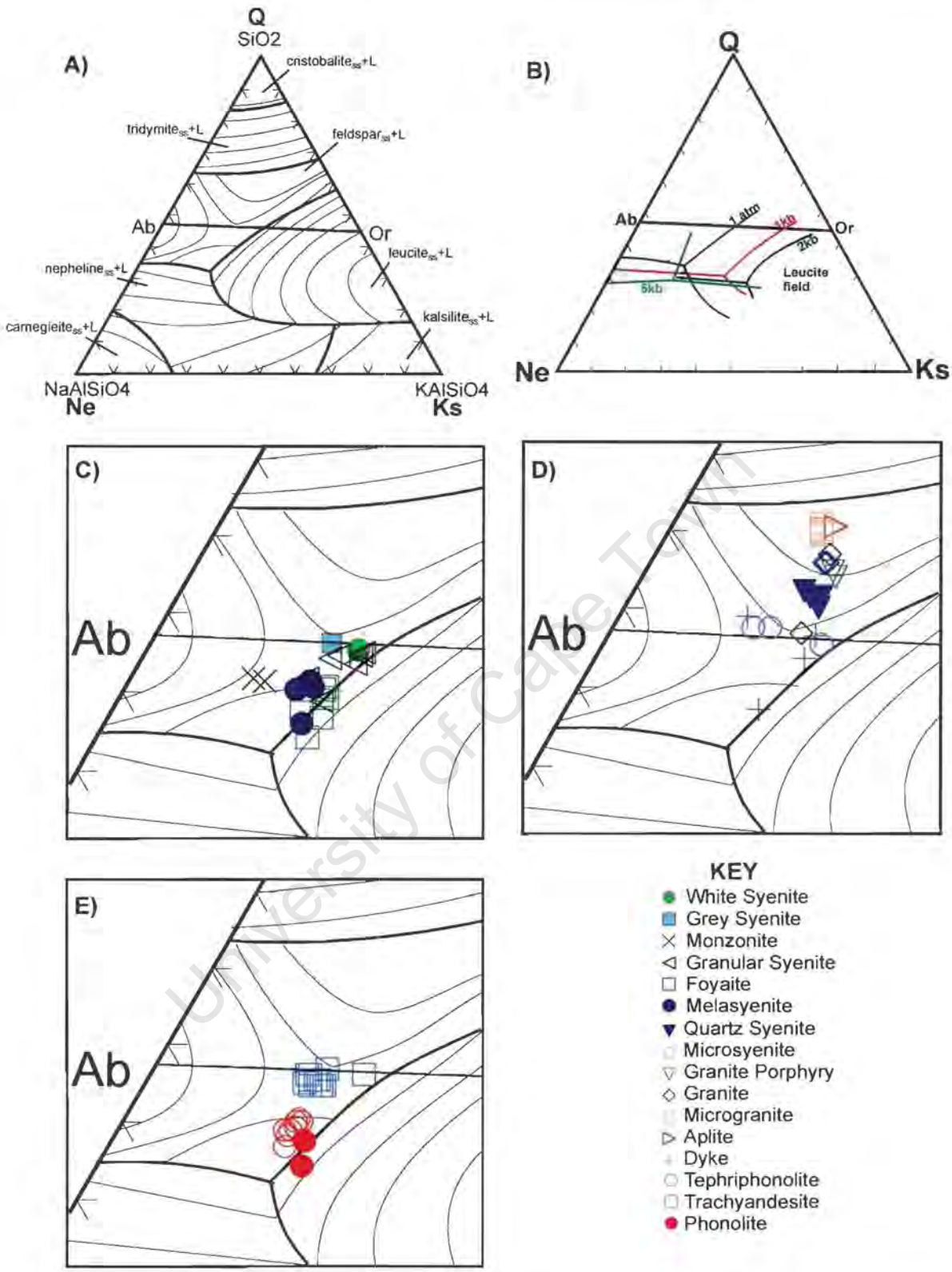

Figure 5.3 Projections onto the plane nepheline-quartz-kasilite from H_2O in the nepheline syenite system. A) The boundaries given for this system at 1atm. B) the contraction of the leucite field at various pressures. C) the Nepheline Syenite Sub-complex. D) The silica-oversaturated units and dykes. E) The pipes that form the basis of this study.

5.2.2.2 Variation with Differentiation Index (DI)

The silica-undersaturated units of the complex (with exception of the xenoliths and dykes) have a relatively wide range in DI values (66-95) while the silica-oversaturated units are limited to high values (85-98) (Figure 5.4). The tephriphonolites and trachyandesites cover similar ranges in DI, from 70 to 90, and as expected the gabbro xenoliths have very low values. Normative quartz within the units increases in the order: quartz syenite, granite porphyry and granite with the highest values noted in microgranite and aplite. Microsyenite, trachyandesite and grey syenite within the KIC are found to contain either low values of normative quartz or nepheline i.e. they appear to be critically saturated. Normative nepheline increases in the silica-undersaturated units in the order white syenite, granular syenite, monzonite, melasyenite, tephriphonolite, foyaite and phonolite.

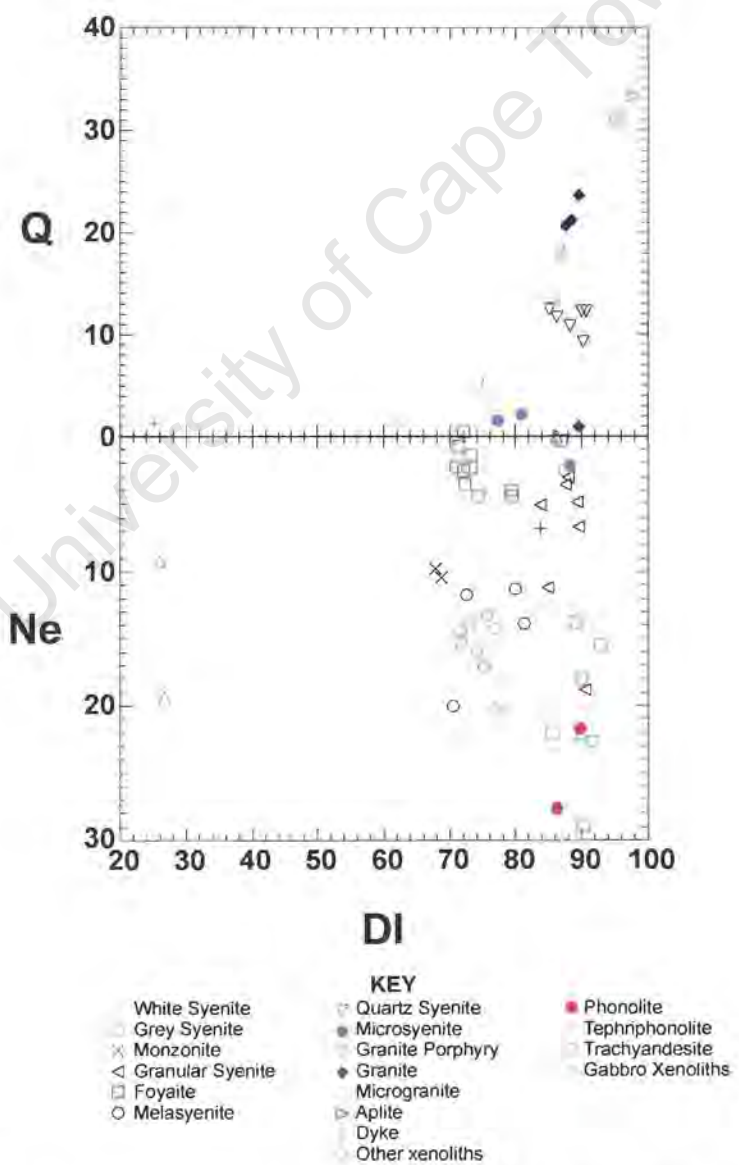

Figure 5.4 Graph of normative nepheline and quartz versus DI, for all of the KIC units.

The tephriponolite samples have higher Al_2O_3, MnO, MgO, CaO and Na_2O for any given DI than the trachyandesite samples, however the opposite is true for SiO_2, TiO_2 and P_2O_5 (Figure 5.5). The concentrations of Fe_2O_3T and K_2O are similar in the tephriphonolites and trachyandesites . The pipes in general contain higher TiO_2, Fe_2O_3T, MnO, MgO, CaO and P_2O_5 than the plutonic units of the KIC with the exception of the gabbro xenoliths and monzonites in the case of TiO_2 CaO and P_2O_5. The phonolites are distinct in that they have low SiO_2 and TiO_2 and high Al_2O_3, MnO and Na_2O when compared to KIC samples of similar DI.

Although the range in DI overlaps for the silica-oversaturated and silica-undersaturated samples of the KIC the silca-undersaturated samples have higher Al_2O_3, MnO, Na_2O and K_2O and lower Al_2O_3. The other major element oxides are found in similar concentrations in both the silica-oversaturated and silica-undersaturated samples.

The microgranite and aplite samples have the highest SiO_2 concentrations in the complex while they have the lowest concentrations for all other major element oxides with the exception of K_2O and Na_2O. Their concentrations of Na_2O are low, but are similar to those of the quartz syenite and granite samples, while their K_2O concentration is higher than the microsyenite, grey syenite and pipes (excluding phonolite samples) and similar to the granites.

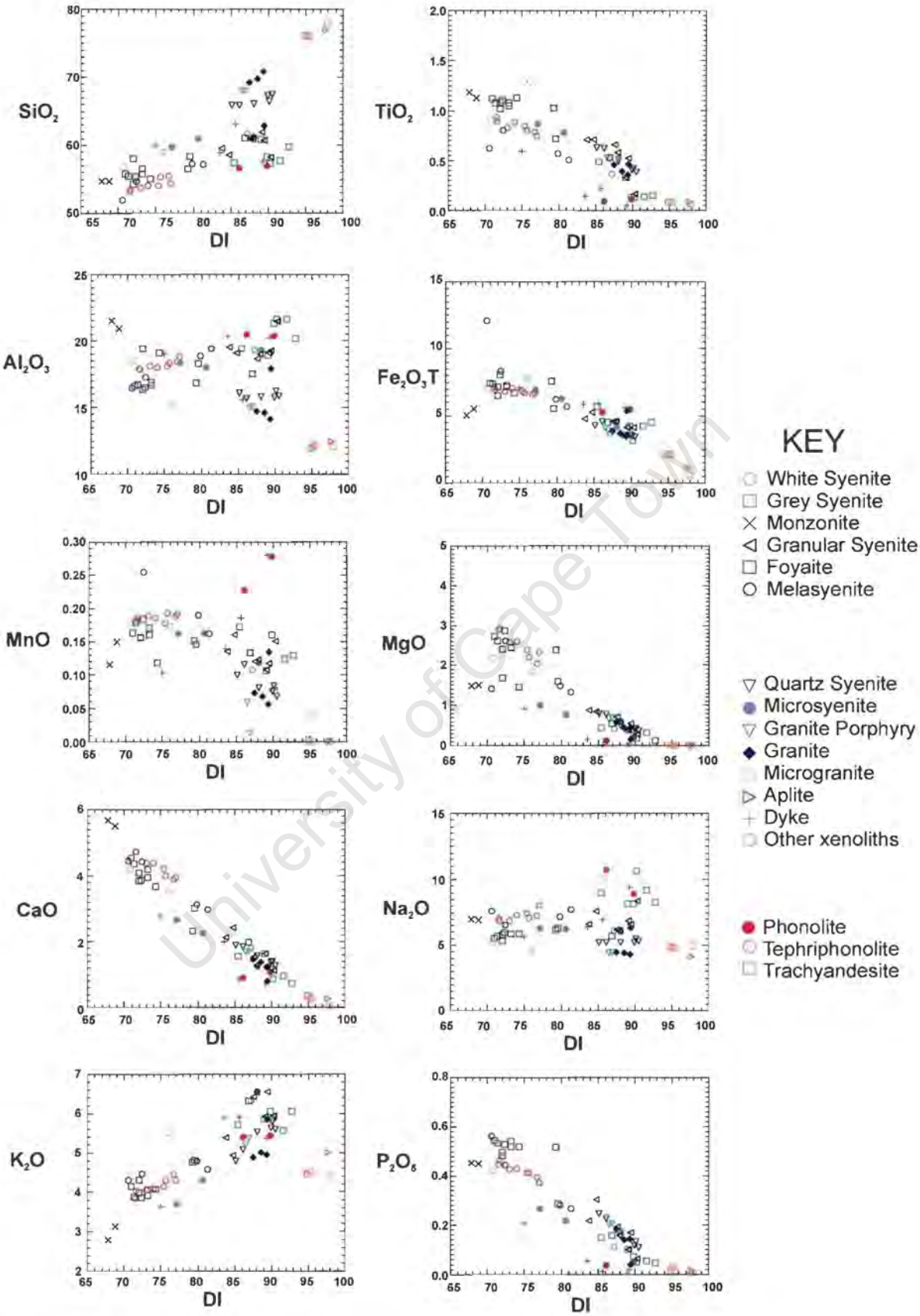

Figure 5.5 Variation diagrams of major element oxides versus DI for the KIC.

5.2.3 Summary of Major Element Data of the Porphyry Pipes

Table 5.3 contains a statistical summary of the major element data for the pale grey phonolites, the tephriphonolites and the trachyandesites. The phonolites have the highest SiO_2 while the tephriphonolites have the lowest, however the trachyandesites have at least one sample that has very high SiO_2 and TiO_2. Although the average Fe_2O_3T content of the samples show that there is an increase in Fe from phonolite to tephriphonolite with the trachyandesites having the highest average value, the tephriphonolites have both the highest and lowest concentrations and therefore the widest variation. MgO and CaO are highest in the tephriphonolites, while almost negligible in the phonolites.

Table 5.3 Summary of major element oxide data for the tephriphonolite, trachyandesite and phonolite samples.

	Average			*Minimum*			*Maximum*			*Standard Deviation*		
	Phonolite	*Tephri-phonolite*	*Trachy-andesite*	*Phonolite*	*Tephri-phonolite*	*Trachy-andesite*	*Phonolite*	*Tephri-phonolite*	*Trachy-andesite*	*Phonolite*	*Tephri-phonolite*	*Trachy-andesite*
SiO_2	56.86	54.60	56.61	56.69	53.28	54.27	57.03	57.03	61.13	0.24	1.27	1.94
TiO_2	0.11	0.76	0.99	0.10	0.12	0.53	0.12	0.93	1.12	0.01	0.27	0.19
Al_2O_3	20.41	18.39	17.36	20.35	17.87	16.37	20.47	20.35	19.42	0.08	0.82	1.08
Fe_2O_3T	5.41	6.72	6.84	5.30	5.51	4.54	5.51	7.17	8.04	0.15	0.52	1.00
MnO	0.25	0.20	0.16	0.23	0.18	0.12	0.28	0.28	0.18	0.03	0.03	0.02
MgO	0.18	2.23	2.11	0.13	0.22	0.56	0.22	2.91	2.87	0.06	0.87	0.70
CaO	0.99	3.93	3.62	0.91	1.07	1.98	1.07	4.74	4.54	0.11	1.19	0.83
Na_2O	9.83	7.37	5.84	8.92	6.89	5.34	10.73	8.92	6.31	1.28	0.66	0.28
K_2O	5.42	4.30	4.38	5.41	3.84	3.87	5.43	5.43	6.32	0.02	0.49	0.72
P_2O_5	0.05	0.38	0.47	0.04	0.05	0.16	0.05	0.47	0.54	0.01	0.13	0.12

5.3 Trace Element Patterns

Trace element variation diagrams for the various units (Figure 5.6 and 5.7) have been plotted relative to DI. Figure 5.6 is a collection of plots of ferro-magnesian related trace elements while Figure 5.7 includes plots of other trace elements. In Figure 5.6 two scales have been used, so that mafic samples with low DI and high ferro-magnesian trace element concentrations can be examined while patterns in the felsic samples can also be distinguished using the second scale.

Preliminary examination of Figure 5.6 reveals that the pipes have higher Ni, Cr, Co, V than most of the plutonic units of the complex. The exception to this is the melasyenite and grey syenite samples. Monzonite has concentration levels that approximate the trachyandesite samples with low concentrations of these elements. The tephriphonolites have higher Ni, Cr and Co at equivalent DI values than the trachyandesites while, the reverse is true for V and Sc. A near linear trend for the tephriphonolites is observed for all ferro-magnesian trace elements where trace element concentration decreases with increasing DI. There is one trachyandesite sample that has low concentrations of ferro-magnesian trace elements, a fact that may be related in part to its silica-oversaturated nature. The phonolites have lower Ni, Cr, Co, V and Sc than the tephriphonolites and trachyandesites but have similar concentrations to the foyaite, granular syenite and white syenite with the exception of Sc in the white syenite.

The other trace elements generally have less variation in concentration between different rock types in Kanabeam. It is noted however that the tephriphonolite concentrations for Sr, Zr and Nb are higher than those of the trachyandesites at a given DI while Ba, Rb and Y are higher in the trachyandesites. Concentrations in the microsyenite are more consistent with those of the trachyandesites even though they have higher DI values. The exception to this observation is Nb which has higher concentrations than both pipe types. Monzonite has high Sr and low Rb when compared to the other rock types in the complex. The phonolite samples have low Ba and Sr, and the highest Zr with the exception of the dykes sampled.

As expected, the microgranite has very low concentrations in all of the ferro-magnesian related trace elements as well as Ba and Sr while they have noticably high Rb concentrations when compared to other KIC samples. The quartz syenite, granite and granite porphyry have relatively low concentrations of ferro-magnesian related trace elements.

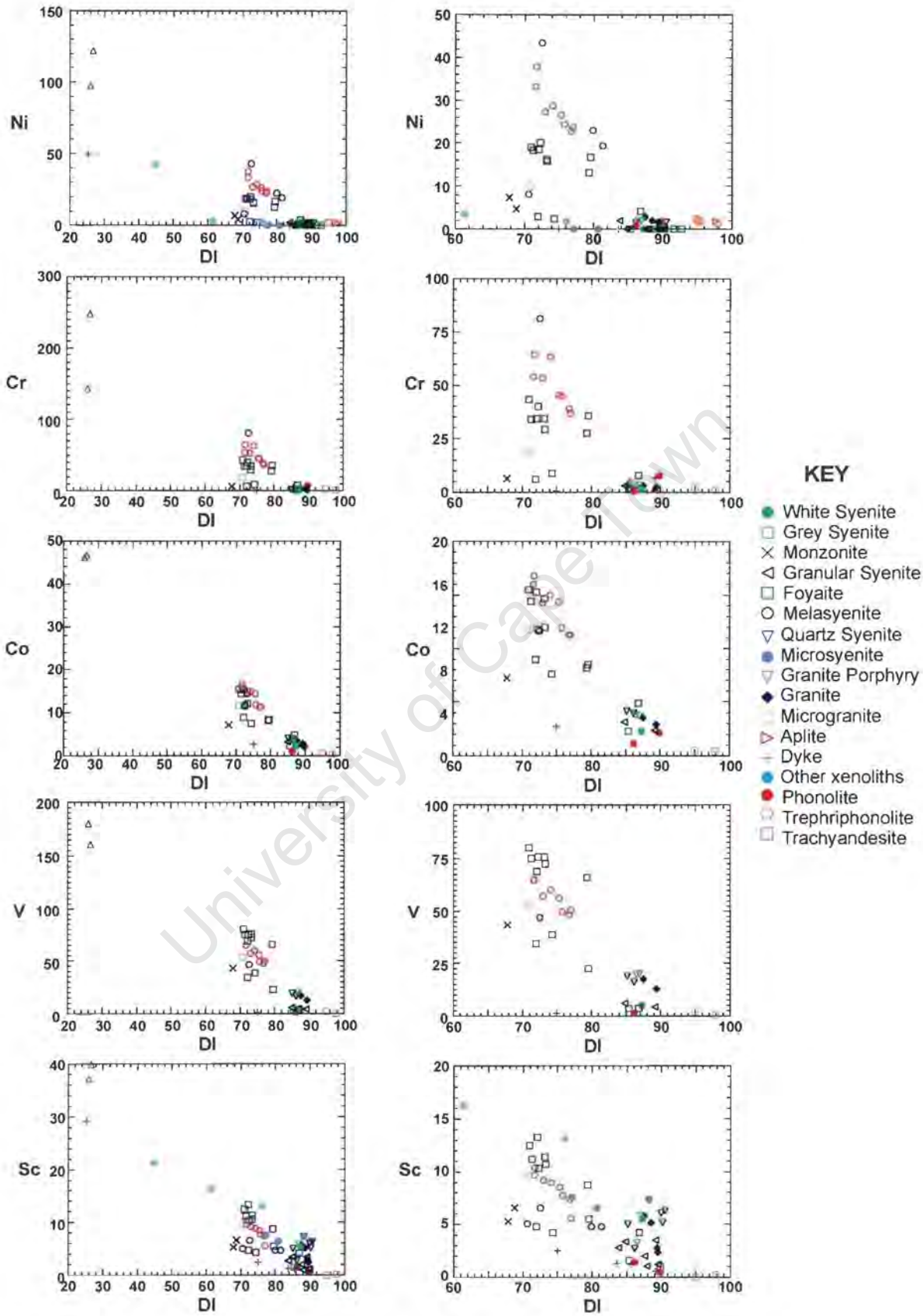

Figure 5.6 Variation diagrams of ferro-magnesian related trace elements versus DI for the KIC.

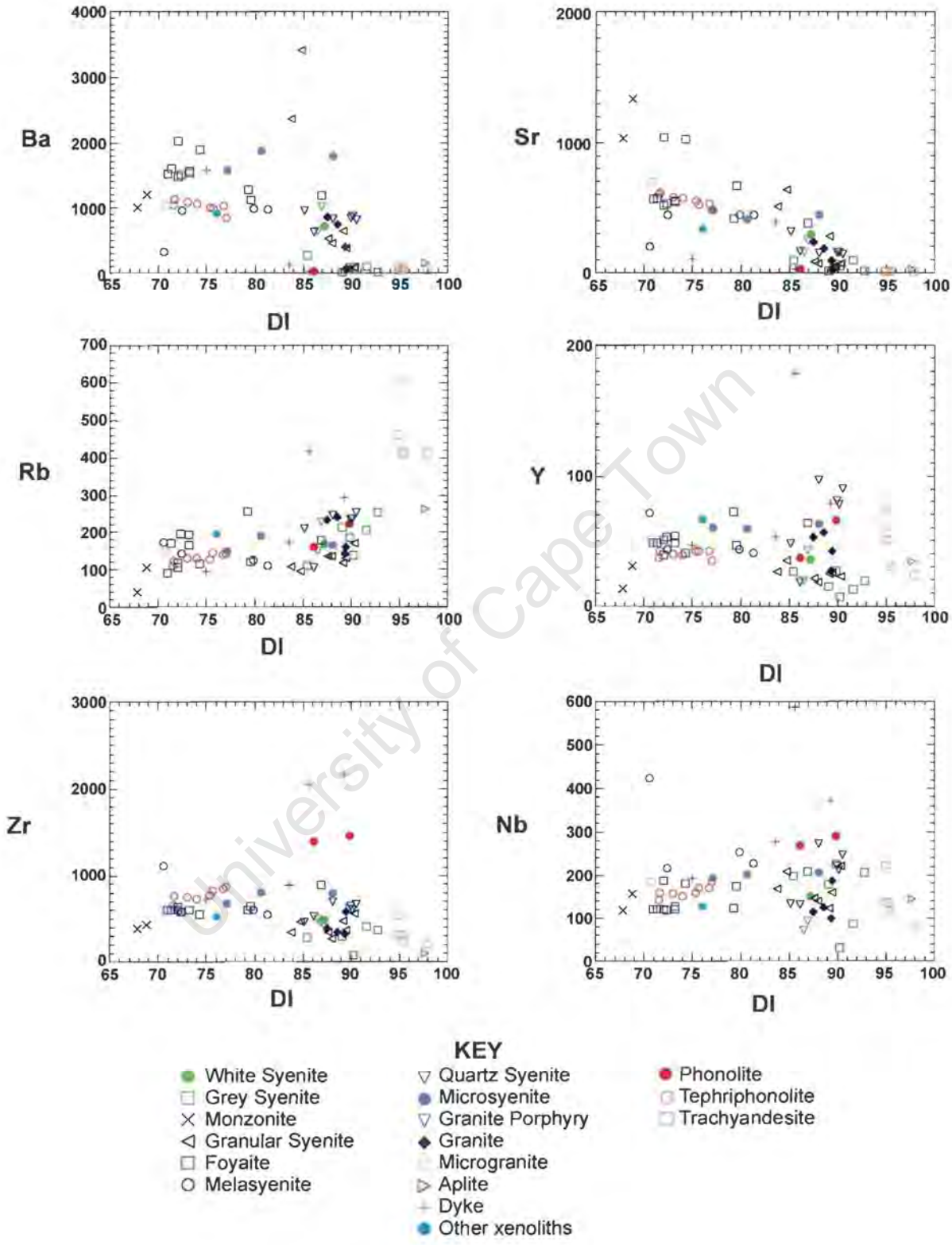

Figure 5.7 Variation diagrams of non ferro-magnesian related trace elements versus DI for the KIC.

5.3.1 Fractional Crystallisation Model

Three trace elements, Ni, Cr and Rb have been modelled for Rayleigh fractionation (Figure 5.8) where

$$C_L/C_O=F^{(D-1)}$$

C_L The average weight concentration of a trace element in a mixed melt
C_O The weight concentration in the parent liquid
F The weight fraction of melt remaining
D The bulk distribution coefficient of the fractionating assemblage during crystal fractionation

The average composition of the gabbro xenoliths was nominated as representing a probable parental composition while values for D can be found in Table 5.4. Three phases were considered in the fractionation calculation: olivine, clinopyroxene and plagioclase. Two models were tested as follows:

- fractionation of olivine to F=0.7, followed by fractionation of 50% olivine and 50% clinopyroxene to F=0.3 and then 50% clinopyroxene and 50% plagioclase.
- fractionation of olivine to F=0.4, followed by fractionation of 50% olivine and 50% clinopyroxene to F=0.1 and then 50% clinopyroxene and 50% plagioclase.

Although the plutonic units from the complex plot along the fractionation trend (albeit at the extreme end), those from the pipes do not. The pipes seem to contain too much Ni and Cr for their Rb contents to be products of fractional crystallisation, so a non fractional crystallisation origin needs to be sought).

Table 5.4. Mineral/melt partition coefficients used for calculation of a fractional crystallisation model. *Data from Gill (1981). All other partition coefficients from a data compilation of Arth (1976); compilation of Pearce and Norry (1979); Green et al. (1989); Schock (1979); Fujimaki et al. (1984); Dostal et al (1983); compilation of Henderson (1982); Leeman and Lindstrom (1978); Lindstrom and Weill (1978) and Green and Pearson (1987) in Rollinson (1993).

	Cr	*Ni*	*Rb*
Olivine	0.7	6	0.0098
Clinopyroxene	34	7	0.031
Plagioclase	0.01*	0.01*	0.071

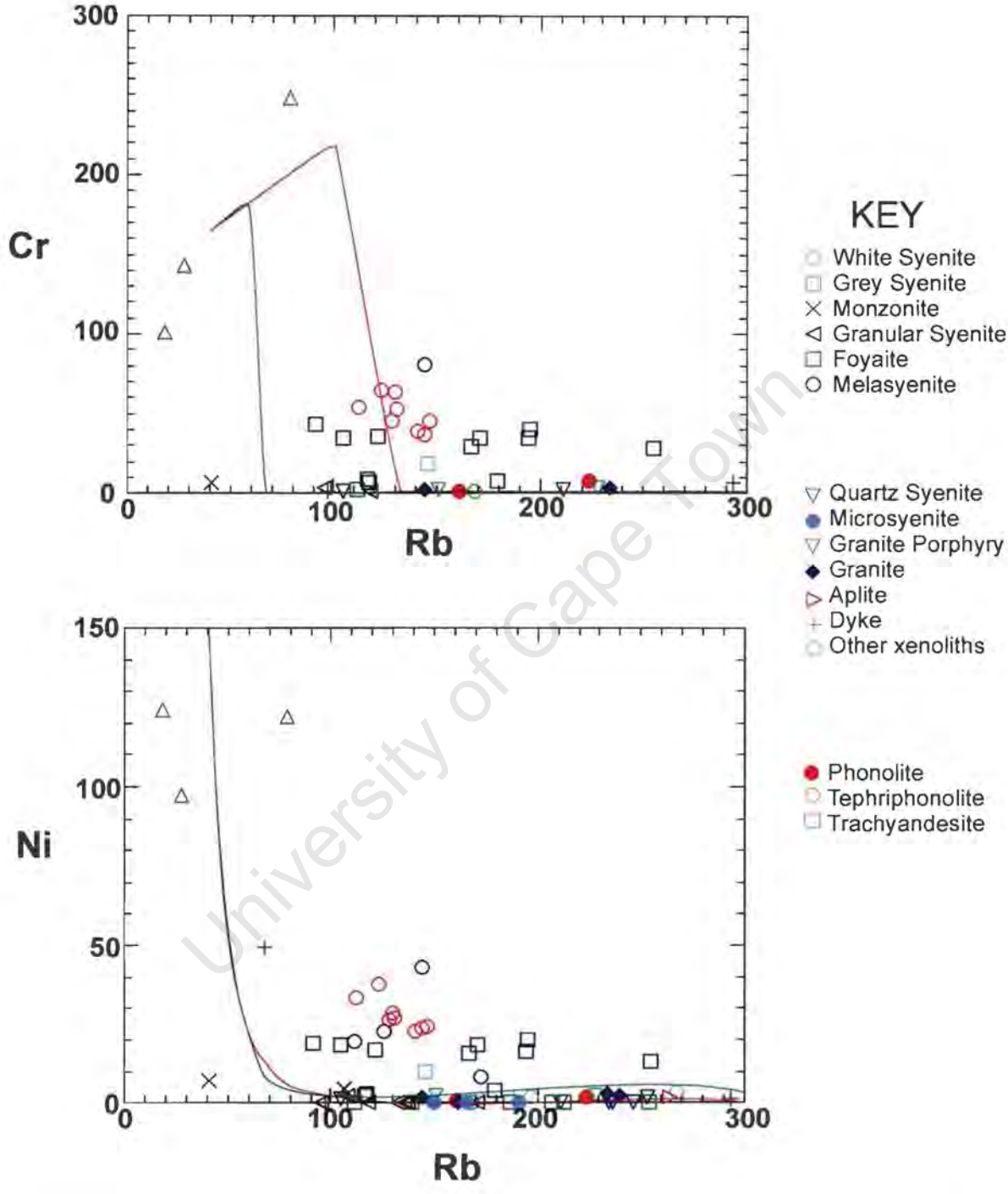

Figure 5.8 Rayleigh fractionation modelling for Ni, Cr and Rb. Green line represents fractionation of olivine to F=0.7, followed by 50% olivine and 50% clinopyroxene to F=0.3 then fractionation of 50% clinopyroxene and 50% plagioclase. The red line represents fractionation of olivine to F=0.4, 50% olivine and 50% clinopyroxene to F=0.1 followed by 50% clinopyroxene and 50% plagioclase.

5.3.2 Inter-element Coherency

Concentrations of Ba, Sr and Rb, three large ion lithophile elements (LIL), in the KIC are compared in Figure 5.9. While Rb is high in the highly fractionated samples (eg microgranites), Sr is high in the least evolved samples (eg gabbro xenoliths). Intermediate samples (those that are neither primitive nor highly differentiated) have high Ba. The trachyandesites have a wide scatter in the concentrations of Ba and Rb, while in all three elements, the tephriphonolites have similar concentrations. Although the phonolites have very low concentrations of Sr and Ba their Rb concentrations are similar to those of the tephriphonolites and trachyandesites. The monzonite samples have very high Sr while the granular syenite samples have very high Ba when compared to the other units of Kanabeam. The gabbro xenoliths have low Rb and Ba concentrations while they have high Sr concentrations.

Concentrations of Zr are extremely high in the phonolites, intermediate in the tephriphonolites and trachyandesites and low in the gabbros (Figure 5.10). If a trend line is projected on the Zr versus Nb plot between the gabbro and the phonolites, most of the tephriphonolites and some of the trachyandesites are observed to plot along or close to this line. The tephriphonolites also have compositions that would fall along a line projected between the gabbros and phonolites on the Zr versus Y graph. On this graph the trachyandesites are scattered.

5.3.3 Discrimination Diagrams

Discrimination diagrams after Pearce *et al.*, (1984) (Figure 5.11) have been employed to show the nature of the "granitic" units of the complex. Even though these discrimination diagrams are for granites, other felsic components of the complex were also included. The discrimination diagrams show that all the felsic components of the complex fall in the within-plate (A-type) granite field. The discrimination diagrams of Harris *et al.* (1986) (Figure 5.12) confirm that they are within plate granites, and are not from volcanic arc or collision related settings.

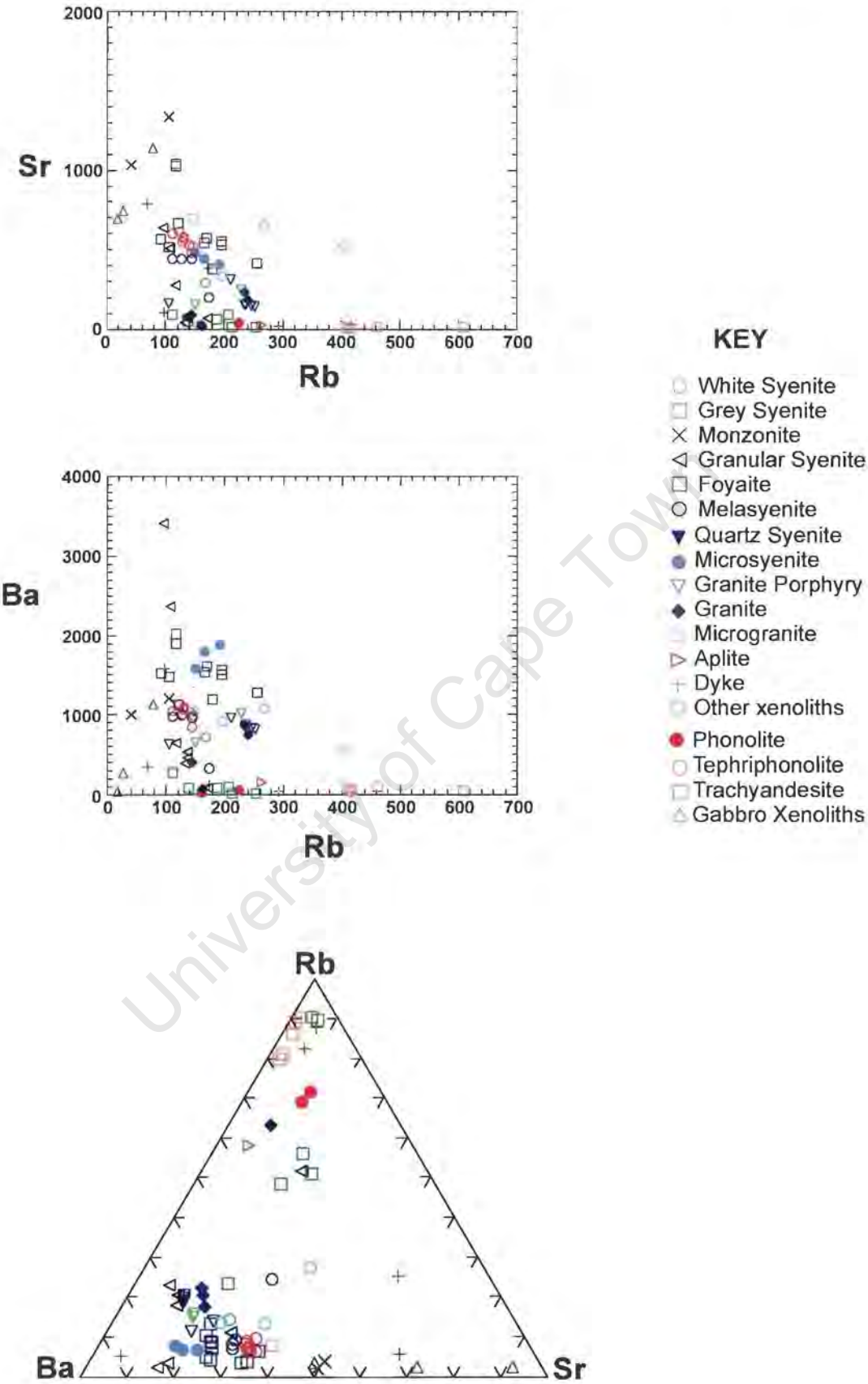

Figure 5.9 Sr versus Rb, Ba versus Rb and Rb-Ba-Sr graphs to illustrate low field strength element coherency.

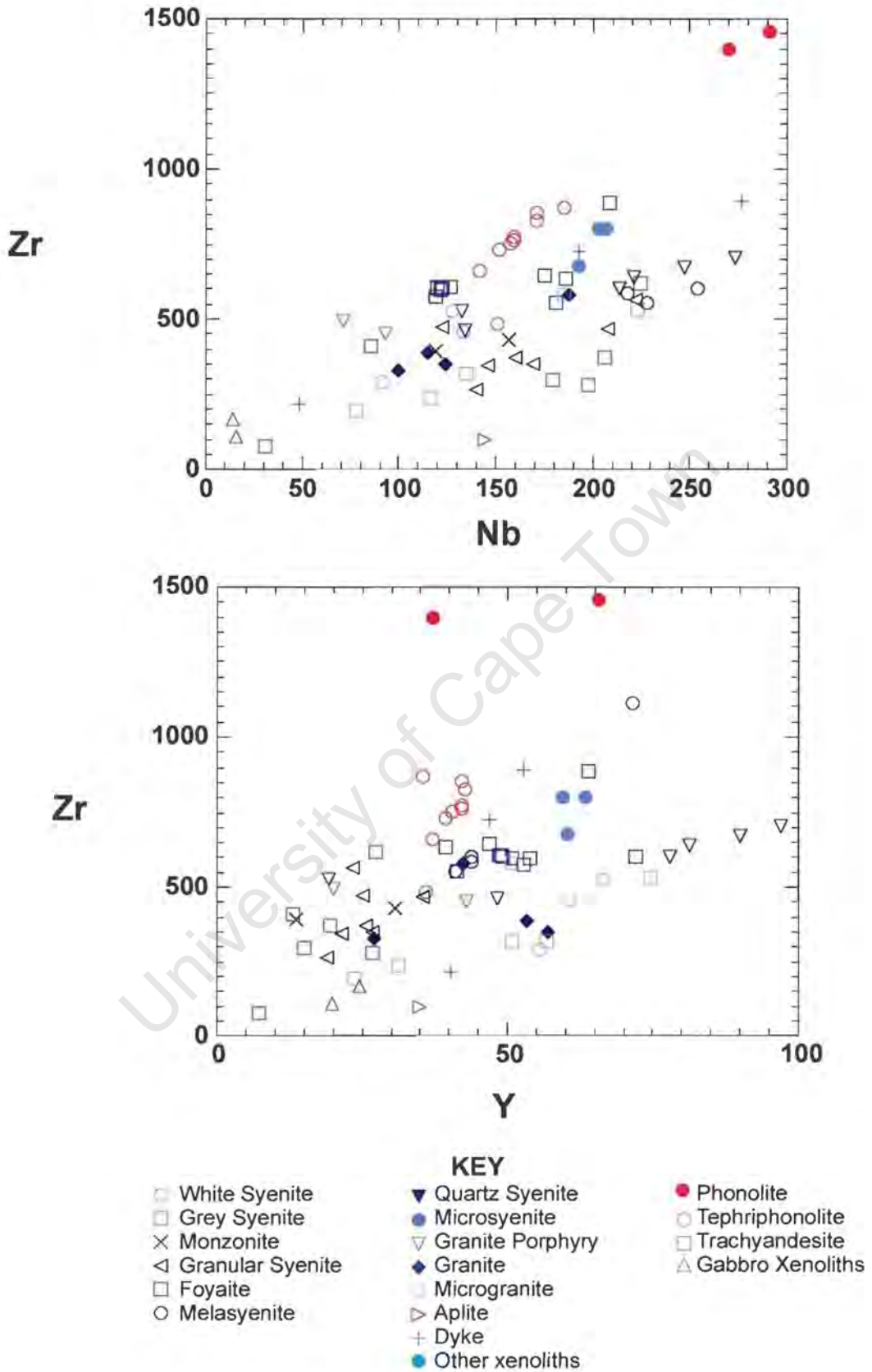

Figure 5.10 Zr versus Nb and Zr versus Y graphs to illustrate high field strength element coherency.

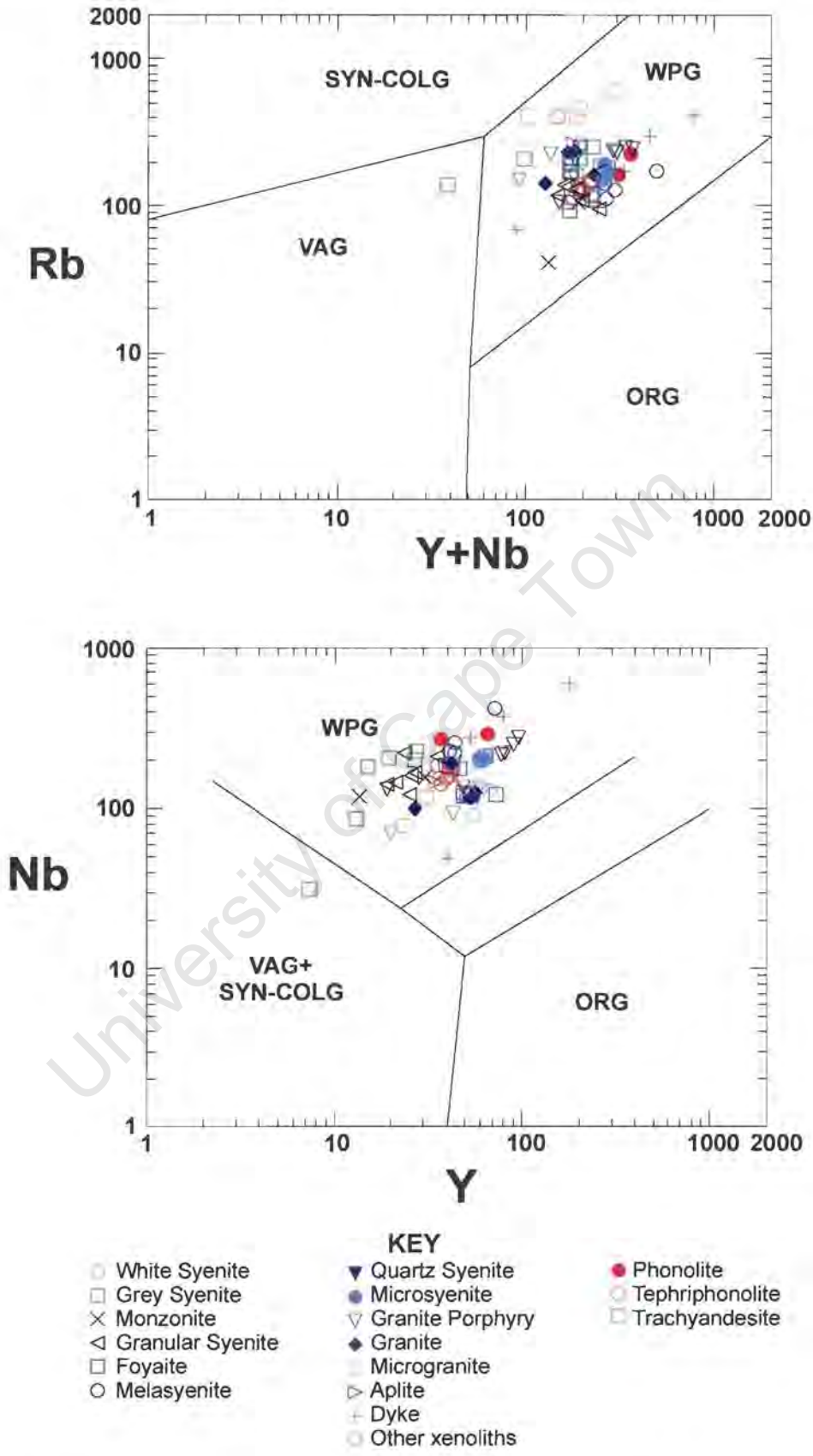

Figure 5.11 Rb versus Y+Nb and Nb versus Y discrimination diagrams using fields of Pearce *et al.* (1984). The fields include volcanic-arc granites, syn-collisional granites (SYN-COLG), within-plate granites (WPG)

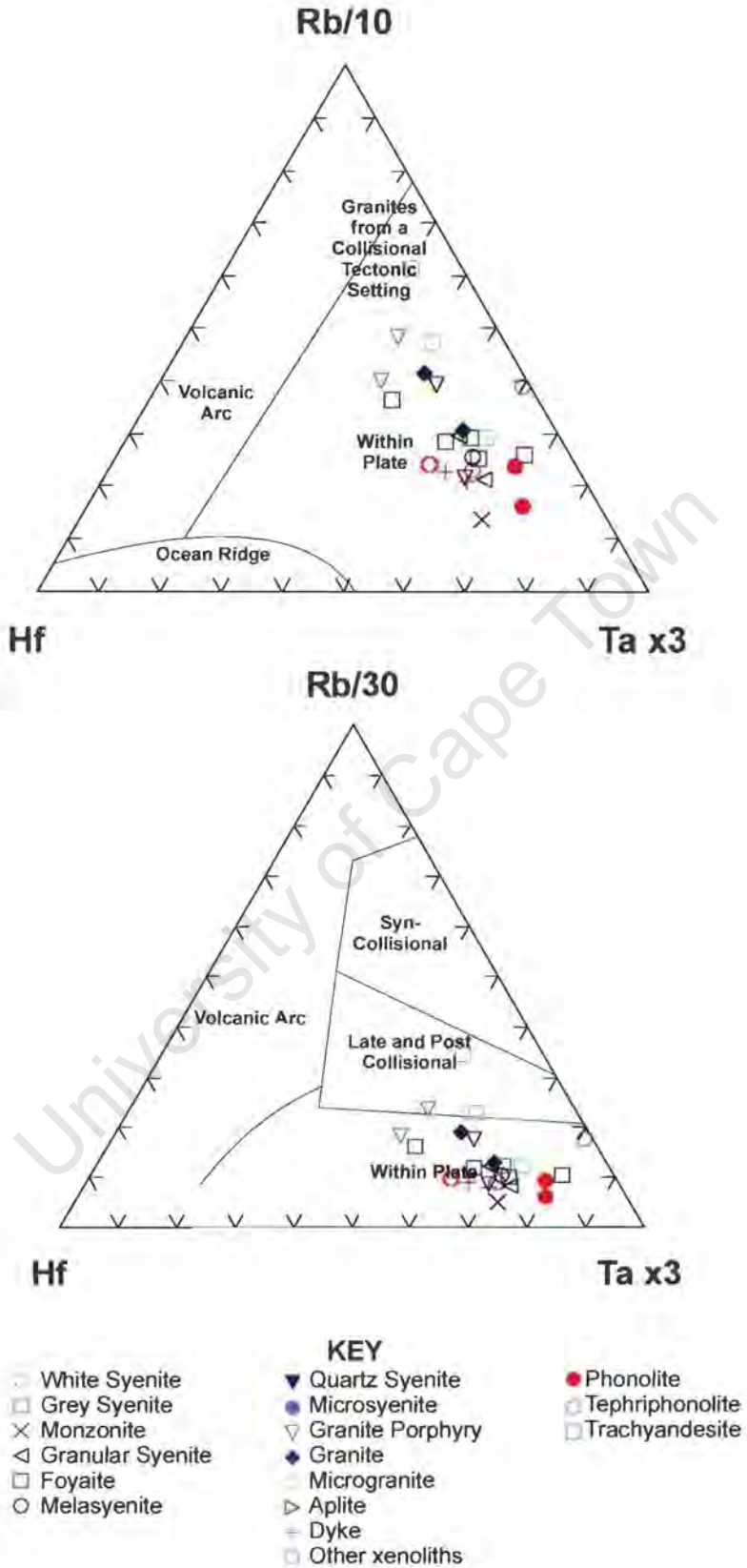

Figure 5.12 The Hf-Rb/10-Tax3 and the Hf-Rb/30-Tax3 discrimination diagrams for granites. Fields after Harris *et al.* (1986).

5.4 Rare Earth Element Data

Chondrite-normalised REE patterns (using the normalising values of Taylor and McLennan, 1985) for both the plutonic and the pipe samples have been plotted in Figure 5.13 to facilitate comparison. All the samples, except for some of the more mafic rock types (gabbro xenoliths), are characterised by strong LREE (light rare earth element) enrichment. Variation in the development of Eu anomalies and HREE (heavy rare earth element) fractionation exists between each of the plutonic rock types and are described below.

5.4.1 General description of trends within the plutonic series

- The ***gabbro xenoliths*** have a wide variation in the degree of fractionation indicated by the variation in LREE enrichment. As enrichment in the LREE increases there is a decrease in the slight positive Eu anomaly.
- ***White syenite*** *and* ***grey syenite*** samples have no Eu anomaly, LREE enrichment and consistent HREE fractionation that yields a flat lying trend.
- The ***monzonite,*** has strong LREE enrichment and a fairly flat HREE signature. The sample has a slightly positive Eu anomaly.
- Positive Eu anomalies exist in both of the ***granular alkali syenite*** samples analysed. The LREE show strong enrichment while the HREE has slight enrichment in Tm, Yb and Lu.
- The ***foyaite*** sample displays a slightly negative Eu anomaly and enrichment in the LREE compared to the HREE.
- As with the foyaite, the ***porphyritic melasyenite*** has a slight negative Eu anomaly but only LREE fractionation is marked while the HREE has a flat lying trend.
- The ***quartz syenite*** trend is virtually identical to the ones for the grey and white syenite samples differing only in that the quartz syenite has a slightly negative Eu anomaly.
- The ***granites*** have a slight negative Eu anomaly while the LREE fractionation and flattening out of the pattern for the MREE is the same as the other rock types. There is a slight increase in the HREE (Tm, Yb and Lu).
- ***Microgranite*** has lower LREE fractionation than the other samples, a strongly negative Eu anomaly and a marked increase in the HREE compared to the MREE and as such is distinct from the other rock types described.

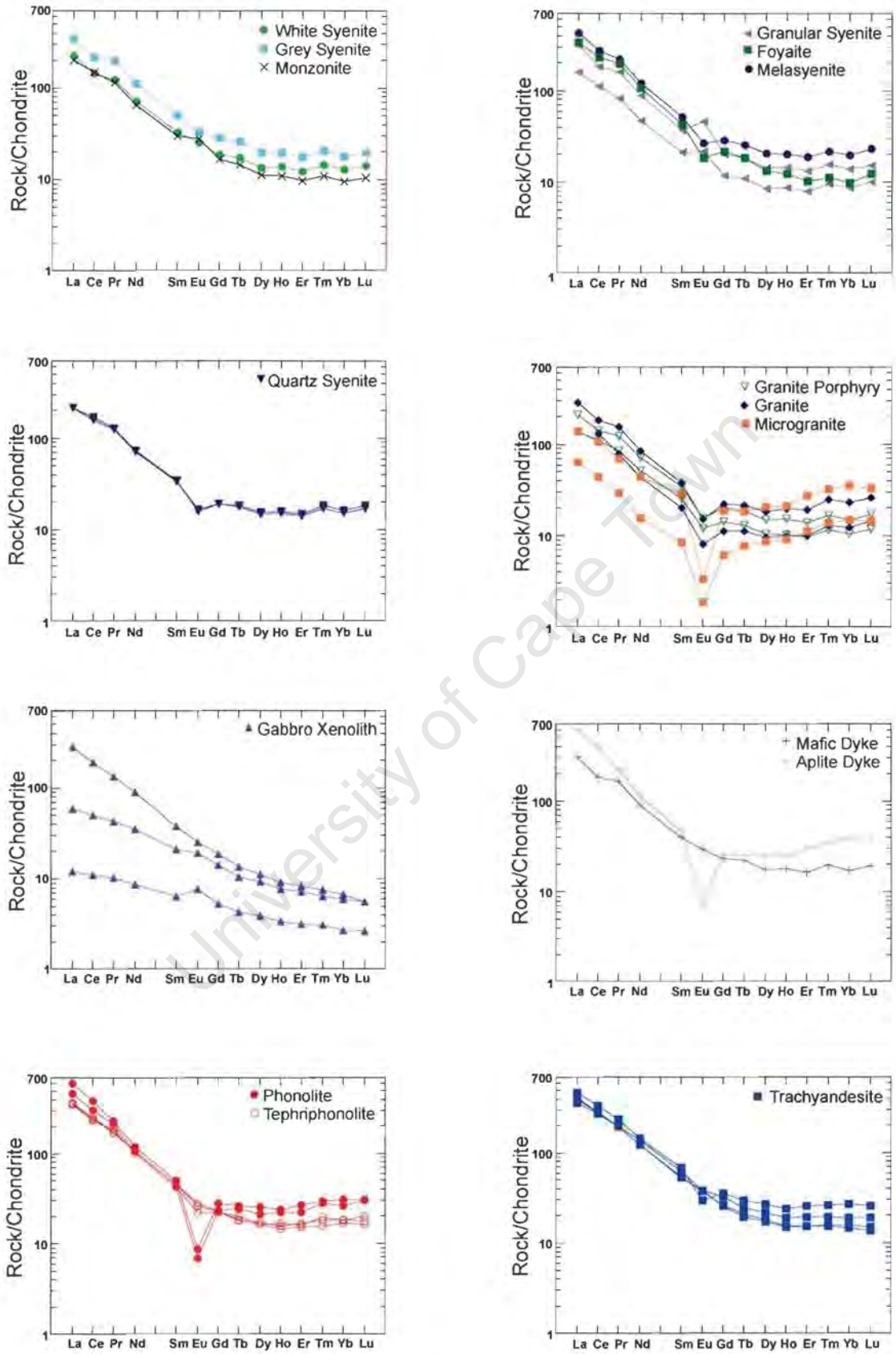

Figure 5.13 Rare earth element abundances for the KIC, normalised to chonditic values after Taylor and McLennan (1985).

5.4.2 The Porphyry Pipes

Inspection of Figure 5.13 reveals that the patterns for the tephriphonolitic and the trachyandesite pipes are very similar. There is strong enrichment in LREE and limited fractionation of HREE. While the majority shows little or no Eu anomalies, two of the tephriphonolitic samples, the phonolite samples, have pronounced negative anomalies. In more detail the tephriphonolite group has slightly lower MREE concentrations than the trachyandesitic group (Figure 5.13).

5.4.3 REE Fractionation and Eu Anomalies

Flat HREE patterns in alkaline magmas may not be the product of source characteristics but may rather be the product of complexing with volatile components such as Cl. Subtle variation in LREE or HREE enrichment, total REE and Eu anomalies can be better illustrated using ratio plots, such as those presented in Figures 5.14 through to 5.17. The magnitudes of the parameters that are presented in these figures are given in Table 5.5.

Table 5.5 Magnitude of profile parameters illustrated in Figures 5.10 through to 5.13.

Sample	Rock Type	Abb	$[La/Yb]_N$	$[La/Sm]_N$	$[Gd/Yb]_N$	Eu/Eu*
ND46 P1	tephriphonolite	PP	19.71	12.06	0.91	0.23
ND10 P4	tephriphonolite	PP	20.12	8.06	1.23	0.81
ND12 P4	tephriphonolite	PP	21.52	7.80	1.37	0.88
RS 15	phonolite	PP	19.70	8.36	1.22	0.73
GE 17	phonolite	PP	17.89	10.95	0.91	0.22
ND22 P8	trachyandesite	PP	27.77	7.49	1.81	0.99
ND23 P9	trachyandesite	PP	25.42	7.53	1.65	1.05
ND26 P11	trachyandesite	PP	19.25	5.90	1.70	0.86
ND35 P15	trachyandesite	PP	17.74	6.80	1.35	0.60
GE 14	white syenite	NS1	17.48	6.80	1.45	1.03
RS 14	grey syenite	NS2	19.38	6.84	1.61	0.86
GE 4	monzonite	NS3	20.90	6.61	1.76	1.24
RS 9	granular syenite	NS4	18.32	7.58	1.36	1.36
VH 3	granular syenite	NS4	22.56	8.42	1.47	1.65
VH 9	foyaite	NS5	34.44	8.01	2.17	0.60
VH 2	melasyenite	NS6	21.56	8.14	1.45	0.70
RS 1	quartz syenite	QS	14.07	6.36	1.26	0.66
GE 1	quartz syenite	QS	13.04	6.13	1.19	0.62
VH 11	granite porphyry	GP	14.12	6.17	1.33	0.60
GE 12	granite porphyry	GP	13.22	5.40	1.38	0.63
GE 11	granite	G	11.26	6.84	0.92	0.54
RS 10	granite	G	12.50	7.62	0.96	0.52
VH 13	microgranite	MG	3.90	4.74	0.53	0.14
VH 12	microgranite	MG	4.36	7.55	0.42	0.25
ND9 D1	dyke within phonolite	dyke	15.88	13.21	0.65	0.20
RS 3	dyke in quartz syenite	dyke	17.82	7.72	1.35	0.97
DRK 72	gabbro xenolith	xen	4.56	1.89	1.99	1.35
ND16A P4	gabbro xenolith	xen	43.02	7.57	2.84	0.94
ND20 P6	gabbro xenolith	xen	10.06	2.83	2.38	1.11

5.4.3.1 REE Fractionation

Overall fractionation of LREE to HREE is presented in Figure 5.14, $(La/Yb)_N$ versus La_N. The degree of REE fractionation in the pipe samples is the same as that for the silica-undersaturated units within the complex, while REE fractionation in the silica-oversaturated units is lower. There is a decrease in amount of La_N in the samples from the pipes to the silica-oversaturated rocks with the silica-undersaturated rocks, having medium La_N values.

LREE fractionation, illustrated in Figure 5.15, is virtually constant for all the individual units within the complex although the tephriphonolitic pipes do display some scatter in values. The Sm_N values like those for La_N decrease from the pipes to the silica-

undersaturated units through to the silica-oversaturated units. There is some overlap between the NSS samples and those of the pipes.

The HREE fractionation diagrams, Figure 5.16, reveal wider variations between the units of the KIC. While the gabbro xenoliths have much higher $(Gd/Yb)_N$ values than the other units the tephriphonolitic and trachyandesitic samples have two distinct trends where the degree of fractionation is inversely proportional to Yb_N. An overall trend has been identified where the amount of REE fractionation decreases with increasing silica saturation.

5.4.3.2 Eu Anomalies

The varying Eu anomalies described in (Chapter 5.4.1) have been assessed in more detail. This entailed compilation of a series of plots, Figure 5.17, that show Eu/Eu* and its variation with LREE fractionation. Values of Eu/Eu* >1 indicate feldspar accumulation while those <1, feldspar fractionation. The more felsic rock types within the complex, the silica-oversaturated units have the lowest Eu/Eu* values (<1) while the other rock types show wide variation. Notably the granular syenite, followed by monzonite have positive Eu/Eu* values perhaps indicative of feldspar accumulation in these rocks, while the other silica-undersaturated units have negative Eu/Eu* values with the foyaite having the lowest values. The white and grey syenites have values that are not indicative of any Eu anomaly.

The tephriphonolite samples define a trend from Eu/Eu* = 1 to values <1 while the trachyandesite samples have values that lie to both sides of the critical value (1). There are two trachyandesite samples, however, that have values defining a negative Eu anomaly. The phonolite samples show extreme feldspar fractionation.

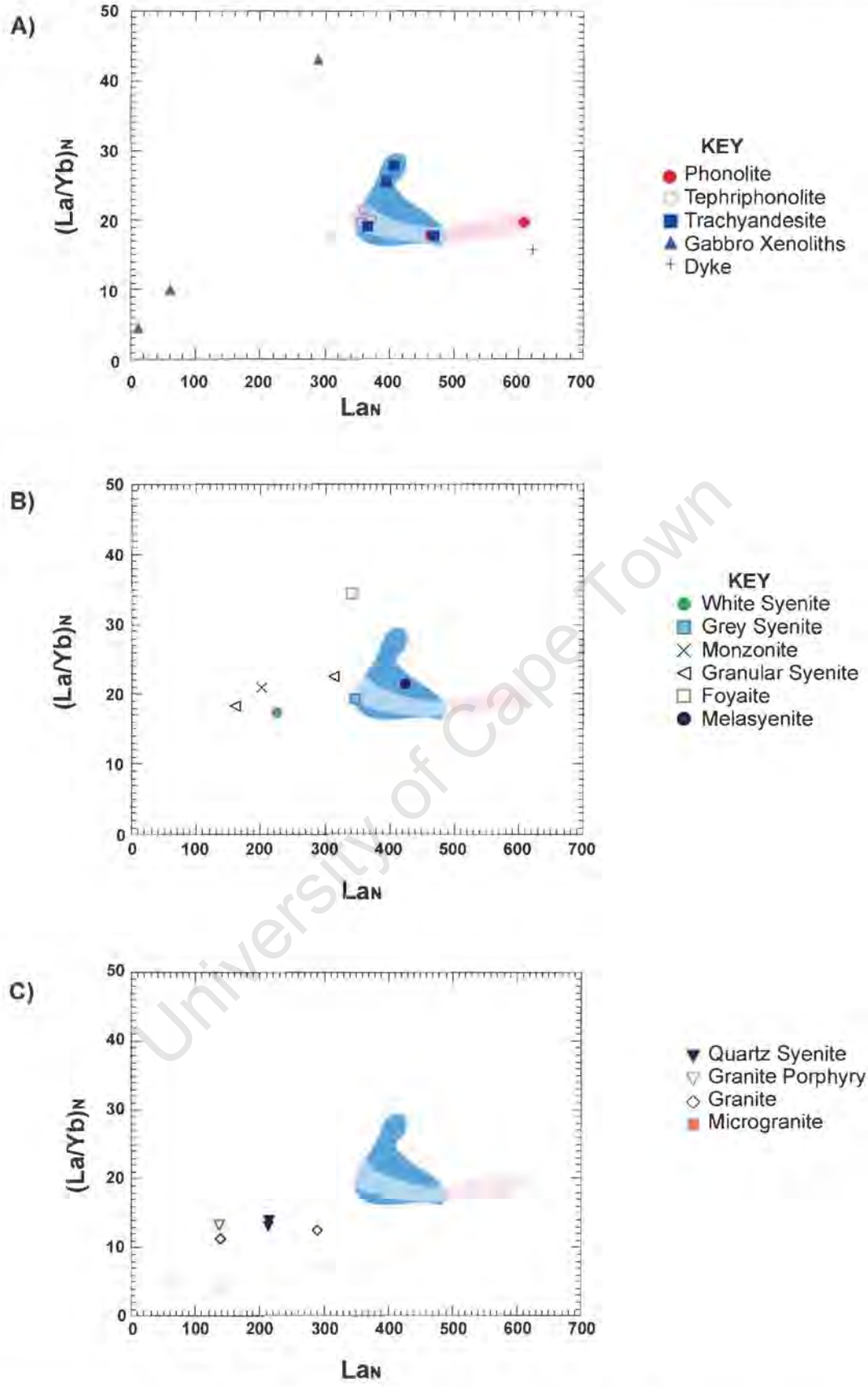

Figure 5.14 $(La/Yb)_N$ versus La_N graphs to illustrate overall REE fractionation. The position of the pipe samples are shaded in pink (tephriphonolites) and turquoise (trachyandesites) A) The pipe samples from Kanabeam. B) The silica-undersaturated units of Kanabeam. C) The silica-oversaturated units of Kanabeam.

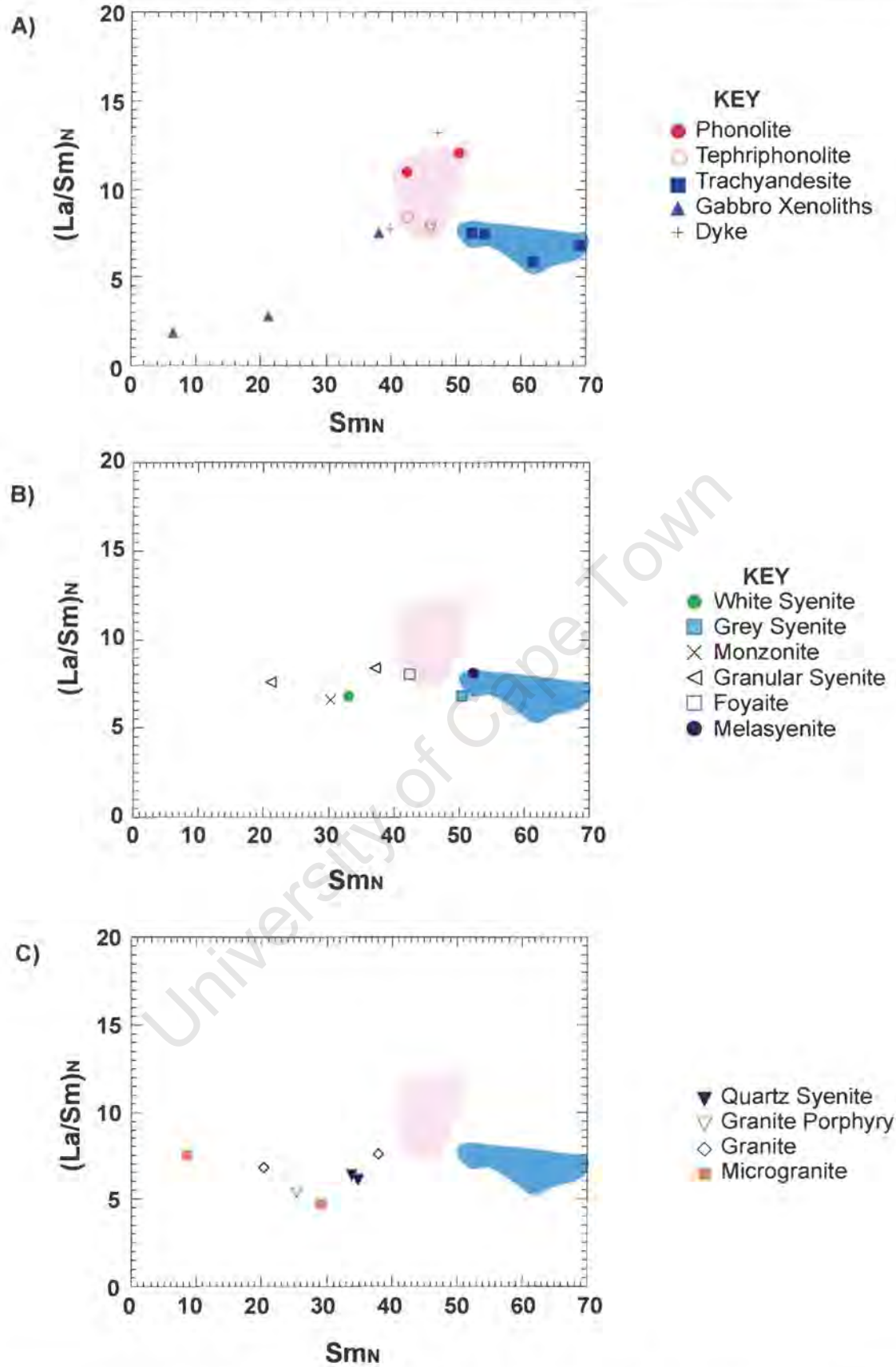

Figure 5.15 $(La/Sm)_N$ versus Sm_N graphs to illustrate light REE fractionation. The position of the pipe samples are shaded in pink (tephriphonolites) and turquoise (trachyandesites) A) The pipe samples from Kanabeam. B) The silica-undersaturated units of Kanabeam. C) The silica-oversaturated units of Kanabeam.

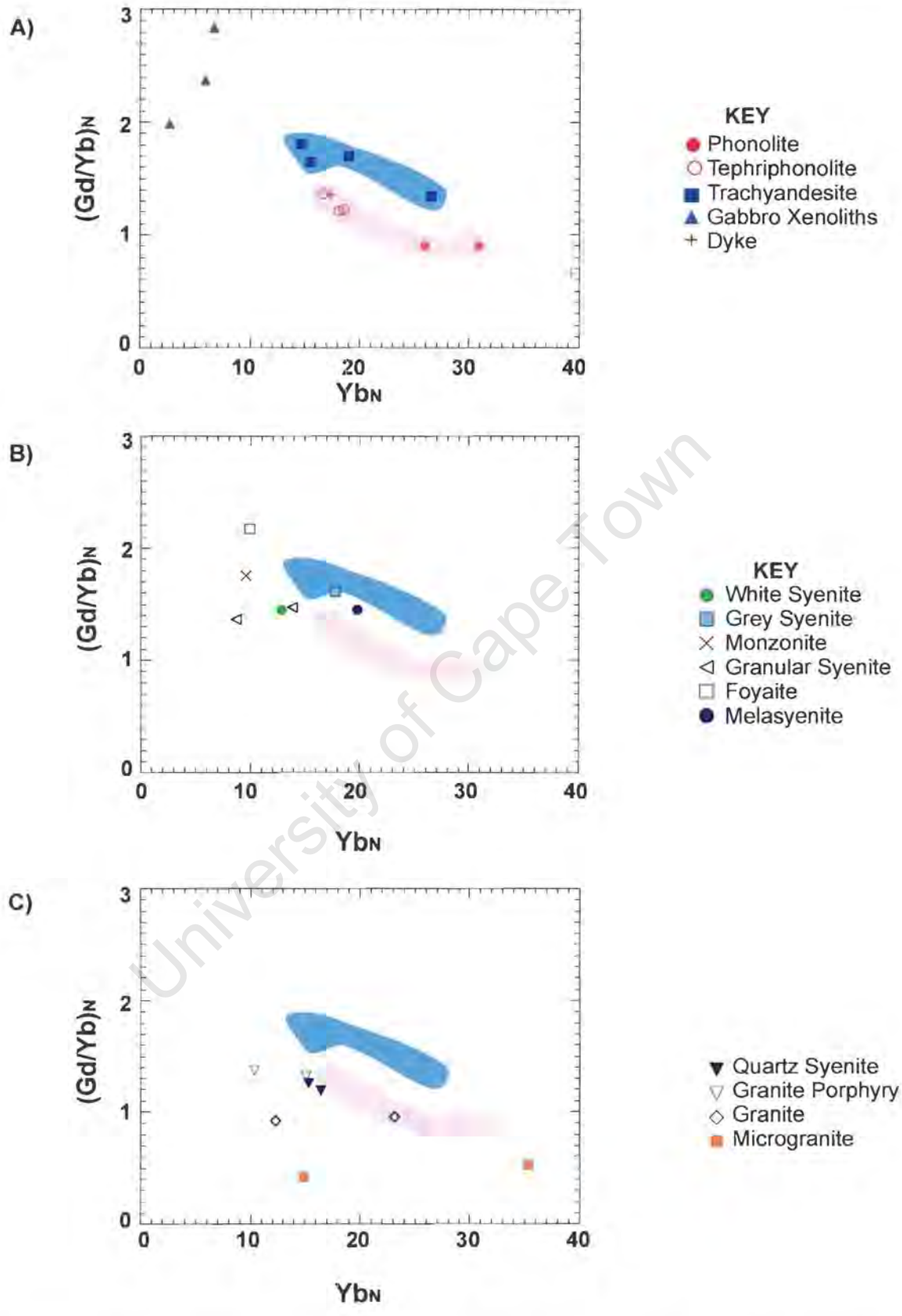

Figure 5.16 $(Gd/Yb)_N$ versus Yb_N graphs to illustrate HREE fractionation. The position of the pipe samples are shaded in pink (tephriphonolites) and turquoise (trachyandesites) A) The pipe samples from Kanabeam. B) The silica-undersaturated units of Kanabeam. C) The silica-oversaturated units of Kanabeam.

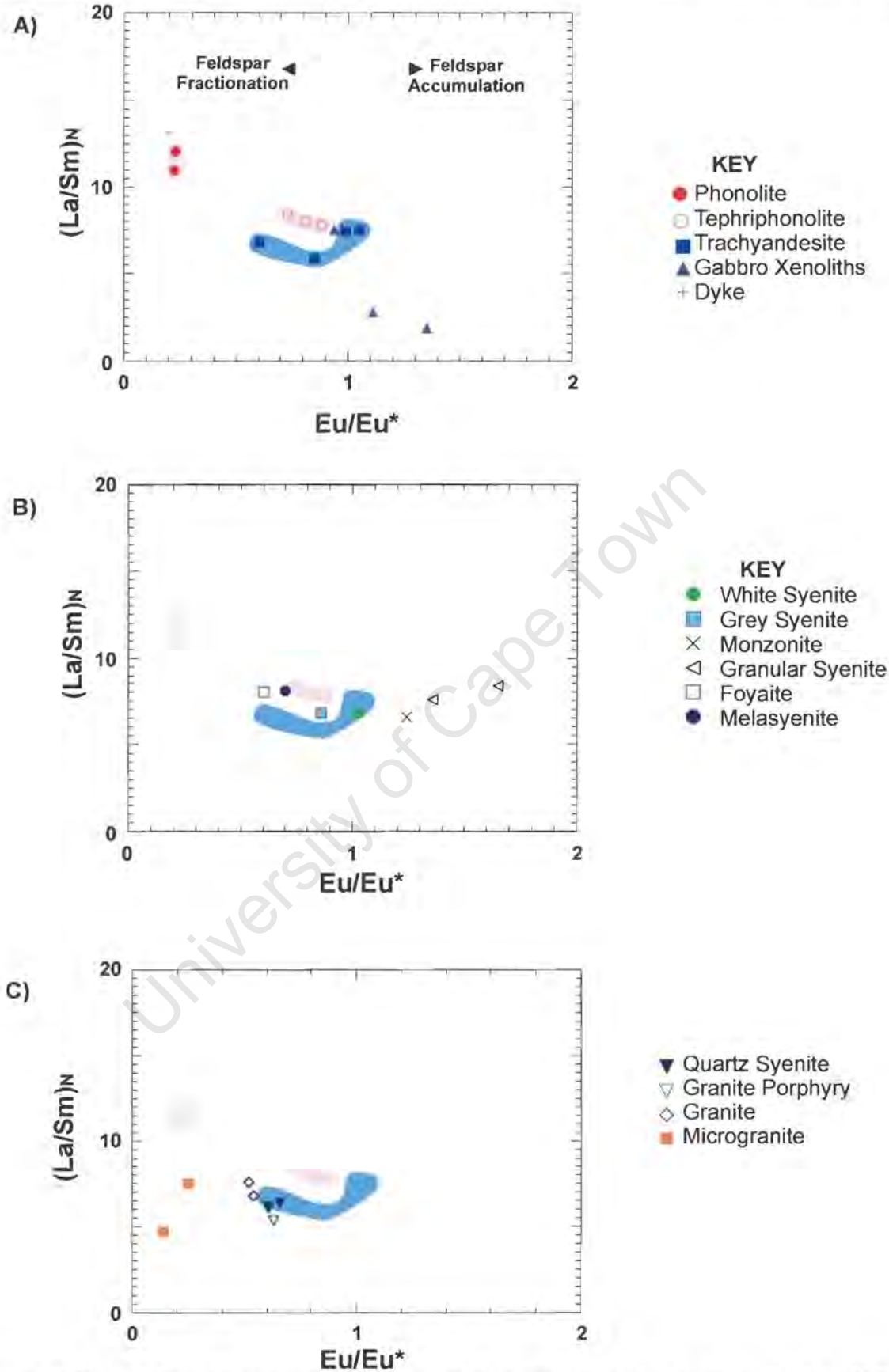

Figure 5.17 Graph of (La/Sm)N versus Eu/Eu* to show how the Eu anomalies vary with light REE fractionation. The position of the pipe samples are shaded in pink (tephriphonolites) and turquoise (trachyandesites) A) the pipe samples, B) the silica-undersaturated units and C) the silica-oversaturated units.

6 RADIOGENIC ISOTOPES

6.1 Introduction

Whole rock Strontium and Neodymium isotope analysis was carried out on 25 selected samples from the Kanabeam Complex to aid in:

- establishing the age of emplacement
- evaluating petrogenetic links between the diverse lithologies
- identifying relative roles of mantle and crustal source regions

Measured Nd and Sr ratios determined by TIMS, together with Rb and Sr elemental concentrations determined by XRF and Sm and Nd determined by ICP-MS, are presented in Table 6.2. Details of the analytical techniques and standard values are given in Appendix 4.

The analysed sample suite included matrix material from the tephriphonolite and trachyandesite pipes, gabbroic xenoliths extracted from some of the pipes, as well as a selection of plutonic rock types. As such they represent the major rock types within the Kanabeam Complex.

6.2 Geochronology

6.2.1 Previous Work

Results of unpublished hornblende and biotite $^{40}Ar/^{39}Ar$ data from several complexes within the KBIP were made available (Table 6.1). These have been compared with previously published age data.

Table 6.1 Results of $^{40}Ar/^{39}Ar$ work from the KBIP (Reid, pers comm). The intrusions are listed from the most southern complexes to the most northerly ones.

Igneous Complex	*Hornblende*	*Biotite*	*Average Age*
Kuboos (zircon 507+6Ma)		507±3Ma	512Ma
Tatasberg	501±3Ma	502±1Ma	502Ma
Grootpenseiland South	503±1Ma		503Ma
Grootpenseiland North	490±2Ma	497±1Ma	494Ma
Marinkas Quellen	495±5Ma		495Ma
Kanabeam (NS3) (NS4) average	484±2Ma 492±2Ma	492±1Ma 486±1Ma	

6.2.1.1 Kuboos Complex

The youngest intrusive phase of the Kuboos Pluton has a single-grain zircon U-Pb age of 507±6Ma (Frimmel, 2000) while past zircon work by Allsopp *et al.* (1979) gave an estimate for the age of emplacement of the Kuboos Pluton as 525±60Ma. The error associated with the multi-grain analysis has been interpreted as being the result of "contamination" by xenocrystic zircons (Frimmel, 2000). The data from Allsopp *et al.* (1979) were highly discordant and therefore the multi-grain analysis can be disregarded for the purpose of providing a reliable age.

As hornblende is absent at Kuboos only $^{40}Ar/^{39}Ar$ biotite ages were obtained. The biotite ages are 516±3Ma and 507±3Ma with an average of 511±3Ma, which correlates within error to the U-Pb zircon age of 507±6Ma. Cooling from zircon U-Pb to the $^{40}Ar/^{39}Ar$ biotite blocking temperatures must have been rapid and therefore the latter technique is assumed to provide reliable estimates of the age of emplacement. The $^{40}Ar/^{39}Ar$ ages of each of the complexes is therefore assumed to be accurate.

6.2.1.2 Kanabeam Complex

Hornblende and biotite from NS4 (granular syenite) yield $^{40}Ar/^{39}Ar$ plateau ages of 492±2Ma and 486±1Ma respectively. These ages are similar and therefore the cooling of the granular syenite through the blocking temperatures was rapid, consistent with the upper crustal intrusive setting given to the complex. The monzonite ring (NS3) yielded a hornblende age of 484±2Ma and biotite age of 492±1Ma (Figure 6.3). These data appear inconsistent, as the hornblende should be older than the biotite based on the blocking temperatures. Since the two NS intrusions were probably synchronous the average data for the hornblende (488Ma) and biotite (489Ma) may be more appropriate. The average of these two ages, 489Ma, has been adopted for calculations of initial values.

6.2.1.3 Other KBIP Complexes

It is apparent from the data that a general age progression for the KBIP from southwest to northeast exists where the most southerly complexes are the oldest and the most northerly the youngest. There are two exceptions to this, the Marinkas Quellen and Grootpenseiland South Complexes.

6.3 Whole Rock Rb-Sr

6.3.1 Kanabeam Complex

The extensive range in rock types at Kanabeam has resulted in a wide spread in the $^{87}Rb/^{86}Sr$ ratio allowing for radiometric dating by the isochron method (Table 6.2). Figure 6.1 however, illustrates that all the data do not conform well to a defined isochron. Regression of the data points produces an errochron (MSWD=89.76) of 547±29Ma and an initial ratio of 0.70398±0.00034. The excess scatter produces a high uncertainty in the errochron age which does not overlap the average $^{40}Ar/^{39}Ar$ age of 489Ma of the KIC, or the 494-512Ma ages of the KBIP.

Table 6.2 Rb and Sr (ppm) measured by XRF, Sm and Nd (ppm) measured by ICP-Ms and $^{87}Sr/^{86}Sr$ and $^{143}Nd/^{144}Nd$ measured by TIMS.

Sample	Lithology	Rb	Sr	$^{87}Sr/^{86}Sr$	$^{87}Rb/^{86}Sr$	$R_o(489Ma)$	Sm	Nd	$^{143}Nd/^{144}Nd$
GE14	NS1	168	294	0.716231±12	1.654669	0.7047±14	8	51	0.512388
RS14	NS2	146	694	0.708750±11	0.608730	0.7045±5	12	80	0.512282
GE4	NS3	85	1395	0.705060±8	0.176246	0.7038±2	5	33	0.512316
RS9	NS4	118	279	0.713042±24	1.224310	0.7045±10	5	34	0.512326
VH9	NS5	111	94	0.727894±23	3.423253	0.7040±29	10	76	0.512347
VH2	NS6	146	458	0.710170±9	0.922527	0.7037±8	12	85	0.512347
RS1	QS	211	319	0.718387±11	1.915721	0.7050±16	8	51	0.512255
GE1	QS	212	300	0.719260±8	2.046879	0.7050±17	4	28	0.512293
GE11	G	234	237	0.726151±65	2.861788	0.7062±24	5	31	0.512208
RS10	G	225	173	0.731170±11	3.771544	0.7049±32	6	38	0.512182
VH11	GP	228	250	0.725370±10	2.643210	0.7070±23	8	51	0.512081
GE12	GP	232	269	0.723970±10	2.499270	0.7066±21	6	34	0.512035
VH12	MG	426	8	1.757370±38	169.886351	0.5736±2764	2	11	0.512234
VH13	MG	608	16	1.655429±22	120.137024	0.8183±1311	7	31	0.512313
ND20	GABBRO	27	747	0.704298±11	0.104541	0.7036±1	5	25	0.512476
DRK72	GABBRO	19	690	0.703490±8	0.079637	0.7029±1	2	6	0.512603
ND10	TP	128	553	0.710350±14	0.669860	0.7057±5	11	75	0.512174
ND12	TP	112	604	0.709310±9	0.536582	0.7056±5	11	76	0.512247
RS15	TP	156	499	0.711840±10	0.904871	0.7055±7	10	70	0.512265
ND22	TA	117	1027	0.707010±9	0.329589	0.7047±3	13	88	0.512268
ND23	TA	117	1041	0.706860±9	0.325152	0.7046±3	12	87	0.51226
ND26	TA	166	548	0.711310±9	0.876734	0.7052±8	14	98	0.512235
ND35	TA	180	378	0.714350±9	1.378637	0.7047±12	16	104	0.512315
GE17	P	227	33	0.838550±11	20.156852	0.6981±220	9	66	0.512357
RS3	MAFIC DYKE	97	109	0.721550±17	2.578220	0.7036±22	9	65	0.512492

For calculations of R_o a blanket error of 1% relative error was used for $^{87}Rb/^{88}Sr$ ratio and 0.006% relative for $^{87}Sr/^{86}Sr$ except for the MG, P and gabbro samples where higher relative errors were used for $^{87}Rb/^{86}Sr$ ratio as a result of their low Rb or Sr concentrations. A 5% relative error was used in all these samples with the exception of VH12 (Sr=8ppm) where a 10% error was used.

Present day ratios quoted at 2σ level and initial ratios at 1σ level.

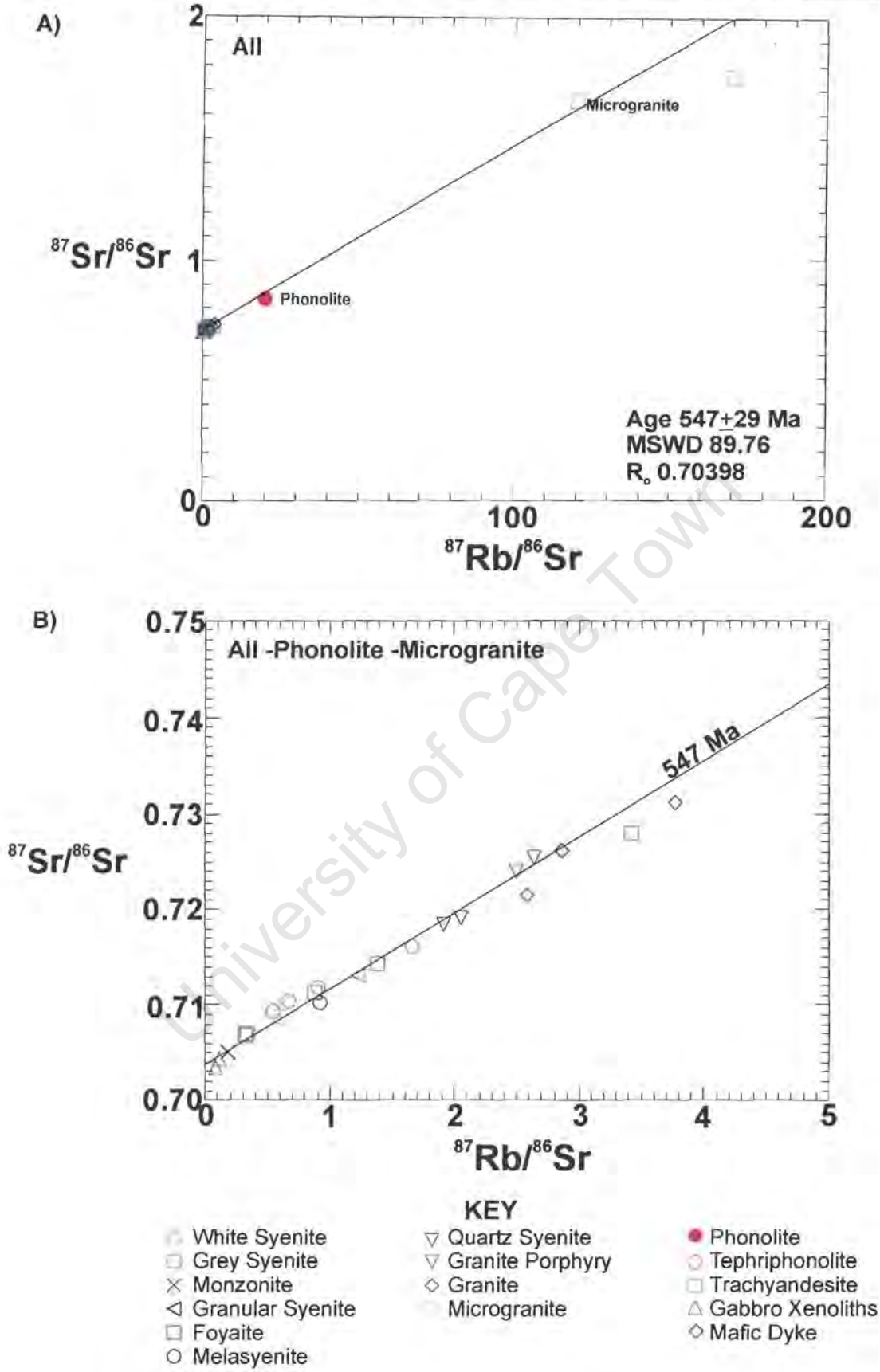

Figure 6.1 $^{87}Sr/^{86}Sr$ versus $^{87}Rb/^{86}Sr$ isochron diagram for rocks from the Kanabeam Complex. The data that is represented in this isochron is found in Table 6.2 and the age represented is shown in A). Diagram B) is a magnification to show detail of the data points.

The microgranite samples (VH12 and VH13) vary significantly from the errochron defined by the other samples (Figure 6.1A). One sample plots on the high $^{87}Rb/^{86}Sr$ side of the graph (VH12) while the other plots on the low side (VH13). Omission of the microgranites does not improve the regression statistics (Table 6.3).

In view of the wide range in composition, including both nepheline and quartz bearing rocks, the errorchron result may perhaps be the result of variable initial ratio, may be coupled with open system behaviour after emplacement. The errochron also may be the result of using low $^{87}Rb/^{86}Sr$ nepheline bearing rocks and higher $^{87}Rb/^{86}Sr$ quartz bearing rocks to calculate a single isochron however, it is admitted that the granitic rocks could be significantly younger, although this is regarded as unlikely.

Subsets from the entire sample collection have been identified, for example the NSS, and ages have been calculated for these groups (Table 6.3). All the subsets represent errorchrons with ages varying between 476±29Ma and 548±68Ma where the high error may be the result of small sample populations, open system behaviour or variable initial ratios. The possibility that the errors are attributed to variable initial ^{87}Sr ratios in the magmas is explored using R_o(489Ma) values.

Table 6.3 Age calculations for subsets of the Kanabeam sample collection analysed for $^{87}Rb/^{86}Sr$.

Group	*Age*	*MSWD*	*Ro*
All	547+29	89.76	0.70398
All-microgranite	547+31	98.10	0.70398
All-microgranite-phonolite	548+31	102.59	0.70397
Nepheline syenite subcomplex	512+25	27.31	0.70389
Nepheline syenite sub-complex+trachyandesite+tephriphonolite	527+48	98.51	0.70438
Nepheline syenite sub-complex +trachyandesite+tephriphonolite+phonolite	526+47	90.73	0.70439
Tephriphonolite	483+36	2.59	0.70565
Tephriphonolite+phonolite	476+29	1.53	0.70572
Trachyandesite	517+29	14.54	0.70454
Silica oversaturated	545+84	54.46	0.70373
Quartz syenite+granite+granite porphyry	548+68	22.99	0.70366

6.3.2 Marinkas Quellen and Grootpenseiland Complexes

The KIC errorchron is consistent with the 529±24Ma (R_o=0.704754±0.00015 and MSWD=2.31) errorchron age for the oldest phase of the Grootpenseiland Complex and the 514±26Ma (R_o=0.704778±0.00043 and MSWD=18.22) errorchron age of the youngest phase of the Marinkas Quellen Complex (Smithies, 1992). These two ages are also within error of the $^{40}Ar/^{39}Ar$ ages (490±2Ma and 495±5Ma respectively).

6.4 Initial Sr Isotope Ratios (R_o at 489Ma)

The average $^{40}Ar/^{39}Ar$ age of 489Ma has been used as the basis for initial ratio calculations, as it is considered the most reliable age of the KIC. Comparison of R_o(489) data (Table 6.2) between the different rock types has been used to determine the variation of initial ratios and the relationship of any variation with a number of parameters ($^{87}Rb/^{86}Sr$, DI, SiO_2 and 1000/Sr) (Figure 6.2).

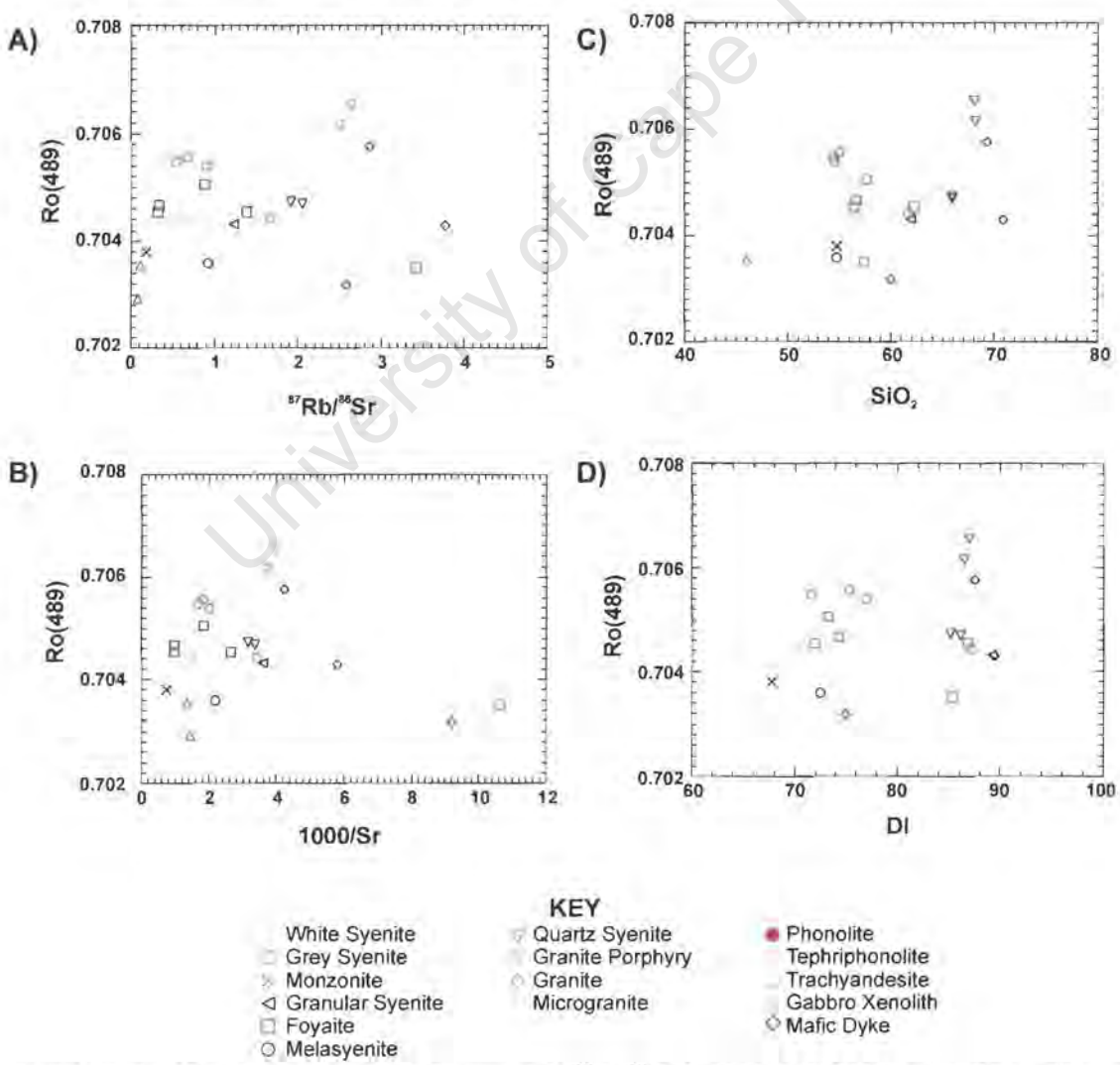

Figure 6.2 Plot of initial strontium R_o(490)) versus A) $^{87}Rb/^{86}Sr$ B) 1000/Sr C) SiO_2 and D) DI for all the data from the KIC with the exception of the microgranites and the phonolite.

Three samples, GE17 (phonolite), VH17 and VH13 (microgranite) have not been included in Figure 6.2 as they have R_o values that differ significantly from the other samples. Despite this, the high errors associated with these samples, resulting from low Sr concentrations, do fall within range of the other samples (the error bars would cross cut each graph) and therefore variation within these samples is attributed to analytical error. Note however that radiogenic Sr migration is quite plausible in GE17 and VH12 samples since these rocks have no Sr "sinks" resulting in values that are below any rational value while the high value of VH13 could be the result of open system behaviour (eg influx of radiogenic Sr from an extraneous source). In view of the extreme contrast in R_o calculated for the two microgranite samples, the results are not considered worthy of further interpretation and must await additional analysis of more samples of this rock type.

A closer look at the range in R_o calculated for all the other samples reveals some interesting patterns. The silica-undersaturated samples have lower R_o values than those of the silica-oversaturated samples. The tephiphonolites however, do not conform to this generalisation as they have high R_o values. The trachyandesites, being critically silica-saturated, plot between the silica-saturated and silica-undersaturated samples. The lowest R_o values belong to the more mafic rocks, namely the mafic dyke and the gabbro xenoliths, while the silica-oversaturated rock types all have R_o greater than 0.704, and the NSS samples cluster around R_O=0.704. Even though there is a wide range in SiO_2, 1000/Sr and DI within the NSS the differences in R_o are relatively small.

6.5 Sm-Nd Isotopes

6.5.1 Epsilon Sr-Nd Patterns

All the data for εSr-εNd have been calculated using the $^{40}Ar/^{39}Ar$ (489Ma) age of the Kanabeam complex (Table 6.4). From these data petrogentic links between the lithologies in the complex are assessed along with the potential role of basement assimilation or melting to form the more felsic units.

Table 6.4 Epsilon Sr and Nd values for samples analysed from the KIC.

Sample	Lithology	εSr	εNd
GE14	NS1	8.4	1.5
RS14	NS2	5.7	-0.4
GE4	NS3	-3.9	0.2
RS9	NS4	5.7	0.6
VH9	NS5	-1.0	1.6
VH2	NS6	-5.2	1.2
RS1	QS	13.2	-1.1
GE1	QS	12.6	-0.3
GE11	G	29.8	-2.2
RS10	G	11.1	-2.2
VH11	GP	40.4	-4.5
GE12	GP	34.7	-5.6
VH12	MG	-1853.4	-2.4
VH13	MG	1622.0	-2.2
ND20	GABBRO	-7.7	1.5
DRK72	GABBRO	-16.7	2.4
ND10	TP	22.3	-2.2
ND12	TP	20.8	-0.7
RS15	TP	20.2	-0.2
ND22	TA	8.6	-0.4
ND23	TA	6.9	-0.4
ND26	TA	15.5	-1.1
ND35	TA	9.0	0.2
GE17	P	-85.4	1.6
RS3	MAFIC DYKE	-7.5	4.2

The plot εNd versus εSr (Figure 6.3) reveals a near linear array defined by the sample suite from the depleted to the enriched quadrant. The three samples with aberrant Sr isotope data are included for reference since their Nd data look rational. Arrows on the diagram show the direction of the deviation of calculated εSr values. Note that error bars for these samples would cross the entire graph and have therefore been left out.

Closer inspection of the Kanabeam sample suite allows for division into 3 main groups. These include the gabbro xenoliths and mafic dyke samples at the one extreme within the depleted quadrant, the NSS, tephriphonolite and trachyandesite samples that straddle the depleted and the enriched quadrants, while the third group consists of the silica-oversaturated units that plot within the enriched quadrant.

Smithies (1992) reported εSr-εNd data for the adjacent Grootpenseiland and Marinkas Quellen complexes which have been included for comparison in Figure 6.3B.

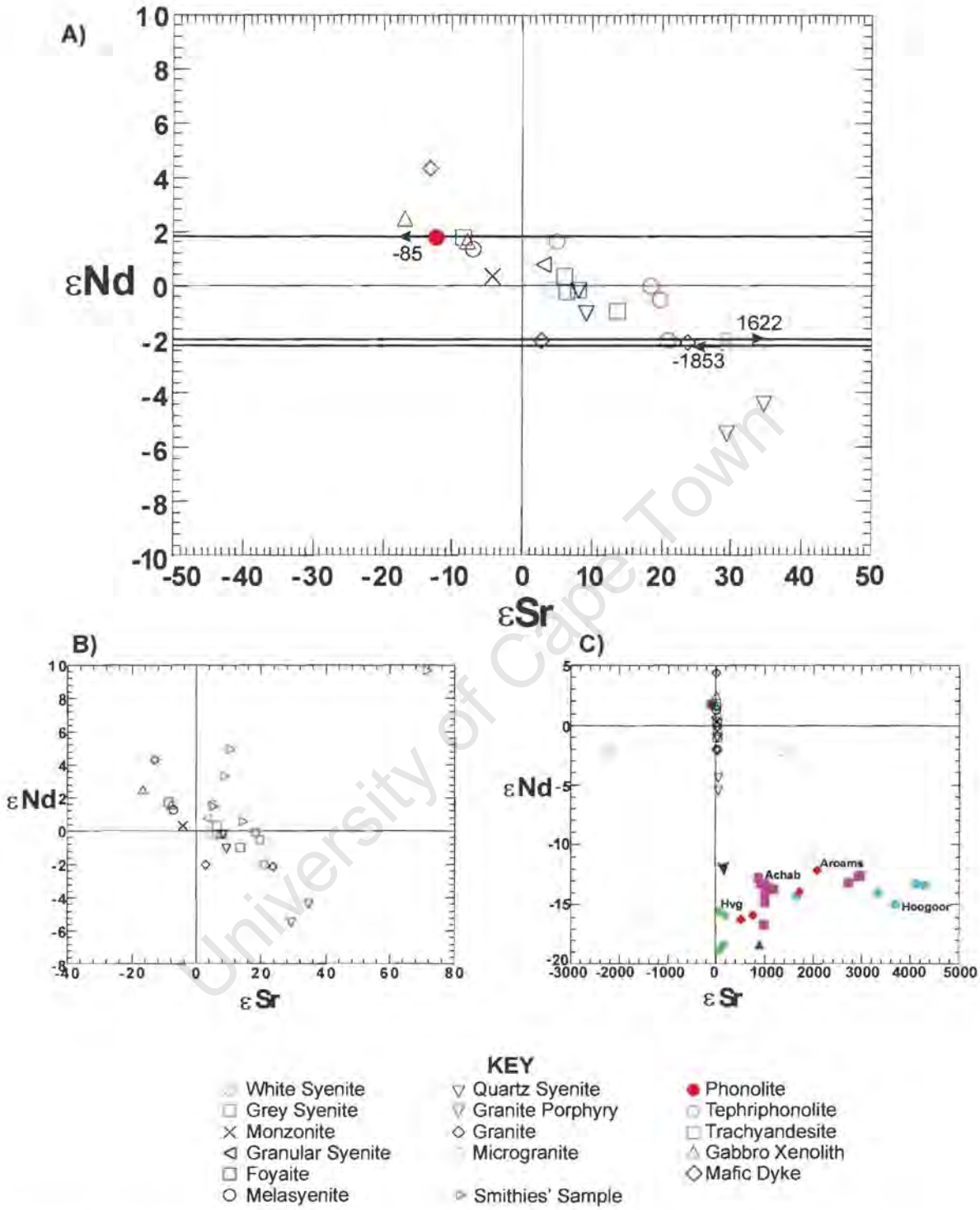

Figure 6.3 εSr versus εNd isotope correlation diagram showing A) the distribution of samples from the Kanabeam Complex. Error bars for VH12, and GE17 are provided as these are the samples with large errors. The error bars on VH13 are not displayed as these do not fall within the limits of the graph (εSr = 599 to 2645) B) with data from the Kanabeam Complex, Marinkas Quellen and Grootpenseilandand and C) variation with data representing Namaqua crust at 489Ma.

6.5.2 Basement Epsilon Sr-Nd Patterns

Epsilon Sr-Nd data for Namaqua age basement have been calculated at 489Ma from published results (Reid *et al.*, 1997; Reid 1997). Inspection of Figure 6.3C reveals that the Namaqua basement occupies a field that is predictably displaced to more negative εNd when compared with the Kanabeam samples. The wide spread in εSr is due to the greater range in the Rb/Sr ratios exhibited by the basement lithologies.

7 DISCUSSION

7.1 Introduction

This chapter is aimed at discussing the possible origins of the magma(s) that could have been responsible for the porphyry pipes. Magmatic processes such as magma mixing, fractional crystallisation, partial melting and assimilation are considered as well as the composite processes of mixing-fractional crystallisation. The pipes are assessed in view of both their petrographical features and geochemistry, as discussed in previous chapters. As the pipes may be related to one or more of the magma types observed in the KIC, the relationship of the pipes to plutonic units is also discussed.

Reid (1991) postulated, from the presence of plagioclase-bearing monzonites within the KIC and alkali gabbro xenoliths within the pipes, that the silica-undersaturated magmas in the KIC were derived from a basanitic parent that evolved to phonolitic derivatives. The silica-oversaturated magma types of Kanabeam were thought to be the products of crustal anatexis brought about by passage of the basanitic magma while the intermediate rock types were the product of magma interactions between the basanitic magma and crustal melt. Smithies (1992) and Smithies and Marsh (1996) however postulated a common mantle melt for both the silica-undersaturated and silica-oversaturated rock series with the latter being produced by protracted assimilation of crustal material in the Grootpenseiland and Marinkas Quellen complexes and possibly also Kanabeam.

Despite the predominance of felsic rock types in the KBIP, it is unlikely that a major igneous lineament of this type did not involve mantle upwelling and/or mantle melting. While limited, direct evidence for mantle derived mafic magmas is documented in the KIC through the presence of mesocratic monzonite (NS3) and numerous alkali gabbro xenoliths in the porphyry pipes. There are also many mafic dykes cutting the country rock and some of the central complexes throughout the KBIP. The study of Frimmel (1995) showed that metamorphic assemblages within the Gariep belt are not consistent with those expected for a tectonically thickened orogenic belt, but reflect higher temperatures due to a thermal anomaly within the underlying mantle which perhaps persisted after orogenesis and extended into the continental interior.

7.2 Mineral Disequilibrium

The pipes, as described in the petrography and mineral chemistry chapter, contain a wide diversity of minerals, including some that are in textural equilibrium within the neighboring matrix and others that are not. Those that are not in equilibrium include olivine, clinopyroxene, opaque oxides and plagioclase feldspar. The reactions that they have undergone include either partial or complete dissolution of the primary mineral, as well as replacement or overgrowth by secondary minerals observed as reaction coronas. The primary mineral now observed as being out of equilibrium with the final melt composition, may have been a phenocryst in the original magmas that subsequently mingled, or the product of assimilative disintegration of solid rock (Vogel, 1982).

Olivine xenocrysts in P1-6 (southern pipes) have multiple coronas similar to those found in the gabbro xenoliths. The coronas may have been brought about by:

- diffusion of elements at different rates from the olivine into the melt,
- from the melt into the olivine or
- two stage re-absorption of the olivine into the melt,

while clusters of diopsidic clinopyroxenes ('wet xenocrysts') present within zones of highly mafic matrix (Plate 4.6) may represent:

- cumulate or partially crystallised clinopyroxene within an intercumulate or trap melt
- a melt that is partially crystallized before coming in contact with a second magma resulting in mixing and subsequent crystallisation of new mineral species
- new magma entering an already present crystallising magma chamber that has subsequently undergone incomplete mixing (mingling)
- a disaggregated xenolith.

As the compositions of the xenocrystic clinopyroxenes within the pipes are similar to those of the gabbro xenoliths (Figure 4.2 and 4.3) it is most likely that they are products of disaggregation of the gabbro xenoliths. Some of these diopside xenocrysts occur as single crystals within the groundmass with hornblende rims (Plate 4.5), the product of heterogeneous nucleation.

In most of the pipe samples hornblende is found as a stable mineral phase, however, in a few cases there are examples where hornblende has become unstable. Such a response could be due to localised immersion in reactive magma batches, where the mineral was out of equilibrium or alternatively, uprise of the porphyry magmas could

have lead to decompression effects.

Plagioclase has in most cases been almost completely reacted resulting in ghost-like patches or irregular relicts with strongly embayed margins. If the melt became highly silica-undersaturated, then plagioclase would be particularly susceptible to resorption. Such an appearance of disequilibrium together with the presence of unaffected alkali feldspar phenocrysts indicate that the original plagioclase was probably calcic.

There seems to be a significant difference in the degree of mineral reaction between the tephriphonolite and trachyandesite groups. The latter shows more complete resorption of xenocrystic material, particularly the olivine from disaggregated gabbro xenoliths. This may be attributed to more protracted periods of interaction in the trachyandesite pipes by virtue of a longer residence time.

7.3 Multiple mineral phases

There are too many mineral phases (8) present in the porphyries to have been formed from a single magma. Moreover, the presence of phases seldom co-precipitating from the same magma, also demand the mixing of diverse magmas (Plate 7.1).

The major mineral phases that have been observed may be grouped as follows:
(1) olivine + clinopyroxene (diopside) $\pm$ plagioclase feldspar (mafic component)
(2) alkali feldspar + nepheline (highly felsic silica-undersaturated component that may be similar in composition to the peralkaline phonolites)
(3) clinopyroxene (augite) + hornblende $\pm$ biotite (intermediate magmatic component)

The olivine-diopside assemblage may be derived from a cognate phyric mafic magma or dissagregation of gabbro xenoliths, cognate being used in the context of part of the KIC igneous system, rather than country rock. The phonolite magma may be the product of prolonged fractionation of the same magma that produced the NSS, while the tephriphonolite and trachyandesite magmas appear to be compositionally similar to those that produced the NSS, in that they both contain alkali feldspar, clinopyroxene, hornblende and biotite and may therefore be derived from the same source.

Figure 4.2, a plot of En-Fs-Wo, displays a continuous trend in the NSS clinopyroxenes from high Mg to high Fe accompanied by a decrease in Ca, while an increase in Na rich clinopyroxenes is illustrated in Figure 4.3. These observations are consistent with

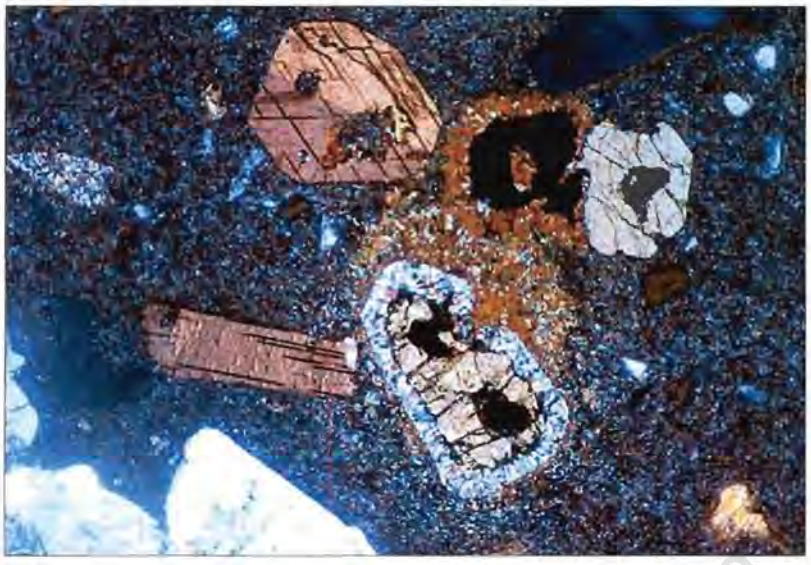

Plate 7.1 Photomicrograph of ND47. This thin section example displays the numerous phases that are observed in the pipes. Included in the fine groundmass are outsized phases, olivine, Fe-Ti oxide (splendid corona textures in two discernable fine secondary reaction products), clinopyroxene, amphibole (twinned hornblende) biotite and feldspar, seen to the lower left. Crossed polarised light, FOV=2.5mm.

fractional crystallisation trend within the NSS units where the clinopyroxenes that crystallise first have the highest Mg content while those that crystallised later have lower Mg. In the pipes however, there are clinopyroxenes that have intermediate Mg#s that plot between those from the gabbro xenoliths (high Mg#) and those from the first NSS intrusions (lower Mg#) (Figure 4.2 and 4.3), a feature that may represent mixing between a mafic and a more evolved magma.

The Di-He-Ae diagram, Figure 4.3, illustrates that the pipes were most likely formed under a higher oxidation state (more Fe^{3+}) than the NSS. This could be the result of lower volume magmas producing the pipes, however it may also be a function of the mixing history. Variation in the augite compositions may be the result of inhomogeneous mixing within the pipes as it rules out simple fractionation processes.

7.4 Inhomogeneous Character

Where mantled, un-mantled and partly mantled crystals co-exist in the system, the system is thought to consist of magmas that have undergone incomplete mechanical mixing (eg Hibbard, 1981). Complete homogenisation of a two-magma mixture requires significant time and energy in the form of heat and kinetic energy that results in turbulent convective mixing. Failure of magma mixing is due to high viscosity and thermal disequilibrium causing rapid crystallisation (Taylor *et al.*, 1980). Where mingling occurs,

movement or segregation processes may concentrate phenocrysts and xenocrysts (Fernandez and Barbarin, 1991 and Barbarin and Didier, 1991). The phenocryst and xenocryst phases within the tephriphonolite pipes are not evenly dispersed in the groundmass (Plates 4.2 and 4.3), consistent with the pipes being the product of mingling of different magmas rather than mixing. This also provides evidence that the pipes were not the products of simple fractional crystallisation processes.

In several thin sections of P1, there are contrasting colour tones (mafic content) within the matrix which supports the likelihood of mingling having taken place (Plate 4.2 and 4.3). Disequilibria textures such as those associated with olivine and diopside also supports mingling between magmas of contrasting differentiation (ie. between a mafic and a felsic magma). Grain size variation also lends support to this argument.

7.5 Geochemical Patterns

Data distribution within Petrogeny's Residua and nepheline and quartz versus DI (Figures 5.2 and 5.3) illustrate that the rocks of the complex encompass both silica-oversaturated, silica saturated and silica-oversaturated rock types. The tephriphonolite pipes are silica-undersaturated (nepheline normative) while the tephriphonolites are silica-saturated implying either different modes of formation or different parents. There is great debate over the possibility that the silica-oversaturated, silica-saturated and silica-undersaturated rock types can form from a single parent magma, due to the presence of the 'thermal divide' in petrogeny's residua system. Henderson *et al.*, (1989) and Stephenson and Upton (1982) put forward a model involving fractional crystallisation of alkali-rich amphibole to enable magmas to cross the divide. However, multiple magmas from diverse sources or alternatively open system processes involving crustal assimilation or activity of fluid phases, have to be considered (eg Mingram *et al.*, 2000; Foland *et al.*, 1993; Panter *et al.*, 1996; Macdonald *et al.*, 1995),.

From plots that show variation in silica-saturation for the complex (Figures 5.2 and 5.3), it could be considered that the tephriphonolite pipes have the same or similar origin to the NSS while the trachyandesites appear to be related to the quartz syenite and microsyenite. It however, becomes obvious when one considers variation of Fe_2O_3T, MgO, Ni, Cr, Co, V and Sc with DI (Figures 5.5 and 5.6) that the mafic content of both sets of pipes is extremely high when compared to other units from Kanabeam. They rather track back towards mafic compositions along paths not predicted by simple fractionation, rather they resemble mixing lines. The only unit within the NSS that has

values similar to the pipes is monzonite (NS3). The pipes (both tephriphonolites and trachyandesites) have significantly higher ferro-magnesian trace element contents (Ni, Cr, Co, V and Sc) than the plutonic rocks of the KIC as well as a higher concentration of Fe_2O_3T and MgO. A simple explanation for this would be the presence of gabbro xenoliths and associated xenocrysts that provided 'contamination', as it was not possible to remove all traces of the xenoliths and xenocrysts during sample preparation, however, high Fe_2O_3 and MgO and related trace element concentrations may represent mixing between an evolved magma and a mafic magma.

Zr-Nb relations in the tephriphonolites (Figure 5.10) could be interpreted as being representative of mixing processes between a parent with compositions similar to, or the same as the gabbro xenoliths and the phonolites. However, some scatter in the tephriphonolite data exists about a line projected between the gabbro xenolith and phonolite samples for Zr versus Y (Figure 5.10). This scatter may be attributed to fractionation following hybridisation and/or multiple mixing events that allow for slight variations in end-member components, however, an intermediate magma may also be involved. This may also be true for the trachyandesites which show scatter in both the Zr versus Nb and Zr versus Y diagrams. The scatter seen for the other KIC units in these graphs may also be the result of fractional crystallisation within a magma chamber combined with convective processes and/or continuous influx of new melts.

All the rock types that make up the KIC (with the exception of some of the gabbro xenoliths and microgranite), show extreme enrichment in LREE over HREE ($(La/Yb)_N$ >10); a feature typical of alkaline magmas (Panter *et al.*, 1997). Enrichment in highly incompatible trace elements (LREE), is consistent with an origin via small degrees of partial melting, derivation through high degrees of fractional crystallisation or having a LREE enriched source region. Fractionation of feldspar is observed to be minimal in the silica-undersaturated KIC units, as a strongly developed negative Eu anomaly is absent (Figures 5.13 and 5.17). The silica-oversaturated units do have negative Eu anomalies indicative of feldspar fractionation this anomaly is best developed in the microgranite. The phonolitic portion of the tephriphonolite pipe also has a strongly negative Eu anomaly possibly the result of extreme fractionation processes. Feldspar accumulation (positive Eu anomaly) is only noticeable in the granular syenite. This may be the result of fractionation within a magma chamber that has undergone periodical replenishment.

While the total alkalis versus silica plots, Figures 3.3 and 3.10, do not indicate a possible parental basanitic mixing component within the rock types encountered at Kanabeam the

gabbro xenoliths may represent the primary magma intruded at depth, that was subsequently entrained by more fractionated, intermediate or felsic melts. The felsic melts may be those represented by the phonolites found within P1 while the intermediates may be the products of fractional crystallisation of a basanitic parental melt If the gabbro xenoliths were representative of a parental magma, or deeper more primative portions of the KIC sampled at depth then the variable LREE enrichment observed in Figure 5.13 may indicate that the source region for the KIC was not LREE enriched. Variable enrichment would more likely be the result of changing degrees of partial melting or fractional crystallisation but may also be controlled by periodic refilling of a magma chamber. This may enrich incompatible elements by increasing the abundance of elements with low partition coefficients (Conticelli *et al*,. 1997).

7.6 Inferences from Isotopes

The εSr-εNd data is useful in providing some insights into the possible origins for both the pipes as well as plutonic units within the KIC. Although both groups of pipes, tephriphonolites and trachyandesites have similar εNd values, their εSr values are different with the trachyandesites having lower values (6.8 to 15.5) than the tephriphonolites (20.2 to 22.3). Despite this, their close proximity to bulk earth values may indicate a mantle plume component. In Damaraland comparable near bulk earth values are noted for nepheline syenites, carbonatites and lamprophyres found within alkaline ring complexes similar to those of the KBIP (Milner and Le Roex, 1996; Le Roex and Lanyon, 1998; Mingram et al, 2000; Harris et al., 1999).

The NSS samples straddle the εSr zero value and have positive εNd values similar to those of the gabbro xenoliths sampled from the pipes. This advocates that the NSS was derived from a mantle-sourced parental mafic magma as previously suggested by Reid (1991). Deviation from bulk earth values, to higher εNd and lower εSr suggests a depleted mantle component. Similar to the NSS samples, the phonolite sample (GE17) also has a positive εNd value suggestive of mantle derivation. Overlapping εSr-εNd values of the NSS and pipe gabbro xenoliths is also found in the Messum and Okenenya complexes, Namibia, where coexisting gabbros and syenites were interpreted to be derived from mantle magmas with minor crustal contamination (Trumbull *et al.*, 1997; Harris *et al.*, 1999; Milner and Le Roex, 1996).

Silica-saturated samples (eg QS) in Kanabeam are found to also plot in the proximity of bulk earth values, while those that are silica-oversaturated are found within the enriched

mantle/crustal quadrant. The significant differences between the εNd values of the silica-oversaturated samples and the local continental crust (Namaqua gneisses) indicates that the parental magmas were not simple crustal melts. Rather the εNd-εSr pattern indicates incorporation of a variable component of Namaqua crust into mantle melts by processes such as assimilation or combined AFC processes, as suggested by Smithies and Marsh (1996).

7.7 Petrogenesis

Figure 7.1 consists of a possible model for the progression of emplacement of the KIC. A summary of the petrogenetic scheme for magmas responsible for the plutonic rocks is presented in Figure 7.2 while Figure 7.3 is a summary of the magmas that are thought to have resulted in the formation of the tephriphonolitic and trachyandesitic pipes.

7.7.1 Silica-undersaturated Units

Isotopic data for the KIC (εNd-εSr) indicates a mantle derived parental magma for the silica-undersaturated rock types within Kanabeam. Evidence from both gabbro xenoliths and characteristics of the NSS and phonolite portion of the pipes indicate a basanite or alkali basalt parental melt. Evolution of this parental magma by fractional crystallisation along the path basanite-tephrite-phonolite must have occurred to produce the NSS. Differences between the NSS units is interpreted as resulting from fractional crystallisation within a magma chamber that underwent periodic replenishment from the source, as there is no indication of major differences in the source characteristics or significant influences resulting from crustal contamination. Phonolitic to tephritic magmas from this lineage may have contributed to those that produced the porphyry pipes.

7.7.2 Silica-saturated and Silica-oversaturated Units

The silica-saturated and silica-oversaturated units within the KIC have variable εNd-εSr values that lie within the enriched quadrant, however their εNd values are not comparable with those of the Namaqua crust at the time of emplacement. From this information it can be concluded that these units are not simple crustal melts, but they are rather products of AFC processes. The wide range in εSr (especially in the KIC granite samples) may be the result of assimilation of crust with variable εSr. Differences in silica-saturation is interpreted to result from varying degrees of assimilation of crustal material. The magmas would have had trachytic to rhyolitic composition. These felsic magmas

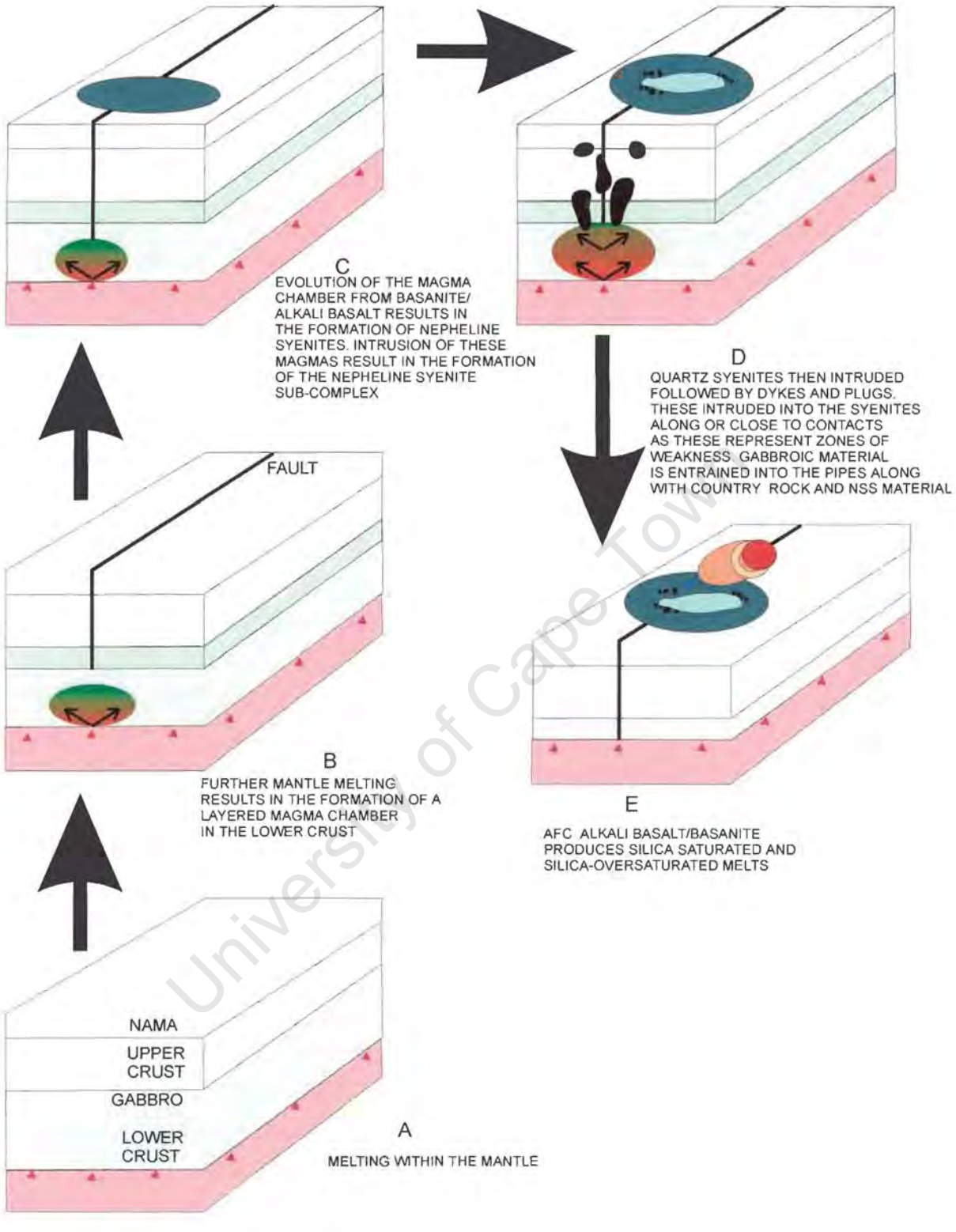

Figure 7.1 A model for the progression of emplacement of the KIC.

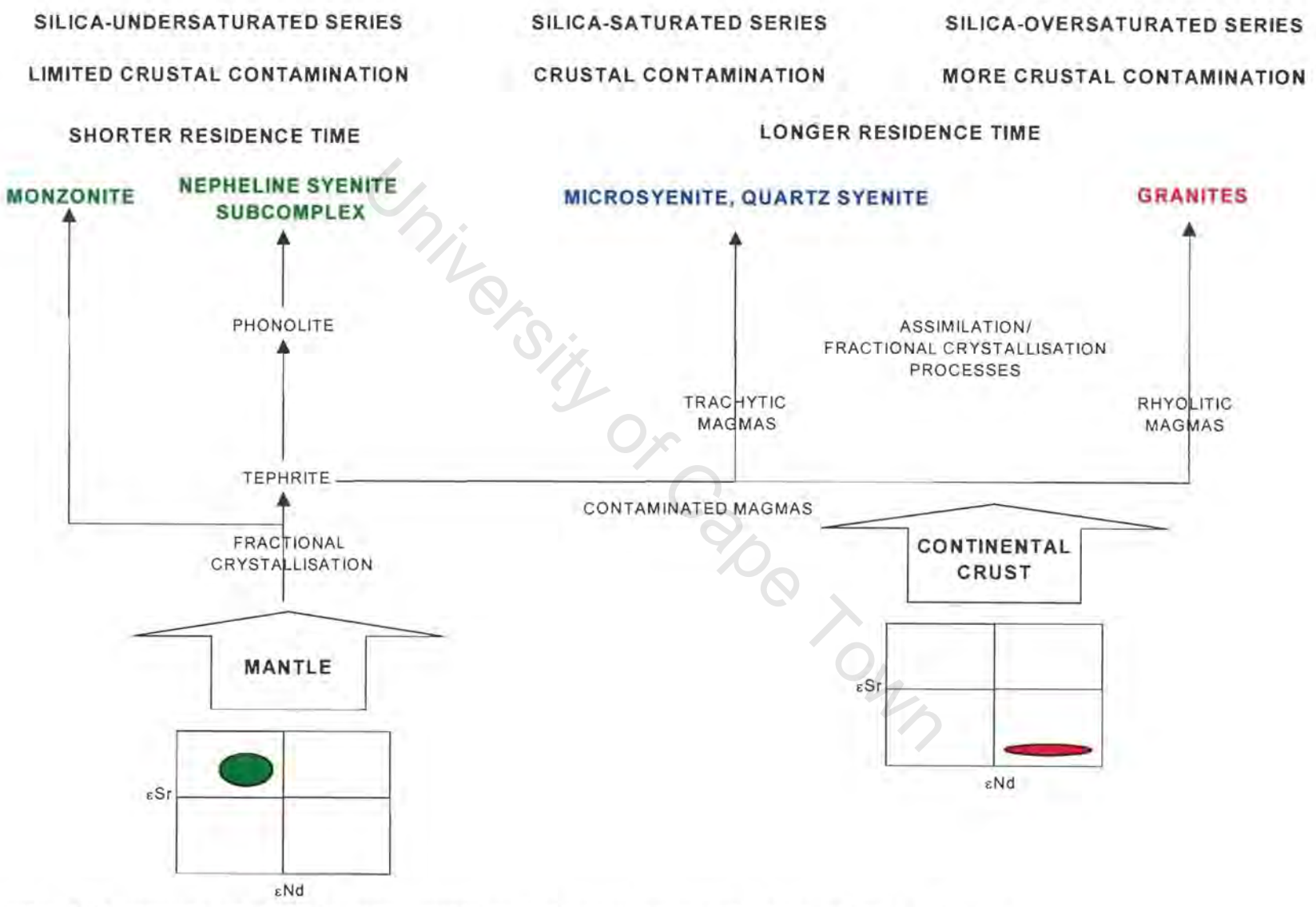

Figure 7.2 Petrogenetic pathway for the magmas responsible for the plutonic rocks in the Kanabeam Igneous Complex

with a strong crustal signature may have also contributed to the porphyry pipes.

7.7.3 Porphyry Pipes

Although the tephriphonolites and trachyandesites share similarities, each represents a distinct evolutionary trend from where each group is not derived by simple fractional crystallisation processes, rather mixing and mingling appears to have occurred. The silica-saturated nature of the trachyandesites indicate more assimilation or, assimilation of more felsic crustal material than the tephriphonolites.

In addition to a mantle derived end member, the high εSr values of these samples indicate another end member with a substantial crustal component. The wide range in εSr for the crust at the time of emplacement of the pipes allows for the observed variation in εSr for the pipes. Since the tephriphonolites have higher εSr than the trachyandesites their crustally contaminated end member could not be the same, and batches with distinct εSr must have existed.

Presence of highly silica-undersaturated phonolite within the tephriphonolitic pipes (especially P1) may be the result of entrainment of a highly evolved magma, similar to that which produced the NSS, by a tephritic melt. The exsistance of gabbro xenoliths, and related disaggregated xenocrysts within the pipes appears to be important in history of the KIC. The gabbro is most likely to be the first product of mantle derived melts within the region of the KIC. Complete crystallisation is not likely have to occurred prior to the emplacement of the complex and this is why gabbro xenoliths and related xenocrysts are observed within the pipes which must have passed through the gabbro intrusion. Absence of olivine in the trachyandesite, a mineral thought to be completely reacted out, suggests a longer residence time prior to eruption, in contrast to the tephriphonolites where the residence time was less. Increased residence time is also predicted for the trachyandesites as they appear to have undergone better mixing, producing a homogenous hybrid magma, compared to the mingling observed in the tephriphonolites.

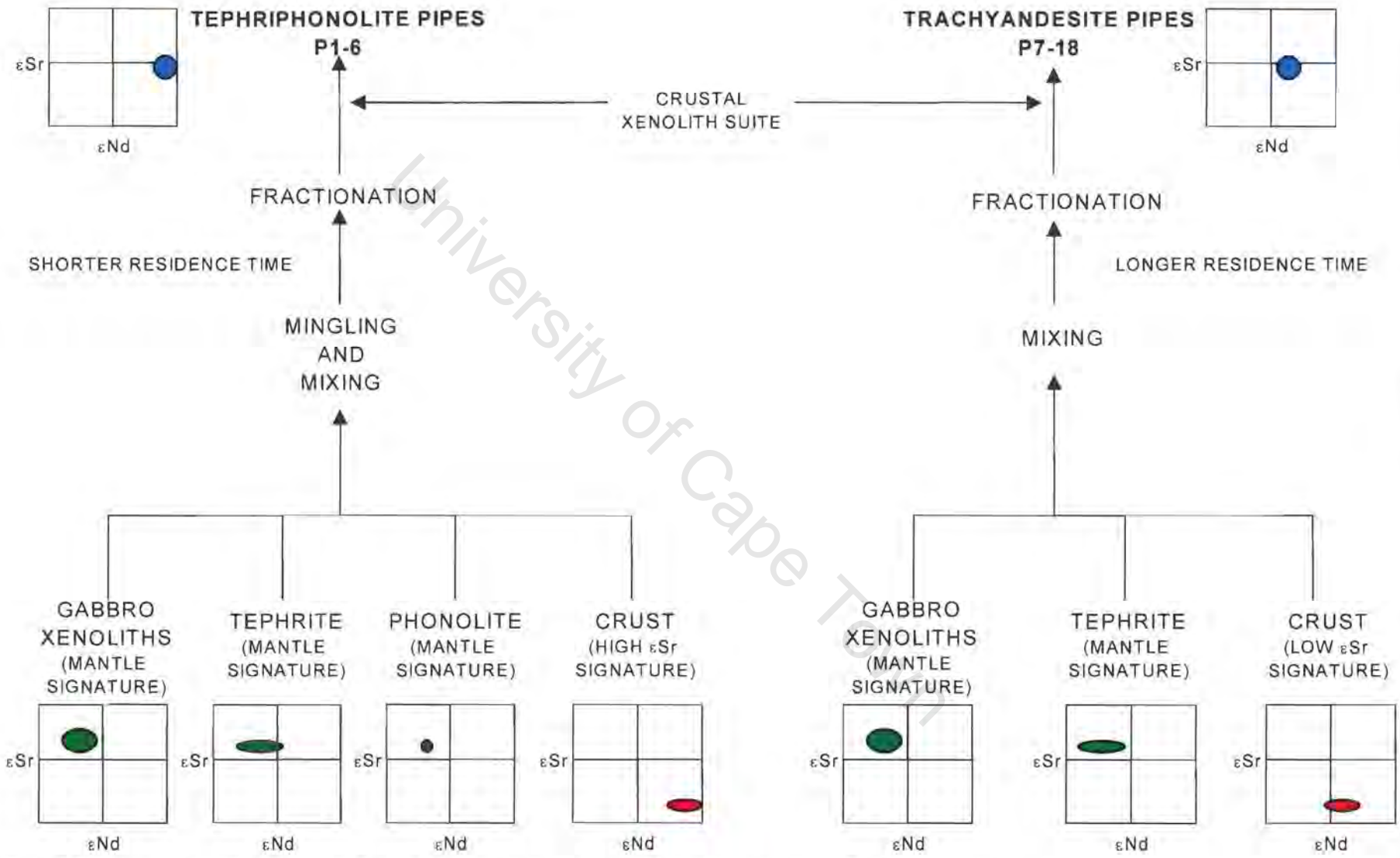

Figure 7.3 Petrogenetic pathway illustrating the possible magma types responsible for the generation of the porphyry pipes.

REFERENCES

Allsopp HL, Köstlin EO, Welke HJ, Burger AJ, Kröner A and Blignault HJ. (1979) Rb-Sr and U-Pb geochronology of late Precambrian – early Palaeozoic igneous activity in the Richtersveld (South Africa) and southern South West Africa. *Trans. Geol. Soc. S. Afr.*, **82**, 185-204.

Armstrong RA, Reid DL, Watkeys MK, Welke HJ, Lipson RD and Compston W (1988). Zircon U-Pb ages from the Aggeneys area, Central Bushmanland. *Ext. Abs. Geol. Soc. S. A. Geocongress '88, Univ. Natal, Durban,* 493-496.

Arth JG (1976) Behaviour of trace elements during magmatic processes – a summary of theoretical models and their applications. *J. Res. U.S. Geol. Surv.*, **4**, 41-47.

Bailey DK (1980) Volatile flux, geotherms and the generation of the kimberlite-carbonatite-alkaline magma spectrum. *Mineralogical Magazine* **43**, pp695-699

Barbarin B and Didier J (1991) Macroscopic features of mafic microgranular enclaves. In: J. Didier and B Barbarin (Editors), Enclaves and Granite Petrology. Elsevier, Amsterdam, pp.253-262

Barton, ES (1983). Reconnaissance isotopic investigations in the Namaqua mobile belt and implications for Proterozoic crustal evolution - Namaqualand geotraverse. *Spec. Publ. Geol. Soc. S. Afr.*, **10**, 45-66.

Basu AR and Tatsumoto M (1980) Nd-Isotopes in selected Mantle-Derived Rocks and Minerals and Their Implications for Mantle Evolution. *Contr. Mineral. Petrol.* **75**, 43-54

Bertrand JM (1976) Granitoids and deformation sequence in the Goodhouse-Henkries. A new interpretation of the relationship between rocks in the Vooilsdrift-Goodhouse area and the Namaqualand and Bushmanland gneisses. Precamb. Research Unit UCT Ann. Rept. 13:61-70

Blignault HJ, Jackson MPA, Beukes GJ, Toogood DJ (1974) The Namaqua Tectonic Province in South West Africa. Precamb Research Unit UCT Bull No15 pp22-47

Blignault HJ, Van Aswegen G, Van Der Merwe SW and Colliston WP (1983) The Namaqua geotraverse and environs: part of the Proterozoic Namaqua mobile belt. In: B.J.V. Botha (Editor), Namaqua Metamorphic Complex, Geological Society of South Africa, Special Publication, 10, 1-30.

Blignaut HJ, Marais JAH, van der Merwe SW, van Aswegen G and Muller JA (1980). The Namaqualand Geotraverse. *Annex to Spec. Publ. Geol. Soc. S. Afr.*, **10**.

Botha BJV (1986). The transition from the Kaapvaal Craton to the Namaqua mobile belt. *In:* Schoch AE, Van Aswegen G, Colliston WP, Botha BJV, Grobler NJ, Geringer GJ & Strydom D. (Eds.), *Excursion guidebook for Namaqualand (Excursion No. 24A).*

Bowen NL (1937). Recent high-temperature research on silicates and its significance in igneous geology. *Am. J. Sci.*, **33**, 1-21.

Colliston WP (1990). A stratigraphic and structural investigation of part of the Namaqua mobile belt between Dabenoris and Steyerkraal. *Unpublished PhD thesis, Univ. Orange Free State, Bloemfontein*, 259pp.

Colliston WP, Praekelt HE and Schoch AE (1989). A broad perspective (Haramoep) of geological relations established by sequence mapping in the Proterozoic Aggeneys terrane, Bushmanland, South Africa. *S. Afr. Jour. Geol.*, **92**, 42-48.

Colliston WP, Praekelt HE and Schoch AE (1991) A progressive ductile shear model for the Proterozoic Aggeneys terrane, Namaqua mobile belt, South Africa. *Preamp. Res.*, **49**, 205 – 215.

Colliston WP, Praekelt HE, Strydom D and Pretorius JJ (1986). Stratigraphic map of Central Bushmanland (1:100 000 geological map). *Dept. Geology, Univ. Orange Free State*, Bloemfontein. 1 sheet.

Conticelli S, Francalanci L, Manetti P, Cioni R and Sbrana A (1997) Petrology and geochemistry of the ultrapotassic rocks from the Sabatini Volcanic Distric, central Italy: the role of evolutionary processes in the genesis of variably enriched alkaline magmas. *Journal of Vol. and Geotherm. Res.* **75**, 107-136

Cox KG, Bell JD and Pankhurst RJ (1979) The interpretation of igneous rocks. George, Allen and Unwin, London, pp. 450.

Deer WA, Howie RA and Zussman J (1992) An introduction to rock-forming minerals. Longman Scientific and Technical, England, pp. 696.

Dostal J, Dupuy C, Carron JP, Le Guen de Kerneizon M and Maury RC (1983) Partition coefficients of trace elements: application to volcanic rocks of St Vincent, West Indies. *Geochim. Cosmochim. Acta*, **47**, 525-533.

Duncan AR, Erlank AJ and Betton PJ (1984). Analytical techniques and database description. *Spec. Publ. Geol. Soc. S. Afr.*, **13**, Appendix 1, 389-395.

Fernandez AN and Barbarin B (1991). Relative rheology of coeval mafic and felsic magmas: Nature of resulting interaction processes and shape and mineral fabrics of mafic microgranular enclaves. In: J. Didier and B Barbarin (Editors), Enclaves and Granite Petrology. Elsevier, Amsterdam, pp.263-275.

Flohr MJK and Ross M (1990) Alkaline rocks of Magnet Cove, Arkansas: mineralogy and geochemistry of syenites. *Lithos* **26**, 87-98.

Foland KA, Landoll JD, Henderson CMB and Jiangfeng C (1993) Formation of cogenetic quartz and nepheline syenites. *Geochim. et Cosmo. Acta*, **57**, 697-704.

Frimmel HE (2000). New U-Pb zircon ages for the Kuboos pluton in the Pan-African Gariep belt, South Africa: Cambrian mantle plume or far field collision effect? *South African Journal of Geology*, **103**, 207-214.

Frimmel HE (1995) Metamorphic evolution of the Gariep Belt. *South African Journal of Geology* **98**, 176-190.

Frimmel HE and Frank W (1998) Neoproterozoic tectonothermal evolution of the Gariep Belt and its basement, Namibia and South Africa. *Precamb. Res.* **90**, 1-28

Fujimaki H, Tatsumoto M and Aoki K (1984) Partition coefficients of Hf, Zr, and REE between phenocrysts and groundmasses. Proceedings of the 14th lunar and planetary science conference, Part 2. *J. Geophys. Res.*, **89**, Suppl. B662-B672.

Germs GJB (1972) The stratigraphy and palaeontology of the lower Nama Group, South West Africa. Precambrian Res. Unit University of Cape Town, Bull. **No. 12.**

Gill JB (1981) Orogenic andesites and plate tectonics. Springer, Berlin.

Gomes CB, Moro SL, Dutra CV (1970) Pyroxenes from the alkaline rocks of Itapirapuã, São Paulo, Brazil. *Am Min.* **55**, 224-230.

Green TH and Pearson NJ (1987) An experimental study of Nb and Ta partitioning between Ti-rich minerals and silicate liquids at high pressure and temperature. *Geochim. Cosmochim. Acta*, **51**, 55-62.

Green TH Sie SH Ryan CG and Cousens DR (1989) Proton microprobe determined partitioning of Nb, Ta, Zr, Sr and Y between garnet, clinopyroxene and basaltic magma at high pressure and temperature. *Chem. Geol.*, **74,** 201-216.

Harris C, Marsh JS and Milner SC (1999) Petrology of the alkaline core of the Messum igneous complex, Namibia: evidence for the progressively decreasing effect of crustal contamination. J Petrol. 40, 1377-1397.

Harris NBW, Pearce JA, and Tindle AG (1986) Geochemical characteristics of collision zone magmatism. In: MP Coward and AC Reis (editors) Collision tectonics, *Spec. Publ. Geol. Soc.*, **19**, 67-81.

Hartnady C Joubert P and Stowe C (1985) Proterozoic Crustal Evolution in Southwestern Africa. *Episodes.* **8**, 236-244.

Henderson P (1982) Inorganic geochemistry. Pergamon, Oxford.

Henderson CMB, Pendlebury K and Foland KA (1989) Mineralogy and petrology of te Red Hill Alkaline Igneous Complex, New Hamshire, USA. *Journal of Petrology* **30**, 627-666.

Hibbard MJ (1981) The Magma Mixing Origin of Mantled Feldspars. *Contrib. Mineral Petrol.* **76**, 158-170

Horstmann UE (1987). Die metamorphische Entwicklung im Damara Orogen, Sudwest Afrika/Namibia, abgeleitet aus K/Ar-Datierungen an detritischen Hellglimmern aus Molassesedimenten der Nama Group. *Gottinger Arb. Geol. Palaont.*, **32**, 78-86.

Jackson MPA (1976) High grade metamorphism and migmatisation of the Namaqua Metamorphic Complex around Aus in the central Namib Desert, South West Africa. Precamb Research Unit UCT Bull No18

Joubert P (1976) The relationship between the Namaqua Metamorphic Complex and the Kheis Group. S. Afr. Jour. Sci. 72:312-313

Joubert P (1971). The regional tectonism of the gneisses of part of Namaqualand. *Bull. Precamb. Res. Unit, Univ. Cape Town,* **10**, 220 p.

Kröner A and Germs GJB (1971). A re-interpretation of the Numees-Nama contact at Ausserikjer, South West Africa. *Transactions of the Geological Society of South Africa*, **74**, part 2; 2, 69-74

Kröner A and Blignault HJ (1976) Towards a definition of some tectonic and igneous provinces in western South West Africa and southern South West Africa. *Trans. Geol. Soc. S.*, **79** 232-238.

Larsen LM (1976) Clinopyroxenes and coexisting mafic minerals from the alkaline Ilimaussaq intrusion, south Greenland. *Journal of Petrology* **17**, 258-290.

Leake BE, Woolley AR, Birch WD, Gilbert MC, Grice JD, Hawthorne FC, Kato A, Kisch HJ, Krivovichev VG, Linthout K, Laird J, Mandarino J, Maresch WV, Nickel EH, Schumacher JC, Smith DC, Stephenson NCN, Whittaker EJW and Youzhi G (1997) Nomenclature of Amphiboles: Report of the Subcommitee on Amphiboles of the International Mineralogical Association Commision on New Minerals and Mineral Names. *Min. Mag.*, **61**, 295-321

Leeman WP and Lindstrom DJ (1978) Partitioning of Ni^{2+} between basaltic melt and synthetic melts and olivines – an experimental study. *Geochim. Cosmochim. Acta*, **42**, 801-816.

Le Maitre RW, Bateman P, Dudek A, Keller J, Lameyre Le Bas MJ, Sabine PA, Schmid R, Sorensen H, Streckeisen A, Woolley AR and Zanettin B (1989) A Classification of igneous rocks and glossary of terms. Blackwell, Oxford.

Le Roex AP and Lanyon R (1998) Isotope and Trace Element Geochemistry of Cretaceous Damaraland Lamprophyres and Carbonatites, Northwestern Namibia: Evidence for Plume-Lithosphere Interactions. *Journal of Petrology* **39**, 1117-1146

Lindstrom DJ and Weill DF (1978) Partitioning of transition metals between diopside and coexisting silicate liquids. I. Nickel, cobalt and manganese. *Geochim. Cosmochim. Acta,* **42**, 817-831.

Macdonald R, Davis GR Upton BGJ, Duncley PN, Smith M and Leat PT (1995) Petrogenesis of Silali volcano, Gregory Rift, Kenya. *Journal of the Geo. Soc. London.* **152**, 703-720.

Martin H (1965) The Precambrian geology of South West Africa and Namaqualand. *Precambrian Res. Unit*, University of Cape Town. 159p.

Middlemost E (1967) Petrography of the Bremen Granite Syenite Complex, South West Africa. *Trans. Geol. Soc. S. Afr.*, **70**, 117-134.

Milner SC and Le Roex AP (1996) Isotope characteristics of the Okenyenya igneous complex, northwestern Namibia: constraints on the composition of the early Tristan plume and the origin of the EM1 mantle component. *Earth and Planetary Science Letters* **141**, 277-291.

Mingram B, Trumbull RB, Littman S and Gerstenberger H (2000) A petrogenetic study of anorogenic felsic magmatism in the Cretaceous Paresis ring complex, Namibia: evidence for mixing of crust and mantle derived components. *Lithos,* **54**, 1-22

Mitchell RH and Platt RG (1982) Mineralogy and petrology of nepheline syenites from the Coldwell Alkaline Complex, Ontario, Canada. *Journal of Petrology* **23**, 186-214.

Morimoto N, Fabrics J, Ferguson AK Ginzburg IV, Ross M, Seifert FA, Zussman J, Aoki K and Gottardi G (1988) Nomenclature of Pyroxenes *Am Mineral.*, **73**, 1123-1133.

Middlemost EAK (1989). Iron oxidation ratios, norms and the classification of volcanic rocks. *Chem. Geol.*, **77**, 19-26.

Nielsen TFD (1979) The occurrence and formation of Ti-aegerines in peralkaline syenites. *Contrib. Mineral Petrol.* **69**, 235-244.

Norish K and Hutton JT (1969). An accurate X-Ray spectrographic method for the analysis of a wide range of geological samples. *Geochim. Cosmochim. Acta,* **33**, 431-453.

Panter K, Kyle PR and Smellie JL (1997) Petrogenesis of a phonolite-trachyte succession at Mount Sidley, Marie Byrd Land, Antarctica. *Journal of Petrology.*, 1225-1253.

Parsons I and Brown WL (1988) Sidewall crystallisation in the Klokken intrusion: zoned ternary feldspars and coexisting minerals. *Contrib. Mineral. Petrol.* **98**: 431-443.

Pearce JA, Harris NBW and Tindle AG (1984) Trace element discrimination diagrams for the tectonic interpretation of granitic rocks. *Journal of Petrology*, **25**, 956-983.

Pearce JA and Norry MJ (1979) Petrogenetic implications of Ti, Zr, Y and Nb variations in volcanic rocks. *Contrib. Mineral. Petrol.*, **69**, 33-47

Praekelt HE, Schoch AE and Visser JNJ (1996) The metasediments of the Aggeneys terrane in the Namaqua Mobile Belt: Sedimentary response to the extensional-compressional variations in a continental environment. *S. Afr. J. Geol.*, **100(1)**, 101-110.

Praekelt HE and Schoch AE Stratigraphical synthesis of the metasediments of the Aggeneys terrane in the Namaqua Mobile Belt. *S. Afr. J. Geol.*, **100(1)**, 85-100.

Praekelt HE, Colliston WP and Strydom D (1984). Stratigraphic correlation of metasediments of the Proterozoic Aggenys Subgroup, Bushmanland, Namaqua Mobile Belt. *Abstr. Int. Conf. Mid-Late Proterozoic Lithosphere Evolution, Precambrian Res. Unit, Univ. Cape Town,* 41-42.

Reid (1997) Sm-Nd age and REE geochemistry of Proterozoic arc-related igneous rocks in the Richtersveld Subprovince, Namaqua Mobile Belt, Southern Africa. *Journal of African Earth Sciences*, **24(4)**. 621-633

Reid DL (1977). Geochemistry of Precambrian igneous rocks in the lower Orange River region. *Bull. Precamb. Res. Unit, Univ. Cape Town,* **22**, 397p.

Reid DL (1979) Total rock Rb-Sr and U-Th-Pb isotopic study of Precambrian metavolcanic rocks in the lower Orange River region, southern Africa. *Earth and Planetary Science Letters* **42**, 368-378.

Reid DL (1982) Age relationships within the Vioolsdrif batholith, lower Orange River region II. A two stage emplacement history and the extent of Kibaran overprinting. *Trans. Geol. Soc. S. Afr.*, **85**, 105-110.

Reid DL (1991) Alkaline rocks in the Kuboos-Bremen igneous province, southern Namibia: The Kanabeam multiple ring complex. *Commun. Geol. Surv. Namibia*. **7**, 3 – 13

Reid DL (1998) Guide for the excursion to the alkaline igneous provinces of southern Namibia. 7th International Kimberlite Conference University of Cape Town.

Reid DL, Ransome IGD, Onstott TC and Adams CJ (1991) Time of emplacement and metamorphism of Late Precambrian mafic dykes associated with the Pan-African Gariep orogeny, Southern Africa: implications for the age of the Nama Group. *Journal of African Earth Sciences*. **13 (3&4)**, 531-541.

Reid DL, Welke HJ, Erlank AJ and Betton PJ (1987). Composition, age and tectonic setting of amphibolites in the central Bushmanland Group, western Namaqua Province, southern Africa. *Precamb. Res.*, **36**, 99-126.

Ritter U (1978) The rocks of the south eastern Richtersveld between Esteenfontein and Klein Helskloof: their relationship to the Gariep metamorphism and tectonism and to the Namaqua metamorphic complex. Precamb. Research Unit. UCT Ann Rept 14/15:83-98.

Rollinson H (1993) Using geochemical data: evaluation, presentation, interpretation. Longman, Essex.

Schairer JF(1950). The alkali feldspar join in the system $NaAlSiO_4$ – $KalSiO_4$ – SiO_2. *J. Geol.*, **58**, 512-517.

Schock HH (1979) Distributions of rare-earth and other trace elements in magnetites. *Chem. Geol.*, **26**, 119-133

Smithies RH (1992). The geochemical evolution of three alkaline complexes in the Kuboos-Bremen igneous province, southern Namibia. *Unpublished PhD thesis,* Rhodes Univ. Grahamstown, 197pp.

Söhnge PG and De Villiers J (1948). The Kuboos pluton and its associated line of intrusives. *Trans. geol. Soc. S. Afr.*, **51**, 1-31.

Stephenson (1976) The South Qoroq Centre nepheline syenites, South Greenland. *Gronl. Geol.Unders. Bull.* **118**, 55p

Stephenson D and Upton BGJ (1982) Ferromagnesian silicates in a differentiated alkaline complex, Kungnat Fjeld, South Greenland. *Mineral Mag,* **46**, 283-300

Strydom D (1982). Geselskapbank-Areb, 1: 100 000 geological map. *Univ. Orange Free State*. 1 sheet.

Strydom D (Ed.), Colliston WP, Praekelt HE, Schoch AE Van Aswegen G, Pretorius JJ, Beukes, GJ, Cilliers B, Watkeys MK & Botes FJ (1987). The tectonic parts of the

Namaqualand, Bushmanland and southern South-West Africa/Namibia (1:250 000 map). *Univ. Orange Free State,* Bloemfontein, 1 sheet.

Tankard AJ, Jackson MPA, Eriksson KA, Hobday DK, Hunter DR and Minter WEL (1982) Crustal evolution of Southern Africa. 3.8 billion years of earth history. *Springer Verlag, New York*, 523p.

Taylor SR and McLennan SM 1985 The continental crust: :its composition and evolution. Blackwell, Oxford

Taylor TR, Vogel TA and Wilband JT (1980). The composite dikes at the Mount Desert Island, Maine; An example of coexisting acidic and basic magmas. *Journal of Geology*, **88**, 433-444

Thornton CP & Tuttle OF (1960). Chemistry of igneous rocks, 1, Differentiation index, *Am. J. Sci.*, **258**, 664-84.

Toogood DJ (1976). Structural and metamorphic evolution of a gneiss terrane in the Namaqua belt near Onseepkans, South West Africa. *Precamb. Research Unit* UCT Bull No**19**.

Trumbull RB, Gerstenberger H, Schmitt A, Minigram B Bhn B and Emmermann R (1997) Mesosoic igneous complexes in Namibia: Crust-mantle interaction on a rifted continental margin. *Terra Nova* **9**, 459, EUG 9, Strasburg, 23-27 March. Abstract Supplement 1.

Van Aswegen G (1983) The Gladkop Suite. *Spec. Publ. Geol. Soc. S. Afr.*, **10**, 31-44.

Van de Merwe SW and Botha BJV (1989). The Groothoek Thrust Belt in western Namaqualand: an example of mid-crustal structure. *S. Afr. J. Geol.*, **92**, 156-166.

Van der Merwe SW (1986). The structural development of part of the Namaqua Mobile Belt, in an area between Springbok abd Vioolsdrift. PhD thesis (unpubl.) Univ. Orange Free State, Bloemfontein, 373pp.

Vogel TA 1982 Magma mixing in the acidic-basic Complex of Ardnarmurchan; Implications on the evolution of shallow magma chambers. *Contributions to mineralogy and Petrology*, **79**, 411-423

Von Veh MW (1993). The stratigraphy and structural evolution of the Late Proterozoic Gariep belt in the Sendelingsdrif – Annisfontein area, northwestern Cape Province. *Bullitin, Precambrian Research Unit*, University of Cape Town, South Africa. **38**, 174pp.

Wilson M (1989) Igneous Petrogenesis. Unwin Hyman, London

Wolff JA (1987) Crystallisation of nepheline syenite in a subvolcanic magma system: Tenerife, Canary Islands. *Lithos* **20**, 207-223.

Woolley AR and Platt RG (1986) The mineralogy of nepheline syenite complexes from the northern part of the Chilwa Province, Malawi. Min. Mag. **50**, 597-610.

Zinder A (1980). Geochemical processes in the Earth's mantle and the nature of crust-mantle interactions: evidence from studies of Nd and Sr isotope ratios in mantle-derived

igneous rocks and lherzolite nodules. *Unpublished PhD thesis,* Massachusetts Institute of Technology.

Zinder A, Hart SR and Frey FA (1979). Nd and Sr isotope ratios and rare earth element abundances in Reykjanes Peninsula basalts: evidence for mantle heterogeneity beneath Iceland. *Earth and Planetary Science Letters* **45**, 249-262.

APPENDICES

PLUTONIC SAMPLE LOCALITY MAP

AND

SAMPLE IDENTIFICATIONS

Kanabeam Samples

Sample number	Pipe number	Description
ND 001	P2	gabbroic xenolith
ND 002	P2	finer gabbroic xenolith
ND 003	P2	small xenoliths
ND 004	P2	**Geochem sample**
ND 005	P2	olivine nodules
ND 006	P2	gabbro nodule
ND 007	P3	Fine grained Xenolith
ND 008	P3	Matrix sample
ND 009	D1	Dyke - fine grained
ND 010	P3	**Geochem sample**
ND 011	P3	Pet sample - oddities
ND 012	P4	**Geochem sample**
ND 013	P4	coarse grained xenolith
ND 014	P4	Fine grained xenolith
ND 015	P4	Fine grained xenolith with large phenocrysts
ND 016A	P4	**Geochem sample**
ND 016B	P4	Pet sample
ND 017	P5	**Geochem sample**
ND 018	P6	Xenolith- pet sample
ND 019	P6	**Geochem sample**
ND 020	P6	**Geochem sample**
ND 021	P7	**Geochem sample**
ND 022	P8	**Geochem sample**
ND 023	P9	**Geochem sample**
ND 024	P10	Hand specimen - large xenolith
ND 025	P10	**Geochem sample**
ND 026	P11	**Geochem sample**
ND 027	P11	pet sample
ND 028	P11	**Geochem sample**
ND 029	P11	metased sample
ND 030	P12	**Geochem sample**
ND 031	P13	**Geochem sample**
ND 032	P13	pet sample
ND 033	P14	pet sample
ND 034	P14	fragment from breccia
ND 035	P15	**Geochem sample**
ND 036	P16	metased sample
ND 037	D2	mafic dyke
ND 038	P17	**Geochem sample**
ND 039	P17	banded metased xenolith
ND 040	P17	**Geochem sample**
ND 041	P17	dark xenolith
ND 042	P18	dark metased xenolith
ND 043	P18	light coloured metased xenolith
ND 044	P1	**Geochem sample**
ND 045	P1	Hand specimen - fine grained material
ND 046	P1	**Geochem sample**
ND 047	P1	**Geochem sample**
ND 048	D3	Dyke

Kanabeam Samples

Sample	Abrev	Name
GE-14	NS1	White Syenite
DRK-72	Gabbro	xen in HP
GE-1	QS	Southern Quartz Syenite
GE-10	G	Northern Granite
GE-11	G	Northern Granite
GE-11B	Xen	in G
GE-12	GP	Granite Porphyry
GE-13	NS3	Monzonite
GE-16	QS	Southern Quartz Syenite
GE-17	HP	(light)
GE-2	QS	Southern Quartz Syenite
GE-3	Xen	in QS
GE-4	NS3	Monzonite
GE-5	MSy	dyke in NS3
GE-6	NS5	Foyaite
GE-7	NS6	Porphyritic Melasyenite
GE-8	NS6	Porphyritic Melasyenite
GE-9	Aplite	in G
RS-1	QS	Southern Quartz Syenite
RS-10	G	Northern Granite
RS-11	MS	Microsyenite
RS-12	G	Northern Granite
RS-13	MS	Microsyenite
RS-14	NS2	Grey Syenite
RS-15	HP	
RS-2	QS	Southern Quartz Syenite
RS-2A	Xen	in QS
RS-3	Dyke	in QS
RS-4	QS	Southern Quartz Syenite
RS-5	NS5	Foyaite
RS-6	NS5	Foyaite
RS-7	NS4	Granular Syenite
RS-8	NS6	Porphyritic Melasyenite
RS-9	NS4	Granular Syenite
VH-1	NS5	Foyaite
VH-10	NS4	Granular Syenite
VH-11	GP	Granite Porphyry
VH-12	MG	Northern Microgranite
VH-13	MG	Northern Microgranite
VH-14	MG	Northern Microgranite
VH-15	Dyke	in MG
VH-16	MG	Northern Microgranite
VH-17	MG	Northern Microgranite
VH-2	NS6	Porphyritic Melasyenite
VH-3	NS4	Granular Syenite
VH-4	NS4	Granular Syenite
VH-5	MS	Microsyenite
VH-6	NS4	Granular Syenite
VH-7	NS4	Granular Syenite
VH-8	NS5	Foyaite
VH-9	NS5	Foyaite

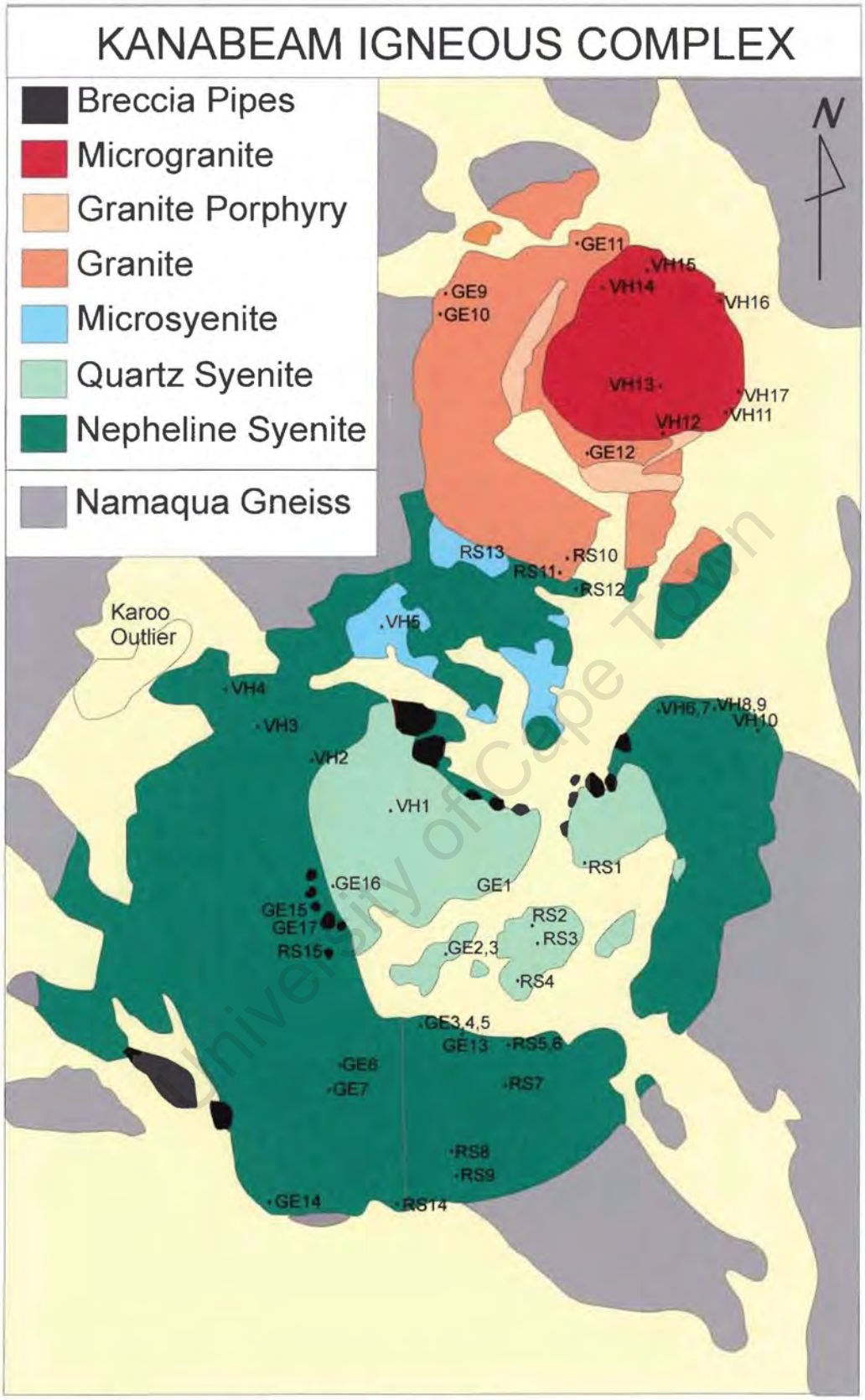

Sample positions for the plutonic units.

ANALYTICAL TECHNIQUES

Electron Microprobe Analysis

Electron microprobe analysis was carried out on 30μm thick, polished sections at the University of Durban Westville on the Joel Electron Microprobe Microanalyser (JXA-8800RL) and at the University of Cape Town on the Cameca Cambax 4-Channel Microprobe. Both instruments were run with a narrow beam at an accelerating voltage of 15kV and a beam current of 40nA. On-line data reduction was carried out.

X-Ray Fluorescence

Whole rock samples were analysed for major and 18 trace elements by X-ray fluorescence spectrometry using the method of Norrish and Hutton (1969) for major elements and pressed powder briquettes for trace elements, as routinely applied in the Department of Geological Sciences at the University of Cape Town. Errors and detection limits based on counting statistics are similar to those reported by le Roex, Erlank and Needham (1991).

Inductively Coupled Plasma Mass Spectrometry (ICP-MS)

Whole rock, rare earth element analysis by ICP-MS was carried out in the Department of Geological Sciences, University of Cape Town after dissolution of the samples in HF-HNO_3. Elements analysed include; La, Ce, Pr, Nd, Sm, Eu, Gd, Pb, Tb, Dy, Ho, Er, Tm, Yb and Lu. Calibration for ICP-MS was carried out by external standardisation. Standard and blank samples were also analysed. Internal standardisation was carried out to ensure that there was no instrument drift or change in signal intensity. Accuracy and precision was approximately 1-3%.

Radiogenic Isotope Analyses

Isotope analyses were performed in the Radiogenic Isotope Facility, Department of Geological Sciences, University of Cape Town. Sr and Nd were separated using conventional ion-exchange techniques and all radiogenic isotope analyses were performed on a VG Sector 7-collector thermal ionisation mass spectrometer operated in dynamic multi-collector mode. Whole rock concentrations of Rb and Sr were found using XRF, while Sm and Nd concentrations were determined by ICP-MS. Beads with two filaments, Ta and Rh were prepared for the Nd sample, using the technique of Zindler *et al.* (1979), and single Ta filament beads, using a technique similar to Zindler (1980) for the Sr sample.

Errors associated with Rb, Sr, Sm and Nd. Rb and Sr by XRF and Sm and Nd by ICP-MS

Sample	*Lithology*	*Rb error ppm*	*Sr error ppm*	*Sm error ppm*	*Nd error ppm*
GE14	NS1	1.02	0.45	0.72	0.98
RS14	NS2	0.24	0.84	0.40	0.45
GE4	NS3	0.47	1.29	2.00	0.98
RS9	NS4	1.88	1.67	0.74	0.78
VH9	NS5	1.88	0.85	0.52	0.87
VH2	NS6	0.58	0.82	1.17	1.95
RS1	QS	0.58	1.75	0.57	0.26
GE1	QS	0.64	0.60	3.44	3.69
GE11	G	0.47	1.30	0.93	1.26
RS10	G	0.59	0.50	1.49	1.85
VH11	GP	0.30	0.44	0.62	2.02
GE12	GP	0.61	0.60	3.14	2.84
VH12	MG	0.63	1.37	0.89	0.95
VH13	MG	0.75	1.20	0.70	0.87
ND20	GABBRO	0.52	1.03	0.65	0.99
DRK72	GABBRO	0.38	1.01	0.89	0.58
ND10	TP	0.50	0.83	1.26	1.10
ND12	TP	0.48	0.87	0.60	0.96
RS15	TP	0.57	0.83	2.21	1.49
ND22	TA	0.48	1.08	0.74	1.30
ND23	TA	0.48	1.08	0.62	0.85
ND26	TA	0.55	0.82	0.84	0.93
ND35	TA	0.54	0.67	0.67	1.20
GE17	P	0.61	0.34	0.59	1.02
RS3	MAFIC DYKE	1.23	0.41	0.66	1.18

ELECTRON MICROPROBE ANALYSIS

KIC OLIVINE DATA - PIPE SAMPLE

Sample	ND8	ND8	ND8	ND8	ND8	ND8	ND8	ND8	ND8	ND8	ND8
Analysis	1	2	3	4	5	6	7	8	9	10	11
SiO2	39.87	39.314	39.905	39.628	40.012	38.602	38.159	40.253	37.603	31.873	38.449
TiO2	0	0	0	0	0	0	0	0	0	0	0
Al2O3	0.047	0.022	0.001	0.036	0	0	0.021	0.007	0.033	0.007	0.025
FeO	14.791	14.898	14.373	16.072	14.629	25.243	28.127	14.968	27.837	55.665	23.882
MnO	0.205	0.16	0.196	0.207	0.224	0.316	0.679	0.251	0.971	4.87	0.433
MgO	43.46	43.744	43.753	42.781	44.377	36.629	34.052	44.112	34.372	8.699	37.232
CaO	0.196	0.315	0.147	0.371	0.315	0.263	0.193	0.273	0.09	0.232	0.138
Na2O	0	0.01	0.016	0	0	0.021	0.02	0	0.004	0.122	0.137
K2O	0	0	0	0	0	0	0	0	0	0	0
Cr2O3	0.001	0.003	0.03	0.001	0.011	0	0.014	0.019	0.01	0.025	0.008
NiO	0.141	0.105	0.064	0.078	0.097	0.051	0.075	0.152	0.064	0.03	0.065
Total	98.711	98.571	98.485	99.174	99.665	101.125	101.34	100.035	100.984	101.523	100.369

KIC OLIVINE DATA - GABBRO XENOLITH

Sample	DRK72	DRK72	DRK72	DRK72	DRK72	DRK72	DRK72	DRK72
Analysis	12	13	14	15	16	17	18	19
SiO2	39.275	39.244	38.779	39.199	38.654	39.08	39.184	38.808
TiO2	0	0	0	0	0	0	0	0
Al2O3	0.03	0.012	0.039	0.025	0.131	0.01	0	0.022
FeO	20.358	20.642	20.722	20.387	20.304	20.603	20.514	20.563
MnO	0.378	0.382	0.408	0.303	0.375	0.341	0.298	0.348
MgO	41.051	40.139	40.541	40.504	40.501	40.364	39.719	39.918
CaO	0.097	0.16	0.063	0.16	0.258	0.223	0.202	0.167
Na2O	0.005	0.035	0.014	0.021	0.077	0	0.059	0.045
K2O	0	0	0	0	0	0	0	0
Cr2O3	0.012	0.035	0.022	0.02	0.015	0	0.005	0.001
NiO	0.073	0.017	0.06	0.058	0.071	0.068	0	0.058
Total	101.279	100.666	100.648	100.677	100.386	100.689	99.981	99.93

KIC OLIVINE DATA - GABBRO XENOLITH

SAMPLE	DRK72	DRK72	DRK72	DRK72	DRK72	DRK72	DRK72	DRK72	DRK72	DRK72	DRK72	DRK72	DRK72	DRK72
ANALYSIS	1	2	3	4	5	6	7	8	9	10	11	12	13	14
SiO2	38.38	38.52	38.57	38.31	38.93	39.00	38.74	36.50	38.79	39.16	39.16	39.55	38.41	37.91
TiO2	0.03	0.03	0.05	0.04	0.05	0.03	0.03	0.04	0.05	0.02		0.04	0.03	0.03
Al2O3	0.04		0.03	0.08		0.03	0.02	1.07	0.02		0.04	0.08	0.02	0.07
Cr2O3														
FeO	20.90	20.45	20.62	19.84	20.39	20.52	21.54	20.21	22.17	20.34	20.46	20.18	20.36	20.80
MnO	0.32	0.34	0.36	0.29	0.36	0.32	0.33	0.28	0.43	0.38	0.38	0.31	0.33	0.40
MgO	40.59	40.80	40.89	40.24	40.93	40.71	40.14	36.19	40.00	41.24	41.04	40.90	40.94	40.61
CaO	0.13	0.17	0.16	0.22	0.12	0.21	0.12	0.89	0.17	0.13	0.12	0.15	0.19	0.17
Na2O			0.06	0.67				0.28		0.03	0.04	0.09	0.03	
K2O				0.24				0.02	0.02			0.02		
NiO	0.07	0.03	0.08	0.04	0.05	0.05		0.02	0.08	0.04	0.11	0.03	0.06	0.04
TOTAL	100.47	100.37	100.84	99.97	100.86	100.88	100.93	95.50	101.73	101.35	101.37	101.35	100.38	100.05

KIC OLIVINE DATA - GABBRO XENOLITH

SAMPLE	DRK72	DRK72	DRK72	DRK72	DRK72	DRK72	DRK72	DRK72	DRK72	DRK72
ANALYSIS	15	16	17	18	19	20	21	22	23	24
SiO2	38.07	39.07	39.18	38.80	39.54	39.37	39.57	39.35	39.10	38.88
TiO2	0.03	0.12		0.05	0.03	0.05	0.04	0.04	0.03	0.03
Al2O3		3.13	0.03	0.44	0.04	0.05	0.02	0.07	0.02	
Cr2O3	0.02	0.02				0.02		0.03		0.03
FeO	21.27	18.05	20.89	21.76	20.70	20.53	20.50	20.09	22.00	20.92
MnO	0.46	0.32	0.46	0.46	0.40	0.38	0.32	0.33	0.45	0.33
MgO	39.98	35.60	39.90	39.26	40.73	40.61	40.44	40.37	39.87	40.62
CaO	0.17	2.87	0.41	0.76	0.16	0.13	0.09	0.20	0.12	0.18
Na2O		0.88	0.03	0.10		0.04		0.04	0.03	0.03
K2O								0.02		
NiO		0.02	0.10	0.05	0.06	0.09		0.05		0.04
TOTAL	100.02	100.09	101.01	101.68	101.68	101.28	101.00	100.59	101.63	101.08

KIC PYROXENE DATA - PIPE SAMPLES

Sample	DRK72	DRK72	DRK72	DRK72	DRK72	DRK72	DRK72	DRK72	DRK72	DRK72
Analysis	1	2	3	4	5	6	7	8	9	10
Location	gr1pt1	gr1pt2	gr1pt3	gr1pt4	gr1pt5	gr2pt1	gr2pt2	gr2pt3	gr2pt4	gr2pt5
Mineral	CPX	CPX	CPX	CPX	CPX	CPX	CPX	CPX	CPX	CPX
SiO2	50.86	50.35	50.40	49.74	50.97	51.03	50.45	51.18	52.05	52.21
TiO2	1.32	1.19	0.91	1.26	0.73	0.87	1.36	1.00	0.82	0.72
Al2O3	6.02	5.36	5.81	5.71	5.30	5.44	5.84	4.73	4.30	4.59
FeO	5.62	5.49	5.61	5.85	5.45	5.38	6.13	5.60	6.00	5.66
MnO	0.12	0.04	0.14	0.09	0.14	0.11	0.15	0.09	0.07	0.06
MgO	14.72	15.47	15.27	14.81	15.32	15.25	14.81	14.94	15.83	16.21
CaO	21.80	21.49	21.41	21.83	21.73	21.71	21.33	21.60	21.68	21.58
Na2O	0.48	0.48	0.53	0.44	0.59	0.50	0.46	0.63	0.34	0.30
Cr2O3	0.18	0.12	0.13	0.27	0.16	0.10	0.37	0.14	0.06	0.10
K2O			0.01				0.01	0.01		
Total	101.13	99.99	100.23	99.98	100.38	100.38	100.91	99.91	101.15	101.43

KIC PYROXENE DATA - PIPE SAMPLES

Sample	ND5	ND5	ND5	ND8	ND8	ND8	ND8	ND8	ND8
Analysis	11	14	15	16	17	18	19	20	21
Location	gr1pt1	gr3pt2	gr3pt3	gr1pt1	gr1pt2	gr1pt3	gr1pt4	gr4pt1	gr6pt1
Mineral	CPX	CPX	CPX	CPX	CPX	CPX	CPX	CPX	CPX
SiO2	50.62	49.10	51.91	49.76	49.70	50.06	49.97	48.63	52.72
TiO2	1.19	1.73	0.89	1.31	1.58	1.09	1.40	1.57	
Al2O3	4.17	5.30	3.19	8.01	7.83	7.15	7.72	7.84	0.46
FeO	12.34	11.39	12.33	5.20	4.82	4.87	5.26	5.88	11.57
MnO	0.55	0.41	0.47	0.07	0.14	0.12	0.12	0.05	0.51
MgO	10.76	11.84	10.21	14.44	14.37	14.58	14.21	13.40	11.27
CaO	18.31	17.64	19.41	21.79	21.60	21.89	21.78	22.25	22.72
Na2O	1.26	0.95	1.49	0.33	0.51	0.36	0.39	0.35	0.81
Cr2O3	0.02	0.09	0.07	0.08	0.15	0.37	0.08	0.31	
K2O	1.79	2.28	1.00		0.02		0.01	0.01	
Total	100.99	100.73	100.97	100.99	100.72	100.49	100.94	100.29	100.06

KIC PYROXENE DATA - PIPE SAMPLES

Sample	ND12	ND12	ND12	ND12	ND12	ND12	ND17	ND17	ND19	ND19	ND25	ND25	ND28	ND28	ND28
Analysis	22	23	24	25	26	27	28	29	30	31	32	33	34	35	36
Location	gr1pt1	gr1pt2	gr1pt3	gr1pt4	gr2pt1	gr2pt2	gr1pt1	gr1pt1	gr1pt1	gr5pt1	gr1pt1	gr1pt2	gr1pt1	gr1pt4	gr2pt2
Mineral	CPX	CPX	CPX	CPX	CPX	CPX	CPX	CPX	CPX	CPX	CPX	CPX	CPX	CPX	CPX
SiO2	50.31	50.60	50.10	51.02	47.66	47.87	48.86	48.26	48.24	49.17	52.51	52.32	49.49	53.01	48.02
TiO2	0.77	0.60	0.68	0.62	2.29	2.37	2.19	2.26	1.87	2.72	0.07	0.00	0.93	0.13	2.13
Al2O3	7.84	7.59	7.50	6.53	6.95	7.05	6.36	8.23	6.90	6.69	0.55	0.56	4.19	1.22	6.97
FeO	4.70	4.38	4.73	4.35	7.35	7.73	6.96	7.36	7.86	6.67	9.58	10.05	15.72	14.56	12.45
MnO	0.02	0.01	0.11	b.d	0.19	0.17	0.27	0.16	0.07	0.18	0.97	0.96	0.63	0.79	0.40
MgO	15.31	15.12	14.95	15.52	12.83	12.47	13.23	12.41	12.58	12.72	13.56	13.49	9.84	9.40	10.49
CaO	20.48	20.61	20.46	20.71	20.80	20.89	21.11	21.83	21.47	21.55	21.06	20.82	19.29	21.93	19.03
Na2O	0.56	0.48	0.58	0.44	0.89	0.77	1.47	0.73	0.72	1.48	0.38	0.40	1.24	0.76	1.39
Cr2O3	0.34	0.42	0.37	0.49	0.00	0.00	0.03	0.09	0.04	0.05	0.04	0.01	0.11	0.10	0.05
K2O	0.05	0.04	0.04	0.03	0.01	0.02	0.06		0.01	0.01			0.43	0.07	0.09
Total	100.37	99.85	99.50	99.70	98.97	99.33	100.55	101.32	99.74	101.26	98.72	98.62	101.87	101.97	101.02

KIC PYROXENE DATA - PIPE SAMPLE

SAMPLE	RS15	RS15	RS15	RS15	RS15	RS15	RS15	RS15	RS15	RS15	RS15	RS15	RS15
ANALYSIS	1	2	3	4	5	6	7	8	9	10	11	12	13
SiO2	49.00	50.15	50.64	49.79	49.90	49.36	45.70	48.49	44.74	48.38	44.56	46.00	48.58
TiO2	0.52	0.57	0.37	0.62	0.15	0.30	2.18	0.88	1.38	0.21	0.92	0.78	0.22
Al2O3	1.59	1.98	1.24	2.02	1.71	1.73	6.15	4.45	6.62	1.70	6.25	4.88	1.75
Cr2O3			0.03					0.15	0.16		0.74	0.75	
FeO	12.77	12.24	13.03	12.85	14.85	13.55	14.78	6.44	15.08	14.77	16.81	15.18	15.54
MnO	0.58	0.63	0.68	0.52	1.11	1.12	0.95	0.29	0.86	1.36	0.76	0.79	1.05
MgO	11.39	11.35	11.19	11.14	8.86	9.94	9.44	13.18	9.60	9.43	8.09	8.69	9.48
CaO	21.78	21.92	22.18	21.95	21.73	21.98	18.07	24.45	17.58	21.68	16.56	19.38	21.99
Na2O	0.84	1.21	1.10	0.96	1.67	1.42	2.21	0.90	2.30	1.44	4.93	2.16	1.47
K2O					0.02	0.02	0.49		0.48	0.03	0.53	0.30	
NiO													
TOTAL	98.48	100.06	100.47	99.85	100.00	99.42	99.97	99.24	98.80	99.00	100.15	98.91	100.09

KIC PYROXENE DATA - PIPE SAMPLE

SAMPLE	RS15	RS15	RS15	RS15	RS15	RS15	RS15	RS15	RS15	RS15	RS15	RS15	RS15
ANALYSIS	24	25	26	27	28	29	30	31	32	33	34	35	36
SiO2	45.53	52.13	49.74	46.94	49.40	49.44	48.73	47.87	42.94	49.68	49.20	49.42	45.11
TiO2	1.64	0.11	0.10	0.63	0.14	0.18	0.81	0.94	1.56	0.30	0.31	0.27	2.38
Al2O3	5.61	0.76	1.60	1.73	1.73	2.08	5.25	4.81	8.00	1.69	1.78+	1.67	7.25
Cr2O3	0.02	0.02					0.41	0.05	0.20				0.02
FeO	16.45	6.94	14.15	21.84	15.11	13.95	4.30	9.42	18.07	13.76	14.14	13.43	10.71
MnO	1.05	0.40	1.42	1.18	1.36	1.23	0.11	0.48	0.71	0.95	0.97	0.99	0.45
MgO	9.21	14.83	9.45	7.38	8.61	9.48	15.44	11.37	8.74	9.70	9.51	9.58	11.25
CaO	18.00	24.84	21.87	18.45	21.23	21.29	23.81	22.98	15.34	22.16	22.17	22.14	20.48
Na2O	2.25	0.61	1.51	1.54	1.80	1.72	0.36	1.27	2.69	1.43	1.50	1.42	1.78
K2O	0.58			0.02	0.04	0.03			0.82	0.02	0.04	0.02	0.27
NiO													
TOTAL	100.34	100.65	99.84	99.71	99.42	99.40	99.22	99.64	99.07	99.69	99.62	98.94	99.70

KIC PYROXENE DATA - PIPE SAMPLE

SAMPLE	RS15	RS15	RS15	RS15	RS15	RS15	RS15	RS15	RS15	RS15
ANALYSIS	14	15	16	17	18	19	20	21	22	23
SiO2	48.25	51.29	47.91	48.49	49.17	49.91	49.37	49.58	45.31	50.31
TiO2	0.20	0.08	0.15	0.33	0.37	0.50	0.46	0.31	1.60	0.17
Al2O3	1.73	3.41	7.33	1.79	1.45	1.60	1.66	1.92	5.85	1.75
Cr2O3	0.04		0.02						0.03	
FeO	14.77	12.64	10.31	14.32	14.15	13.58	12.39	15.65	16.25	13.83
MnO	1.15	0.69	0.69	1.03	0.70	0.64	0.65	1.00	0.82	1.22
MgO	9.17	8.71	6.78	9.52	10.29	11.41	10.83	8.61	8.83	9.56
CaO	21.75	18.68	17.94	21.90	22.36	22.06	22.32	21.55	18.02	22.02
Na2O	1.52	4.51	6.93	1.45	0.94	0.76	1.35	1.74	2.27	1.43
K2O	0.02	0.03	0.05		0.02	0.02		0.02	0.51	0.06
NiO										
TOTAL	98.60	100.04	98.11	98.83	99.45	100.49	99.03	100.38	99.49	100.35

KIC PYROXENE DATA - PIPE SAMPLE

SAMPLE	RS15	RS15	RS15	RS15	RS15	RS15	RS15	RS15	RS15
ANALYSIS	37	38	39	40	41	42	43	44	45
SiO2	46.13	43.84	49.38	45.36	46.32	49.35	45.94	47.27	45.53
TiO2	1.85	2.35	0.45	2.29	1.60	0.89	1.71	1.10	1.47
Al2O3	6.42	7.94	2.36	6.67	5.18	2.73	6.58	4.66	5.18
Cr2O3		0.05					0.14	0.18	0.19
FeO	9.64	15.05	15.56	10.90	11.96	11.09	12.90	14.28	14.92
MnO	0.47	0.70	0.94	0.60	0.65	0.89	0.77	0.89	0.90
MgO	11.79	10.05	9.08	10.94	10.52	11.28	9.92	9.37	9.48
CaO	20.30	16.46	20.81	20.66	20.30	22.80	19.19	19.79	18.80
Na2O	1.71	2.38	1.64	1.81	1.86	1.17	2.01	1.98	2.00
K2O	0.19	0.69	0.19	0.17	0.31	0.05	0.29	0.26	0.74
NiO									
TOTAL	98.51	99.51	100.41	99.40	98.70	100.25	99.45	99.78	99.21

KIC PYROXENE DATA - GRANULAR SYENITE

SAMPLE	VH10	VH10	VH10	VH10	VH10	VH10	VH10	VH10	RS9	RS9	RS9	RS9	RS9
ANALYSIS	1	2	3	4	5	6	7	8	1	2	3	4	5
SiO2	50.51	49.68	50.05	49.80	49.41	49.72	50.12	49.51	50.64	49.17	48.27	49.91	50.80
TiO2	0.33	0.30	0.29	0.24	0.31	0.28	0.48	0.27	0.17	0.39	0.33	0.27	0.17
Al2O3	1.04	1.12	0.93	0.84	1.39	1.00	1.70	1.35	0.70	1.42	1.29	1.61	0.75
Cr2O3													
FeO	20.24	20.48	19.73	20.09	19.87	19.45	16.16	19.60	17.54	22.78	21.20	17.90	17.95
MnO	1.44	1.38	1.43	1.45	1.29	1.40	0.85	1.17	1.09	1.28	1.06	0.96	1.28
MgO	5.33	4.76	5.24	5.19	5.48	5.37	8.14	5.41	7.45	3.56	4.74	7.09	7.28
CaO	19.59	18.88	20.02	18.87	19.98	19.66	21.27	20.12	21.64	20.42	20.44	21.34	21.22
Na2O	2.23	2.58	1.97	2.51	1.89	2.13	1.06	1.98	1.24	1.69	1.66	1.19	1.35
K2O													
NiO													
TOTAL	100.71	99.18	99.66	98.99	99.62	99.01	99.78	99.41	100.47	100.71	98.99	100.27	100.80

KIC PYROXENE DATA - GREY SYENITE AND GRANULAR SYENITE

SAMPLE	RS14	RS14	RS14	RS14	RS14	RS14	RS14	RS7	RS7	RS7	RS7	RS7	RS7	RS7
ANALYSIS	1	2	3	4	5	6	7	1	2	3	4	5	6	7
SiO2	52.23	50.89	51.18	50.69	50.85	51.09	50.35	50.54	49.52	49.98	49.79	49.60	49.50	49.32
TiO2	0.11	0.38	0.18	0.37	0.15	0.17	0.15	0.08	0.17	0.16	0.13	0.24	0.24	0.28
Al2O3	0.39	1.54	0.72	1.38	0.81	0.93	0.97	1.35	1.46	1.52	1.04	0.92	1.11	1.03
Cr2O3														
FeO	11.69	13.78	14.69	14.97	13.93	14.44	13.69	20.23	17.66	18.70	23.36	24.52	24.46	25.59
MnO	0.79	0.70	0.86	0.79	0.77	0.84	0.75	1.39	1.01	1.14	1.41	1.49	1.49	1.37
MgO	1.86	9.87	9.70	9.08	9.85	9.20	9.99	5.13	7.41	6.42	3.26	2.06	2.12	1.78
CaO	22.98	22.61	22.70	22.45	22.49	22.84	22.88	19.26	21.20	21.00	17.24	16.20	16.23	15.31
Na2O	0.63	0.84	0.73	0.91	0.81	0.84	0.80	2.61	0.96	1.28	3.70	4.16	4.28	4.78
K2O														
NiO														
TOTAL	90.68	100.61	100.76	100.64	99.66	100.35	99.58	100.59	99.39	100.20	99.93	99.19	99.43	99.46

KIC PYROXENE DATA - PORPHYRITIC MELASYENITE

SAMPLE	GE7	GE7	GE7	GE7	GE7	GE7	GE7	GE7	GE7	GE7	GE7	GE7	GE7	GE7
ANALYSIS	15	16	17	18	19	20	21	22	23	24	25	26	27	28
SiO2	49.26	49.27	49.79	49.97	49.67	50.10	49.66	49.87	49.99	50.24	49.36	49.85	50.63	49.38
TiO2	0.21	0.22	0.37	0.21	0.29	0.21	0.27	0.31	0.17	0.17	0.45	0.23	0.19	0.18
Al2O3	1.13	1.42	0.97	1.04	1.04	1.19	1.11	1.03	0.93	1.06	3.13	1.06	0.97	1.03
Cr2O3														
FeO	21.85	21.61	23.07	20.77	21.91	21.91	22.11	22.00	20.27	20.70	21.81	21.12	19.92	21.19
MnO	1.51	1.46	1.19	1.29	1.40	1.38	1.43	1.40	1.40	1.46	1.22	1.37	1.23	1.44
MgO	3.73	3.87	2.92	5.02	3.35	3.09	3.33	3.52	5.27	5.01	2.69	4.40	5.37	4.47
CaO	18.09	17.62	13.65	19.94	17.00	17.16	16.59	16.68	20.10	20.01	14.37	18.19	20.37	19.54
Na2O	3.17	3.37	5.60	1.85	3.54	3.66	3.59	3.75	1.72	1.80	5.49	2.29	1.71	2.00
K2O			0.40								0.30			
NiO														
TOTAL	98.97	98.86	97.61	100.11	98.22	98.72	98.11	98.58	99.87	100.47	98.83	98.53	100.41	99.25

KIC PYROXENE DATA - FOYAITE

SAMPLE	VH1	VH1	VH1	VH1	VH1	VH1	VH1	VH1	VH1	VH1	VH1	VH1
ANALYSIS	1	2	3	4	5	6	7	8	9	10	11	12
SiO2	50.44	49.51	50.22	49.38	49.88	49.70	50.15	49.42	49.96	49.25	49.75	49.96
TiO2	0.16	0.13	0.13	0.17	0.14	0.15	0.16	0.20	0.23	0.18	0.11	0.17
Al2O3	1.23	1.17	1.17	1.20	1.01	1.06	1.04	1.03	1.08	1.03	0.99	1.03
Cr2O3												
FeO	21.42	22.28	23.16	23.63	24.26	21.13	22.31	23.75	23.24	22.24	21.79	21.40
MnO	1.65	1.73	1.66	1.60	1.63	1.75	1.69	1.38	1.56	1.72	1.62	1.57
MgO	4.04	3.24	2.92	2.70	2.31	4.11	3.44	2.66	2.72	3.26	3.46	3.93
CaO	15.36	15.43	14.21	13.84	14.56	16.25	14.74	13.42	14.69	16.17	15.14	15.06
Na2O	4.70	4.47	5.32	5.27	5.03	4.13	5.15	5.88	5.00	4.12	4.72	4.83
K2O												
NiO												
TOTAL	99.00	97.96	98.79	97.79	98.82	98.28	98.68	97.74	98.48	97.97	97.58	97.95

KIC PYROXENE DATA - GABBRO XENOLITH

SAMPLE	DRK72	DRK72	DRK72	DRK72	DRK72	DRK72	DRK72	DRK72	DRK72	DRK72	DRK72	DRK72	DRK72	DRK72
ANALYSIS	1	2	3	4	5	6	7	8	9	10	11	12	13	14
SiO2	45.22	46.80	46.90	47.44	47.03	47.41	47.47	47.85	49.88	49.74	47.61	47.20	46.48	44.34
TiO2	3.05	3.17	2.90	2.79	2.58	2.07	1.85	1.58	1.15	1.02	1.52	1.76	1.90	3.50
Al2O3	7.44	7.37	7.09	6.88	6.58	5.87	5.87	5.23	5.03	4.64	5.31	5.30	5.41	7.89
Cr2O3	0.02				0.03	0.03		0.03	0.08	0.09	0.03	0.03	0.04	
FeO	6.02	6.77	6.28	6.79	6.51	6.32	5.99	5.78	5.52	5.48	5.93	6.18	6.24	6.32
MnO	0.12	0.10	0.10	0.15	0.14	0.14	0.14	0.12	0.10	0.13	0.10	0.19	0.15	0.14
MgO	12.93	12.78	13.16	13.34	13.54	14.11	14.20	14.60	15.11	15.24	14.60	14.52	14.16	12.60
CaO	20.02	21.87	21.98	21.91	22.07	21.91	21.76	21.80	22.20	22.06	21.86	21.89	21.96	22.27
Na2O	0.98	0.77	0.89	0.67	0.68	0.56	0.53	0.48	0.46	0.40	0.48	0.48	0.60	0.81
K2O	0.02													
NiO		0.07	0.20	0.02	0.03				0.04					0.05
TOTAL	95.83	99.71	99.32	100.00	99.19	98.43	97.83	97.42	99.58	98.81	97.45	97.56	96.95	97.92

KIC PYROXENE DATA - GABBRO XENOLITH

SAMPLE	DRK72	DRK72	DRK72	DRK72	DRK72	DRK72	DRK72	DRK72	DRK72	DRK72	DRK72	DRK72	DRK72	DRK72
ANALYSIS	15	16	17	19	20	21	22	23	24	25	26	27	28	29
SiO2	43.58	43.51	44.12	49.54	42.04	45.44	46.29	47.21	47.24	45.27	44.92	49.33	46.56	46.45
TiO2	3.99	3.91	3.21	1.95	4.29	3.23	3.29	2.78	2.77	3.21	3.39	1.71	3.16	3.19
Al2O3	8.64	8.55	8.75	5.70	13.06	8.11	7.75	6.05	6.41	8.14	7.83	4.30	7.15	7.19
Cr2O3	0.03	0.05		0.02	0.04	0.04		0.02		0.03	0.05		0.03	0.03
FeO	6.41	6.51	6.31	5.99	9.94	6.66	6.57	6.82	6.64	6.56	6.51	6.55	6.06	6.31
MnO	0.11	0.11	0.18	0.13	0.12	0.20	0.07	0.15	0.17	0.14	0.11	0.14	0.14	0.15
MgO	12.15	11.79	12.96	12.77	12.17	12.71	12.43	13.58	13.51	13.30	12.40	12.86	12.68	12.79
CaO	22.13	22.27	21.29	22.64	13.75	21.26	22.01	21.87	21.86	21.08	22.30	23.77	22.27	21.94
Na2O	0.95	1.18	1.37	1.12	3.07	1.09	0.92	0.72	0.68	0.85	0.84	0.61	1.20	1.17
K2O			0.04	0.03	0.40	0.08	0.04			0.03	0.02	0.03		
NiO					0.03		0.02			0.03	0.02			
TOTAL	98.01	97.88	98.24	99.89	98.91	98.82	99.40	99.20	99.29	98.64	98.39	99.31	99.25	99.23

KIC PYROXENE DATA - GABBRO XENOLITH

SAMPLE	DRK72	DRK72	DRK72	DRK72	DRK72	DRK72	DRK72	DRK72	DRK72	DRK72	DRK72	DRK72	DRK72	DRK72
ANALYSIS	30	31	32	33	34	35	36	37	38	39	40	41	42	43
SiO2	47.37	47.43	48.18	49.81	49.95	49.93	49.59	47.08	45.55	48.37	50.44	49.78	50.79	49.92
TiO2	2.58	2.16	1.85	0.71	0.78	0.85	0.88	1.64	3.39	1.05	0.90	1.22	0.83	1.02
Al2O3	6.39	5.85	5.58	4.65	4.60	4.61	4.75	5.83	7.95	7.03	4.96	5.37	4.56	4.92
Cr2O3	0.02	0.02	0.04	0.17	0.12	0.03	0.14	0.08	0.02	0.12	0.15	0.06	0.11	0.12
FeO	6.25	6.13	6.04	5.68	5.67	6.07	5.74	5.57	6.33	5.62	5.34	5.72	5.34	5.65
MnO	0.13	0.15	0.12	0.15	0.08	0.17	0.17	0.11	0.15	0.14	0.15	0.16	0.11	0.18
MgO	13.37	13.68	14.00	15.17	15.17	15.11	14.93	14.21	12.32	15.11	15.22	14.82	15.30	15.10
CaO	21.89	21.98	21.97	22.15	22.15	21.93	22.21	21.06	22.21	19.63	22.16	22.11	22.12	21.90
Na2O	1.03	0.82	0.81	0.40	0.40	0.43	0.56	0.86	1.13	1.77	0.39	0.44	0.43	0.43
K2O				0.10			0.02							
NiO	0.02			0.10				0.02			0.06		0.02	0.05
TOTAL	99.06	98.23	98.60	99.09	98.92	99.14	98.99	96.47	99.05	98.85	99.77	99.68	99.61	99.29

KIC PYROXENE DATA - GABBRO XENOLITH

SAMPLE	DRK72	DRK72	DRK72	DRK72	DRK72	DRK72	DRK72	DRK72	DRK72	DRK72	DRK72	DRK72
ANALYSIS	44	45	46	47	48	49	50	51	52	53	54	55
SiO2	44.91	45.65	47.29	46.76	47.75	48.10	48.43	49.08	49.39	48.94	49.43	49.70
TiO2	1.06	1.22	1.05	1.13	0.87	0.94	0.97	0.85	0.85	1.50	1.34	1.10
Al2O3	5.16	5.49	5.10	6.04	4.72	4.97	4.91	4.79	4.87	5.49	5.50	5.54
Cr2O3	0.21	0.21	0.16	0.11	0.13	0.16	0.12	0.17	0.12	0.11	0.22	0.20
FeO	5.90	5.76	5.74	5.79	5.63	5.70	5.80	5.45	5.63	5.75	5.71	5.54
MnO	0.13	0.08	0.12	0.13	0.15	0.13	0.11	0.17	0.12	0.15	0.14	0.08
MgO	14.54	14.43	14.83	14.10	15.20	14.86	14.86	15.04	15.05	14.34	14.54	14.57
CaO	21.70	21.99	22.17	21.70	22.06	22.27	21.92	22.14	22.28	22.44	22.25	22.28
Na2O	0.46	0.46	0.42	0.59	0.37	0.40	0.43	0.43	0.36	0.78	0.44	0.36
K2O						0.02						
NiO	0.05	0.07	0.06	0.05	0.02	0.03			0.04		0.02	
TOTAL	94.13	95.37	96.94	96.41	96.90	97.58	97.57	98.14	98.71	99.50	99.60	99.37

KIC AMPHIBOLE DATA - PIPE SAMPLES

Sample	ND5	ND5	ND5	ND8	ND8	ND17	ND17	ND17	ND17	ND17	ND17
Analysis	1	2	3	4	5	6	7	8	9	10	11
SiO2	41.93	41.73	41.88	40.95	42.17	40.67	40.63	40.60	41.63	41.72	40.56
TiO2	4.54	3.99	3.77	3.88	4.07	3.47	3.42	3.18	3.87	2.50	3.19
Al2O3	11.22	11.19	11.45	10.71	11.36	11.19	11.10	11.17	11.11	11.33	10.62
FeO	18.72	19.34	19.24	22.61	17.96	21.71	20.77	21.79	20.36	18.32	23.19
MnO	0.54	0.58	0.65	0.66	0.56	0.75	0.67	0.71	0.71	0.55	0.90
MgO	8.39	8.22	7.71	7.65	8.39	6.70	7.12	6.74	7.43	9.14	6.20
CaO	10.70	10.73	10.39	10.02	10.78	10.44	10.51	10.52	10.68	10.67	10.35
Na2O	3.21	3.43	3.48	3.12	3.21	3.19	3.35	3.19	3.14	3.27	3.15
Cr2O3		0.02		0.01	0.01	0.02	0.01	0.01	0.01		0.01
K2O	1.30	1.31	1.37	1.40	1.27	1.44	1.39	1.46	1.45	1.42	1.58
Total	100.55	100.53	99.93	101.01	99.77	99.57	98.98	99.36	100.41	98.91	99.74

KIC AMPHIBOLE DATA - PIPE SAMPLES

Sample	ND19	ND19	ND19	ND19	ND19	ND19	ND19	ND19	ND19	ND28
Analysis	12	13	14	15	16	17	18	19	20	21
SiO2	41.67	41.27	41.28	41.34	40.88	41.54	41.70	41.16	41.32	40.56
TiO2	3.83	3.92	3.60	2.93	2.74	4.45	4.38	2.79	2.18	1.64
Al2O3	11.42	11.61	11.45	11.36	11.17	11.09	11.18	11.08	11.66	11.62
FeO	19.37	19.20	19.88	20.77	20.64	18.91	19.75	23.23	21.08	19.26
MnO	0.68	0.77	0.81	0.79	0.89	0.50	0.57	0.67	0.80	0.36
MgO	8.51	8.30	7.95	7.55	7.63	8.55	8.05	5.89	7.40	8.99
CaO	10.69	10.68	10.69	10.63	10.71	10.66	10.67	10.24	10.56	13.25
Na2O	3.41	3.33	3.17	3.17	3.32	3.28	3.47	3.24	3.16	3.06
Cr2O3	0.05	0.00		0.02		0.01			0.02	0.20
K2O	1.41	1.37	1.49	1.54	1.51	1.43	1.37	1.58	1.66	0.62
Total	101.03	100.47	100.31	100.08	99.48	100.40	101.14	99.87	99.82	99.56

KIC AMPHIBOLE DATA - GRANULAR SYENITE AND PORPHYRITIC MELASYENITE

SAMPLE	VH10	VH10	VH10	VH10	VH10	VH10	GE7	GE7	GE7	GE7	GE7	GE7	GE7
ANALYSIS	17	18	19	20	21	22	8	9	10	11	12	13	14
SiO2	38.57	38.90	38.26	38.31	39.10	39.07	39.79	39.79	38.80	38.86	39.48	38.97	38.03
TiO2	3.31	3.38	3.36	2.40	2.29	2.11	1.94	1.93	2.15	4.61	2.75	2.51	2.63
Al2O3	11.10	10.70	10.81	10.91	10.46	9.98	10.04	9.76	9.81	11.02	10.43	10.03	9.59
Cr2O3													
FeO	24.72	23.88	25.66	26.65	26.52	26.68	26.07	26.44	27.63	19.36	23.52	26.15	27.11
MnO	1.00	0.80	1.09	1.13	1.10	1.12	1.14	1.08	1.31	0.97	1.10	1.18	1.21
MgO	5.05	5.50	4.43	4.02	4.51	4.51	4.78	4.67	3.97	8.26	6.39	4.41	4.08
CaO	10.35	10.53	10.23	9.99	9.77	9.74	10.03	9.34	9.50	9.69	10.01	9.94	9.62
Na2O	3.04	3.01	3.08	3.32	3.25	3.38	3.36	3.49	3.58	3.83	3.56	3.44	3.66
K2O	1.45	1.40	1.54	1.63	1.56	1.60	1.28	1.52	1.37	1.19	1.26	1.28	1.32
TOTAL	98.59	98.10	98.46	98.36	98.56	98.19	98.44	98.03	98.13	97.80	98.51	97.92	97.26

KIC AMPHIBOLE DATA - QUARTZ SYENITE AND GRANULAR SYENITE

SAMPLE	GE1	GE1	GE1	GE1	GE1	GE1	GE1	GE1	GE1	GE1	RS9	RS9	RS9
ANALYSIS	1	2	3	4	5	6	7	8	9	10	6	7	8
SiO2	42.57	42.48	42.51	42.44	42.50	42.54	42.84	43.42	43.31	43.07	38.68	40.18	38.59
TiO2	1.92	2.02	1.89	2.00	2.11	1.89	1.99	1.50	1.78	2.11	2.26	2.60	1.44
Al2O3	7.18	7.73	7.17	7.47	7.59	7.21	7.31	6.98	7.32	7.58	11.16	10.66	11.58
Cr2O3													
FeO	25.94	26.29	26.70	26.28	25.00	27.69	27.14	27.04	26.00	25.14	26.45	22.51	26.51
MnO	0.75	0.72	0.87	0.76	0.82	0.82	0.79	0.94	0.87	0.73	0.95	0.88	0.90
MgO	6.32	6.50	5.89	6.20	6.03	5.30	5.65	5.88	6.51	6.19	4.05	6.93	4.39
CaO	9.90	10.18	10.03	10.14	10.24	9.96	9.99	9.90	10.11	10.20	10.61	10.86	10.39
Na2O	2.31	2.33	2.30	2.33	2.35	2.11	2.29	2.15	2.26	2.32	3.02	3.07	2.96
K2O	0.98	0.95	0.89	0.96	1.02	0.95	0.09	0.86	0.93	1.02	1.52	1.43	1.70
TOTAL	97.88	99.21	98.26	98.59	97.67	98.48	98.10	98.68	99.10	98.37	98.70	92.12	98.46

KIC AMPHIBOLE DATA - GRANULAR SYENITE, FOYAITE AND GREY SYENITE

SAMPLE	RS7	RS7	RS7	RS7	RS7	VH1	VH1	VH1	VH1	VH1	RS14	RS14	RS14	RS14	RS14
ANALYSIS	8	9	10	11	12	19	20	21	22	23	8	9	10	11	12
SiO2	39.26	39.11	40.35	38.81	38.68	42.59	42.27	42.07	42.20	41.75	40.01	39.16	39.18	39.53	38.89
TiO2	1.28	1.40	1.31	1.11	0.98	0.84	0.93	0.84	0.88	0.87	2.95	2.82	2.47	2.40	2.26
Al2O3	10.59	10.37	7.75	10.70	10.54	7.08	7.23	7.52	7.64	7.66	10.80	11.06	11.33	11.51	11.38
Cr2O3															
FeO	27.49	26.95	30.99	28.43	28.23	26.74	27.04	27.07	27.75	27.01	22.45	23.03	23.10	23.17	23.00
MnO	1.18	1.08	1.56	1.29	1.21	1.96	1.86	2.02	1.90	2.02	0.62	0.83	0.89	0.71	0.77
MgO	4.06	4.31	2.50	3.54	3.86	4.58	4.46	4.47	4.05	4.32	6.85	6.27	6.10	6.30	6.37
CaO	9.63	9.88	7.89	9.65	9.63	7.63	7.35	7.84	7.04	7.63	11.26	11.17		10.97	11.22
Na2O	3.32	3.27	4.25	3.28	3.41	4.65	4.74	4.49	4.97	4.46	2.68	2.67	2.69	2.67	2.75
K2O	1.64	1.58	1.67	1.48	1.61	1.56	1.59	1.54	1.59	1.50	1.33	1.53	1.54	1.57	1.58
TOTAL	98.45	97.95	98.27	98.29	98.15	97.63	97.47	97.86	98.02	97.22	98.95	98.54	87.30	98.85	98.22

KIC AMPHIBOLE DATA - MONZONITE AND MICROSYENITE

SAMPLE	GE13	GE13	GE13	GE13	GE13	GE13	GE13	GE13	GE13	VH5	VH5	VH5	VH5	VH5	VH5	VH5	VH5	VH5	VH5
ANALYSIS	10	11	12	13	14	15	16	17	8	9	10	11	12	13	14	15	16	17	
SiO2	38.09	39.43	38.01	40.79	39.38	38.45	38.73	39.66	39.14	39.54	39.05	39.17	39.61	39.27	37.46	38.88	39.44	39.22	
TiO2	3.54	3.67	3.79	4.00	3.79	3.41	4.01	4.09	6.10	3.65	3.25	2.23	3.93	2.88	4.92	1.88	3.53	3.52	
Al2O3	12.25	11.62	12.57	11.05	11.37	11.88	12.00	11.43	11.26	10.34	10.10	9.07	10.49	9.90	10.80	9.72	10.12	10.15	
Cr2O3	0.00	0.00	0.00	0.00	0.00	0.00	0.00	0.00											
FeO	24.78	21.01	22.73	16.93	22.44	23.92	22.77	20.08	16.73	25.78	26.25	27.81	24.36	26.33	23.37	27.84	25.06	25.58	
MnO	0.83	0.66	0.62	0.42	0.70	0.07	0.65	0.62	0.43	0.79	0.86	0.86	0.82	0.88	0.77	0.95	0.80	0.81	
MgO	4.31	6.82	5.63	9.76	6.04	4.99	5.90	7.53	10.27	4.49	4.00	3.88	5.00	3.85	5.51	3.59	4.54	4.17	
CaO	10.86	11.10	10.82	11.16	11.01	10.86	11.41	11.47	10.98	10.79	10.61	10.15	10.80	10.49	10.50	10.74	10.72	10.55	
Na2O	2.51	2.77	2.52	3.05	2.78	2.57	2.66	2.83	3.09	2.86	2.67	2.48	2.92	2.74	2.75	2.36	2.68	2.76	
K2O	1.69	1.41	1.66	1.05	1.39	1.55	1.69	1.54	1.02	1.47	1.52	1.28	1.20	1.44	1.07	1.65	1.39	1.48	
TOTAL	98.87	98.50	98.36	98.22	98.91	97.71	99.83	99.26	99.02	99.71	98.31	96.93	99.13	97.78	97.15	97.61	98.28	98.24	

KIC FELDSPAR DATA - PIPE SAMPLES

Sample	ND8	ND8	ND8	ND8	ND8	ND8	ND8	ND8	ND8	ND8	ND8
Analysis	1	2	3	4	5	6	7	8	9	10	11
SiO2	50.28	50.95	66.39	67.31	65.16	67.40	60.64	54.90	65.92	50.05	64.45
TiO2	0.04	0.17	0.15				0.03	0.01		0.20	
Al2O3	31.44	31.44	20.90	21.40	20.20	21.11	24.87	28.58	21.68	31.77	19.74
FeO	0.06	0.14	0.11	0.06	0.00	0.09	0.08	0.10	0.14	0.11	0.06
CaO	12.43	12.36	1.02	1.26	0.56	0.95	4.89	9.06	1.74	12.88	0.28
Na2O	4.09	4.29	10.13	10.40	5.78	10.12	8.18	6.02	9.62	3.79	5.56
K2O	0.09	0.10	1.53	0.55	8.09	1.38	0.32	0.11	0.74	0.05	8.61
Total	98.43	99.45	100.24	100.99	99.78	101.05	99.01	98.79	99.84	98.84	98.69

KIC FELDSPAR DATA - PIPE SAMPLES

Sample	ND19	ND19	ND19	ND19	ND19	ND19	ND19	ND19	ND19	ND19	ND19
Analysis	12	13	14	15	16	17	18	19	20	21	22
SiO2	66.41	66.09	65.89	64.71	66.83	65.45	60.11	67.85	44.86	66.34	65.16
TiO2	0.03	0.01	0.01		0.14	0.06	0.01	0.02	0.04	0.06	
Al2O3	21.84	22.71	22.66	19.52	21.80	20.47	25.25	21.26	34.63	21.18	22.71
FeO	0.16	0.03	0.16	0.00	0.15	0.14	0.02	0.08	0.14	0.09	0.07
CaO	1.69	2.30	2.51	0.05	1.76	0.69	5.50	1.08	0.95	0.98	2.45
Na2O	10.37	10.16	9.74	1.77	10.29	7.90	8.15	10.84	15.89	9.02	9.97
K2O	0.31	0.31	0.40	14.42	0.57	5.50	0.16	0.35	5.26	3.12	0.24
Total	100.80	101.60	101.37	100.46	101.53	100.20	99.20	101.48	101.78	100.79	100.61

KIC FELDSPAR DATA - PIPE SAMPLES

Sample	ND17	ND17	ND17	ND17	ND17	ND17	ND17	ND17	ND17	ND17	ND17	ND17
Analysis	23	24	25	26	27	28	29	30	31	32	33	34
SiO2	65.78	65.57	64.03	65.84	66.36	65.96	66.88	64.16	65.41	63.95	65.84	63.93
TiO2	0.07			0.04	0.06			0.01	0.02			0.04
Al2O3	21.98	22.12	21.95	22.74	21.81	22.20	21.95	19.92	22.31	19.51	21.91	19.79
FeO	0.12	0.09	0.04	0.11	0.15	0.12	0.18	0.09	0.10	0.21	0.08	0.12
CaO	2.05	2.09	2.25	2.34	1.58	2.01	1.67	0.36	1.97	0.10	1.80	0.32
Na2O	9.84	10.08	10.16	10.16	10.70	10.30	9.91	3.62	9.96	1.78	10.43	2.92
K2O	0.31	0.19	0.13	0.14	0.15	0.20	0.51	11.48	0.26	14.29	0.17	12.58
Total	100.15	100.13	98.55	101.37	100.81	100.80	101.09	99.63	100.04	99.82	100.24	99.70

KIC FELDSPAR DATA - PIPE SAMPLES

Sample	ND12	ND12	ND12	ND12	ND12	ND12
Analysis	42	43	44	45	46	47
SiO2	64.02	64.99	64.56	64.86	64.60	62.93
TiO2	0.01			0.01	0.04	0.02
Al2O3	20.27	22.73	22.95	22.75	22.67	22.83
FeO	0.05	0.03	0.09	0.14	0.06	0.06
CaO	0.35	1.94	2.24	2.20	2.12	2.29
Na2O	4.03	10.59	10.37	10.44	10.05	10.37
K2O	10.57	0.41	0.43	0.42	0.53	0.16
Total	99.29	100.69	100.63	100.83	100.08	98.66

KIC FELDSPAR DATA - PIPE SAMPLES

Sample	DRK72	DRK72	DRK72	DRK72	DRK72	DRK72	DRK72
Analysis	35	36	37	38	39	40	41
SiO2	48.18	47.90	48.62	50.37	49.31	42.30	48.69
TiO2	0.07	0.07	0.06	0.01	0.08		0.01
Al2O3	33.43	35.11	34.07	33.13	33.77	36.46	32.89
FeO	0.06	0.00	0.06	0.06	0.07	0.17	0.06
CaO	14.74	15.79	14.60	13.50	14.44	3.63	14.71
Na2O	2.94	2.31	2.84	3.62	3.07	14.54	2.91
K2O	0.01		0.03	0.02	0.01	4.38	0.02
Total	99.43	101.19	100.27	100.72	100.75	101.48	99.29

KIC FELDSPAR DATA - PIPE SAMPLES

Sample	ND28	ND28	ND28	ND28	ND28	ND28	ND28	ND25	ND25	ND25	ND25	ND25
Analysis	58	59	60	61	62	63	64	65	66	67	68	69
SiO2	59.82	64.14	65.72	63.52	64.88	66.23	65.00	66.37	65.28	66.39	64.67	59.80
TiO2	0.01	0.00	0.00	0.08	0.04	0.01	0.00	0.00	0.04	0.06	0.04	
Al2O3	26.16	23.80	22.48	21.34	22.14	21.89	21.61	21.19	20.76	21.40	20.25	19.33
FeO	0.12	0.13	0.09	0.09	0.12	0.11	0.09	0.11	0.12	0.12	0.07	4.69
CaO	4.91	3.08	2.26	1.59	1.86	1.43	1.83	0.89	0.75	0.93	0.30	0.38
Na2O	9.85	9.84	10.37	7.86	8.87	9.17	9.23	8.21	6.39	9.10	2.19	2.48
K2O	0.49	0.46	0.23	4.30	3.16	3.12	2.53	4.64	7.46	3.04	13.59	12.70
Total	101.35	101.44	101.15	98.77	101.08	101.96	100.30	101.40	100.79	101.04	101.12	99.38

KIC FELDSPAR DATA - PIPE SAMPLES

Sample	ND35	ND35	ND35	ND35	ND35	ND35	ND30	ND30	ND30	ND30	ND30
Analysis	70	71	72	73	74	75	76	77	78	79	80
SiO2	61.61	65.09	64.27	64.22	64.30	63.77	64.04	63.98	63.48	63.30	63.18
TiO2	0.04	0.06	0.08		0.06	0.02	0.12	0.06	0.01		0.10
Al2O3	23.93	22.45	22.44	23.10	22.94	22.84	22.43	22.73	22.64	22.09	22.11
FeO	0.04	0.23	0.05	0.15	0.16	0.10	0.04	0.24	0.09	0.15	0.07
CaO	3.78	2.31	2.19	3.07	2.79	3.07	2.46	2.41	2.52	2.16	1.97
Na2O	8.02	9.90	9.94	9.69	9.94	9.67	9.40	9.03	9.78	7.67	7.67
K2O	1.48	0.30	2.06	0.31	0.39	0.54	0.60	1.90	0.29	3.27	3.54
Total	98.91	100.34	101.02	100.53	100.59	100.02	99.08	100.34	98.81	98.63	98.63

KIC FELDSPAR DATA - PIPE SAMPLES

Sample	ND5	ND5	ND5	ND5	ND5	ND5	ND5	ND5	ND5	ND5
Analysis	48	49	50	51	52	53	54	55	56	57
SiO2	66.25	66.27	64.52	64.69	65.30	65.29	65.48	67.58	67.43	66.56
TiO2		0.02		0.10	0.04		0.09		0.06	
Al2O3	21.90	21.88	20.30	21.71	21.75	22.13	21.78	21.17	21.37	21.37
FeO	0.07	0.10	0.06	0.05	0.06	0.07	0.12	0.06	0.09	0.07
CaO	1.25	1.28	0.54	1.38	1.44	1.63	1.34	0.59	0.75	0.86
Na2O	10.54	10.74	5.08	10.34	10.20	10.36	10.40	11.28	11.26	10.94
K2O	0.33	0.22	8.81	0.25	0.47	0.48	0.62	0.16	0.23	0.25
Total	100.34	100.51	99.30	98.53	99.26	99.93	99.83	100.84	101.17	100.05

WHOLE ROCK GEOCHEMISTRY

Kanabeam Igneous Complex Whole Rock Analysis Data (XRF and ICP-MS)

Sample	DRK-72	GE-1	GE-10	GE-11	GE-11B	GE-12	GE-13	GE-14	GE-16	GE-17	GE-2	GE-3	GE-4	GE-5	GE-6	GE-7	GE-8	GE-9
SiO2		65.879	69.776	69.253	49.477	68.112	54.702	61.686	67.562	56.69	66.445	53.666	54.714	58.984	58.323	51.907	57.276	77.026
TiO2		0.621	0.392	0.462	2.139	0.532	1.128	0.37	0.39	0.097	0.425	2.165	1.184	0.143	0.141	0.624	0.574	0.087
Al2O3		15.681	14.61	14.737	16.054	15.031	20.927	19.304	15.841	20.467	16.267	15.627	21.479	20.348	21.292	16.464	18.853	12.478
Fe2O3		4.549	3.733	3.883	13.168	4.076	5.541	3.738	3.441	5.298	3.522	10.724	5.081	5.867	4.23	12.12	6.22	1.131
MnO		0.116	0.068	0.073	0.259	0.059	0.149	0.108	0.068	0.228	0.084	0.22	0.116	0.14	0.16	0.514	0.19	0.001
MgO		0.776	0.45	0.587	5.415	0.679	1.505	0.44	0.387	0.131	0.432	3.323	1.487	0.167	0.393	1.411	1.496	0.001
CaO		1.852	1.373	1.468	6.378	1.691	5.503	1.799	1.28	0.908	1.411	5.035	5.677	1.992	1.162	4.449	3.14	0.268
Na2O		5.225	4.441	4.475	3.155	4.415	6.96	6.116	5.327	10.728	5.477	4.848	7.008	6.416	8.175	7.63	7.183	4.123
K2O		5.075	5.018	4.879	2.991		3.133	6.326	5.595	5.413	5.806	3.114	2.8	5.888	6.05	4.32	4.788	5.003
P2O5		0.227	0.14	0.183	0.965	0.204	0.451	0.112	0.109	0.039	0.133	1.277	0.454	0.055	0.073	0.562	0.282	0.018
Total		100.001	100.001	100	100.001	94.799	99.999	99.999	100	99.999	100.002	99.999	100	100	99.999	100.001	100.002	100.136
Ba	48.3	640	741	861	549	652	1210	714	826	33.7	872	1075	1001	135	81.7	328	990	158
Rb	17.9	105	240	234	404	151	106	168	253	161	236	267	41.1	174	187	173	126	264
Sr	693	163	186	237	524	161	1330	294	146	30.2	161	651	1031	385	66.4	201	444	30.8
Y	7.99	19.1	56.9	53.3	55.7	20	30.6	36	90.1	37.2	77.9	60.7	13.6	52.8	27.3	71.4	43.7	34.8
Zr		527	349	390	289	494	430	487	672	1400	601	460	393	895	619	1115	600	97.6
Nb	3.59	132	124	115	91	71.2	157	151	247	270	214	133	119	277	225	424	254	144
Th	0.3	19.7	70.4	61.9	16.9	20.4	19.5	27.7	65.6	62	56.4	29.3	11.4	61.5	33.3	45.6	25.2	46
Pb	4.09	19.7	33.9	20.8	21.1	14.6	40.5	40.3	39	37.8	33.1	15.9	30.6	53.8	78.5	15.3	28.1	19.8
Zn		67.089	54.589	53.622	192.446	52.473	90.711	65.976	59.27	95.872	55.493	167.684	71.712	93.322	89.262	196.53	108.286	6.707
Cu	6.23	5.72	1.647	1.716	3.375	5.74	11.739	2.381	5.624	3.67	2.431	8.601	14.4	79.726	7.466	42.933	10.378	2.439
Ni	124	1.4	2.03	2.811	42.335	2.01	4.665	0.001	1.686	0.88	0.001	3.371	7.32	0.001	0.001	8.135	22.898	1.889
V	55.3	16.27		17.65		19.91		5.12		1.47			43.35					
Cr	101	1.25		3.45		2.07		1.56		0.78			6.68					
Hf	0.83	9.36		8.92		8.96		0.54		12.32			6.18					
Cs	0.9	1.17		1.33		1.24		1.76		2.76			2.49					
Sc	33.2	2.72	5.2	5.8	21.2	3.28	6.6	5.5	6.3	1.47	5.2	16.3	5.34	1.3	1	5.1	4.8	-0.7
Ta	0.27	9.58		8.02		4.53		8.54		23.4			6.58					
Co	49.2	3.98		3.63		3.83		2.33		1.19			7.23					
Li																		
U	0.081	4.53	18	9.5	-11.8	2.98	-10	-9	20.1	25.4	9.5	-11.2	4.8	9.8	11.5	14.3	-9.8	29.6
Mo		5.1	4.7	3.9	10.2	7.4	8.3	6.9	6.3	15.4	7.9	8.7	10	16.6	8.3	10.3	8.7	-2.2
La	4.44	78.42		50.86		50.45		82.34		170.39			73.56					
Ce	10.4	162.61		125.52		104.36		137.58		295.83			140.56					
Pr	1.39	17.58		10.85		11.69		16.91		29.47			15.54					
Nd	6.23	52.05		31.2		36.44		50.82		73.09			46.37					
Sm	1.48	8.06		4.68		5.88		7.62		9.79			7					
Eu	0.68	1.4		0.71		1.04		2.22		0.6			2.43					
Gd	1.62	5.97		3.48		4.38		5.71		7.2			5.15					
Tb	0.25	1.08		0.65		0.75		1.01		1.43			0.84					
Dy	1.5	5.89		3.6		4		5.21		8.05			4.27					
Ho	0.29	1.35		0.86		0.88		1.19		1.91			0.93					
Er	0.79	3.74		2.52		2.43		3.11		5.56			2.45					
Tm	0.11	0.65		0.46		0.41		0.62		0.99			0.39					
Yb	0.66	4.06		3.05		2.58		3.18		6.44			2.38					
Lu	0.1	0.7		0.55		0.45		0.54		1.16			0.4					

Kanabeam Igneous Complex Whole Rock Analysis Data (XRF and ICP-MS)

Sample	RS-1	RS-10	RS-11	RS-12	RS-13	RS-14	RS-15	RS-2	RS-2A	RS-3	RS-4	RS-5	RS-6	RS-7	RS-8	RS-9
SiO2	65.922	70.851	60.939	62.942	59.747	56.893	54.478	67.366	59.078	59.979	66.156	60.83	59.802	58.267	57.259	61.953
TiO2	0.632	0.359	0.782	0.469	0.866	0.9	0.747	0.408	1.293	0.597	0.493	0.331	0.154	0.166	0.513	0.334
Al2O3	16.089	14.139	18.022	17.908	18.332	18.522	18.803	15.78	15.261	19.028	15.813	18.935	20.172	21.462	19.428	19.093
Fe2O3	4.319	3.512	6.305	5.375	6.958	7.037	6.727	3.59	7.786	7.101	4.449	3.622	4.511	4.155	5.696	3.577
MnO	0.1	0.056	0.164	0.135	0.162	0.177	0.193	0.075	0.173	0.103	0.081	0.107	0.129	0.151	0.162	0.108
MgO	0.789	0.447	0.769	0.156	0.999	2.187	2.328	0.429	1.849	0.908	0.503	0.392	0.127	0.298	1.335	0.4
CaO	1.895	1.236	2.252	0.79	2.661	4.191	3.96	1.382	3.519	2.766	1.582	1.629	0.745	1.121	2.993	1.647
Na2O	5.218	4.29	6.234	6.324	6.312	5.274	8.079	5.214	4.671	5.672	5.231	8.197	8.262	8.38	7.767	6.87
K2O	4.789	4.964	4.315	5.86	3.697	4.397	4.312	5.636	5.508	3.64	5.537	5.854	6.054	5.937	4.582	5.917
P2O5	0.247	0.145	0.217	0.042	0.266	0.422	0.374	0.119	0.863	0.207	0.154	0.102	0.045	0.063	0.267	0.101
Total	100	99.999	99.999	100.001	100	100	100.001	99.999	100.001	100.001	99.999	99.999	100.001	100	100.002	100
Ba	964	404	1875	70.9	1580	1030	849	845	917	1580	838	10.2	14.7	88.9	970	654
Rb	211	144	191	162	150	146	144	235	197	96.8	246	213	254	171	111	118
Sr	319	95.2	407	23.4	482	694	484	158	338	109	151	14.5	12.5	71.1	442	279
Y	48.2	27.1	59.5	42.3	60.3	50.7	35.5	81.3	66.4	47	97	15	19.6	23.4	41	25.2
Zr	463	328	803	580	679	581	871	642	525	724	702	294	370	563	552	474
Nb	134	100	203	188	193	185	185	221	127	193	273	179	206	222	228	122
Th	49.1	34.9	33.8	58.4	27.1	32.4	43.9	5736	30.3	25.5	61	38.2	35.1	31.7	27.7	-9.6
Pb	21.3	14	23.3	26	21	39	32.5	28.1	80.2	41.1	35.1	36.7	92.3	24.8	23.5	30.5
Zn	57.529	49.933	115.975	82.311	81.237	122.439	98.777	55.899	176.187	147.556	81.443	78.861	85.761	60.419	90.492	51.146
Cu	2.184	4.14	1.928	4.074	0.001	6.739	19.1	2.607	5.581	3.457	2.627	1.759	5.827	0.001	10.31	0.001
Ni	0.001	1.63	0.001	0.001	0.001	9.901	23.6	0.001	1.907	0.001	0.001	0.001	0.001	0.001	19.417	0.001
V	19.16	12.79				53.93	50.47			1.42						4.44
Cr	2.09	2.6				18.68	36.93			0.83						1.13
Hf	8.04	7.18				5.95	10.8			9.06						6.54
Cs	1.2	1.07				4.79	2.92			0.37						1.1
Sc	5	2.84	6.5	2.4	7.6	9.6	5.59	6.1	13.1	2.5	7.3	-0.7	-0.7	-0.8	4.8	3.5
Ta	8.15	8.49				9.73	12.4			9.32						7.25
Co	4.15	2.98				11.67	11.25			2.72						2.35
Li																
U	11.5	6.02	12.5	12.3	12	10.5	12.3	12	-10.2	-9.6	13.2	11.8	-8.9	13.8	10.4	-9
Mo	5.6	5.4	8.3	602	4.6	9.4	15.1	10.9	14.3	7.6	8.1	8.1	5.2	5.7	7	5.6
La	78.88	105.98				126.66	130.8			113.25						58.65
Ce	150.78	174.69				209	226.74			176.88						106.58
Pr	17.27	21.52				26.65	25.72			22.78						11.39
Nd	51.18	60.1				80.07	71.87			65.02						33.72
Sm	7.8	8.75				11.66	9.84			9.23						4.87
Eu	1.46	1.32				2.86	1.95			2.57						1.87
Gd	5.87	6.77				8.78	6.74			7.16						3.64
Tb	1.05	1.27				1.51	1.18			1.28						0.64
Dy	5.67	6.97				7.51	6.28			6.7						3.24
Ho	1.3	1.67				1.7	1.42			1.54						0.74
Er	3.57	4.76				4.41	4			4.08						1.97
Tm	0.61	0.88				0.73	0.7			0.7						0.34
Yb	3.79	5.73				4.42	4.49			4.29						2.16
Lu	0.65	1				0.76	0.77			0.74						0.38

Kanabeam Igneous Complex Whole Rock Analysis Data (XRF and ICP-MS)

Sample	VH-1	VH-10	VH-11	VH-12	VH-13	VH-14	VH-15	VH-16	VH-17	VH-2	VH-3	VH-4	VH-5	VH-6	VH-7	VH-8	VH-9
SiO2	57.782	60.793	68.026	77.93	76.083	76.231	46.736	76.063	76.109	54.782	58.585	59.608	61.281	60.936	61.015	57.367	57.423
TiO2	0.136	0.523	0.519	0.074	0.088	0.088	2.049	0.082	0.083	0.8	0.713	0.708	0.526	0.662	0.58	0.13	0.487
Al2O3	21.618	19.232	15.078	12.073	12.018	11.925	17.019	12.198	12.087	17.28	19.063	19.516	19.277	18.636	18.99	21.606	19.429
Fe2O3	4.267	4.164	3.917	0.612	2.123	2.177	13.215	2.085	2.145	8.343	5.297	4.788	4.184	4.576	4.618	3.206	5.682
MnO	0.124	0.117	0.014	0.001	0.001	0.003	0.22	0.001	0.041	0.255	0.16	0.136	0.118	0.12	0.123	0.077	0.172
MgO	0.327	0.563	0.709	0.001	0.001	0.001	6.852	0.001	0.001	2.623	0.851	0.889	0.593	0.723	0.589	0.186	0.444
CaO	0.949	1.25	1.708	0.058	0.364	0.353	10.247	0.31	0.262	4.431	2.427	2.138	1.261	1.538	1.276	0.868	1.546
Na2O	9.171	6.641	4.443	4.957	4.874	4.828	2.027	4.807	4.802	6.568	7.657	6.618	6.014	6.185	6.11	10.634	8.963
K2O	5.572	6.547	5.379	4.424	4.465	4.472	1.108	4.531	4.531	4.474	4.944	5.38	6.569	6.43	6.54	5.88	5.705
P2O5	0.056	0.17	0.206	0.005	0.023	0.016	0.527	0.016	0.032	0.444	0.303	0.219	0.176	0.192	0.157	0.048	0.149
Total	100.002	100	99.999	100.135	100.04	100.094	100	100.094	100.093	100	100	100	99.999	99.998	99.998	100.002	100
Ba	102	395	1020	42.8	49.9	101	347	82.3	56.7	965	3405	2370	1795	526	456	94.3	268
Rb	207	132	228	413	608	462	68.1	409	416	144	95.2	108	166	136	137	139	111
Sr	97.2	43.7	250	7.43	15.6	15.6	792	14	11.3	444	636	509	447	88.6	71	53.9	94
Y	13.1	25.8	43	23.8	74.5	58.7	40.3	31.2	50.8	43.9	35.4	26.7	63.4	21.4	18.9	7.3	26.9
Zr	407	372	450	196	535	317	214	240	316	586	467	351	800	343	266	73.7	283
Nb	85.7	160	93	78.2	223	135	48.7	116	135	218	208	169	207	146	140	31	198
Th	16	19.8	45.7	62.2	200	98.3	-12.8	83.8	118	25.1	22.7	16.7	38.5	19.9	20.5	-9.6	21.1
Pb	18.9	34.4	30.5	9.54	53.2	50	-14.2	49	45.3	22.8	29	28.3	25.2	32.4	17.8	-10.6	12
Zn	56.689	76.848	48.62	38.063	109.421	69.617	95.296	48.92	65.162	134.379	85.047	80.604	96.92	76.326	63.243	17.807	56.198
Cu	0.001	3.301	0.001	2.52	1.533	0.001	23.953	0.001	0.001	19.4	5.493	4.077	2.907	2.515	0.001	0.001	0.001
Ni	0.001	0.001	2.018	1.52	2.114	2.289	49.329	1.936	1.599	43.3	0.001	2.054	0.001	0.001	0.001	0.001	0.001
V			20.18	0.36	2.27					47.04	6.1						3.7
Cr			3.4	0.97	2.4					81.19	3.39						2.17
Hf			8.04	5.46	15.34					9.09	7.33						5.51
Cs			1.47	1.08	3.55					3.22	2.13						0.72
Sc	-0.7	1.2	5.9	0.24	0	-0.7	29.1	-0.7	-0.7	6.63	3.4	2.8	7.4	2	1.1	-0.8	1.6
Ta			5.44	6.78	17.51					11.03	9.41						7.09
Co			3.72	0.43	0.5					11.58	3.2						2.31
Li																	
U	-8.9	-9.1	14.5	10.1	21.2	22.8	-12	14	15.3	5.84	-9.6	-9.6	11.6	9.3	-9.3	-8.9	-9.3
Mo	2.7	6.1	5	-2.1	4.1	4	4.6	5.4	4.2	10.1	11.4	10	8.3	5.8	7.6	4.9	7.3
La			78.14	23.7	50.63					156	114.96						124.86
Ce			135.5	42.2	101.2					260.01	177.39						220.25
Pr			16.97	4.05	9.63					30.43	21.95						27.04
Nd			50.89	11.2	31.36					85.81	62.43						75.79
Sm			7.97	1.98	6.72					12.07	8.6						9.81
Eu			1.36	0.16	0.29					2.35	3.96						1.59
Gd			6.12	1.89	5.74					8.77	6.25						6.57
Tb			1.09	0.45	1.08					1.5	1.07						1.07
Dy			5.64	3.31	7.91					7.83	5.47						5.05
Ho			1.3	0.78	1.82					1.73	1.24						1.05
Er			3.5	2.77	6.82					4.65	3.28						2.53
Tm			0.6	0.49	1.16					0.77	0.56						0.4
Yb			3.74	3.68	8.77					4.89	3.44						2.45
Lu			0.65	0.56	1.25					0.88	0.58						0.47

CIPW NORM CALCULATION

SAMPLE	Quartz	Corundum	Orthoclase	Albite	Anorthite	Leucite	Nephelite	Acmite	Sod Metas	Diopside	Hypersthene	Olivine	Cal Ortho	Magnetite	Ilmenite	Apatite	m#
ND4	0	0	26.56	34.56	4.31	0	15.09	0	0	10.37	0	3.7	0	2.98	1.51	0.92	0.575
ND9	0	0	32.51	33.14	0	0	23.12	3.75	0.01	3.08	0	4.24	0	0	0.11	0.05	0.028
ND10	0	0	24.96	31.9	3.44	0	17.89	0	0	12.42	0	3.69	0	3.08	1.63	0.98	0.61
ND12	0	0	23.18	31.61	5.59	0	16.19	0	0	12.55	0	4.76	0	3.26	1.81	1.05	0.647
ND16a	0	0	0	0	19.46	7.34	19.42	0	0	37.21	0	9.23	1.21	3.28	2.09	0.77	0.871
ND17	0	0	24.55	33.28	6.38	0	14.59	0	0	10.66	0	4.79	0	3.12	1.62	1.01	0.626
ND19	0	0	25.73	35.42	5.1	0	13.99	0	0	10.07	0	4.15	0	3.03	1.54	0.96	0.588
ND20	0	0	4.44	10.37	28.85	0	10.26	0	0	26.92	0	11.68	0	4.03	2.61	0.84	0.833
ND21	0	0	28.8	45.25	7.19	0	5.02	0	0	5.07	0	4.12	0	2.5	1.37	0.67	0.563
ND22	0	0	25.13	43.34	12.23	0	5.22	0	0	2.51	0	5.03	0	3.08	2.21	1.25	0.513
ND23	0	0	24.69	43.39	15.23	0	3.35	0	0	1.08	0	5.88	0	3.01	2.17	1.2	0.544
ND25	0	0	24.96	42.22	8.29	0	3.11	0	0	9.04	0	5.57	0	3.36	2.16	1.29	0.638
ND26	0	0	23.82	46.58	8.13	0	2.25	0	0	6.98	0	5.7	0	3.27	2.05	1.24	0.615
ND28	0	0	23.45	45.68	9.3	0	1.56	0	0	7.34	0	5.96	0	3.35	2.1	1.25	0.621
ND30	0	0	23.39	43.82	6.81	0	4.44	0	0	7.62	0	6.86	0	3.66	2.14	1.25	0.623
ND31	0	0	25.75	45.88	7.94	0	0	0	0	7.72	4.02	2.4	0	3.21	1.95	1.13	0.614
ND35	0	0	37.99	47.65	3.52	0	0.86	0	0	4.62	0	1.91	0	2.06	1.02	0.38	0.349
ND38	0	0	24.45	44.92	7.1	0	3.19	0	0	8.57	0	5.14	0	3.28	2.08	1.28	0.614
ND40	0	0	28.77	45	3.83	0	4.88	0	0	3.74	0	7.12	0	3.45	1.99	1.22	0.594
ND44	0	0	24.57	31.99	4.06	0	16.89	0	0	12.42	0	4.17	0	3.18	1.71	1.01	0.622
ND46	0	0	32.65	34.34	0	0	22.41	0.97	0	4.44	0	3.01	0	1.84	0.22	0.12	0.114
ND47	0	0	24.38	31.38	5.85	0	15.33	0	0	12.28	0	4.79	0	3.17	1.74	1.1	0.652
ND48	0.5	0	35.97	48.92	0	0	0	4	1.39	3.75	5	0	0	0	0.44	0.03	0.01
GE-1	10.86	0	30.09	44.35	4.36	0	0	0	0	2.84	3.76	0	0	2.03	1.18	0.53	0.439
GE-2	8.67	0	34.39	46.46	2.66	0	0	0	0	2.97	2.16	0	0	1.57	0.81	0.31	0.353
GE-3	0	0	18.54	41.33	11.77	0	0	0	0	4.1	11.15	1.18	0	4.81	4.14	2.98	0.63
GE-4	0	0	16.61	40.44	18.95	0	10.33	0	0	5.2	0	2.9	0	2.27	2.26	1.06	0.636
GE-5	0	0	34.94	40.75	9.37	0	7.46	0	0	0.17	0	4.3	0	2.62	0.27	0.13	0.094
GE-6	0	0	35.86	35.14	3.54	0	18.55	0	0	1.52	0	3.06	0	1.89	0.27	0.17	0.251
GE-7	0	0	25.98	22.2	0	0	21.4	2.61	0	16.1	0	5.46	0	3.73	1.21	1.33	0.283
GE-8	0	0	28.42	38.98	5.08	0	11.95	0	0	7.28	0	3.76	0	2.78	1.09	0.66	0.497
GE-9	33.06	0	29.55	34.87	0.76	0	0	0	0	0.4	0.66	0	0	0.5	0.17	0.04	0.004
GE-10	20.47	0	29.73	37.68	5.12	0	0	0	0	0.67	3.59	0	0	1.67	0.75	0.33	0.344
GE-11	19.89	0	28.91	37.97	5.73	0	0	0	0	0.32	4.15	0	0	1.73	0.88	0.43	0.404
GE-11B	0	0	17.84	26.94	21	0	0	0	0	3.73	11.94	6.28	0	5.92	4.1	2.26	0.671
GE-12	17.48	0	30.82	37.46	5.85	0	0	0	0	1.03	4.05	0	0	1.82	1.01	0.47	0.437
GE-13	0	0	18.59	38.66	16.67	0	11.08	0	0	6.41	0	2.91	0	2.48	2.15	1.05	0.595
GE-14	0	0	37.48	46.52	6.55	0	2.91	0	0	1.42	0	2.49	0	1.67	0.7	0.26	0.33
GE-16	11.63	0	33.14	45.18	2.79	0	0	0	0	2.44	2.27	0	0	1.54	0.74	0.25	0.332
GE-17	0	0	32.51	27.08	0	0	26.69	3.54	2.44	3.82	0	3.65	0	0	0.19	0.09	0.063

CIPW NORM CALCULATION

SAMPLE	Quartz	Corundum	Orthoclase	Albite	Anorthite	Leucite	Nephelite	Acmite	Sod Metas	Diopside	Hypersthene	Olivine	Cal Ortho	Magnetite	Ilmenite	Apatite	m#
RS-1	11.69	0	28.39	44.29	6.35	0	0	0	0	1.22	4.36	0	0	1.93	1.2	0.57	0.463
RS-2	11.68	0	33.39	44.23	3.01	0	0	0	0	2.63	2.4	0	0	1.6	0.78	0.28	0.345
RS-2A	2.25	0	32.73	39.74	4.43	0	0	0	0	6.19	6.71	0	0	3.49	2.47	2.01	0.542
RS-3	3.86	1.23	21.62	48.23	12.43	0	0	0	0	0	7.83	0	0	3.18	1.14	0.48	0.349
RS-4	10.12	0	32.82	44.4	3.32	0	0	0	0	3.02	3.02	0	0	1.99	0.94	0.36	0.333
RS-5	0	0	34.98	40.24	0	0	13.69	2.41	0.21	6.47	0	1.13	0	0	0.64	0.24	0.253
RS-6	0	0	35.89	40.49	0.07	0	16.06	0	0	2.94	0	2.14	0	2.01	0.29	0.1	0.094
RS-7	0	0	35.19	35.44	3.42	0	19.33	0	0	1.51	0	2.8	0	1.86	0.32	0.15	0.208
RS-8	0	0	27.18	39.2	4.63	0	14.51	0	0	7.13	0	3.2	0	2.55	0.98	0.62	0.491
RS-9	0	0	35.05	48.57	3.79	0	5.26	0	0	3.2	0	1.66	0	1.6	0.64	0.23	0.316
RS-10	22.96	0	29.41	36.39	4.67	0	0	0	0	0.45	3.54	0	0	1.57	0.68	0.34	0.357
RS-11	0.98	0	25.61	52.98	8.48	0	0	0	0	1.12	6.01	0	0	2.82	1.49	0.51	0.352
RS-12	0.08	0	34.76	53.71	3.18	0	0	0	0	0.42	4.45	0	0	2.4	0.89	0.1	0.107
RS-13	0.28	0	21.95	53.67	10.82	0	0	0	0	0.59	7.3	0	0	3.11	1.65	0.62	0.392
RS-14	0	0	26.11	43.21	13.95	0	0.89	0	0	3.45	0	6.55	0	3.15	1.72	0.98	0.583
RS-15	0	0	25.6	29.79	2.32	0	21.07	0	0	12.33	0	3.59	0	3.01	1.43	0.87	0.598
VH-1	0	0	33.03	35.04	1.37	0	23.18	0	0	2.59	0	2.5	0	1.91	0.26	0.13	0.219
VH-2	0	0	26.59	32.5	4.48	0	12.68	0	0	12.18	0	5.28	0	3.74	1.53	1.03	0.566
VH-3	0	0	29.32	43.19	3.05	0	11.83	0	0	5.95	0	2.22	0	2.37	1.36	0.7	0.42
VH-4	0	0	31.9	45.89	7.68	0	5.58	0	0	1.28	0	3.67	0	2.14	1.35	0.51	0.465
VH-5	0	0.4	38.93	46.24	5.12	0	2.6	0	0	0	0	3.42	0	1.87	1	0.41	0.387
VH-6	0	0	38.12	45	4.11	0	4.06	0	0	1.93	0	3.02	0	2.04	1.26	0.45	0.425
VH-7	0	0	38.77	45.23	5.09	0	3.59	0	0	0.2	0	3.58	0	2.06	1.11	0.36	0.363
VH-8	0	0	35.09	26.9	0	0	28.31	2.13	1.96	3.53	0	1.72	0	0	0.25	0.11	0.145
VH-9	0	0	34.3	29.41	0	0	21.64	3.8	0.46	5.92	0	3.17	0	0	0.94	0.35	0.194
VH-10	0	0	38.8	43.19	3.34	0	7.13	0	0	1.5	0	2.79	0	1.86	1	0.4	0.376
VH-11	16.69	0	31.87	37.7	5.33	0	0	0	0	1.53	3.67	0	0	1.75	0.99	0.48	0.466
VH-12	34.21	0	26.16	37.49	0	0	0	0.4	0.9	0.23	0.46	0	0	0	0.14	0.01	0.006
VH-13	31.15	0	26.55	37.18	0	0	0	1.4	0.5	1.48	1.51	0	0	0	0.17	0.05	0.001
VH-14	31.56	0	26.58	36.64	0	0	0	1.44	0.52	1.48	1.58	0	0	0	0.17	0.04	0.001
VH-15	0	0	6.61	17.31	34.38	0	0	0	0	10.9	16.75	2.96	0	5.94	3.93	1.23	0.718
VH-16	30.68	0	26.92	37.72	0	0	0	1.38	0.25	1.28	1.59	0	0	0	0.16	0.04	0.002
VH-17	31.05	0	26.92	37.15	0	0	0	1.42	0.36	0.98	1.89	0	0	0	0.16	0.07	0.001